



5-2008

## **Development of an Accelerated Ash Loading Protocol for Rapid Evaluation of Diesel Particulate Filters Including Comprehensive Characterization of Ash-loaded Substrates**

Adam Daniel Youngquist  
*University of Tennessee - Knoxville*

Follow this and additional works at: [https://trace.tennessee.edu/utk\\_gradthes](https://trace.tennessee.edu/utk_gradthes)

 Part of the [Mechanical Engineering Commons](#)

---

### **Recommended Citation**

Youngquist, Adam Daniel, "Development of an Accelerated Ash Loading Protocol for Rapid Evaluation of Diesel Particulate Filters Including Comprehensive Characterization of Ash-loaded Substrates. " Master's Thesis, University of Tennessee, 2008.  
[https://trace.tennessee.edu/utk\\_gradthes/451](https://trace.tennessee.edu/utk_gradthes/451)

This Thesis is brought to you for free and open access by the Graduate School at TRACE: Tennessee Research and Creative Exchange. It has been accepted for inclusion in Masters Theses by an authorized administrator of TRACE: Tennessee Research and Creative Exchange. For more information, please contact [trace@utk.edu](mailto:trace@utk.edu).

To the Graduate Council:

I am submitting herewith a thesis written by Adam Daniel Youngquist entitled "Development of an Accelerated Ash Loading Protocol for Rapid Evaluation of Diesel Particulate Filters Including Comprehensive Characterization of Ash-loaded Substrates." I have examined the final electronic copy of this thesis for form and content and recommend that it be accepted in partial fulfillment of the requirements for the degree of Master of Science, with a major in Mechanical Engineering.

Ke Nguyen, Major Professor

We have read this thesis and recommend its acceptance:

Bruce G. Bunting, David K. Irick, J. Roger Parsons, Todd J. Toops

Accepted for the Council:

Carolyn R. Hodges

Vice Provost and Dean of the Graduate School

(Original signatures are on file with official student records.)



To the Graduate Council:

I am submitting herewith a thesis written by Adam Daniel Youngquist entitled "Development of an accelerated ash loading protocol for rapid evaluation of diesel particulate filters including comprehensive characterization of ash-loaded substrates." I have examined the final electronic copy of this thesis for form and content and recommend that it be accepted in partial fulfillment of the requirements for the degree of Master of Science, with a major in Mechanical Engineering.

---

**Dr. Ke Nguyen**  
Major Professor

We have read this thesis  
and recommend its acceptance:

---

**Dr. Bruce G. Bunting**

---

**Dr. David K. Irick**

---

**Dr. J. Roger Parsons**

---

**Dr. Todd J. Toops**

Accepted for the Council:

---

**Dr. Carolyn R. Hodges**  
Vice Provost and  
Dean of Graduate School

(Original signatures are on file with official student records)

**DEVELOPMENT OF AN ACCELERATED ASH LOADING  
PROTOCOL FOR RAPID EVALUATION OF DIESEL  
PARTICULATE FILTERS INCLUDING COMPREHENSIVE  
CHARACTERIZATION OF ASH-LOADED SUBSTRATES**

**A  
Thesis  
Presented for the  
Master's of Science Degree  
The University of Tennessee, Knoxville**

**Adam Daniel Youngquist  
May 2008**

## **DEDICATION**

To my mother, Sharon, and my grandparents, Dee and Joe.

## **ACKNOWLEDGEMENTS**

I would first like to thank my major professor, Dr. Ke Nguyen, for providing me an opportunity to continue my education, and for his continued encouragement, support, patience and insight throughout this entire endeavor. I would also like to express my sincere gratitude to my co-advisor, Dr. Bruce Bunting, for his willingness to share his vast technical knowledge and wisdom. In addition, I would like to thank my committee members, Dr. J. Roger Parsons, Dr. David “Butch” Irick and Dr. Todd J. Toops, for their individual contributions not only to my research, but also to my intellectual growth and confidence. I want to express my appreciation to Allan Patchen and Greg Jones at the University of Tennessee for contributing their particular expertise and knowledge throughout my entire graduate career, and to my laboratory colleagues Scott Eaton, Adam Foster and Nathan Ottinger, for their friendship and support during this project.

Lastly, I want to thank the Office of Vehicle Technologies within the United States Department of Energy and the Oak Ridge National Laboratory for their financial support of this research with Steve Goguen and Kevin Stork as sponsors.

## **ABSTRACT**

The accelerated ash loading of diesel particulate filters (DPFs) by lube-oil derived products is investigated in the present study. A 517-cc single-cylinder, naturally aspirated direct-injection diesel engine is used to accelerate ash formation by artificially increasing the rate of lube-oil consumption to approximately 40 times that observed during normal engine operation. Lube-oil consumption (LOC) is accelerated by blending diesel fuel with 5% by volume of standard 15-w40 lube oil and is subsequently injected through the fuel injector into the combustion chamber.

The ash loading protocol is a backpressure-based method of determining the amount of soot present within the DPF and initiating active regeneration upon achieving the target soot loading of 3 grams per liter. The final protocol employed a backpressure threshold that is defined for each individual loading by adding 0.20 psi to the baseline backpressure observed for that cycle, and consistently achieved the target soot loading. The active regeneration strategy was also refined to gradually increasing DPF temperatures to approximately 700°C.

A total of five full experiments are carried out in the present investigation. Two cordierite substrates, one silicon carbide substrate, and two mullite substrates are utilized to evaluate the performance of the accelerated ash loading protocol and make necessary refinements. The rate of backpressure increase with respect to ash accumulation varies substantially between substrates. Soot lightoff temperatures for all substrates are observed to be approximately 600°C, with ash having a minimal effect on this value

except in the highly-catalyzed substrates, where lightoff temperatures are initially lower but increase as ash accumulation limits exposure of the PGM to the soot layer.

Characterization techniques such as Electron Probe Microanalysis (EPMA), Scanning Electron Microscopy with Energy Dispersive Spectroscopy (SEM-EDS), X-ray Diffraction (XRD), and Inductively Coupled Plasma Atomic Emission Spectroscopy (ICP-AES) are used to analyze the ash layer for comparison to previously published results. All characterization results depict an ash layer that increases in thickness along the direction of flow within the DPF. The relative thickness of each ash layer is observed to be a strong function of the channel wall topography as well as the presence of catalyst and washcoat material.

## TABLE OF CONTENTS

<b>INTRODUCTION.....</b>	<b>1</b>
1.1 Overview.....	1
1.2 Legislation and Regulations.....	5
1.3 Long-Term DPF Durability .....	12
1.4 Scope of Investigation.....	14
<b>LITERATURE REVIEW .....</b>	<b>18</b>
2.1 Basic DPF Operation, Principles and Considerations.....	19
2.2 Field Observations of DPFs and Ash.....	28
2.3 Engine Bench Aging.....	31
2.4 Lube Oil and Ash Analysis .....	35
2.5 Accelerated Ash Loading.....	44
<b>EXPERIMENTAL APPARATUS AND PROCEDURES .....</b>	<b>53</b>
3.1 Engine Bench for Accelerated Ash Loading .....	53
3.1.1 Overall Description of Accelerated Ash Loading Engine Bench System .....	53
3.1.2 Diesel Engine.....	58
3.1.3 Drive Motor .....	58
3.1.4 Engine Load Controller.....	61
3.1.5 Post-Injection System.....	62
3.1.6 Instrumentation and Display.....	62
3.1.7 Data Acquisition System .....	66
3.2 Engine Operating Procedures and Strategies.....	69
3.2.1 Engine Start-up Procedure .....	69
3.2.2 DPF PM Loading.....	70
3.2.3 DPF Forced Regeneration.....	71
3.3 Experimental Filters and Upstream Catalysts.....	72
3.4 Characterization Techniques.....	73
3.4.1 Electron Probe Microanalysis .....	74
3.4.2 Scanning Electron Microscopy with Energy Dispersive X-Ray Spectroscopy .....	78

3.4.3 Powder X-ray Diffraction .....	80
3.4.4 Inductively Coupled Plasma - Atomic Emission Spectrometry.....	82
<b>RESULTS AND DISCUSSION .....</b>	<b>88</b>
4.1 Cordierite Substrate with Low PGM Loading .....	90
4.1.1 Cordierite Substrate with Low PGM Loading - Experimental Results.....	90
4.1.2 Cordierite Substrate with Low PGM Loading - Characterization Results.....	94
4.2 Cordierite Substrate with high PGM Loading .....	105
4.2.1 Cordierite Substrate with High PGM Loading – Experimental Results.....	105
4.2.2 Cordierite Substrate with High PGM Loading - Characterization Results...	109
4.3 Mullite Substrate with no PGM Loading.....	119
4.3.1 Mullite Substrate with No PGM Loading – Experimental Results .....	119
4.3.2 Mullite Substrate with no PGM - Characterization Results .....	124
4.4 Mullite Substrate with High PGM Loading.....	135
4.4.1 Mullite Substrate with High PGM Loading – Experimental Results .....	135
4.4.2 Mullite Substrate with High PGM Loading - Characterization Results.....	137
4.5 Silicon Carbide Substrate With No PGM Loading.....	149
4.5.1 SiC Substrate With No PGM Loading – Experimental Results .....	149
4.5.2 SiC Substrate With No PGM Loading) - Characterization Results.....	155
4.6 Overall Performance Evaluation and Comparisons.....	165
4.6.1 Effects of ash accumulation on system performance .....	165
4.6.2 Chemical Analysis of Fuel, Lube-oil and Ash-loaded Substrates.....	170
4.7 Comparisons of Characterization Results to Literature .....	177
<b>CONCLUSION .....</b>	<b>184</b>
<b>LIST OF REFERENCES .....</b>	<b>189</b>
<b>VITA.....</b>	<b>204</b>



## LIST OF TABLES

TABLE	PAGE
1.1. EPA emission and durability standards for US passenger vehicles produced after model year 2004 <sup>[8,9]</sup> .....	10
1.2. EPA emission and durability standards for US passenger vehicles produced after model year 2009 <sup>[8,9]</sup> .....	11
2.1. Analysis of mileage, lube oil consumption and ash characterization <sup>[47]</sup> .....	30
2.2. Chemical analysis of several lube oil formations <sup>[27]</sup> .....	37
2.3. Analysis of ash in a DPF after 200 hours of ash accumulation <sup>[27]</sup> .....	38
3.1. List of available signals and components handled by the DAQ System .....	66
3.2. Supplemental fuel injection settings and flow rates .....	72
3.3. Experimental DPF and DOC Specifications .....	73
4.1. DPF test matrix with ash accumulation and performance summary .....	170
4.2. Quantification of ash constituents in oil, fuel and ash-loaded substrates.....	171

## LIST OF FIGURES

FIGURE	PAGE
1.1. Breakdown of diesel engine usage worldwide in 1995, by type <sup>[1]</sup> .....	2
1.2. US oil import by country of origin (Data taken from October 2007 EIA estimates <sup>[4]</sup> .....	3
1.3. Global temperature departure from long-term mean between 1850 and 2000 <sup>[7]</sup> ..	5
1.4. US light duty emission standards through 2010 (data from US EPA regulations) <sup>[8]</sup> .....	7
1.5. US Heavy Duty Emission Standards (data from US EPA regulations) <sup>[8]</sup> .....	7
1.6. List of techniques currently available to reduce diesel exhaust emissions <sup>[9]</sup> .....	9
1.7. X-Ray analysis of ash accumulation in a DPF after 90,000 km of operation [10] .....	12
2.1. NO <sub>2</sub> formation as a function of exhaust gas temperature <sup>[31]</sup> .....	20
2.2. Experimental PM oxidation as a function of exhaust gas temperature for NO <sub>2</sub> and O <sub>2</sub> <sup>[31]</sup> .....	21
2.3. Experimental PM oxidation in the presence and absence of a fuel-borne catalyst as a function of exhaust gas temperature and composition <sup>[32]</sup> .....	22
2.4. NO conversion performance for two catalysts before and after catalyst regeneration at 450°C <sup>[33]</sup> .....	23
2.5. Example soot formation and deposition rate plot <sup>[38]</sup> .....	24
2.6. Typical DPF temperatures during regeneration <sup>[41]</sup> .....	25
2.7. Visualization of soot loading in DPF as a function of time <sup>[46]</sup> .....	27
2.8. Visualization of regeneration with inlet gas temperature of 799°C <sup>[46]</sup> .....	27
2.9. Visualization of regeneration with inlet gas temperature of 867°C <sup>[46]</sup> .....	27
2.10. Vehicle speed and associated NO <sub>x</sub> formation versus time for an urban bus application <sup>[50]</sup> .....	31
2.11. Exhaust backpressure vs. soot loading <sup>[53]</sup> .....	32
2.12. Photographs of soot layer in a cordierite substrate <sup>[53]</sup> .....	33
2.13. Peak temperature experiences during regeneration vs. DPF temperature ramping rate <sup>[54]</sup> .....	34

2.14.	PM oxidation rate vs. gas temperature for different DPF and DOC configurations <sup>[55]</sup> .....	35
2.15.	Engine setting regions facilitating continuous regeneration for two DPF and DOC Configurations <sup>[55]</sup> .....	35
2.16.	DPF ash accumulation as a function of oil consumption <sup>[26]</sup> .....	36
2.17.	Ash distribution along the length an ash-loaded DPF for three lube oil formulations <sup>[28]</sup> .....	39
2.18.	SEM image of soot particles (10K X) <sup>[29]</sup> .....	41
2.19.	SEM image of soot particles (100K X) <sup>[29]</sup> .....	41
2.20.	SEM of ash layer on channel wall of a SiC DPF <sup>[27]</sup> .....	42
2.21.	Optical microscope analysis of ash layer at various locations of DPFs aged using three oil formulations <sup>[28]</sup> .....	43
2.22.	EPMA elemental maps of ash layer in a cordierite substrate aged with a low-ash lube oil A (200X) <sup>[28]</sup> .....	43
2.23.	EPMA elemental maps of ash layer in a cordierite substrate aged with a low-ash lube oil B (200X) <sup>[28]</sup> .....	43
2.24.	EPMA backscatter image and elemental map showing calcium in the ash layer of a cordierite substrate (1000X) <sup>[28]</sup> .....	44
2.25.	Schematic of accelerated lube oil consumption mechanisms (1. PCV Blow-by, 2. Valve seal leakage, 3. Leakage past piston rings) <sup>[30]</sup> .....	46
2.26.	Lube oil consumption calculation based on calcium and zinc <sup>[30]</sup> .....	46
2.27.	DPF weight increase as a function of oil consumption during 120-hour test for 3 engines of different ages <sup>[66]</sup> .....	47
2.28.	Variation in the lube oil consumption over a 40-hour experiment <sup>[66]</sup> .....	48
2.29.	SEM images of the ash and soot layer formed using intake manifold oil injection <sup>[67]</sup> .....	49
2.30.	DPF weight increase versus lube oil consumption using doped fuel <sup>[67]</sup> .....	49
2.31.	DPF weight increase versus lube oil consumption using oil misting <sup>[67]</sup> .....	51
2.32.	Backpressure increase as a function of time for experiments using doped and non-doped fuel <sup>[68]</sup> .....	52

2.33.	SEM images of ash layers for three oil consumption mechanisms <sup>[68]</sup> .....	52
3.1.	Schematic of the RPEB System .....	54
3.2.	Photograph of the rapid aging engine bench with system components .....	56
3.3.	Photograph of the Hatz diesel engine used for rapid DPF aging .....	59
3.4.	Photograph of the Baldor drive motor used to control the Hatz engine.....	60
3.5.	Photograph of the engine load controller assembly .....	61
3.6.	Photograph of the supplemental fuel injector.....	63
3.7.	Photograph of the supplemental fuel pump and temperature control .....	64
3.8.	Photograph of the supplemental fuel injection control panel.....	65
3.9.	Wiring diagram of the DAQ system and ancillary equipment.....	67
3.10.	LabVIEW user interface numerical “Data Monitoring” tab .....	68
3.11.	LabVIEW user interface “Time-Elapsed Graphs” tab .....	68
3.12.	Photograph of the drive motor power and control units.....	70
3.13.	Schematic of available electron emission pathways <sup>[71]</sup> .....	75
3.14.	Photograph of the Cameca Electron Probe Microanalysis hardware .....	76
3.15.	Photograph of the scanning electron microscopy hardware with energy dispersive spectrometry detector .....	81
3.16.	Photograph of the scanning electron microscopy hardware with energy dispersive spectrometry detector .....	84
3.17.	Schematic and photograph of a typical ICP torch <sup>[76]</sup> .....	86
3.18.	Photograph of an Inductively Couple Plasma Atomic Emission Spectrometer.....	87
4.1.	DPF solid temperatures versus time for cordierite substrate with low PGM loading .....	92
4.2.	Exhaust gas temperatures at various locations versus time for cordierite substrate with low PGM loading .....	92
4.3.	Exhaust backpressure versus time for cordierite substrate with low PGM loading .....	93
4.4.	DPF mass data versus time for cordierite substrate with low PGM loading.....	93
4.5.	Photograph of one-quarter sample from front section of cordierite substrate	

	with low PGM loading .....	95
4.6.	Photograph of one quarter sample from rear section of cordierite substrate with low PGM loading .....	95
4.7.	Photographs of representative samples extracted from the front, front-middle, middle and rear sections of the cordierite substrate with low PGM loading .....	96
4.8.	EPMA Elemental maps of front section of cordierite substrate with low PGM loading .....	97
4.9.	EPMA Elemental maps of front section of cordierite substrate with low PGM loading .....	97
4.10.	EPMA Elemental maps of middle section of cordierite substrate with low PGM loading .....	98
4.11.	EPMA Elemental maps of middle section of cordierite substrate with low PGM loading .....	98
4.12.	EPMA Elemental maps of rear section of cordierite substrate with low PGM loading .....	99
4.13.	EPMA elemental maps of rear section of cordierite substrate with low PGM loading .....	99
4.14.	SEM image of front section channel (38X).....	102
4.15.	SEM image of middle section channel (38X) .....	102
4.16.	SEM image of rear section channel (38X) .....	102
4.17.	SEM image of front section channel (110X).....	103
4.18.	SEM image of rear section channel (110X) .....	104
4.19.	DPF solid temperatures versus time for cordierite substrate with high PGM loading .....	106
4.20.	Exhaust gas temperatures at various locations versus time for cordierite substrate with high PGM loading.....	106
4.21.	Exhaust backpressure versus time for cordierite substrate with high PGM loading .....	108
4.22.	DPF mass data versus time for cordierite substrate with high PGM loading....	108
4.23.	Photograph of one- quarter sample from front section of cordierite substrate	

	with high PGM loading .....	109
4.24.	Photograph of one- quarter sample from rear section of cordierite substrate with high PGM loading .....	109
4.25.	Photographs of representative samples extracted from the front, middle, middle-rear and rear sections of cordierite substrate with high PGM loading .....	110
4.26.	Elemental maps of front section of cordierite substrate with high PGM loading .....	111
4.27.	Elemental maps of front section of cordierite substrate with high PGM loading .....	111
4.28.	Elemental maps of middle section of cordierite substrate with high PGM loading .....	112
4.29.	Elemental maps of middle section of cordierite substrate with high PGM loading .....	112
4.30.	Elemental maps of rear section of cordierite substrate with high PGM loading	114
4.31.	Elemental maps of rear section of cordierite substrate with high PGM loading	114
4.32.	SEM image of front section channel (38X).....	115
4.33.	SEM image of middle section channel (38X) .....	115
4.34.	SEM image of rear section channel (38X) .....	115
4.35.	SEM image of front section channel (110X).....	117
4.36.	SEM image of rear section channel (110X) .....	118
4.37.	DPF solid temperatures versus time for non-catalyzed mullite substrate .....	122
4.38.	Exhaust gas temperatures at various locations versus time for non-catalyzed mullite substrate .....	122
4.39.	Exhaust backpressure versus time for non-catalyzed mullite substrate .....	123
4.40.	DPF mass data versus time for non-catalyzed mullite substrate .....	123
4.41.	Photograph of one-quarter sample from front section of non-catalyzed mullite substrate .....	124
4.42.	Photograph of one-quarter sample from rear section of non-catalyzed mullite substrate .....	124
4.43.	Photographs of representative samples extracted from the front, front-middle,	

	middle and rear sections of non-catalyzed mullite substrate.....	125
4.44.	Elemental maps of front section of non-catalyzed mullite substrate.....	126
4.45.	Elemental maps of front section of non-catalyzed mullite substrate.....	126
4.46.	Elemental maps of middle section of non-catalyzed mullite substrate .....	127
4.47.	Elemental maps of middle section of non-catalyzed mullite substrate .....	127
4.48.	Elemental maps of rear section of non-catalyzed mullite substrate .....	128
4.49.	Elemental maps of rear section of non-catalyzed mullite substrate .....	128
4.50.	SEM image of front section channel (38X).....	130
4.51.	SEM image of middle section channel (38X) .....	130
4.52.	SEM image of rear section channel (38X) .....	130
4.53.	SEM image of front section channel (110X).....	132
4.54.	SEM image of rear section channel (110X) .....	133
4.55.	DPF solid temperatures versus time for mullite substrate with high PGM loading .....	136
4.56.	Exhaust gas temperatures at various locations versus time for mullite substrate with high PGM loading .....	136
4.57.	Graphic representation of ash layer formation stages for mullite DPF .....	137
4.58.	Exhaust backpressure versus time for mullite substrate with high PGM loading .....	138
4.59.	DPF mass data versus time for mullite substrate with high PGM loading.....	138
4.61.	Photograph of one-quarter sample from middle section of mullite substrate with high PGM loading .....	139
4.62.	Photograph of one-quarter sample from middle section of mullite substrate with high PGM loading .....	139
4.63.	Photographs of representative samples extracted from the front, front-middle, middle and rear sections of mullite substrate with high PGM loading .....	140
4.64.	Elemental maps of front section of mullite substrate with high PGM loading .	141
4.65.	Elemental maps of front section of mullite substrate with high PGM loading .	141
4.66.	Elemental maps of middle section of mullite substrate with high PGM loading .....	142

4.67.	Elemental maps of middle section of mullite substrate with high PGM loading .....	142
4.68.	Elemental maps of rear section of mullite substrate with high PGM loading...	143
4.69.	Elemental maps of rear section of mullite substrate with high PGM loading...	143
4.70.	SEM image of front section channel (38X).....	145
4.71.	SEM image of middle section channel (38X) .....	145
4.72.	SEM image of rear section channel (38X) .....	145
4.73.	SEM image of front section channel (110X)..... <b>Error! Bookmark not defined.</b>	
4.74.	SEM image of rear section channel (110X) .....	148
4.75.	DPF solid temperatures versus time for non-catalyzed SiC substrate.....	151
4.76.	Exhaust gas temperatures at various locations versus time for non-catalyzed SiC substrate.....	151
4.77.	Exhaust backpressure versus time for non-catalyzed SiC substrate.....	153
4.78.	DPF mass data versus time for non-catalyzed SiC substrate .....	154
4.79.	DPF mass data versus time for non-catalyzed SiC substrate .....	154
4.80.	Photograph of one-quarter sample from front section of non-catalyzed SiC substrate.....	155
4.81.	Photograph of small cross-section from middle section of non-catalyzed SiC substrate.....	155
4.82.	Photographs of representative samples extracted from the front, front-middle, middle and rear sections of non-catalyzed SiC substrate .....	156
4.83.	Elemental maps of front section of non-catalyzed SiC substrate .....	157
4.84.	Elemental maps of front section of non-catalyzed SiC substrate .....	157
4.85.	Elemental maps of middle section of non-catalyzed SiC substrate.....	158
4.86.	Elemental maps of middle section of non-catalyzed SiC substrate.....	158
4.87.	Elemental maps of rear section of non-catalyzed SiC substrate .....	159
4.88.	Elemental maps of rear section of non-catalyzed SiC substrate .....	159
4.89.	SEM image of front section channel (38X).....	161
4.90.	SEM image of middle section channel (38X) .....	161
4.91.	SEM image of rear section channel (38X) .....	161



4.92.	SEM image of front section channel (110X).....	163
4.93.	SEM image of rear section channel (110X) .....	164
4.94.	Baseline backpressure averages versus ash accumulation .....	166
4.95.	Baseline backpressure averages versus ash accumulation .....	167
	(modified view) .....	167
4.96.	Soot lightoff temperature versus ash accumulation .....	169
4.97.	Quantification of ash constituents by location in lightly-catalyzed cordierite substrate (Test 3) .....	173
4.98.	Quantification of ash constituents by location in non-catalyzed SiC substrate (Test 4) .....	173
4.99.	Quantification of ash constituents by location in highly-catalyzed mullite substrate (Test 5) .....	174
4.100.	XRD patterns of accumulated ash in non-catalyzed SiC DPF .....	176
4.101.	XRD patterns of accumulated ash in highly-catalyzed mullite DPF.....	176
4.102.	XRD patterns of accumulated ash in highly-catalyzed cordierite DPF.....	177
4.103.	Visual comparison of ash layers formed in two cordierite substrates.....	179
4.104.	EPMA elemental map comparison of ash layers formed in two cordierite substrates.....	180
4.105.	SEM image comparison of ash agglomerates formed in two cordierite substrates 181	
4.106.	SEM image comparison of ash particles formed in two cordierite substrates ..	182

## NOMENCLATURE

%.....	percentage
$\Phi$ .....	work function
$\theta$ .....	angle
$\lambda$ .....	wavelength
$\mu\text{A}$ .....	microamperes
$\mu\text{m}$ .....	micrometers
$\nu$ .....	frequency
$^{\circ}$ .....	degrees
$^{\circ}\text{C}$ .....	degrees Celsius
$^{\circ}\text{F}$ .....	degrees Fahrenheit
A.....	amperes
AC.....	alternating current
Al.....	aluminum
$\text{Al}_2\text{O}_3$ .....	alumina
Ar.....	argon
C.....	carbon atom
Ca.....	calcium
CaO.....	calcium oxide
$\text{CaSO}_3$ .....	calcium sulfite
$\text{CaSO}_4$ .....	calcium sulfate
$\text{Ca}_3(\text{PO}_4)_2$ .....	calcium phosphate
CAA.....	Clean Air Act
cc.....	cubic centimeters
cc/min.....	cubic centimeters per minute
Ce.....	cerium
$\text{CeO}_2$ .....	ceria
cm.....	centimeters

CO.....	carbon monoxide
CO <sub>2</sub> .....	carbon dioxide
cpsi.....	cells per square inch
CR-DPF.....	continuously-regenerating diesel particulate filter
CSF.....	catalyzed soot filter
Cu.....	copper
d.....	distance
DAQ.....	data acquisition system
DC.....	direct current
DI.....	direct injection
dm <sup>3</sup> .....	cubic decimeters
DOC.....	diesel oxidation catalyst
DPF.....	diesel particulate filter
e.....	electron
EDS.....	energy dispersive spectroscopy
EIA.....	Energy Information Administration
EPA.....	Environmental Protection Agency
EPMA.....	electron probe microanalysis
eV.....	electron volts
FBC.....	fuel borne catalyst
ft.....	feet
FTP.....	federal testing protocol
g.....	grams
g/ft <sup>3</sup> .....	grams per cubic foot
GHSV.....	gas hourly space velocity
GHz.....	giga-Hertz
HC.....	hydrocarbon
hp.....	horsepower
hr.....	hours

hr <sup>-1</sup>	per hour
Hz	Hertz
in.	inches
in-lbs.	inch pounds
km.	kilometer
kW	kilowatts
L	liters
L/min	liters per minute
lbs.	pounds
LCD	liquid crystal display
LNT	lean NO <sub>x</sub> trap
LPM	liters per minute
m.	meters
m <sup>2</sup>	square meters
M	mass
mA	milli-amperes
MFC	mass flow controller
mi.	miles
min.	minutes
mm.	mm
mph.	miles per hour
NA	naturally-aspirated
NDIR	non-dispersive infrared
nm.	nanometers
NMR	nuclear magnetic resonance
NO	nitric oxide
NO <sub>2</sub>	nitrogen dioxide
NO <sub>x</sub>	oxides of nitrogen
O	oxygen

O <sub>2</sub>	oxygen molecule
O <sub>3</sub>	ozone
P	phosphorus
PC	personal computer
PGM	platinum group metals
PM	particulate matter
ppm	parts per million
psi	pounds per square inch
psig	pounds per square inch gage
Pt	platinum
PT	pressure transducer
RPM	revolutions per minute
s	seconds
SEM	scanning electron microscopy
Si	silicon
SI	spark ignition
SiO <sub>2</sub>	silicon dioxide
SOF	soluble organic fraction
STP	standard temperature and pressure
TC	thermocouple
THC	total hydrocarbon
TWC	three-way catalyst
UHV	ultra-high vacuum
V	volume/volt
wt	weight
XRD	X-ray diffraction
ZDDP	zinc dialkyldithiophosphate
ZEV	zero emission vehicle
Zn	zinc

$\text{ZnO}$ .....zinc oxide  
 $\text{Zn(PO}_3)_2$ .....zinc phosphate  
 $\text{ZnSO}_4$ .....zinc sulfate

# **CHAPTER 1**

## **INTRODUCTION**

This chapter provides the relevant background information that motivates the study of diesel particulate filters (DPFs). An overview of the benefits and challenges presented by the use of diesel engines for various automotive applications are presented in Section 1.1. A brief description of current and future trends in domestic and foreign emission regulations as well as the techniques and technologies being employed to meet these increasingly stringent requirements is provided in Section 1.2. A discussion of the challenges facing the wide spread implementation of DPF systems and a detailed discussion of the current investigation are presented in Sections 1.3 and 1.4, respectively.

### **1.1 Overview**

Diesel engines are widely used as source of power for various applications all around the world, with transportation-related applications responsible for the majority of diesel engine usage. A study conducted in 1995 by Mori [1] estimated the total number of vehicles owned worldwide was approximately 640 million, with roughly 67 million of them powered by diesel engines. Diesel engines are classified into different categories according to the duty-cycle and total power requirement, both of which depend on the intended application. A breakdown of diesel engine usage, shown in Figure 1.1, shows that more than two-thirds are used in passenger cars, with a notable portion of more than

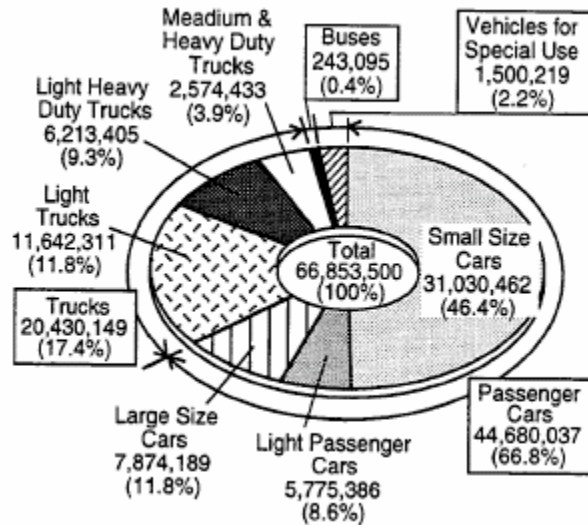


**Figure 1.1: Breakdown of diesel engine usage worldwide in 1995, by type[1]**

17% belonging to the truck market. While spark-ignition engines dominate the US vehicle market at the time this study was carried out, diesel engines have been the subject of increased research and implementation as of late. Diesel engines traditionally possess an inherently high fuel efficiency coupled with long-term durability, both of which are important to a market that is becoming increasingly concerned with rising fuel costs and environmental protection. The increase in efficiency is the result of the required air/fuel ratios for each engine. Spark-ignition engines employ a throttling process and require a stoichiometric air/fuel ratio for three-way catalyst operation, resulting in throttling losses and higher HC and CO emissions. Diesel engines do not employ a throttling process, instead utilizing significantly higher compression ratios with a lean air/fuel ratio, resulting in a larger percentage of fuel being consumed during the power stroke which, when combined with a higher density fuel, results in better fuel economy. With regard to longevity of usage, typical SI engines are designed for a lifetime of approximately



100,000 miles, while typical diesel engines are design to exceed 500,000 miles of usage, with some heavy-duty engines designed to achieve over 1,000,000 miles [2,3]. These combined benefits of diesel engines ensure its place in global infrastructure, making it the almost exclusive powerplant of choice for buses, trains and heavy construction machinery.

Recently, diesel engines have become the subject of increased research for employment with hybrid vehicles and other alternative power applications, all of which are intended to reduce US dependence on foreign oil. Figure 1.2 represents a breakdown of US oil import from various countries in thousands of barrels per day in the month of October 2007. These figures, published by the Energy Information Administration (EIA) indicate that the US imports more than 10 million barrels of crude oil daily. Since approximately one third of this oil originates in countries that the US deems “hostile,” this emphasizes the need to reduce the amount of oil imported from these regions in order to secure future energy supplies for the United States.

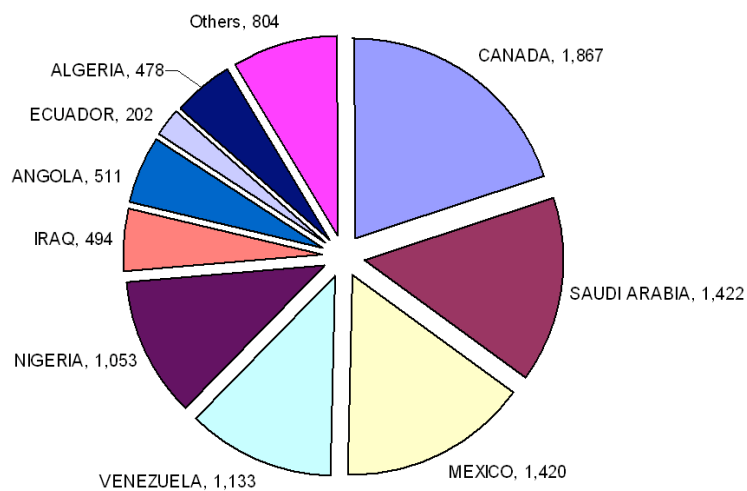


**Figure 1.2: US oil import by country of origin (Data taken from October 2007 EIA estimates<sup>[4]</sup>)**

Another issue prompting increased implementation of diesel engine technologies is global warming from the production of greenhouse gases. In 2003, the EIA estimated that global CO<sub>2</sub> production from the production and combustion of petroleum products, natural gas and coal was approximately 25.2 billion metric tons per year, an increase of nearly 20 percent from 1993 [5]. The use of gasoline, diesel fuel and other petroleum products is responsible for more than 42 percent of that total, with the United States responsible for approximately one quarter of global CO<sub>2</sub> production [6]. The EPA estimates that these increased CO<sub>2</sub> levels in the atmosphere are responsible for a global temperature increase of approximately 1°F over the last 100 years, as shown in Figure 3. A pronounced increase in the departure from the long-term global average temperature is clearly visible over the last 30 years during which CO<sub>2</sub> production rates have been highest [7]. Given the current global CO<sub>2</sub> production rate, the EPA estimates that by the year 2100, the average global temperature will rise by as much as 5°F, which will significantly impact global weather in unknown ways.

In response to elevated CO<sub>2</sub> production rates, the US and many other countries are considering placing limits on the amount of CO<sub>2</sub> that can be released by the production and combustion of fossil fuels. Since diesel engines are inherently more fuel-efficient than their spark-ignition counterparts, their presence in the passenger transport market is becoming commonplace. However, the fuel-saving benefits associated with diesel engines are associated with an increase in the production of both particulate matter (PM) and oxides of nitrogen (NO<sub>x</sub>), which have been identified as contributors to smog formation, greenhouse effects, and even acid rain, and have also been shown to result in

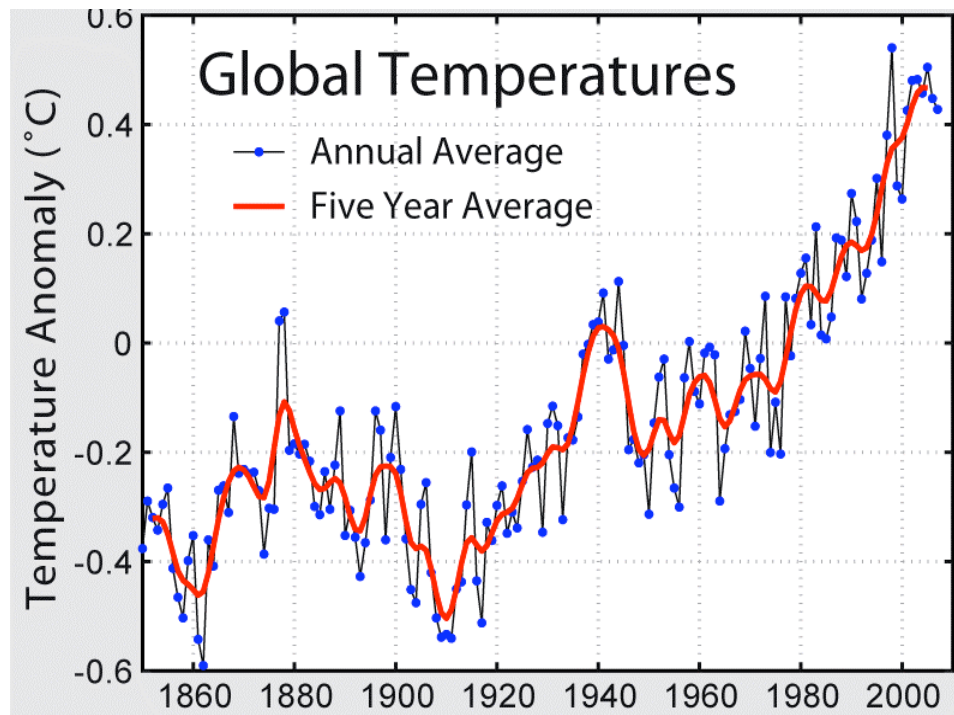


**Figure 1.3: Global temperature departure from long-term mean between 1850 and 2000<sup>[7]</sup>**

health issues such as lung cancer. Ongoing research aims at reducing these harmful products, thus legitimizing the use of diesel engines as cleaner, more efficient sources of power.

## 1.2 Legislation and Regulations

In 1970, Congress established the Environmental Protection Agency and assigned it the responsibility for regulating pollution generated by motor vehicles. By 1975, most new gasoline powered cars were equipped with catalytic converters to reduce the emission of HC, CO and NO<sub>x</sub>; they were the first aftertreatment devices to be employed on a large scale. In 1990, Congress enacted the Clean Air Act (CAA) to investigate automotive emissions and establish emission standards aimed at reducing these

emissions. The Clean Air Act placed stringent compliance deadlines for the consistent reduction of air-borne pollutants from all sources including passenger vehicles and heavy-duty equipment. Numerous amendments have since been added, each successively reducing the allowable amount of pollutant emission, with the eventual goal of developing zero emission vehicles (ZEVs). To evaluate these emissions consistently on a widespread scale, the EPA developed the dynamometer-based Federal Testing Protocol (FTP), in which actual driving conditions are simulated, and emission levels of PM, THC, CO and NO<sub>x</sub> are measured.

Of primary concern with diesel engines is the emission of particulate matter and oxides of nitrogen. Both the US and Europe have established several deadlines spanning from 1998 to 2010, each of which requires the reduction in the emission of one of both of these pollutants. Figure 1.4 is a graphical representation of emission standards for light duty vehicles through 2010. These standards are based on grams per mile, with the most stringent emissions window belonging to Tier 2 Bin 5 vehicles, requiring emission levels of less than 0.1 grams per mile for PM and 0.07 grams per mile for NO<sub>x</sub>. This graphic representation provides a visual understanding of the target windows over the timeline set forth by the EPA.

For heavy-duty vehicles, maximum allowable emission levels are defined in grams per horsepower per hour, a basis of comparison more suitable for commercial trucks and buses. Once again, graphical representation of the heavy duty vehicle emission standards, seen in Figure 1.5, demonstrates the target windows for the two pollutants of primary concern, culminating in the 2010 limits of 0.01 grams per horsepower hour of PM and 0.2 grams per horsepower hour of NO<sub>x</sub> [8].

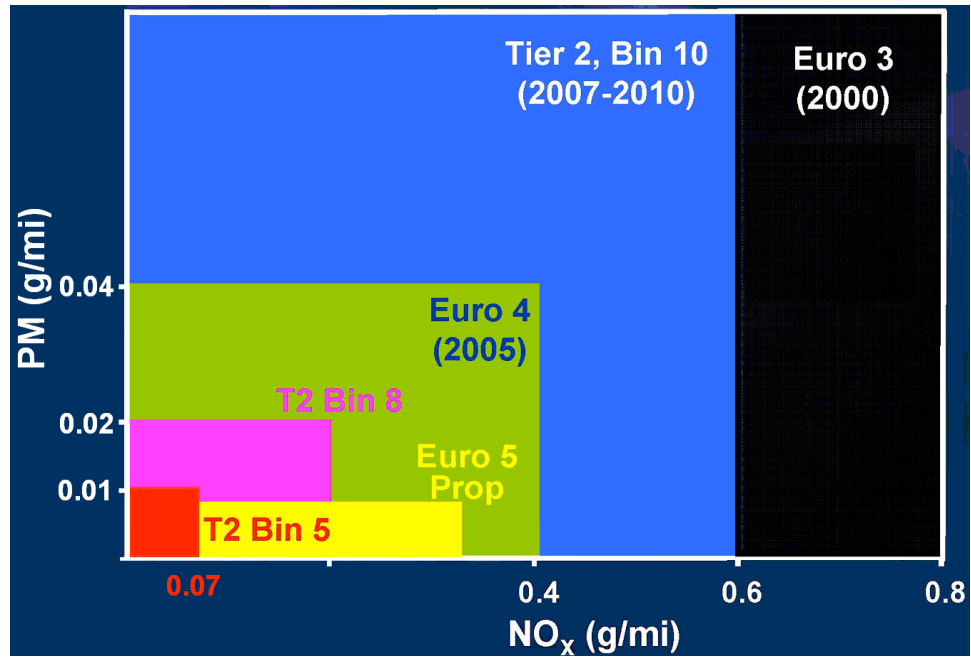


Figure 1.4: US light duty emission standards through 2010 (data from US EPA regulations)<sup>[8]</sup>

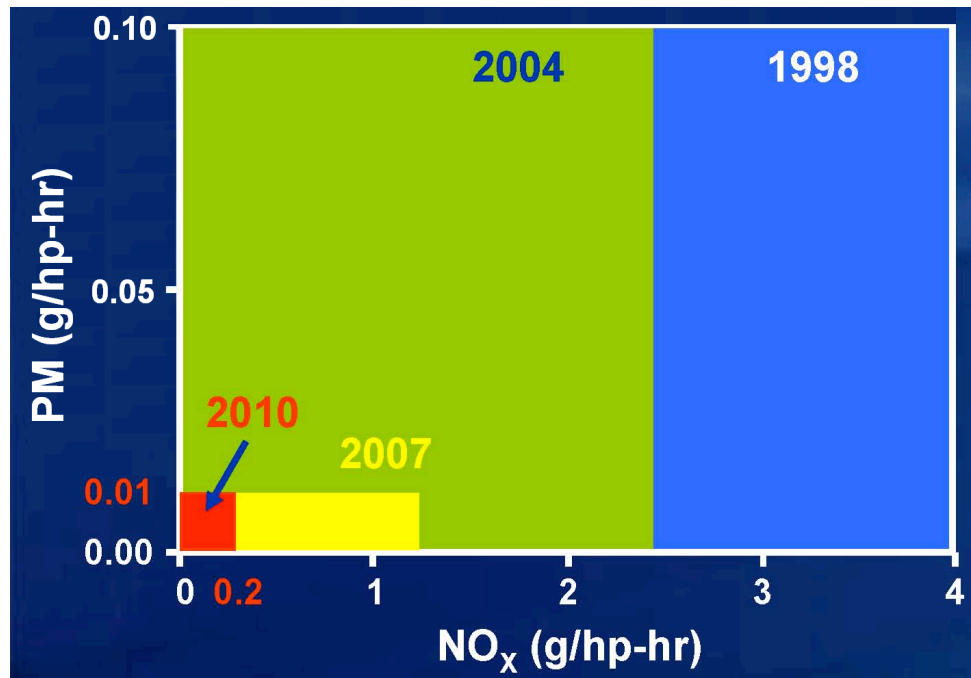


Figure 1.5: US Heavy Duty Emission Standards (data from US EPA regulations)<sup>[8]</sup>

The vast majority of early diesel aftertreatment devices were engineered to reduce the soluble organic fraction (SOF) and other particulate matter through oxidation. SOF often represents a significant portion of the soot produced and can be readily oxidized in the typically lean exhaust of diesel engines. Hence, vehicle manufacturers could often achieve these limits simply by targeting the SOF components of the diesel exhaust.

More stringent regulations that have been passed recently have required more sophisticated systems and techniques to achieve emission levels below the allowable limits. Several techniques that are currently being employed to achieve desired emission levels and meet EPA regulations are shown in Figure 1.6 [9]. More recent legislation includes durability requirements for aftertreatment products in which light duty systems must remain compliant over a lifetime of 100,000 miles or more. A tier system based on vehicle size and duty cycle has been developed to rate the performance of vehicles manufactured after the year 2000, and allowable emission levels for specific mileages. These standards published in tabular form based on year of vehicle manufacture, can be found in Tables 1.1 and 1.2. For these new regulations, vehicle manufacturers designate the tier in which each vehicle belongs as long as the entire fleet is below a specific average emission standard. For the 2009 model year compliance deadline, tiers 9 and 10 are defined as intermediate steps targeted for 2006 and 2008.

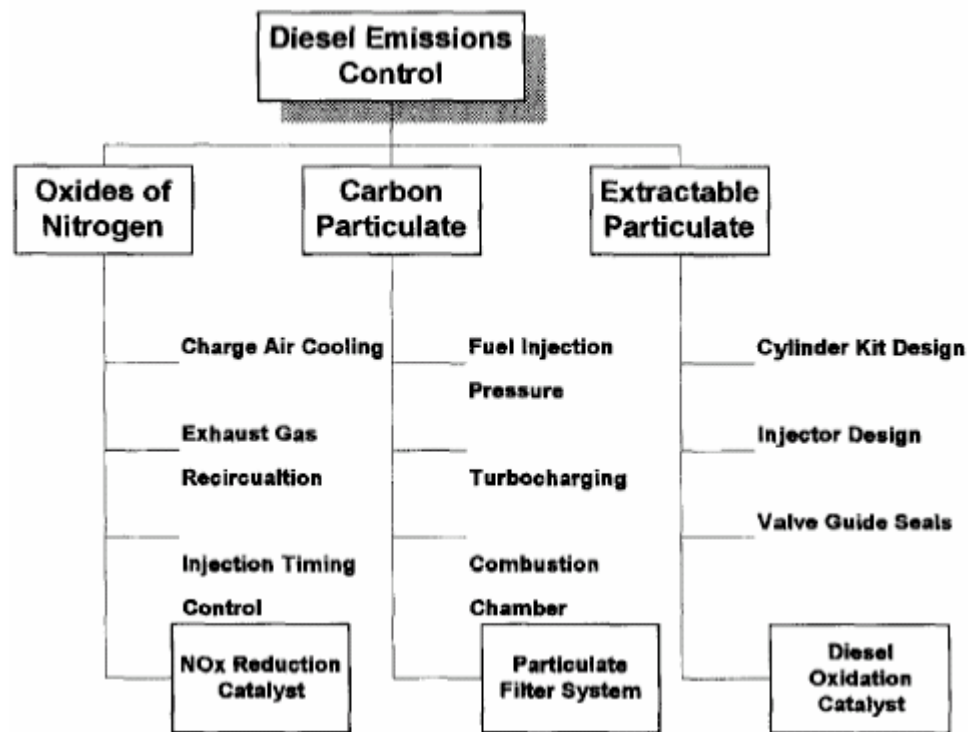


Figure 1.6: List of techniques currently available to reduce diesel exhaust emissions<sup>[9]</sup>

**Table 1.1: EPA emission and durability standards for US passenger vehicles  
produced after model year 2004<sup>[8,9]</sup>**

Category	50,000 miles / 5 years						100,000 miles / 10 years <sup>1</sup>					
	THC	NMHC	CO	NO <sub>x</sub> CI	NO <sub>x</sub> SI	PM	THC	NMHC	CO	NO <sub>x</sub> CI	NO <sub>x</sub> SI	PM
<b>Passenger Cars</b>	0.41	0.25	3.4	1.0	0.4	0.08	-	0.31	4.2	1.25	0.6	0.10
<b>LLDT, LVW &lt;3750 lbs</b>	-	0.25	3.4	1.0	0.4	0.08	0.80	0.31	4.2	1.25	0.6	0.10
<b>LLDT, LVW &gt;3750 lbs</b>	-	0.32	4.4	-	0.7	0.08	0.80	0.40	5.5	0.97	0.97	0.10
<b>HLDT, ALVW &lt;5750 lbs</b>	0.32	-	4.4	-	0.7	-	0.80	0.46	6.4	0.98	0.98	0.10
<b>HLDT, ALVW &gt;5750 lbs</b>	0.39	-	5.0	-	1.1	-	0.80	0.56	7.3	1.53	1.53	0.12
All units are in g/mile												
All standards apply to FTP 75												
1 - Useful life 120,000 miles / 11 years for all HLDT standards and for THC standards for LDT												
Abbreviations												
LVW - Loaded Vehicle Weight (curb weight + 300 lbs)												
ALVW - Adjusted LVW (numerical average of the curb weight and the GVWR)												
LLDT - Light Light-Duty Truck (below 6,000 lbs)												
HLDT - Heavy Light-Duty Truck (above 6,000 lbs)												



**Table 1.2: EPA emission and durability standards for US passenger vehicles  
produced after model year 2009 <sup>[8,9]</sup>**

Bin #	50,000 miles					120,000 miles				
	NMOG	CO	NO <sub>x</sub>	PM	HCHO	NMOG	CO	NO <sub>x</sub> <sup>*</sup>	PM	HCHO
<b>Temporary Bins</b>										
<b>MDPV<sup>c</sup></b>						0.28	7.3	0.9	0.12	0.032
<b>10<sup>a,b,d,f</sup></b>	0.125 (0.160)	3.4 (4.4)	0.4	-	0.015 (0.018)	0.156 (0.230)	4.2 (6.4)	0.6	0.08	0.018 (0.027)
<b>9<sup>a,b,e</sup></b>	0.075 (0.140)	3.4	0.2	-	0.015	.090 (.0.180)	4.2	0.3	0.06	0.018
<b>Permanent Bins</b>										
<b>8<sup>b</sup></b>	0.100 (0.125)	3.4	0.14	-	0.015	0.125 (0.156)	4.2	0.20	0.02	0.018
<b>7</b>	0.075	3.4	0.11	-	0.015	0.090	4.2	0.15	0.02	0.018
<b>6</b>	0.075	3.4	0.08	-	0.015	0.090	4.2	0.10	0.01	0.018
<b>5</b>	0.075	3.4	0.05	-	0.015	0.090	4.2	0.07	0.01	0.018
<b>4</b>	-	-	-	-	-	0.070	2.1	0.04	0.01	0.011
<b>3</b>	-	-	-	-	-	0.055	2.1	0.03	0.01	0.011
<b>2</b>	-	-	-	-	-	0.010	2.1	0.02	0.01	0.004
<b>1</b>	-	-	-	-	-	0.000	0.0	0.00	0.00	0.000
All units are g/mile										
All standards apply to FTP 75										
* - Average manufacturer fleet NO <sub>x</sub> standard is 0.07 g.mi										
a - Bin deleted at end of 2006 model year (2008 for HLDTs)										
b - The higher temporary NMOG, CO and HCHO values apply only to HLDTs and expire after 2008										
c - An additional temporary bin restricted to MDPVs expires after model year 2008										
d - Optional temporary NMOG standard of 0.195 g/mi (50,000) and 0.280 g/mi (120,000) applies for qualifying LDT4s and MDPVs only										
e - Optional temporary NMOG standard of 0.100 g/mi (50,000) and 0.130 g/mi (120,000) applies for qualifying LDT2s only										
f - 50,000 mile standard optional for diesels certified to bin 10										

### 1.3 Long-Term DPF Durability

The most recent EPA benchmarks place larger emphasis on the durability of aftertreatment devices, requiring an operational lifetime in excess of 120,000 miles. As a result, aftertreatment design engineers must contend with both catalyst deactivation resulting from a number of parameters, and the accumulation of residual ash within the DPF. The rate of ash formation and accumulation is a strong function of lube oil formulation and consumption. Initially, the ash distribution within the DPF is fairly uniform, but as the ash layer begins to increase in thickness, agglomerates of ash break loose from the layer and deposit in the rear of the filter as seen in Figure 1.7. The presence of an ash layer decreases the permeability of the channel walls, and accumulation of ash in the rear of the DPF decreases the effective filtration volume. These effects combine to increase engine backpressure and results in higher soot production, lower efficiency and higher fuel penalty for both engine operation and regeneration. Decreasing the amount of ash produced by the engine is thus recognized as a key area of focus in the development of effective and durable aftertreatment systems.

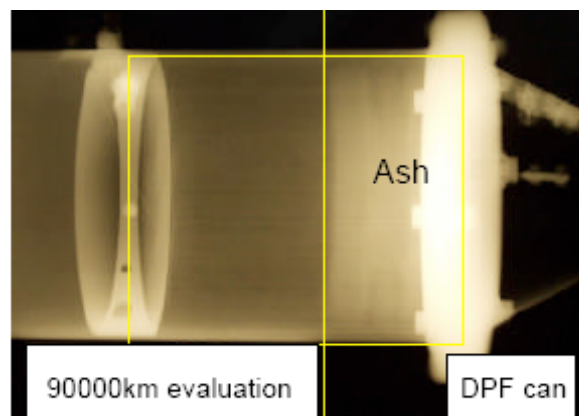


**Figure 1.7: X-Ray analysis of ash accumulation in a DPF after 90,000 km of operation<sup>[10]</sup>**

Lube oil consumption is the combined result of natural mechanisms such as migration of oil past the piston rings and positive crankcase ventilation (PCV) system blow-by, as well as other mechanisms such as leakage from faulty valve stem or turbocharger seals. Natural consumption of lube oil by the engine will inherently remain a contributing factor to the formation of ash, with proper engine maintenance becoming imperative in order to minimize the total volume of oil being combusted. Even with proper maintenance, increased engine age often results in increased oil consumption rates due to both engine wear with associated oil migration past piston rings, as well as other minor seal failures that may go unnoticed and uncorrected by the operator.

The rate of ash accumulation within the DPF also increases in the presence of a fuel-borne catalyst (FBC), which is typically a cerium, iron or copper-based fuel additive that can be used to better facilitate continuous regeneration of particulate matter. Though FBC additives are not used in US markets, the magnitude of these effects has been shown to be directly related to the formulation of the additive as well as the dosing rate [11-16].

Another element that can affect the long-term performance of DPF systems is the durability of catalyst material present in either an upstream oxidation catalyst or in the DPF itself. This system, typically referred to as a continuously regenerating diesel particulate filter (CR-DPF) or continuously regenerating trap (CRT) system, is designed to facilitate the combustion of the carbonaceous portion of the soot by lowering the temperatures required to achieve this oxidation. Previous works have been dedicated to the study of deactivation mechanisms for different catalyst materials, with sulfur and phosphorus both identified as key factors in performance degradation [17-21].

Finally, in addition to the mass and volume of ash accumulated within the filter, the morphology of the ash and ash layer has significant influence with regard to engine backpressure. Many published works have included basic characterization of ash-loaded DPF substrates to determine the morphology and distribution of ash resulting from a variety of applications and operating environments [10, 22-29].

#### **1.4 Scope of Investigation**

The objective of the present investigation is to develop an accelerated ash-loading protocol that produces ash with characteristics similar to that observed in previous investigations of other field-aged and bench-aged systems. The protocol is intended to serve as a tool for evaluating the performance of both current and future DPF substrate materials and configurations, providing a method for consistently accumulating a predetermined amount of soot and ash in the filter and including an effective and repeatable regeneration strategy to remove the carbonaceous material from the DPF.

The engine utilized for the development of this ash-loading protocol is a 517 cc, naturally aspirated direct injection (NA/DI) single cylinder diesel engine. The rate of ash formation is accelerated by using ultra low sulfur #2 diesel fuel (15 ppm) with 5 percent by volume of commercially available 10w40 lube oil. The increase in the oil consumption rate is estimated to be 40 times greater than the rate of oil consumption via natural mechanisms experienced during normal operation using un-doped fuel [30]. A total of 60 liters of fuel blended with an additional 3 liters of lube oil are consumed during each experiment. Given the relatively short duration of the experiments and the

relatively large increase in lube-oil consumption rate, oil consumed by natural mechanisms in the engine is considered negligible and thus is not measured.

Several substrate materials were aged and evaluated during the development of this protocol. Cordierite and SiC are both currently being used in industry as a DPF substrate, and mullite has been introduced more recently as a potential material for future applications. Differences in substrate porosity result in varying backpressure profiles, which in turn affects the rate of soot production by the engine. Thus, time cannot be used as a method of determining the amount of soot accumulation within the filter. Instead, engine backpressure is monitored and the DPF periodically removed and weighed to determine the mass of soot accumulation associated with each given increase in backpressure. A soot loading of 3 grams per liter is selected as the target loading, and the associated backpressure increase is found to be approximately 0.20 psi. The protocol applied for all substrates begins the recording of a baseline backpressure following a 5-minute stabilization period for engine warm-up or post-regeneration cool-down prior to each loading cycle. The loading cycle backpressure threshold is defined by adding 0.20 psi to the recorded baseline backpressure, with the regeneration strategy initiated upon engine backpressure reaching this threshold.

The regeneration strategy itself must effectively remove carbonaceous deposits from the DPF without damaging the substrate. In addition, the conditions produced by the engine bench and active regeneration system for this strategy should be similar to conditions encountered in actual applications, thus increasing the likelihood that this accelerated protocol accurately mimics phenomena observed in field-aged devices. Regeneration begins by slowly increasing DPF temperatures from approximately 425°C

to 700°C over a 15-minute period by injecting supplemental fuel into the exhaust upstream of the DOC. Increasing these temperatures too rapidly can result in rapid and uncontrolled oxidation of soot, often producing temperature excursions capable of damaging the DPF. Other considerations include closely monitoring the system and initiating the regeneration immediately upon backpressure reaching the aforementioned threshold, minimizing the amount of additional soot accumulation that could also result in rapid and uncontrolled regeneration.

Upon completion of each experiment, the DPF is removed from the canning system and cut into 4 sections for characterization using a multitude of analytical techniques. Electron Probe Microanalysis (EPMA) is used to examine cross-sectional ash distributions for individual channels from various locations throughout the DPF, using known ash constituents such as calcium and sulfur as representative elements to observe the overall channel morphology with elemental maps. Scanning electron microscopy is used to examine the ash layer under higher magnification, including individual ash particles and the interface between the ash layer and the substrate wall. Inductively-Coupled Plasma Atomic Emission Spectroscopy is used to analyze the fuel, oil and aged substrate to quantify ash content, recovery and distribution throughout the filter. Finally, X-Ray Diffraction is employed to identify compounds present within the ash, providing further information regarding the ash itself and the associated formation mechanisms. All of these tools can provide a greater understanding of trends in ash composition and distribution, allowing more detailed evaluation of aged systems and providing a reference for performance comparisons and predictions in future systems.

It is expected that this work will produce a valuable means by which new DPF materials and systems can be rapidly evaluated to determine durability with respect to ash accumulation. Furthermore, additional knowledge gained from a comprehensive characterization of each substrate should provide a better understanding of ash composition and morphology, thus contributing to the improvement of all relevant technologies affecting DPF performance and durability

## **CHAPTER 2**

### **LITERATURE REVIEW**

This chapter presents an overview of the relevant technical background necessary for the study of diesel particulate filters. Particulate filters have been used in non-road applications since 1980, and started being used in automotive applications in 1996. Initially designed to reduce the emission of particulate matter from generators used in mining applications, the DPF was soon recognized as a partial solution to increasingly stringent emission regulations placed on passenger and commercial vehicles. The performance of a DPF is characterized based on both filtration efficiency and exhaust backpressure increase. As particulate matter accumulates within the filter, backpressure increases and hinders engine performance. Thus, the particulate matter must be removed by oxidizing the carbonaceous material, also known as regenerating the DPF. The complex nature of this soot accumulation and oxidation makes engineering and development based on fundamental physics difficult, forcing the engineer to rely heavily on experimental observation. Therefore, the majority of material cited in this section focuses on experimental evaluation of various aspects affecting DPF performance. Section 2.1 describes diesel particulate filter operation including its substrate material, structure and possible catalyst coating. In Section 2.2, observations in field-aged filters are considered. Section 2.3 discusses various results obtained using engine bench aging. Section 2.4 outlines the chemical aspects with regard to both lube oils and ash. Finally, Section 2.5



provides information regarding techniques for accelerating ash accumulation in which high-mileage field-service DPF ash loading is simulated within a laboratory.

## **2.1 Basic DPF Operation, Principles and Considerations**

To meet increasingly stringent emissions regulations, several different aftertreatment devices will be required. It is expected that a diesel particulate filters and lean NO<sub>x</sub> traps, in conjunction with improved engine controls, will be utilized to achieve desired exhaust concentrations of the target exhaust gases produced by diesel engines. The presence and configuration of these aftertreatment devices, as well other exhaust components such as oxidation catalysts, resonators and mufflers, can have significant implications with regard to various system performance characteristics. For this study, the exhaust system consists of approximately 2 m in length of 5.7 cm-diameter exhaust pipe, an upstream oxidation catalyst for generating an exotherm for soot regeneration and conversion of NO to NO<sub>2</sub>, and the DPF.

The upstream diesel oxidation catalyst (DOC) is designed primarily to facilitate continuous regeneration of particulate matter by forming NO<sub>2</sub> from NO and O<sub>2</sub> present in the exhaust gases. Engine bench experiments carried out by several individuals including Allansson et al. [31] have demonstrated that soot can be continuously oxidized at much lower temperatures using NO<sub>2</sub>. For PM oxidation by O<sub>2</sub>, temperatures must be in excess of 550°C, whereas oxidation using NO<sub>2</sub> occurs at temperatures of approximately 250°C. This enhanced continuous regeneration performance at lower temperatures provides a distinct advantage in allowing soot to be oxidized at temperatures commonly experienced during typical engine operation. It is observed in experimental data shown in Figure 2.1

that the formation of NO<sub>2</sub> at various temperatures shows the largest concentrations of NO<sub>2</sub> are formed when exhaust gas temperatures are between 275 to 325°C. These temperatures are commonly experienced during the operation of the experiments from which the data originated. Bench flow experiments carried out during the same investigation provide data illustrating the relative oxidation performance of NO<sub>2</sub> and O<sub>2</sub>, shown in Figure 2.2, further demonstrating the advantage of using an upstream oxidation catalyst.

In bench flow experiments carried out to investigate the oxidation performance of NO<sub>2</sub> and O<sub>2</sub> in a variety of conditions, Jacquot et al. [32] further demonstrated that PM is more readily oxidized by NO<sub>2</sub> than O<sub>2</sub>, as observed in Figure 2.3, especially at lower temperatures. Results also indicate that the presence of a fuel-borne catalyst further improves this oxidation performance, though no fuel-borne catalyst is used in the current investigation.

As the system is aged on the engine bench or in the field, it has been widely observed that the oxidation performance of the DOC is degraded due to strong interactions between sulfur from the fuel and lube-oil and the active platinum sites on the

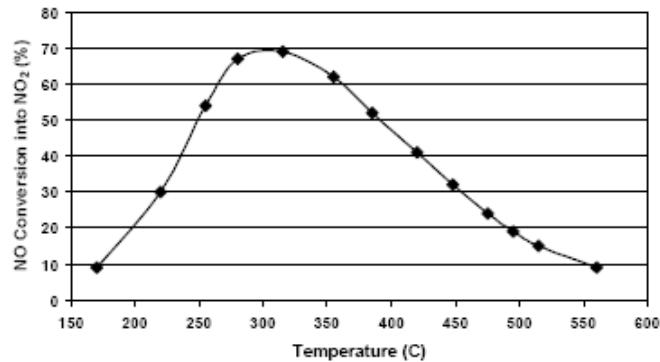


**Figure 2.1: NO<sub>2</sub> formation as a function of exhaust gas temperature<sup>[31]</sup>**

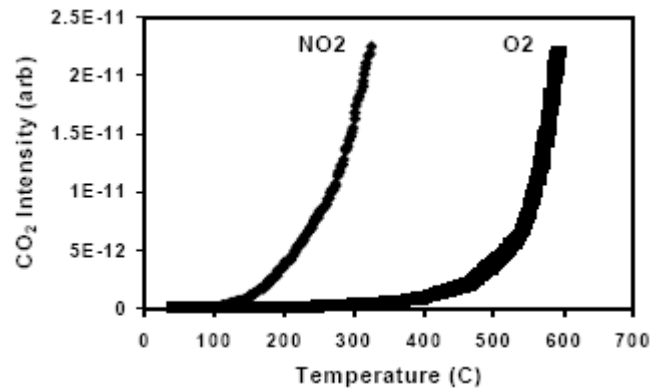


**Figure 2.2: Experimental PM oxidation as a function of exhaust gas temperature for NO<sub>2</sub> and O<sub>2</sub><sup>[31]</sup>**

catalyst surface. Allansson et al. [33] demonstrated that some of this degraded performance could be recovered by regenerating the DOC by exposing it to temperatures of 450°C for approximately 20 minutes. In the experiment, the oxidation catalysts are aged at 300°C for 100 hours. Engine bench evaluations of NO conversion are then carried out both before and after this regeneration to determine the effect of the regeneration on oxidation performance. As seen in Figure 2.4, significant improvement in NO conversion is observed immediately following the regeneration. It is widely documented that DOC performance is irreversibly degraded by sulfur and phosphorus over the life of the DOC. For most applications, the frequency of necessary catalyst regenerations will be far exceeded by the number of required DPF regenerations, effectively maintaining oxidation performance at or near the highest levels achievable. Several other experiments have been conducted to further investigate the performance of an upstream oxidation catalyst in various exhaust gas environments, and subsequent effects on both continuous and active regeneration [34-37].

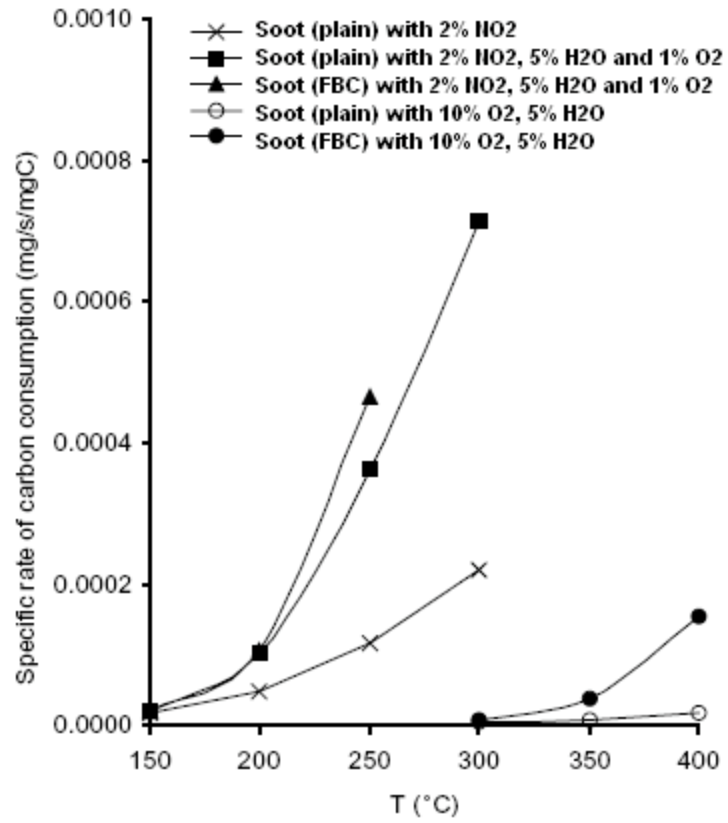
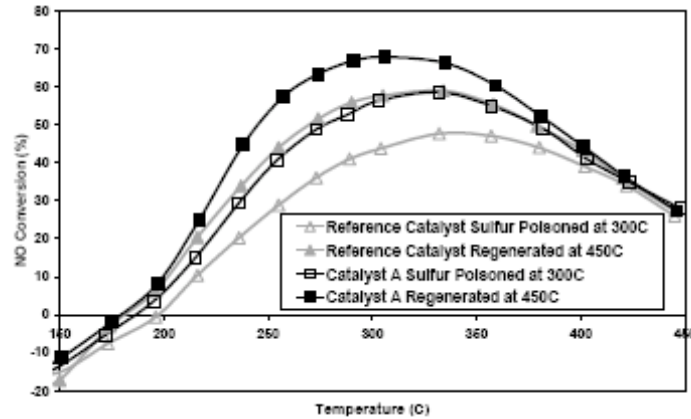
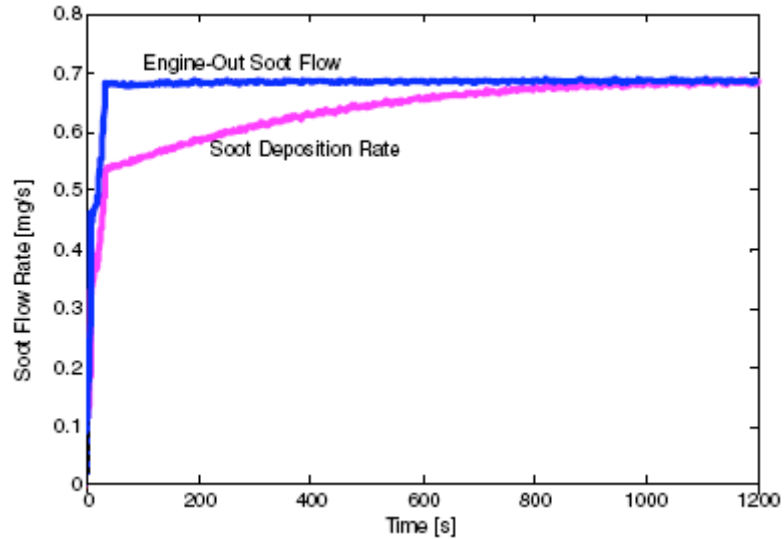


Figure 2.3: Experimental PM oxidation in the presence and absence of a fuel-borne catalyst as a function of exhaust gas temperature and composition<sup>[32]</sup>



**Figure 2.4: NO conversion performance for two catalysts before and after catalyst regeneration at 450°C<sup>[33]</sup>**

A portion of the PM formed will be oxidized by  $\text{NO}_2$  formed in the upstream catalyst during operation, though the amount of material that is continuously regenerated is a strong function of operating conditions. The soot that is not immediately oxidized will deposit and accumulate within the DPF. The rate of continuous regeneration and accumulation is difficult to quantify in real time. England et al. have combined several empirical models constructed from results from various engine experiments [38]. Based on several pieces of data including CO and  $\text{CO}_2$  levels present in the DPF exit gases, the amount of soot being continuously regenerated can be approximated. If the rate of soot production is known, the rate of soot accumulation can be approximated, as seen in Figure 2.5. As soot accumulates within the filter, backpressure will increase. Initially, the data indicates that approximately 30% of the soot is continuously regenerated, with the remainder of the soot depositing in the DPF. Over time, the deposition curve approaches the engine-out soot curve, indicating that continuous regeneration efficiency degrades. Since the rate of soot formation is nearly constant, it is assumed for this case



**Figure 2.5: Example soot formation and deposition rate plot<sup>[38]</sup>**

that there is negligible backpressure increase, and that the change in soot deposition rate is a function of only the exhaust gas composition and associated continuous regeneration efficiency.

The effect of soot accumulation on backpressure is a function of several parameters such as substrate material and particle size, and does not directly correlate with the amount of soot present within the DPF. Soot loading is typically defined in terms of grams per liter, or grams of soot per liter of overall DPF volume. Acceptable limits range from 3 grams per liter to as high as 12 grams per liter, depending on both the application and the effect of soot loading on backpressure [39]. Backpressure has a profound effect on both the rate of soot formation as well as the relative size of soot particles being formed [40]. Engine out soot should be minimized in order to enhance continuous regeneration efficiency as well as improve engine performance. Thus, low backpressure drop across the DPF is a key performance consideration.

To maintain a relatively low engine backpressure, the filter must periodically be regenerated. The configuration and application of each system will determine the normal operational temperatures, which in turn outline the active regeneration requirements and frequency based on soot accumulation rate and continuous regeneration efficiency. To actively regenerate the DPF, exhaust gas temperatures must be raised in excess of  $700^{\circ}\text{C}$ , typically by injecting supplemental fuel into the exhaust stream. Lee et al. [41] investigated the regeneration performance of a SiC DPF with different exhaust gas concentrations and soot loadings. Typically, regeneration is initiated by increasing the engine load to raise the engine-out exhaust temperature, and supplemental fuel is added to the exhaust stream to further increase gas temperatures. These results show that soot oxidation reactions can result in temperature excursions, as seen in Figure 2.6. For large soot loadings, as well as high concentrations of  $\text{O}_2$  and  $\text{NO}_2$ , these excursions may result in high temperatures and gradients capable of damaging the DPF.

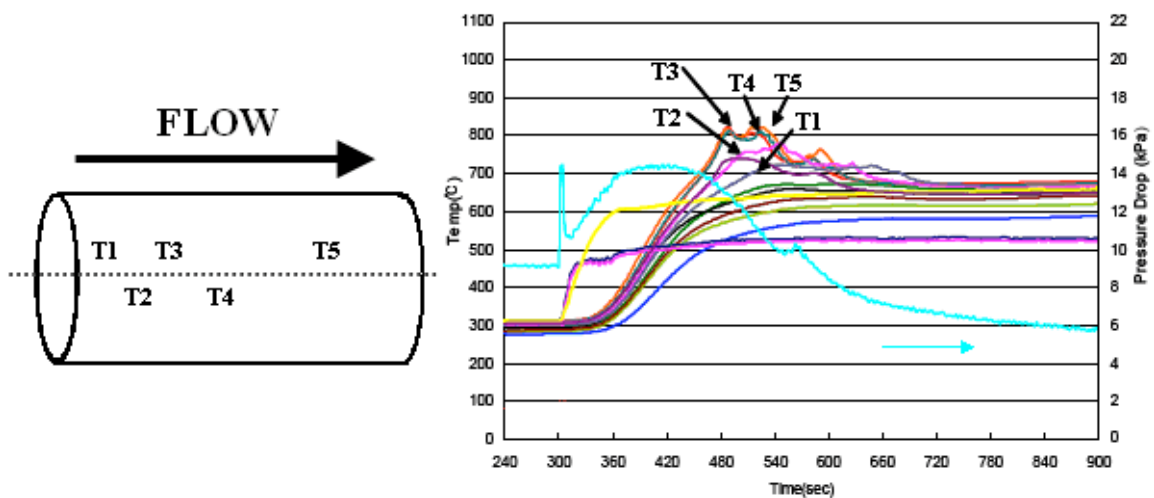
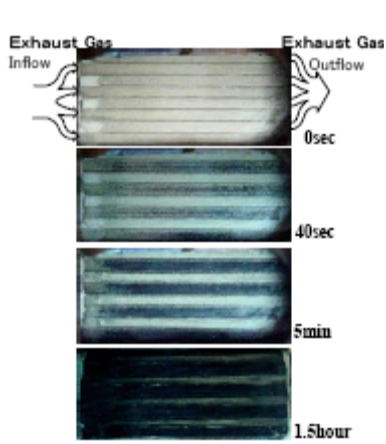


Figure 2.6: Typical DPF temperatures during regeneration<sup>[41]</sup>

The severity of these temperature excursions is strongly dependent on the soot loading, gas hourly space velocity and exhaust gas composition. Previous investigations have shown that regenerating a DPF at temperatures in excess of 600°C effectively oxidizes the majority of soot within the filter, with the regeneration time required varying based on soot loading amount and operational settings [42-45]. To avoid damaging the aftertreatment system, it is imperative to possess a comprehensive understanding of the active regeneration behavior as well as the physical limitations of the materials present.

Hanamura et al. [46] provide visualization of regeneration phenomena occurring within a DPF by using half-cylindrical DPF covered with a quartz plate, allowing several channels to be observed. As seen in Figure 2.7, the inlet channels exposed to the incoming exhaust gas turn black as soot accumulates. Some photographs are taken using flash to better illustrate the presence and location of soot, while the remaining photographs are captured with only ambient light and allow the observer to see the oxidation front. The amount of soot loaded for this experiment is approximately 28 grams per liter, which is a very high loading level corresponding to a backpressure increase of 14.5 kilopascals (~1.5 psi). It is observed that the point of initial soot ignition varies as a function of inlet gas temperature. For an inlet gas temperature of 700°C and oxygen concentration of 8.5%, Figure 2.8 indicates that the soot is first ignited near the middle of the DPF and propagates in both the upstream and downstream direction. However, for a hotter inlet gas temperature of 867°C with identical oxygen concentration of 8.5%, the initial ignition point is fairly close to the inlet and propagates toward the rear of the DPF, as shown in Figure 2.9. In both cases, there appears to be no particulate matter remaining in regions through which the regeneration front has passed. In a similar





**Figure 2.7: Visualization of soot loading in DPF as a function of time<sup>[46]</sup>**

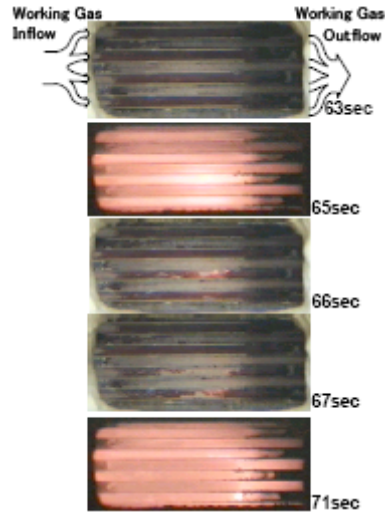


**Figure 2.8: Visualization of regeneration with inlet gas temperature of 799°C<sup>[46]</sup>**

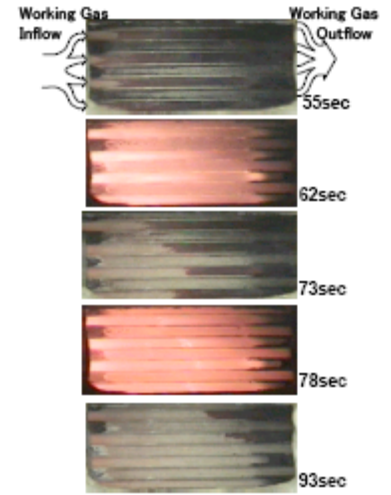


**Figure 2.9: Visualization of regeneration with inlet gas temperature of 867°C<sup>[46]</sup>**

experiment carried out with an inlet temperature of 658°C and oxygen concentration of 8.5%, there is no distinct area of brightness, i.e., a reaction zone, indicating that PM is consumed uniformly throughout the filter. In all cases, DPF temperatures following the passage of the propagating reaction zone are approximately 800°C. The temperature excursions experienced for inlet gas temperatures of 658°C, 799°C and 867°C resulting in temperature excursions of approximately 25 °C, 100 °C and 150 °C, respectively. Further experiments carried out at the same inlet gas temperatures with oxygen concentration of 10% resulted in a temperature excursion of 300°C for the highest inlet gas temperature, with temperatures exceeding 1100°C in the middle section of the DPF approximately 60 seconds after the initiation of regeneration, and in the rear section of the DPF approximately 20 seconds later. This phenomenon underlies the importance of system monitoring and control both to regulate the amount of soot that accumulates prior to

regeneration, and to vary operating conditions in order to achieve appropriate exhaust temperatures and oxygen concentrations.

## **2.2 Field Observations of DPFs and Ash**

The primary goal of developing an accelerated testing protocol is to rapidly duplicate results observed in field-aged applications. Since the current investigation is not intended to mimic any specific application or operating condition, a broad understanding of DPF behavior and results is required for the development of the desired protocol.

Kimura et al. [47] performed a study in which nine fuel deliver trucks were retrofitted with passive DPF systems to investigate effects engine age and lube-oil formulation on the rate of ash formation. Three lube oil formulations are selected and compared both using data acquired during operation as well as post-experiment characterization of the ash. Each system was operated for 18 months, which resulted in approximately 160,000 miles. Microloggers were used to record DPF inlet gas temperatures as well as pressure drop across the DPF, providing valuable feedback for real-time control and post-experiment performance analysis. The study shows that mileage and backpressure increase do not correlate well with ash accumulation, but instead showed that ash formation is a strong function of the age and associated mileage of the vehicle. The two oldest trucks were observed to produce ash at nearly twice the rate of the two newest vehicles, highlighting the effect of engine wear on ash formation and accumulation. Subsequent characterization of the ash material revealed that the primary ash constituents are  $\text{CaSO}_4$ ,  $\text{CaO}$  and  $\text{Zn}_3(\text{PO}_4)_2$ . There was good consistency

observed between the ash from different lube oils with regard to the relative concentration of the key constituents. On average, calcium and phosphorus are present in the greatest amounts, as shown in Table 2.1, and the presence of iron resulting from engine wear is observed to vary greatly between the vehicles. The most notable result is found in the total amount of lube ash formed, which was observed in some cases to vary drastically with lube oil formulation. This has significant implications with regard to DPF service life, which will inherently vary based not only on application but also the relative age and performance of each engine and the formulation of the lube oil.

Similar experiments were carried out by McGeehan et al. [48] confirmed that  $\text{CaSO}_4$  is the primary ash constituent, though zinc and phosphorus are also present in significant amounts. Again, little difference is observed in the composition of the ash formed by different lube oil formulations, though the total amount of ash accumulated is observed to vary. Comparisons based on differences in lube-oil formulation can be made in a variety of ways based on the points of interest, such as by evaluating the calcium-to-zinc ratio. Even in non-road applications such as tractors and generators, studies have shown that ash accumulated in these filters is comprised of the same elements in approximately the same relative concentrations [49].

Another important factor emphasized by Richards et al. [50] is the duty cycle incurred by the system. Inner city applications such as transit buses and refuse trucks are characterized by stop-and-go operation, presenting difficulty for system monitoring and regeneration performance. While PM production is not monitored, experimental data shows that emission levels are a strong function of vehicle speed, illustrated in Figure 2.10. Since the system cannot predict a period of sustained high-load operation, a

**Table 2.1: Analysis of mileage, lube oil consumption and ash characterization<sup>[47]</sup>**

<b>Filter Substrate Ash Analysis</b>			
<b>Vehicle #</b>	<b>8308</b>	<b>8311</b>	<b>8288</b>
<b>Lube Oil</b>	<b>EX</b>	<b>Base</b>	<b>ES</b>
Filter Serial #	105100	105097	105092
Vehicle Miles	345,463	423,550	416,565
DPF Miles	<b>252,451</b>	<b>291,700</b>	<b>245,361</b>
Miles during the program	<b>165,358</b>	<b>157,794</b>	<b>171,280</b>
Miles after program completion	<b>87,093</b>	<b>133,906</b>	<b>74,081</b>
Lube Oil Consumption, Liters/day	0.048	0.026	0.110
Ash Accumulation, grams	256.9	326.2	241.4
Ash Accumulation, mg/mile	1.02	1.12	0.98
<b>Analyte</b>	<b>Weight %</b>	<b>Weight %</b>	<b>Weight %</b>
Al	26.5	25.7	24.5
Ca	5.63	6.26	5.49
Co	0	0	0
Cr	0	0	0
Cu	0	0	0
Fe	3.52	2.49	4.08
Mg	11.5	11	11.4
Mn	0	0	0
Mo	0	0	0
Ni	0.24	0.2	0.57
P	3.78	4.97	6.85
Si	39.3	39.2	37.4
Sr	0	0	0
Ti	0	0	0
Zn	2.2	3.25	3.84
Zr	0	0	0
ZrO <sub>2</sub>	0	0	0
Total	92.67	93.07	94.13
<b>Normalized</b>			
<b>Cordierite</b>	<b>83.41</b>	<b>81.55</b>	<b>77.87</b>
<b>Corrosion Material</b>	<b>4.06</b>	<b>2.89</b>	<b>4.94</b>
<b>Lube Ash</b>	<b>12.53</b>	<b>15.56</b>	<b>17.19</b>
<b>Total</b>	<b>100.00</b>	<b>100.00</b>	<b>100.00</b>

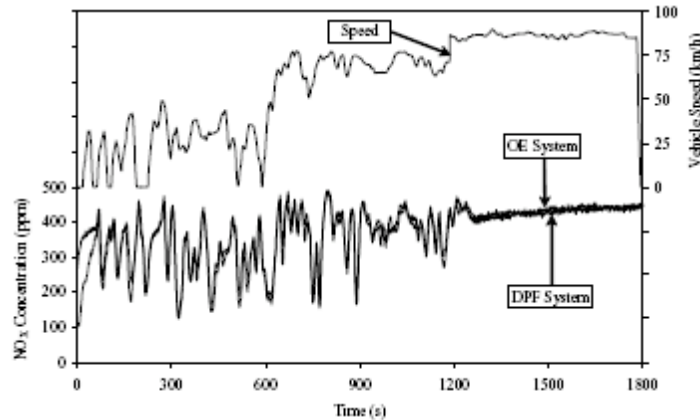


**Figure 2.10: Vehicle speed and associated NO<sub>x</sub> formation versus time for an urban bus application<sup>[50]</sup>**

specialized regeneration strategy that can be applied and adapt to changes in operating conditions is required [51,52].

While it is impossible to develop a universal testing protocol to simulate the performance demands of every feasible application, the composition and distribution of ash appear to remain consistent across a wide spectrum of functions. It is also noted that there have been very few characterization results such as SEM and EPMA images published and made available for comparison. These considerations will be addressed further in Section 2.4.

### **2.3 Engine Bench Aging**

While field testing of aftertreatment technologies allows performance to be evaluated in the actual operating environment, there is an inherent lack of repeatability between tests. In addition, complications with regard to the installation of equipment such as gas analyzers and data acquisition systems on mobile platforms pose a large

logistical challenge with associated increase in cost. Thus, engine bench testing using a dynamometer to control engine load has been widely used to evaluate aftertreatment devices such as the DPF in controlled environment and under repeatable conditions.

In order to evaluate the performance parameter of interest, a repeatable testing protocol must be developed and implemented such that the operational parameters provide consistent exhaust conditions with minimal variation between experiments. With regard to DPF testing, factors such as soot loading, backpressure, regeneration strategy and ash accumulation are all key factors in developing a testing protocol.

Target soot loadings depend on what aspect of DPF performance to be evaluated. Relatively low soot loadings of approximately 2 grams per liter are typically used for investigating oxidation kinetics, while larger soot loadings as high as 20 grams per liter are utilized to evaluate soot loading limits with respect to backpressure thresholds and potential temperature excursions resulting from rapid uncontrolled oxidation [53-60]. Schaefer-Sindlinger et al. evaluated the pressure drop associated with various soot

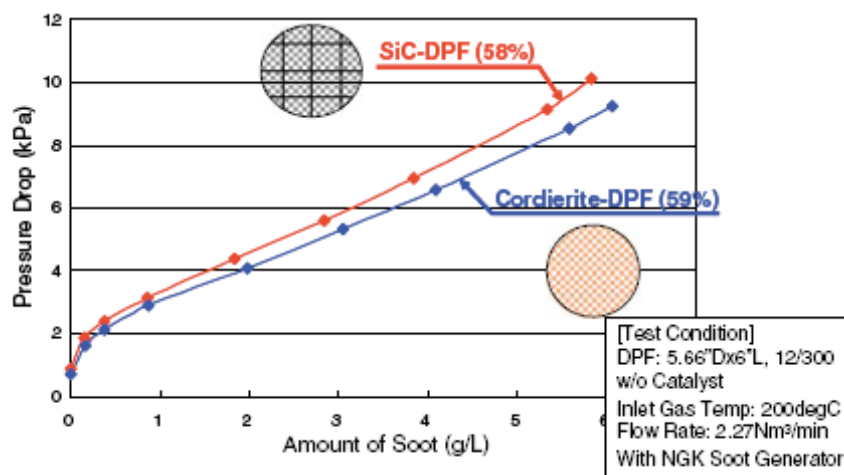
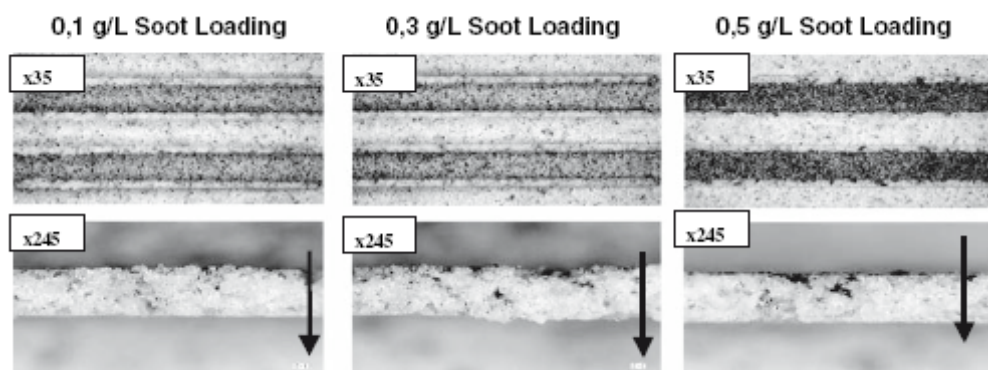


Figure 2.11: Exhaust backpressure vs. soot loading<sup>[53]</sup>

loadings in both a cordierite and silicon carbide DPF, shown in Figure 2.11 [53]. While baseline backpressure for the two filters is nearly identical in the absence of soot, there is a clear difference in backpressure as soot accumulates, indicating a difference in the way soot accumulates within the DPF.

In order to understand the effect of soot accumulation on backpressure, the distribution and morphology of the soot layer must be examined. The filtration efficiency of typical DPF substrates is on the order of 99.9%, though the differing channel wall morphology results not only different ash layer morphology, but can also allow PM to penetrate the channel wall to various depths [53, 61-65]. Photographs taken of a cordierite DPF with a low soot loading level, shown in Figure 2.12, show PM penetration as far as halfway through the channel wall. This penetration has clear implications with regard to backpressure, even though the effect of soot penetration is not directly evaluated in any investigations found in research.

Another aspect of soot loading is its effect on temperature excursions experienced loadings can result in rapid and uncontrolled soot oxidation, resulting in high temperature



**Figure 2.12: Photographs of soot layer in a cordierite substrate<sup>[53]</sup>**

during active regeneration. While the operating conditions and regeneration strategy have the substantial effect on regeneration temperature profiles, large soot excursions. Regeneration strategies are typically defined by the prescribed temperature profiles that are applied as a function of time. Zhan et al. [54] demonstrated the effect of temperature ramping rate on peak temperatures experienced by the cordierite DPFs with soot loadings of 8 g per liter, shown in Figure 2.13. The data shows good correlation between this ramping rate and the peak DPF temperatures, indicating that lower temperature ramping rates are less likely to produce uncontrolled regenerations and associated temperature excursions.

As mentioned earlier in this chapter, the configuration of the aftertreatment system has perhaps the most profound effect on system performance. The addition of upstream oxidation catalysts facilitates the formation of  $\text{NO}_2$  for continuous regeneration, while catalyzing the DPF substrate itself also improves regeneration performance.

Hiranuma et al. [55] performed several engine bench experiments to evaluate the relative performance of different combinations of these technologies. The investigation focused on the oxidation rate of PM, shown in Figure 2.14 and the continuous

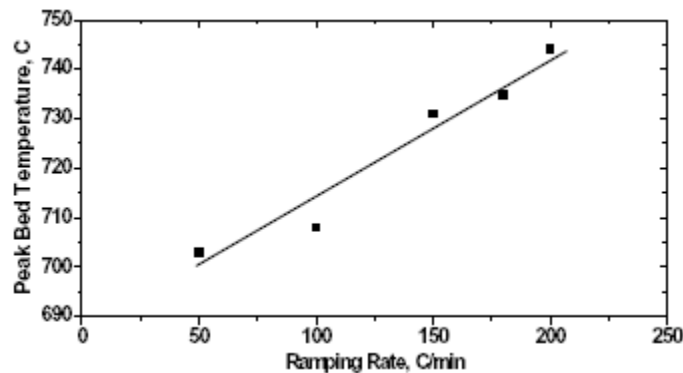


**Figure 2.13: Peak temperature experiences during regeneration vs. DPF temperature ramping rate<sup>[54]</sup>**



regeneration operation regions, shown in Figure 2.15, within different system configurations. Results indicate that the use of an upstream catalyst in addition to a catalyzed DPF yields the highest PM oxidation rate for the given operating conditions. Other studies have indicated that the addition of the upstream DOC has the most significant impact on regeneration efficiency [56, 57, 59, 60].

Engine bench testing allows the investigator to effectively evaluate aftertreatment devices such as DPFs in a controlled environment, improving repeatability and eliminating complications associated with mobile analytical platforms. The engines used for testing can be either those actually used in the desired application, or an appropriate surrogate engine capable of providing comparable exhaust conditions. While field-aged results remain essential as a basis for comparison, engine bench testing has proven a valuable tool for the research and development of all aftertreatment technologies.

## 2.4 Lube Oil and Ash Analysis

Chemical analysis of both the engine lube oil and the ash accumulated within the

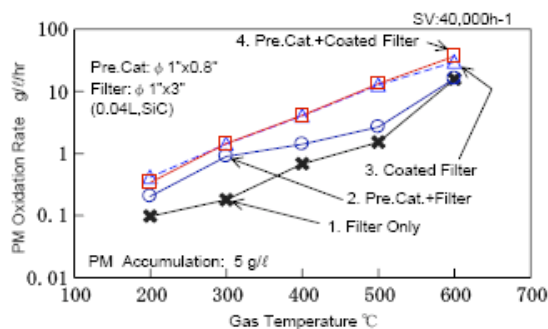


**Figure 2.14: PM oxidation rate vs. gas temperature for different DPF and DOC configurations<sup>[55]</sup>**

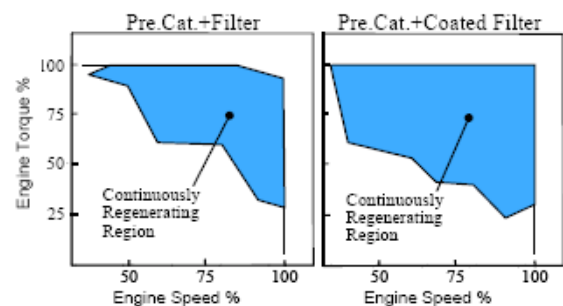


**Figure 2.15: Engine setting regions facilitating continuous regeneration for two DPF and DOC configurations<sup>[55]</sup>**

DPF provides valuable information, allowing for the calculation of ash formation rate and ash recovery efficiency. Several recent studies have been conducted to identify the primary ash constituents in various lube oil formulations, and evaluate the elemental contribution to the total ash accumulation [11, 23,24]. Bardasz et al. have demonstrated fairly linear relationships between ash accumulation and engine oil consumption, shown in Figure 2.16, for various lube oil formations [26]. Variations in the ash masses are attributed to several causes including residual PM resulting from incomplete regeneration, as well as the resolution of the scale used to determine the total DPF can mass.

Investigations carried out by Givens et al. examined the compositions of eight lube oil formations, quantifying the concentrations of specific elements such as calcium, zinc, sulfur and phosphorus, as well as sulfated ash, shown in Table 2.2 [27]. By measuring the amount of oil consumed during each experiment, the ash recovery efficiency can be calculated. It is also noted in the same investigation that the relative concentrations of ash-forming metals such as calcium, magnesium and zinc are higher in

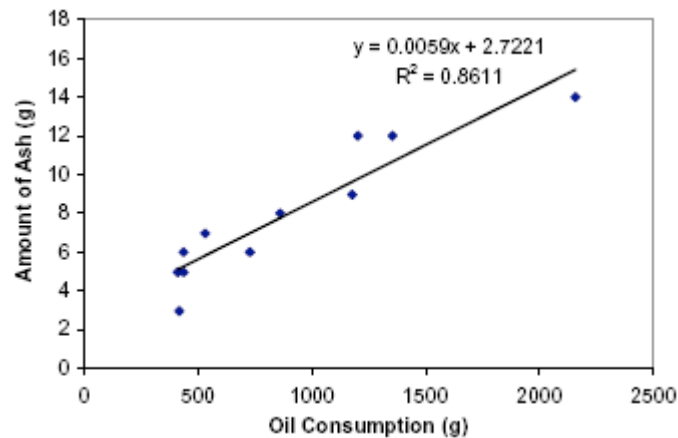


**Figure 2.16: DPF ash accumulation as a function of oil consumption<sup>[26]</sup>**

the used oil drained from the engine than in the fresh oil. The lighter hydrocarbon constituents of the fresh lube oil are more easily volatilized in the cylinder, resulting in increased metal concentrations in the lube oil drained from the engine and lower metal concentrations in the DPF. Thus, ash recovery cannot be calculated solely by using the metal concentrations in the fresh oil and the mass of lube oil consumed, but must instead use the metal concentrations observed in the oil drained from the engine following the experiment.

Predicting ash formation and calculating ash recovery are important factors in determining optimal lube oil formulations. While ICP analysis can be used to quantify the presence of the elements of interest, XRD analysis can be used to identify the compounds present in the ash. The identification of these compounds is useful for comparison between ash resulting from normal lube oil consumption and ash formed as the result of accelerated lube oil consumption. Analysis performed by Givens et al. identified several possible compounds for each lube-oil, presented in Table 2.3, including  $\text{CaSO}_4$ , and oxides of iron, which have been identified in previous investigations [23, 27,

**Table 2.2: Chemical analysis of several lube oil formations<sup>[27]</sup>**

Candidate	1	2	3	4	5	6	7	8
Additive System Detergents	Ca/Mg	Ca/Mg	Ca Only	Ca Only	Mg Only	Ca/Mg	Ca/Mg	Ca/Mg
Antiwear	ZDDP @ 1.0 %wt	ZDDP @ 1.0 %wt	ZDDP @ 0.5 wt% + Mo	ZDDP @ .2 %wt + Mo	ZDDP @ 1.0 %wt	ZDDP @ 1.0 %wt	Mo Only	ZDDP @ .2 %wt + Mo
Detergent S, ppm	1083	370	798	429	171	610	1483	486
Antiwear S, ppm	2000	1960	1040	440	2000	2000	0	420
Base Stocks	Group IV/V	--	Group III	Group IV/V	Group IV/V	Group IV/V	Group III	Group IV/V
	Ref. Oil							
SAE Grade	0W-40	5W-30	5W-30	0W-40	0W-40	0W-40	5W-30	0W-40
Calcium [wt%]	0.169	0.055	0.110	0.094	0.0007	0.092	0.096	0.096
Magnesium [wt%]	0.063	0.021	0.0006	--	0.070	0.047	0.15	0.061
Zinc [wt%]	0.108	0.098	0.052	0.022	0.100	0.109	--	0.021
Boron [wt%]	0.018	--	0.0064	0.024	0.017	0.019	0.052	0.029
Molybdenum [wt%]	--	--	0.015	0.018	--	0.01	0.017	0.019
Phosphorus [wt%]	0.101	0.089	0.048	0.020	0.098	0.103	--	0.019
Sulfur [wt%]	0.308	0.233	0.184	0.087	0.217	0.261	0.148	0.091
Total Base No.	8.46	3.72	4.62	3.55	4.24	3.87	13.56	6.44
Sulfated Ash [wt%]	0.96	0.51	0.50	0.42	0.51	0.49	1.05	0.63

**Table 2.3: Analysis of ash in a DPF after 200 hours of ash accumulation<sup>[27]</sup>**

<b>Candidate 1 (Reference Oil), Test 1, Engine #1</b>			
<b>Element</b>	<b>wt %</b>	<b>mg</b>	<b>Compounds</b>
Al	0.43	76.50	
B	0.07	12.14	
Ca	10.80	1944.00	CaSO <sub>4</sub> , Ca <sub>x</sub> Cu <sub>y</sub> (PO <sub>4</sub> ) <sub>2</sub> , Ca <sub>x</sub> Fe <sub>y</sub> O <sub>z</sub>
Co	0.17	29.70	
Cr	1.08	193.50	
Cu	1.51	271.80	Ca <sub>x</sub> Cu <sub>y</sub> (PO <sub>4</sub> ) <sub>2</sub>
Fe	12.91	2322.90	Fe <sub>2</sub> O <sub>3</sub> , Fe <sub>3</sub> O <sub>4</sub> , Ca <sub>x</sub> Fe <sub>y</sub> O <sub>z</sub>
K	0.08	13.50	
Mg	3.81	684.90	Zn <sub>2</sub> Mg(PO <sub>4</sub> ) <sub>2</sub>
Mn	0.11	19.80	
Mo	0.03	5.40	
Na	0.23	40.50	
Ni	0.46	81.90	
P	5.79	1041.30	Zn <sub>2</sub> Mg(PO <sub>4</sub> ) <sub>2</sub> , Ca <sub>x</sub> Cu <sub>y</sub> (PO <sub>4</sub> ) <sub>2</sub>
Pb	0.22	38.70	
S	5.52	992.70	CaSO <sub>4</sub>
Si	0.68	122.40	SiC
Zn	7.37	1325.70	Zn <sub>2</sub> Mg(PO <sub>4</sub> ) <sub>2</sub>

28]. The relatively low concentration of sulfur in the lube oil indicates that a significant amount of ash sulfur originates from the fuel. Variations in oil formulation, engine operation and operating environment can have a significant impact on the compounds formed and the relative amounts of each.

Analysis performed by Nemoto et al. utilized the quantification of Ca concentration at specific points in the center of an ash-loaded DPF to demonstrate the distribution of ash along the length of the DPF [28]. It is observed that the ash distribution produced by two low-ash lube oils is more axially uniform compared to the ash distribution resulting from the use of standard DH-1 class oil, as seen in Figure 2.17. XRD and XPS analyses were then used to approximate the relative concentrations of the primary compounds present. This information is once again useful for the comparison of ash formed during normal engine operation and ash formed utilizing accelerated lube oil consumption methods. Approximate quantification of the ash constituents is presented in Table 2.4.

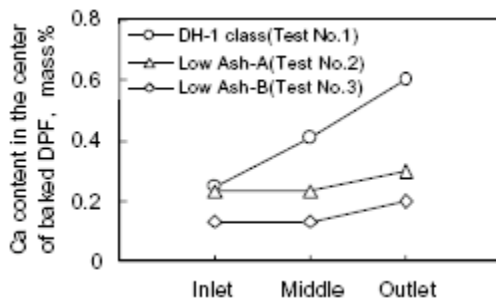


**Figure 2.17: Ash distribution along the length an ash-loaded DPF for three lube oil formulations<sup>[28]</sup>**

**Table 2.4: Estimated components of oil derived ash for three lube oil formulations<sup>[28]</sup>**

	[mass %]		
Test No.	1	2	3
Test Oil	DH-1 Class	Low Ash-A	Low Ash-B
CaSO <sub>4</sub>	75±6	66±6	65±14
CaCO <sub>3</sub>	(2±1)	(3±1)	(3±3)
Zn(PO <sub>3</sub> ) <sub>2</sub>	15±3	21±6	24±9
ZnSO <sub>4</sub>	(2±1)	(5±3)	(<1)
ZnO	(5±2)	(5±3)	(9±3)

While understanding the chemical composition of lube oils, soot and ash is very important to the performance evaluation of engines, lubricants and aftertreatment products, it is also necessary to determine the morphological characteristics of the soot produced by the engine as the residual ash. The size and shape of the soot and ash particles have significant implications with regard to the backpressure increase associated with the accumulation of soot on the channel walls during loading as well as the accumulation of residual ash over the usable life of the DPF. Nord et al. examined soot particles produced by a diesel engine running at 50% load, shown Figures 2.18 and 2.19 [29]. The particles appear to be chain-like agglomerates, and Raman spectroscopy indicates that the agglomerates consist primarily of carbon. Although dependent on engine operating conditions, the amount of carbon present in the soot far outweighs the amount of ash material, making it difficult to observe ash material prior to regeneration. Thus, ash is typically analyzed once a fairly large amount has accumulated and the DPF is completely regenerated.

In addition to quantifying ash-forming elements in lube oils and identifying compounds present in ash material, Givens et al. also observed the ash layer in a DPF using scanning electron microscopy, shown in Figure 2.20 [27]. It is noted that the experimental ash loading of approximately 7.2 grams did not produce an ash layer thick enough to be susceptible to ash breakaway, but did produce a layer that completely covers the channel wall. The ash layer that forms is the result of soot layers being repeatedly formed and regenerated, leaving the non carbonaceous material in a porous layer. Results indicate that the presence of a soot layer has a greater impact on engine backpressure than the long-term accumulation of ash, where soot loadings of

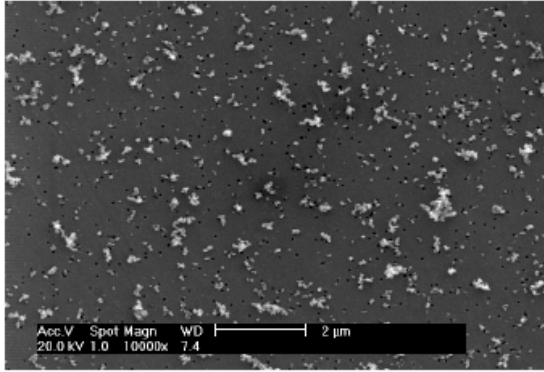


**Figure 2.18: SEM image of soot particles (10K X)<sup>[29]</sup>**

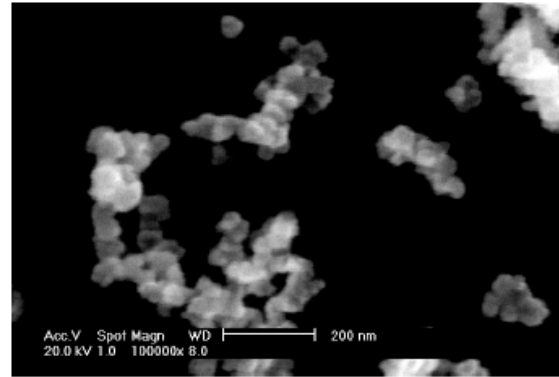


**Figure 2.19: SEM image of soot particles (100K X)<sup>[29]</sup>**

approximately 3 g per liter were observed to result in a backpressure increase comparable to an ash accumulation in excess of 20 grams per liter [53, 56, 58].

Further analysis carried out by Givens et al. provides detailed information regarding the formation of the ash layer in a cordierite substrate [27]. Optical observations show an ash layer that increases in thickness along the length of the DPF channel from front to rear, regardless of lube oil formulation, as shown in Figure 2.21. The low ash lube oil formulations clearly produce less ash, resulting in thin ash layers. The ash layers formed using the two low-ash oils are relatively thin compared to the sample aged using the reference oil. Observation of ash accumulation in the rearmost section of the DPF shows some channels are completely plugged with ash produced by the reference oil, while the low-ash oils produced a thin layer with no observable breakaway and plugging. This trend is consistent with all results found in similar experiments [25-29].

Analysis of elemental maps for calcium deposits in these DPFs under high magnification reveals a small but visible difference in the ash layers resulting from the

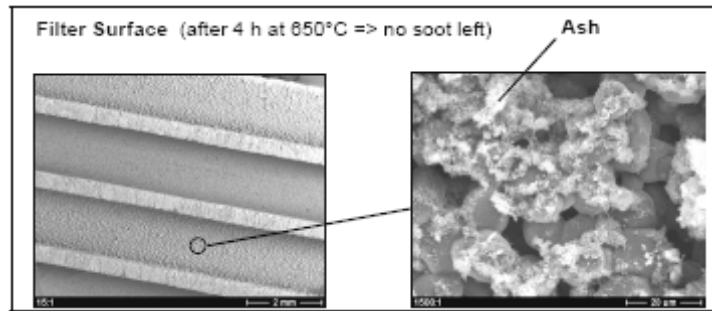


**Figure 2.20: SEM of ash layer on channel wall of a SiC DPF<sup>[27]</sup>**

two low-ash oil formulations, shown in Figures 2.22 and 2.23. The backscatter images and elemental maps show a thicker ash layer for oil formulation A, while the distribution and relative intensities of the elements are approximately equal between the two formulations. Calcium and sulfur are again shown to be present in relatively large quantities, while zinc, phosphorus and iron are present in small but detectable quantities. Upon examining the ash-substrate interface under higher magnification, shown in Figure 2.24, it can be seen that there is minimal penetration of ash material into the channel wall, and it is likely that the material present in the wall is the result of contamination during sample preparation. This suggests that the ash agglomerates that break away from the ash layer are larger than the substrate pores, resulting in highly efficient ash recovery.

It has been shown that by determining the composition of the lube oil being used, one can roughly predict the amount of ash that will be produced. Experiments have demonstrated good agreement between oil consumption and ash formation, though volumetric consumption of lube oil does not directly correlate with the presence of ash forming metals in the DPF. Variations in lube oil formulations have been observed to greatly affect the amount of ash produced as well as the manner in which the ash layer is



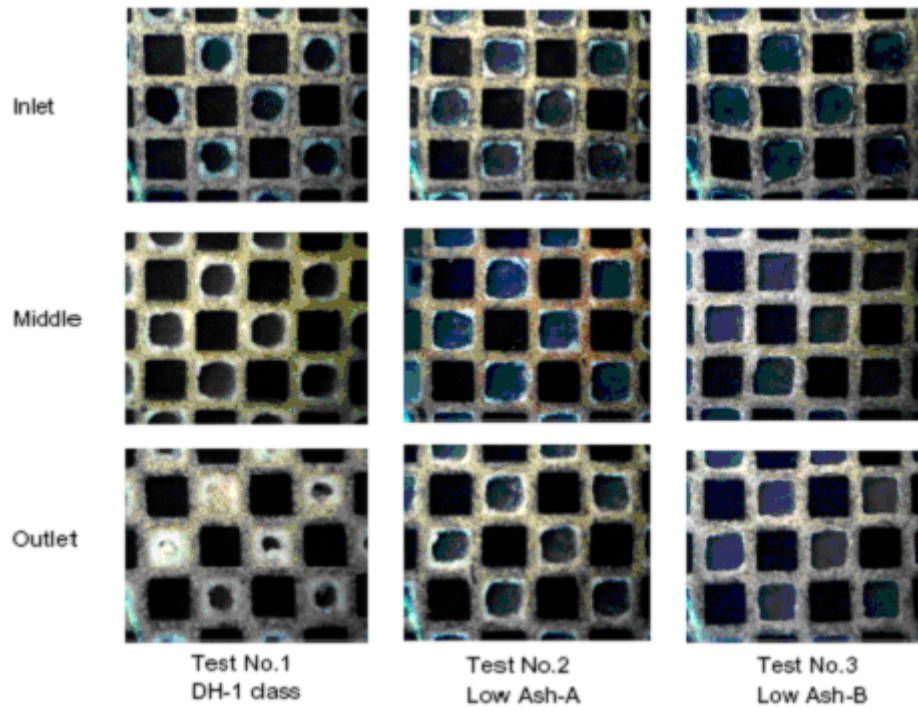


**Figure 2.21: Optical microscope analysis of ash layer at various locations of DPFs aged using three oil formulations<sup>[28]</sup>**

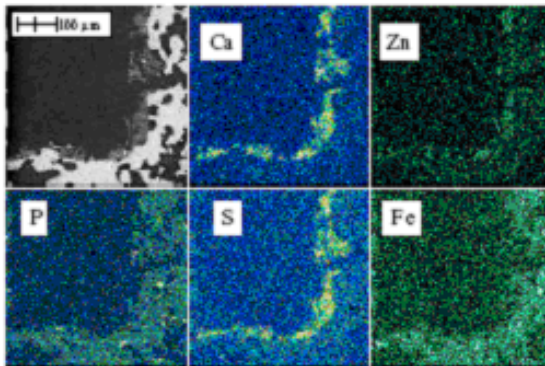


**Figure 2.22: EPMA elemental maps of ash layer in a cordierite substrate aged with a low-ash lube oil A (200X)<sup>[28]</sup>**

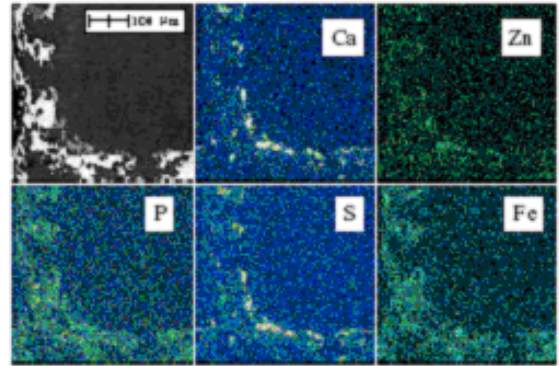


**Figure 2.23: EPMA elemental maps of ash layer in a cordierite substrate aged with a low-ash lube oil B (200X)<sup>[28]</sup>**

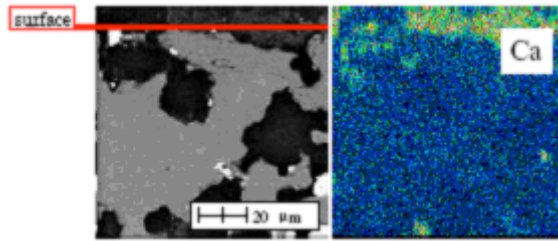


**Figure 2.24: EPMA backscatter image and elemental map showing calcium in the ash layer of a cordierite substrate (1000X)<sup>[28]</sup>**

distributed throughout the filter. Perhaps most importantly, the ash layer has been shown to be fairly porous and that ash itself to be more dense than soot.. Thus, the backpressure increase resulting from ash accumulation is much lower than that associated with soot loading when compared on a grams per liter basis. However, ash accumulation within the DPF and subsequent backpressure increase still remains an important factor in determining the usable life of the system.

## **2.5 Accelerated Ash Loading**

Exhaust aftertreatment systems being developed to fulfill increasingly stringent emissions requirements must be able to perform effectively over a lengthy life cycle with minimal maintenance. The most prominent complication affecting the life cycle of a DPF is the accumulation of residual ash, resulting in decreased filtration volume, increased engine backpressure and associated fuel penalty. As mentioned in the previous sections, ongoing research and development of low ash lube-oils have shown progress in minimizing the amount of ash formed and accumulated within the DPF. The difficulty in evaluating the performance of these lube-oils as well as aftertreatment technologies over the desired length of time is quite simply the time and expense involved. Many

aftertreatment devices are required to perform for mileages in excess 100,000 miles, with some intended to function beyond 435,000 miles. Since it is not feasible to evaluate these products for the desired mileage via on-road experiments, engine bench testing has been employed to simulate these driving distances by replicating the desired operating conditions. The use of engine bench testing produces repeatable conditions that allow for direct performance comparisons between different devices and products. While this enables the experiments to be carried out in controlled environments while being monitored with more sophisticated equipment, the issue of required test time is a problem for evaluating multiple systems. For evaluating DPF technologies, increasing the rate of ash formation significantly decreases the required length of the experiment. However, special care must be taken to ensure that the characteristics of the ash formed via these accelerated methods compares favorably to ash formed by conventional lube oil consumption.

There are several methods by which lube oil consumption can be increased during an engine bench experiment. Investigations carried out by Stetter et al [30] mention several means by which oil is naturally consumed by the engine and describes ways to increase that consumption intentionally. These consumption mechanisms, illustrated in Figure 2.25, include blow-by gases that are reintroduced to the working volume during the intake stroke by the PCV system, leakage past the valve stem seals, leakage past the piston rings, and leakage from the turbocharger. Of these, only the leakage past the valve stem seals and piston rings were examined in the course of the investigation. Results indicate that natural lube oil consumption is a strong function of operating conditions, and is typically in the range of 0.1 to 0.5 percent of the full load fuel consumption. This

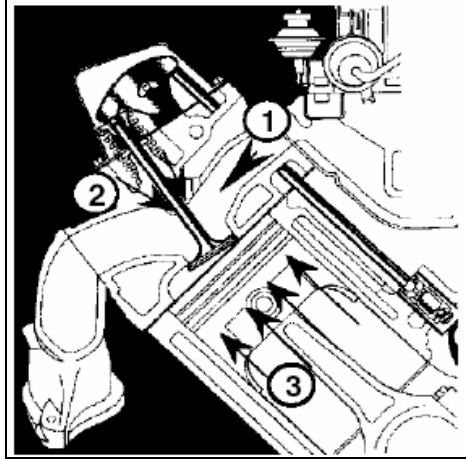


**Figure 2.25: Schematic of accelerated lube oil consumption mechanisms (1: PCV Blow-by, 2: Valve seal leakage, 3: Leakage past piston rings)<sup>[30]</sup>**

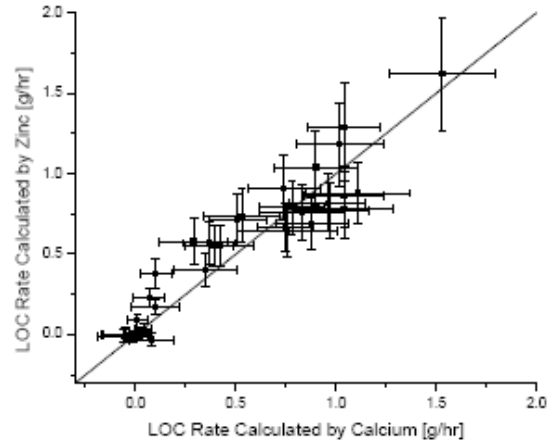


**Figure 2.26: Lube oil consumption calculation based on calcium and zinc<sup>[30]</sup>**

translates to approximately 7 to 50 grams per hour for the 2333 cc engine used in the investigation. It is also noted that the consumption of lubricating oil had no apparent effect on particulate size distributions.

Another method for accelerating the consumption of lube oil was studied by Manni et al., in which oil was injected into the air intake manifold [66]. This allows for precise control of the amount of additional oil being consumed, while natural oil consumption is monitored separately. The age of the engine was shown to have a significant impact on the amount of oil naturally consumed by the engine. Data recorded over three experiments, shown in Figure 2.27, shows a significant variation in oil consumption between tests carried out on engines of varying age, though increasing age did not consistently result in increased oil consumption. The correlation between oil consumption and DPF weight increase, however, demonstrated excellent correlation for all experiments.

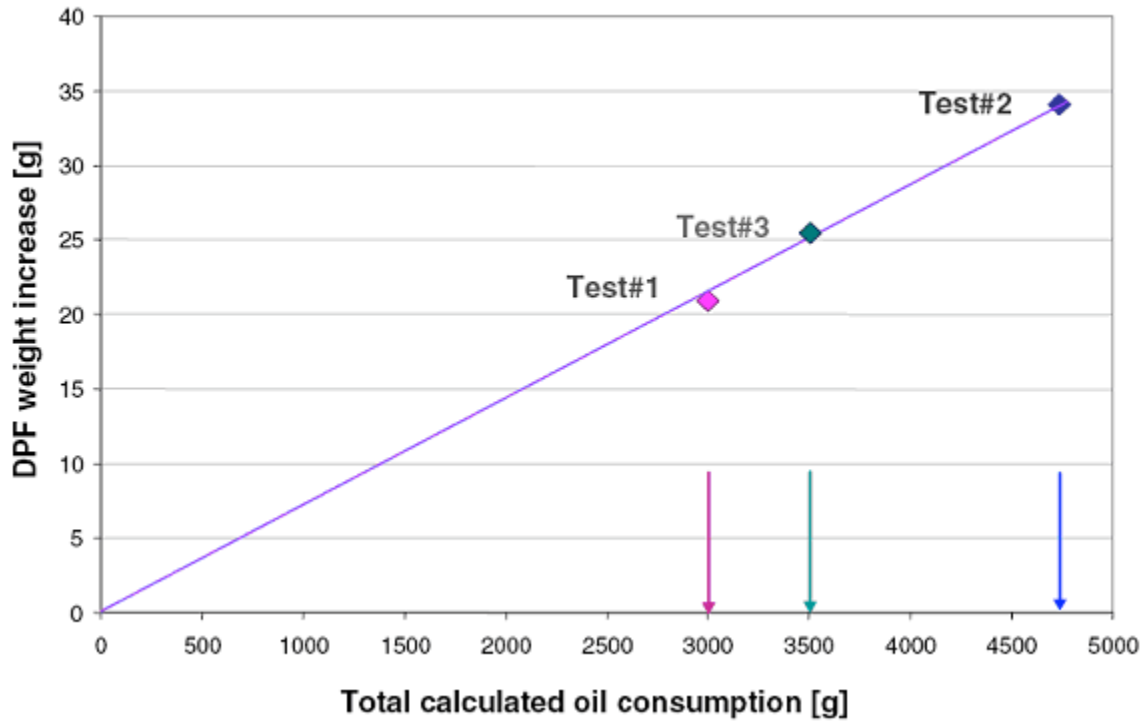


**Figure 2.27: DPF weight increase as a function of oil consumption during 120-hour test for 3 engines of different ages<sup>[66]</sup>**

Manni et al also observed that natural oil consumption varied considerably over the course of a single experiment, as shown in Figure 2.28, demonstrating a complication with regard to the real-time monitoring of lube oil. However, by artificially increasing the amount of oil being consumed, these variations may become smaller in magnitude relative to overall oil consumption depending on the rate of artificial oil consumption. In that experiment, the rate of oil consumption is slightly more than doubled.

Characterization of the aged DPF was carried out to determine the morphology and composition of the ash layer. Images acquired using SEM, shown in Figure 2.29, show a fairly dense ash layer of consistent thickness within the region being observed. There is also a layer of organic material observed on top of the ash layer, which is the result of running the engine for thirty minutes following the final regeneration. Analysis

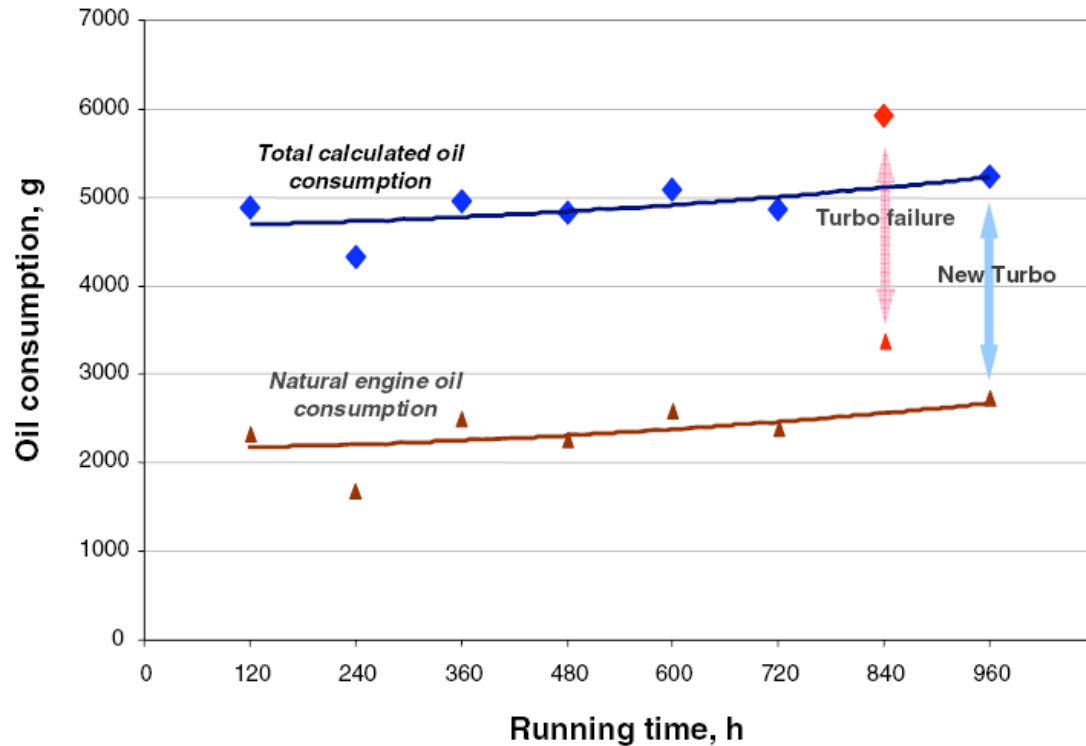


**Figure 2.28: Variation in the lube oil consumption over a 40-hour experiment<sup>[66]</sup>**

of the ash using XRD again revealed the presence of calcium sulfate and zinc phosphates.

Experiments carried out by Sutton et al. examined the rate of ash formation by blending lube-oil with the fuel as the acceleration method [67]. Excellent correlation between ash formation and lube oil consumption on a mass basis was once again observed, shown in Figure 2.30, as well as associated increases in backpressure. Overall, the results indicated that this method of accelerating lube-oil consumption provides results that are comparable in morphology and composition to field-aged substrates. Thus, it is believed that this approach provides a valid method of accelerated oil consumption.

Sutton et al. also discussed two significant issues regarding the validity of using oil-doped fuel as a method of accelerating oil consumption. First, the lubricant is

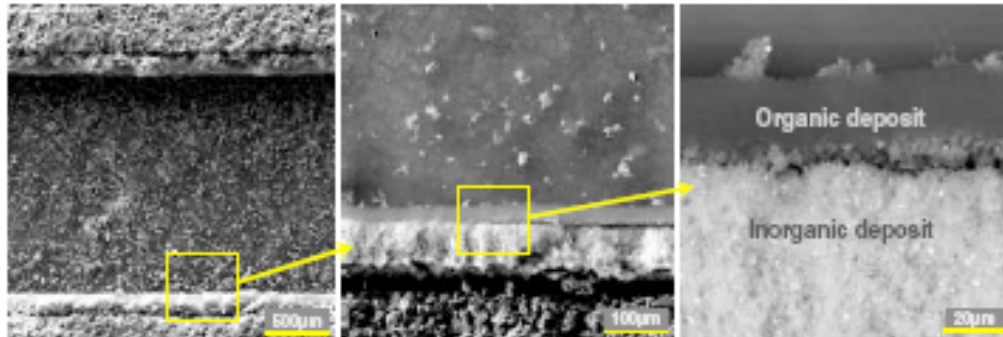


Figure 2.29: SEM images of the ash and soot layer formed using intake manifold oil injection<sup>[67]</sup>

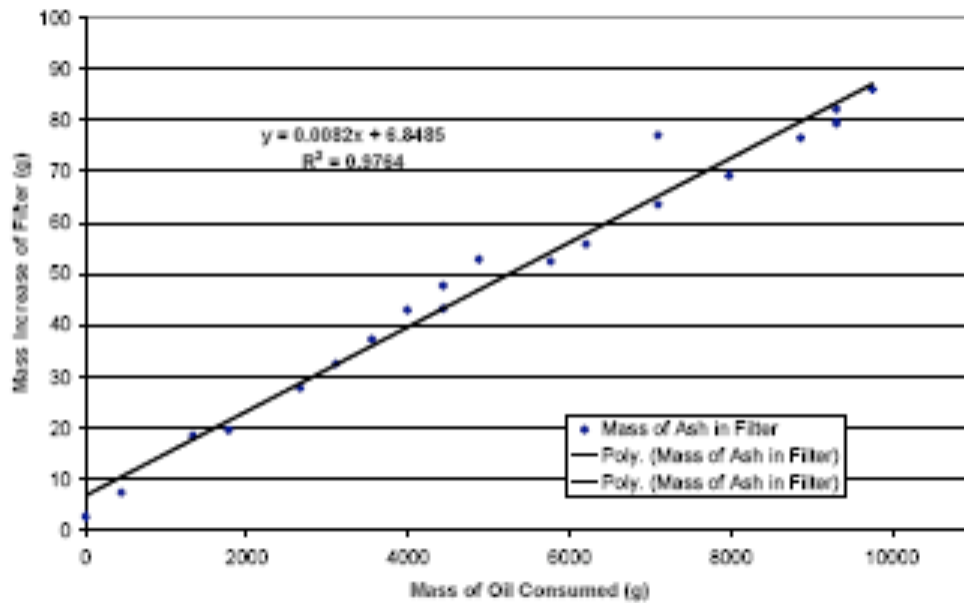


Figure 2.30: DPF weight increase versus lube oil consumption using doped fuel<sup>[67]</sup>

introduced to a different part of the combustion process, being combusted in the diffusion part of the flame rather than in the air-rich regions along the cylinder wall. Second, disturbances in the chemical structure of the lubricant can form partially suspended sludges of metallic components, which may not burn normally.

SEM photos of two substrates, shown in Figure 2.31, provide a method of comparison to evaluate the effects of accelerated lube-oil consumption. The first substrate is aged for 1118 hours using standard fuel, while the second is aged for only 165 hours using fuel doped with lube-oil. Both ash layers appear visually similar with regard to density, though the 1118-hour ash appears to be more porous. The white spots observed in both ash layers represent areas that are very rich in ash metals such as calcium and zinc. Overall, this method is believed to produce acceptable results.

A simpler way of introducing additional oil to the combustion process is by doping the diesel fuel itself with a predetermined amount of lube oil by volume. Experiments conducted by Bardasz et al. demonstrated the results of fuel doping by adding 0.2 percent by weight of oil to the fuel [68]. The effects of this increased oil consumption are immediately visible in the experimental data, shown in Figure 2.32, where backpressures experienced for cases in which doped fuel was used nearly doubled that observed for non-doped fuel in only 10 hours and forcing the experiments to be concluded earlier than the one in which non-doped fuel was used.

Analysis of the ash layers for the three experiments using scanning electron microscopy reveals that the ash layer formed by the high ash oil with doping is significantly denser than other two layers, as shown in Figure 2.33, which explains the steep increases in backpressure. It is believed that the relatively high rate at which ash is



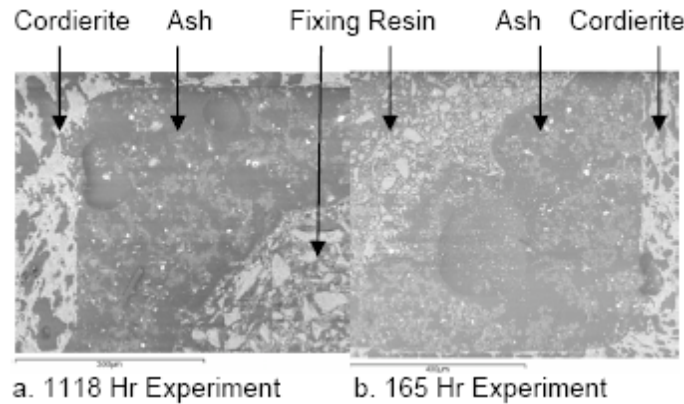


**Figure 2.31: DPF weight increase versus lube oil consumption using oil misting<sup>[67]</sup>**

accumulating within the DPF is responsible for these variations in ash layer density.

Several methods of accelerating the consumption of lube oil have been discussed. It is understood that every method of artificially increasing oil consumption represents a movement away from natural oil consumption, and will be accompanied by associated variations in results. The extent of these variations is dependent not only on the method being used, but also the extent to which the oil consumption rate is being increased. Ash layers formed during experiments employing accelerated oil consumption protocols produced ash layers that were comparable in thickness to samples aged by only natural oil consumption. However, the ash layers formed using these accelerated protocols consistently produced ash layers that are visibly less porous, resulting in the increased backpressures observed in experimental data. Based on these results, doping the fuel with a predetermined amount of oil by volume appears to be the simplest method of accelerating oil consumption. Characterization results confirm the validity of this method, though a more comprehensive characterization study would be useful to compare results from standard aging with results obtained using accelerated protocols.

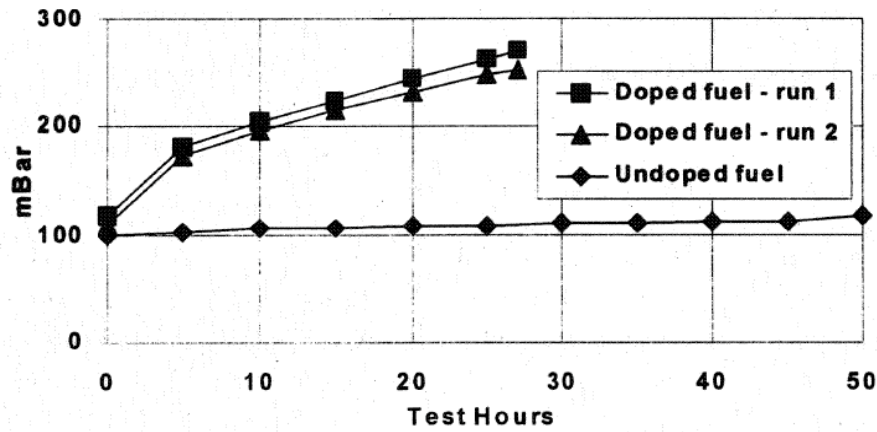


Figure 2.32: Backpressure increase as a function of time for experiments using doped and non-doped fuel<sup>[68]</sup>

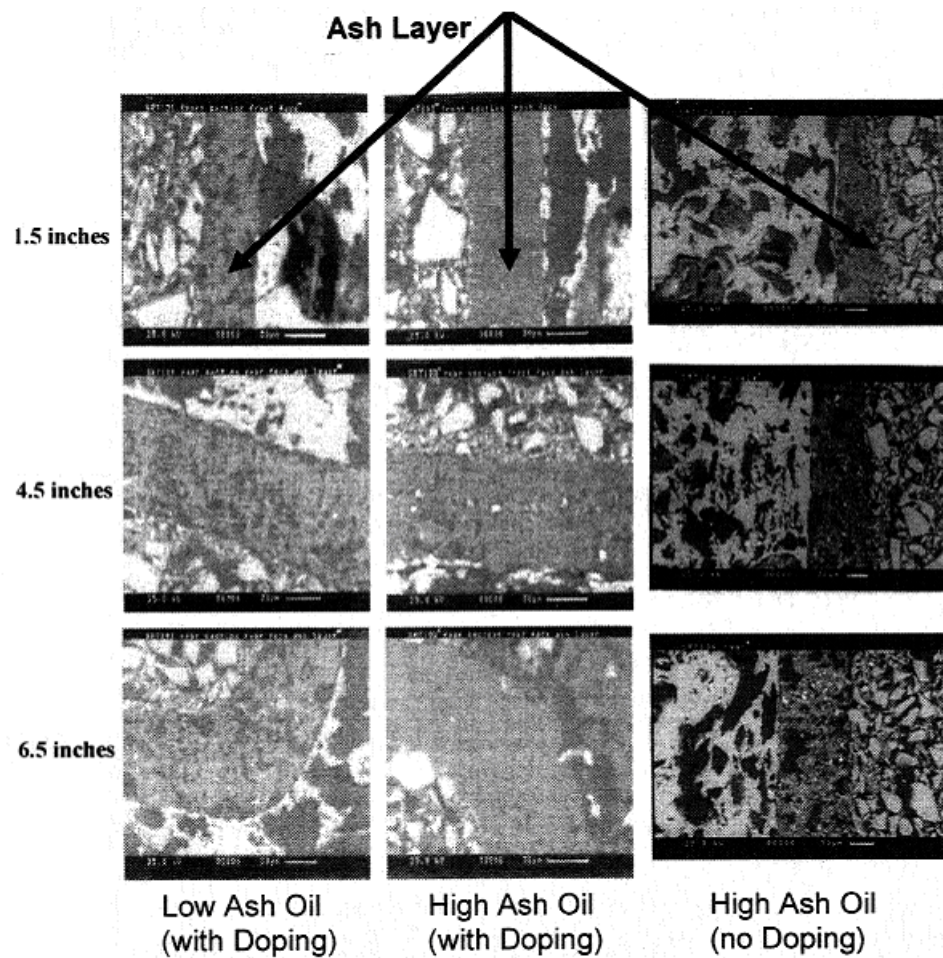


Figure 2.33: SEM images of ash layers for three oil consumption mechanisms<sup>[68]</sup>

## CHAPTER 3

### EXPERIMENTAL APPARATUS AND PROCEDURES

This chapter outlines the experimental apparatus used, the properties of each DOC-DPF combination investigated, as well as the engine operating envelope for accurately simulating full-scale experimental and real-world conditions. A description of surface characterization techniques is also provided. Section 3.1 offers an overview of the engine bench used for accelerated ash loading. Section 3.2 outlines the operation procedures for the engine including start-up as well as the soot loading and active regeneration strategies. The geometric, mechanical, chemical and thermal properties for each DPF and the upstream oxidation catalyst used in the present investigation are given in Section 3.3. Finally, Section 3.4 provides an in-depth overview of the various characterization techniques employed throughout this study.

#### 3.1 Engine Bench for Accelerated Ash Loading

##### *3.1.1 Overall Description of Accelerated Ash Loading Engine Bench System*

The small engine bench used for these experiments is located at the Oak Ridge National Laboratory within the Fuels, Engines and Emissions Research Center. The engine bench is very similar to that described by Bunting et al [69] and had previously been used by Eaton [19] to investigate the effects of accelerated poisoning of diesel oxidation catalysts using zinc dialkyldithiophosphate (ZDDP). A schematic of the rapid

aging engine bench is shown in Figure 3.1. The engine bench is comprised of three primary components: a bench-mounted single-cylinder diesel engine, an electric motor with variable frequency drive, and a modular exhaust system. The Hatz diesel engine and Baldor electric drive motor are bolted to the same bench and connected via a flexible shaft coupling. The bench is isolated from the control room by a wall with acoustically-sealed doors and windows. The engine test chamber itself is outfitted with both forced circulating fresh air and vacuum exhaust system. The engine has a displacement of 517 cc and was selected to minimize operating and maintenance expenses, and to allow the use of small scale exhaust and catalyst components.

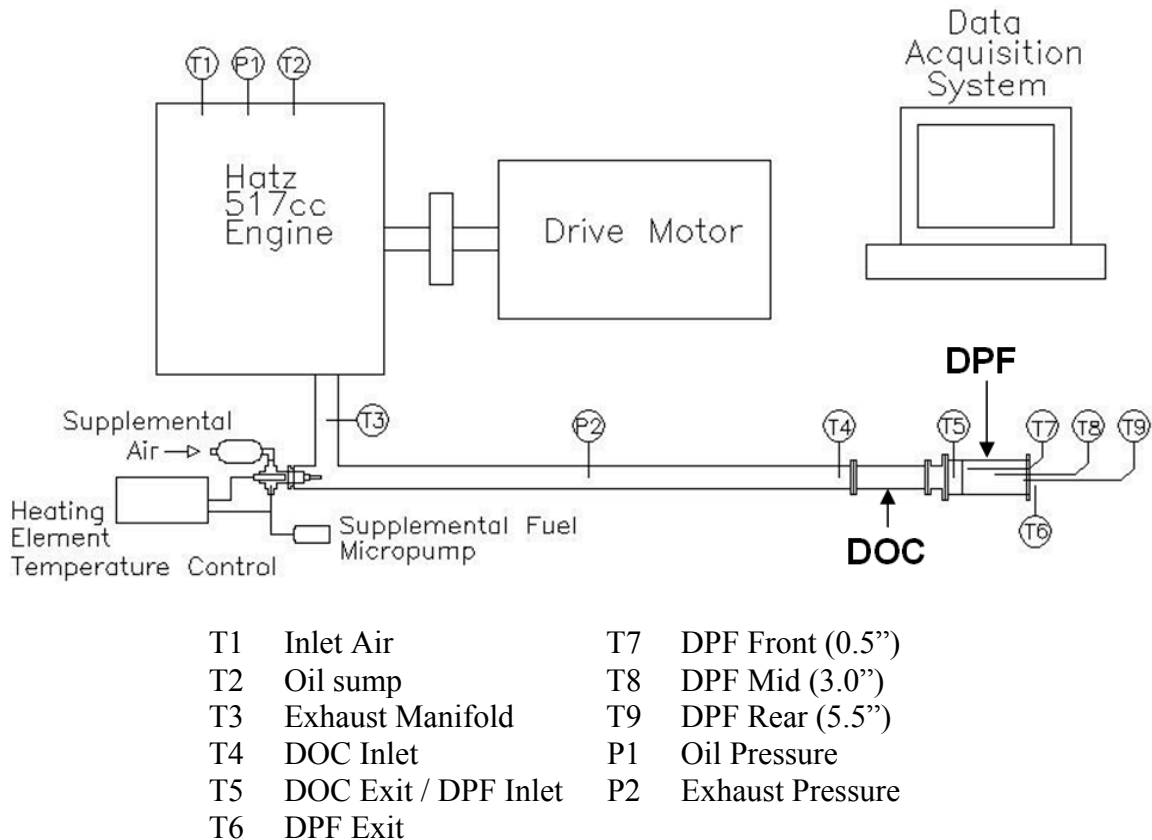


**Figure 3.1: Schematic of the RPEB System**

The DPFs and DOCs used in this study represent the various substrate materials which are currently in use or will be commercially available for heavy-duty and light-duty engine applications in the future. A full-size diesel particulate filter typically has a diameter ranging from 15 to 32 cm, with lengths from 15 to 40 cm. The length of a single DPF channel is often several orders of magnitude larger than the cell inlet width. For this study, DPFs are 7.62 cm in diameter and 15.24 cm in length. The upstream oxidation catalysts used in all experiments are 5.08 cm in diameter, with length ranging from 7.62 cm to 15.24 cm. Of particular interest with respect to this geometry is the accurate scaling of gas hourly space velocity, which has direct impact on engine backpressure, soot oxidation, and heat transfer between the filter and the exhaust gas.

Throughout the investigation, BP-15 ultra-low sulfur fuels ranging from 3 to 15 ppm sulfur are used in an attempt to minimize catalyst poisoning and subsequent degradation of catalyst performance. The fuel is doped with 5% by volume standard 15w-40 Shell Rotella motor oil, thus accelerating the consumption of lube oil and resulting in an accelerated ash loading on the filter walls.

The engine is operated at a constant speed of 1500 RPM with engine load controlled by a servo-motor linked to the engine's governor and controlled by an analog feedback system; a potentiometer with numeric dial is located in the control room and used to vary the servo-motor position. This allows for precise and repeatable control of engine operating conditions, namely, exhaust temperature. A photograph of the rapid aging engine bench and ancillary equipment is shown in Figure 3.2.

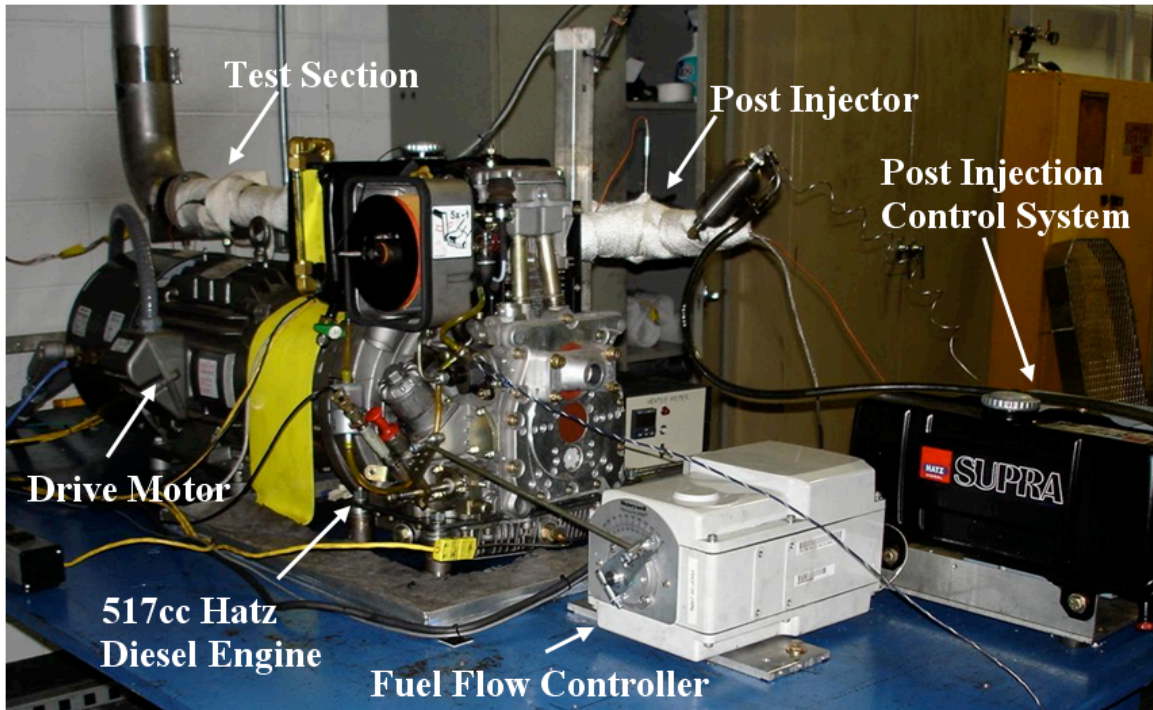


**Figure 3.2: Photograph of the rapid aging engine bench with system components**

Exhaust gas temperatures are measured at four different locations along the modular exhaust system using type-K thermocouples. The first thermocouple is located approximately 0.3 m from the engine exhaust manifold and measures the engine-out exhaust temperature. The second thermocouple located approximately 15 cm upstream of the DOC is used to monitor the temperature of gas entering the DOC. The third and fourth thermocouples located approximately 1 cm upstream and downstream of the DPF are used to measure the DPF inlet gas temperatures, as well as verify post-injection and DOC performance during regeneration and the DPF exit gas temperature, respectively.

Three thermocouples are positioned inside the DPF to monitor the temperature of the substrate. The thermocouples are inserted from the rear of the DPF and positioned

axially within the exit channels at locations 1.27, 7.62 and 13.97 cm from the filter inlet along the center axis. These thermocouples are used to determine the temperature profile along the length of the filter, as well as for the detection of exotherms during active regeneration.

Two pressure transducers located near the exhaust manifold are used to measure engine backpressure resulting from losses through the system as well as PM and ash accumulation within the filter. One transducer measures absolute pressure while the other measures gage pressure, providing redundancy and a method of verifying proper instrument performance. Since the pressure at the DPF exit is atmospheric, the pressure drop across the system can be measured by measuring only the exhaust backpressure.

The modular test section is installed approximately 2.0 m from the engine exhaust manifold. The DOC is mounted in a 5.08 cm-diameter pipe using a vermiculite-coated ceramic fiber matt placed between the DOC and the pipe walls. The matting serves as insulation, prevents gas slip and providing a buffer for protection against breakage due to thermal expansion. The DPF is mounted in a 7.62 cm-diameter pipe using matting similar to that used with the DOC. A backing plate with an inside diameter of 7 cm is installed at the rear of the DPF pipe to prevent the filter from being driven out of the pipe by the exhaust pressure. The DPF is mounted 10.16 cm downstream of the DOC.

Accelerated ash loading is achieved by introducing lube oil into the system at a rate several orders of magnitude faster than seen with normal engine wear. A total of 57 liters of fuel is mixed with 3 liters of lube oil resulting in a fuel doping of 5% by volume. The oil is then injected into the combustion chamber with the fuel, burned and expelled through the exhaust manifold. The resulting exhaust gas and material then encounter the



aftertreatment section, passing through the DOC to the DPF where PM and ash particles are trapped. Due to the introduction of relatively high volumes of lube oil into the combustion chamber, the fuel injector is removed and cleaned daily to prevent ash buildup and the associated hindrance of fuel distribution within the cylinder.

### ***3.1.2 Diesel Engine***

The engine selected for the test bench is a naturally aspirated, direct-injection (NA/DI) Hatz diesel engine, shown in Figure 3.3. With a displacement of 517 cc, this single-cylinder engine produces 7.0 kW at 2700 RPM. The electric drive motor is used to start and maintain the engine at a constant speed of 1500 RPM during operation, producing a near-constant gas hourly space velocity (GHSV) of 80,000 hr<sup>-1</sup> through the aftertreatment system. Standard BP-15 low sulfur diesel fuel is used to minimize the impact of fuel-derived sulfur on catalyst performance.

### ***3.1.3 Drive Motor***

The induction motor is used to start the Hatz diesel engine and maintain engine speed while load is varied by adjusting fuel flow. The drive motor is capable of delivering/absorbing 15 hp at 1765 RPM with a maximum speed of 4000 RPM. The motor is controlled by a Baldor Vector drive variable frequency conversion unit that is programmable to maintain either constant torque or constant RPM while motoring the engine. During DPF accelerated ash loading tests, the motor is set to maintain a constant speed of 1500 RPM while enabling the engine to operate under various loads to achieve desired exhaust conditions. A photograph of the drive motor assembly is shown in Figure 3.4.



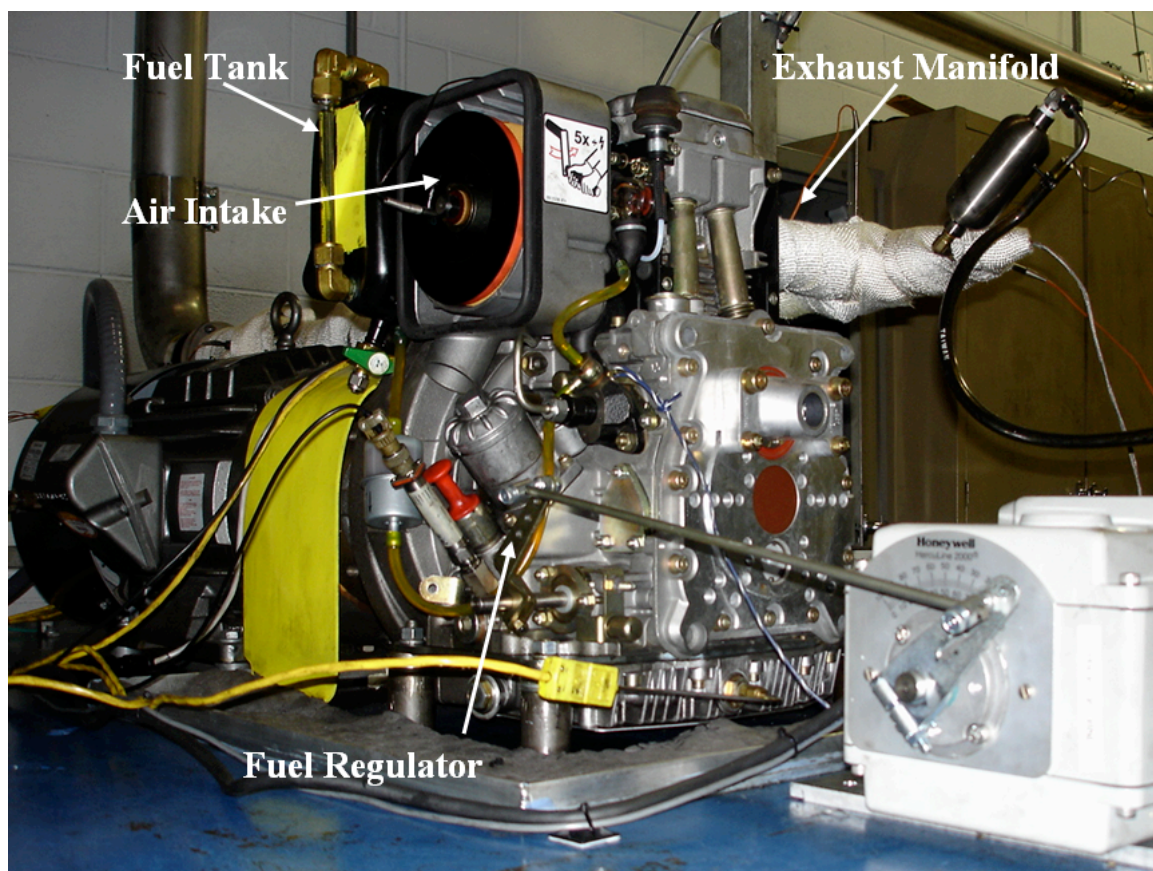


**Figure 3.3: Photograph of the Hatz diesel engine used for rapid DPF aging**

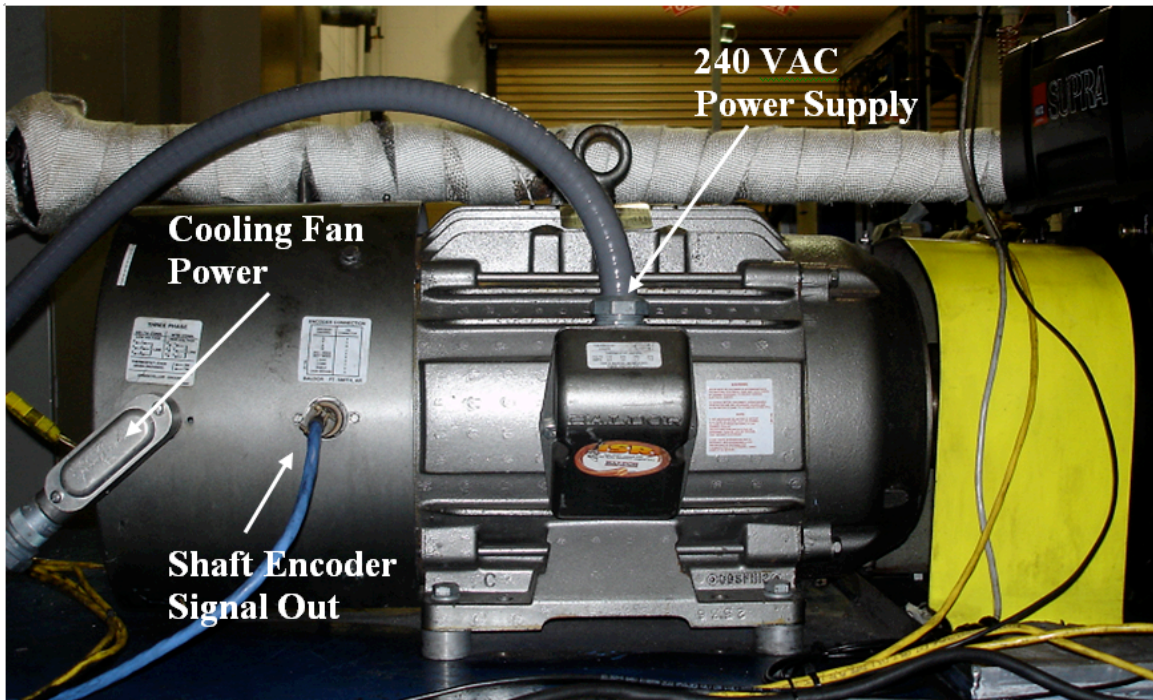


**Figure 3.4: Photograph of the Baldor drive motor used to control the Hatz engine**

### ***3.1.4 Engine Load Controller***

The amount of fuel injected into the combustion chamber is regulated using an external controller. The controller consists of a Honeywell Process Solutions Herculine 2000 series rotary actuator, and is controlled via LabView. An Omega CCT-01-0/10V DIN rail signal conditioner is used to convert the 0-10 VDC LabView output signal to a 4-20 mA signal that is sent to the actuator. The system is calibrated to provide repeatable engine operating points by adjusting the LabView control to predetermined settings. A picture of the actuator and linkage is shown in Figure 3.5. The governor of the engine is intact and provides protection for the system in the even of drive motor failure during both low speed and high speed operation.

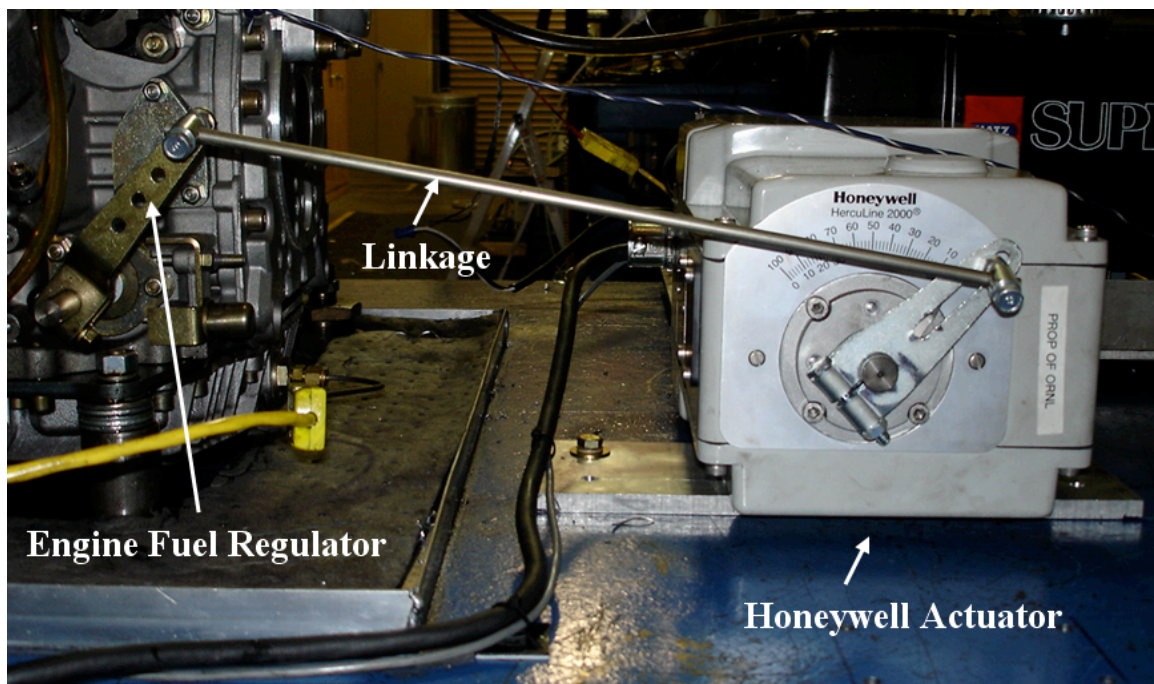


**Figure 3.5: Photograph of the engine load controller assembly**

### ***3.1.5 Post-Injection System***

A five-way union used to inject supplemental fuel for active regeneration is installed approximately 0.3 m downstream of the exhaust manifold, and can be seen in Figure 3.6. Fuel is pumped through a 1/16” stainless steel tube into the fitting using an FMI Lab Pump Model RHV pump controlled by an FMI V200 Stroke Rate Controller, allowing for precise and repeatable fuel injection rates. The fuel is atomized using a 1/4” cartridge heater and swept into the exhaust stream by supplemental air. An anti-blowback chamber has been installed to prevent fuel from being pushed back into the air line by the backpressure spike that occurs with each engine exhaust stroke. Heater cartridge temperatures are monitored with a type-K thermocouple and maintained at approximately 550°C using an external temperature controller. The pump, supplemental fuel tank and temperature controller can be seen in Figure 3.7, whereas the fuel pump control panel in Figure 3.8.

### ***3.1.6 Instrumentation and Display***

Three pressure transducers are used to monitor system performance and detect potential problems. An Omega Model PX61 pressure transducer mounted on the engine block is used to measure engine lube-oil pressure. The remaining two pressure transducers, Omega Models PX61 and PX177, are located approximately 0.3 meters downstream of the exhaust manifold and used to measure absolute and gage exhaust backpressures, respectively. The transducers located in the exhaust pipe are crucial in the execution of the loading and regeneration protocol developed in this study.



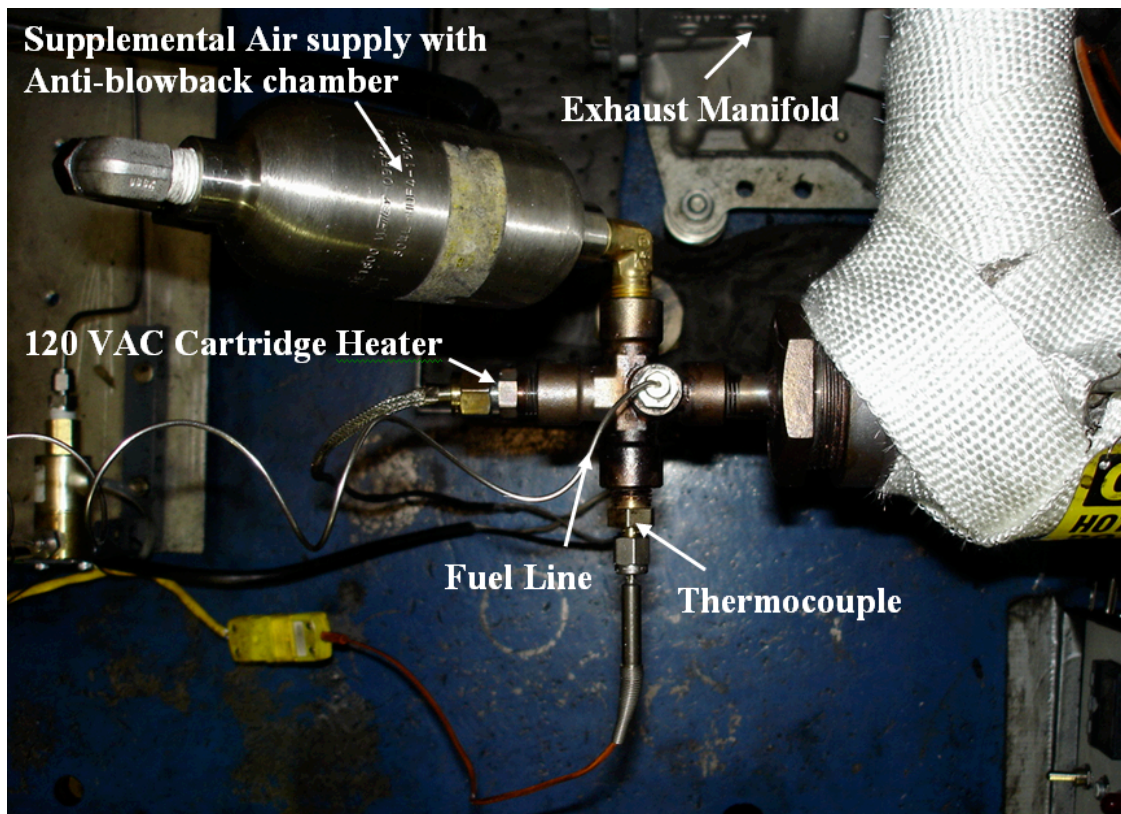


**Figure 3.6: Photograph of the supplemental fuel injector**

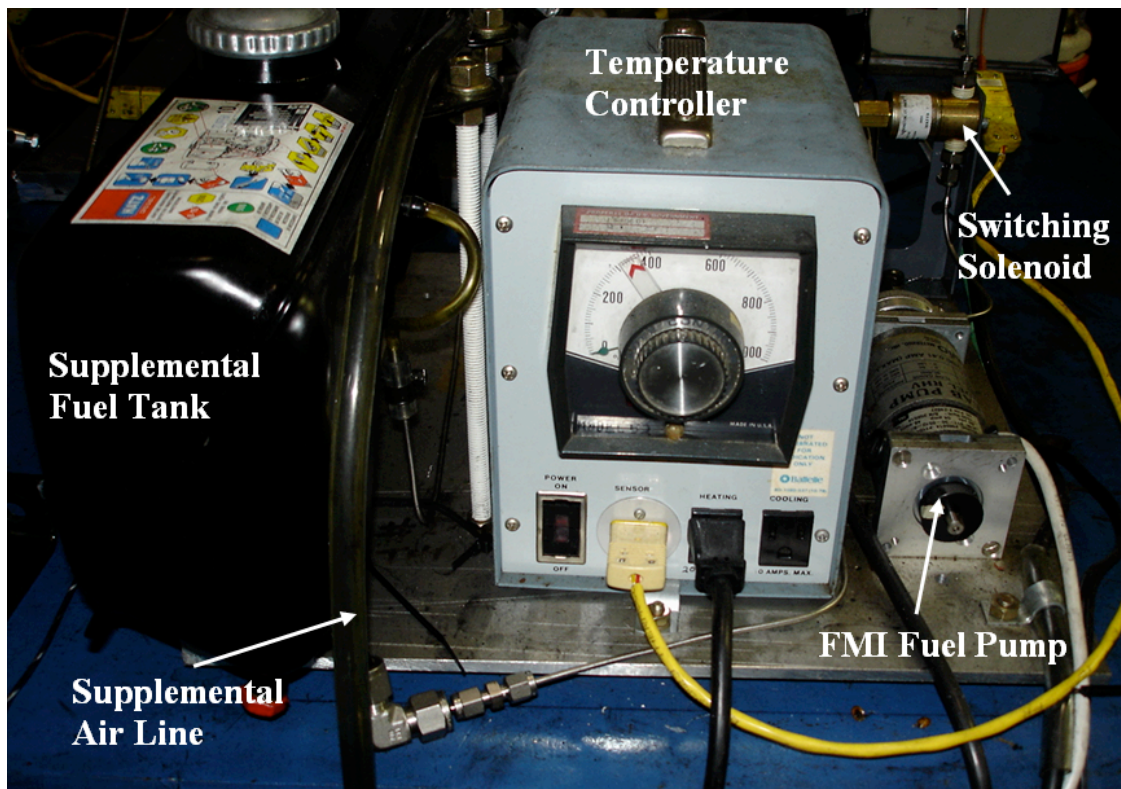
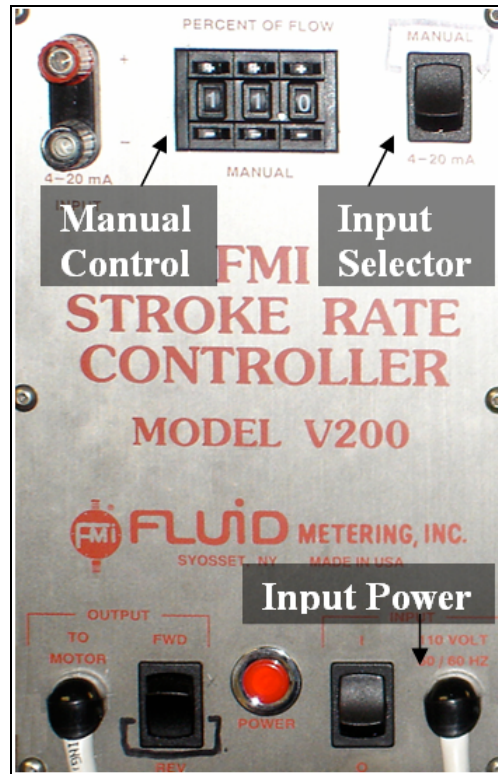


Figure 3.7: Photograph of the supplemental fuel pump and temperature control



**Figure 3.8: Photograph of the supplemental fuel injection control panel**

Nine Omega type-K thermocouples are installed throughout the system to measure temperatures of the ambient air, oil sump and exhaust system. Two thermocouples, located within the intake manifold and the oil pan, are used only to monitor engine performance and detect problems during operation. Four thermocouples are used to measure exhaust gas temperatures at specific locations within the exhaust pipe and test sections. The first is located approximately 0.3 m from the engine exhaust manifold to monitor engine-out exhaust temperature and verify repeatability of fuel regulator set points. The remaining three thermocouples are positioned 7.62 cm upstream of the DOC, 2.54 cm upstream of the DPF inlet and 1.0 cm from the DPF exit. The temperature of the DPF substrate is monitored at three different locations using 0.5 mm-

diameter thermocouples positioned along the center axis at locations 1.27, 7.62 and 14.0 cm from the filter.

### ***3.1.7 Data Acquisition System***

The data acquisition system (DAQ) is used to monitor and store data recorded during engine bench experiments. The DAQ is capable of acquiring voltage and current signals listed in Table 3.1. The primary components of the DAQ include a PC with LabVIEW 8.2 installed, data acquisition boards, terminal blocks, patch cables, panels and adapters. An instrumentation cabinet within the test cell supplies electrical power to the pressure transducers and measures voltage signals from the thermocouples and pressure transducers. Each instrument is connected to a terminal block where the analog signals

**Table 3.1: List of available signals and components handled by the DAQ System**

<b>Component</b>	<b>Source Type</b>
Oil Pressure	Voltage
Exhaust Pressure PT (abs.)	Voltage
Exhaust Pressure PT (gage)	Voltage
Drive Motor Torque	Current
Shaft Encoder	Voltage
Inlet Air Temp TC	Voltage
Oil Pan Temp TC	Voltage
Exhaust Gas Temp TC	Voltage
Catalyst Inlet Gas Temp TC	Voltage
Cat Out/DPF Inlet Gas Temp TC	Voltage
DPF Exit Gas Temp TC	Voltage
DPF Front Solid Temp TC	Voltage
DPF Mid Solid Temp TC	Voltage
DPF Rear Solid Temp TC	Voltage



are then converted to digital signals by a National Instruments cFP-2120 Compact FieldPoint controller. This is represented by the schematic shown in Figure 3.9. This digital feed is then connected to the building local area network (LAN) via a CAT-6 ethernet cable and is accessible by any computer with the associated LabVIEW executable.

The LabVIEW program used for acquiring and storing data from the Compact FieldPoint controller is called “User Interface2,” and uses a tab system to switch between the data saving routine page and the real-time customizable charts. Figure 3.10 shows a screen capture of the “Data Monitoring” tab. This tab displays system data in numerical form, as well as allows the user to calibrate channels, vary data saving parameters and

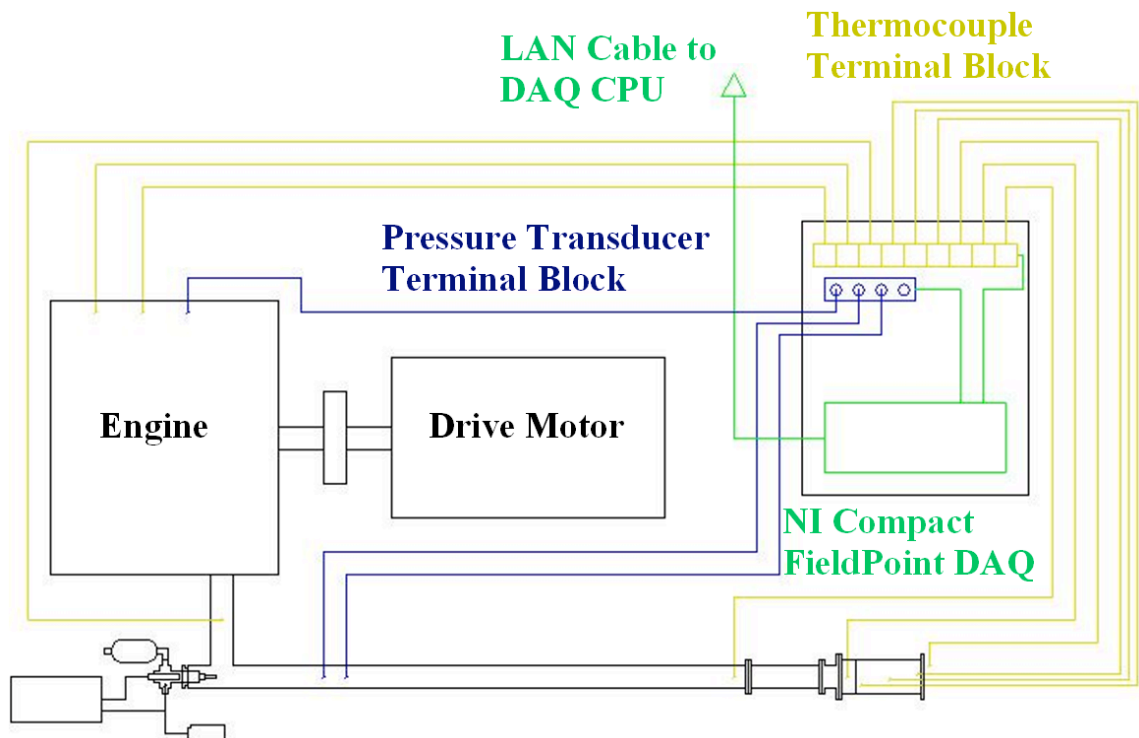


**Figure 3.9: Wiring diagram of the DAQ system and ancillary equipment**

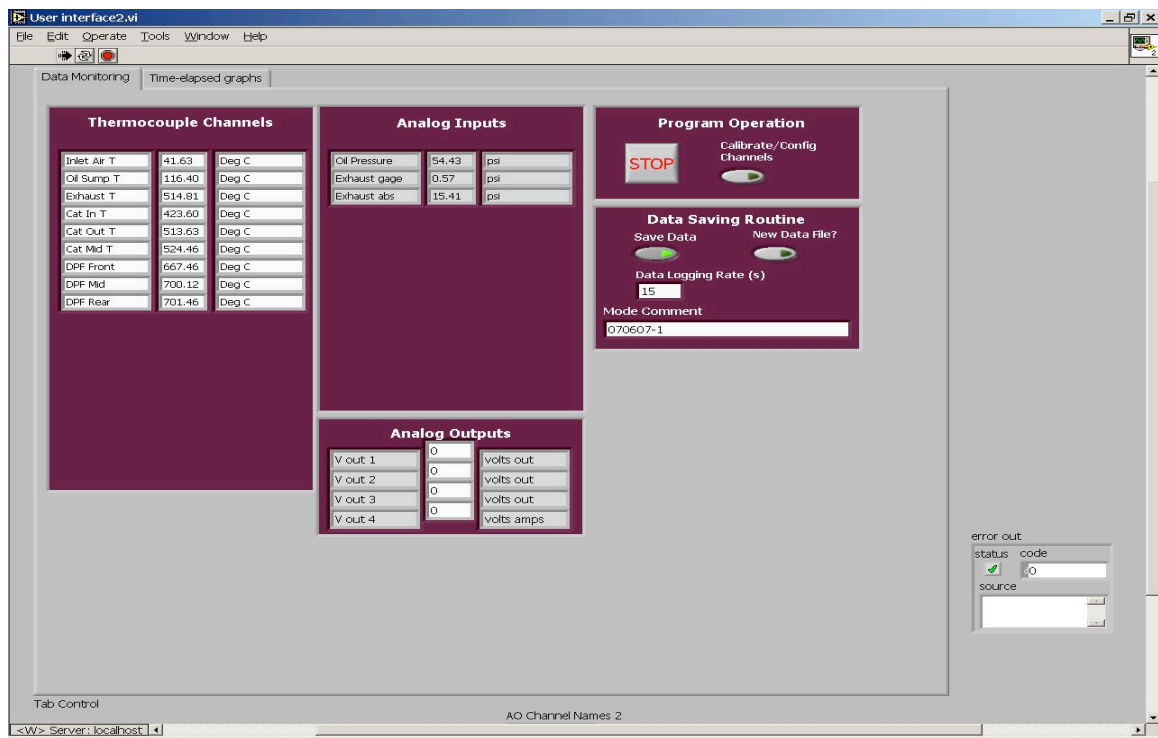


Figure 3.10: LabVIEW user interface numerical “Data Monitoring” tab

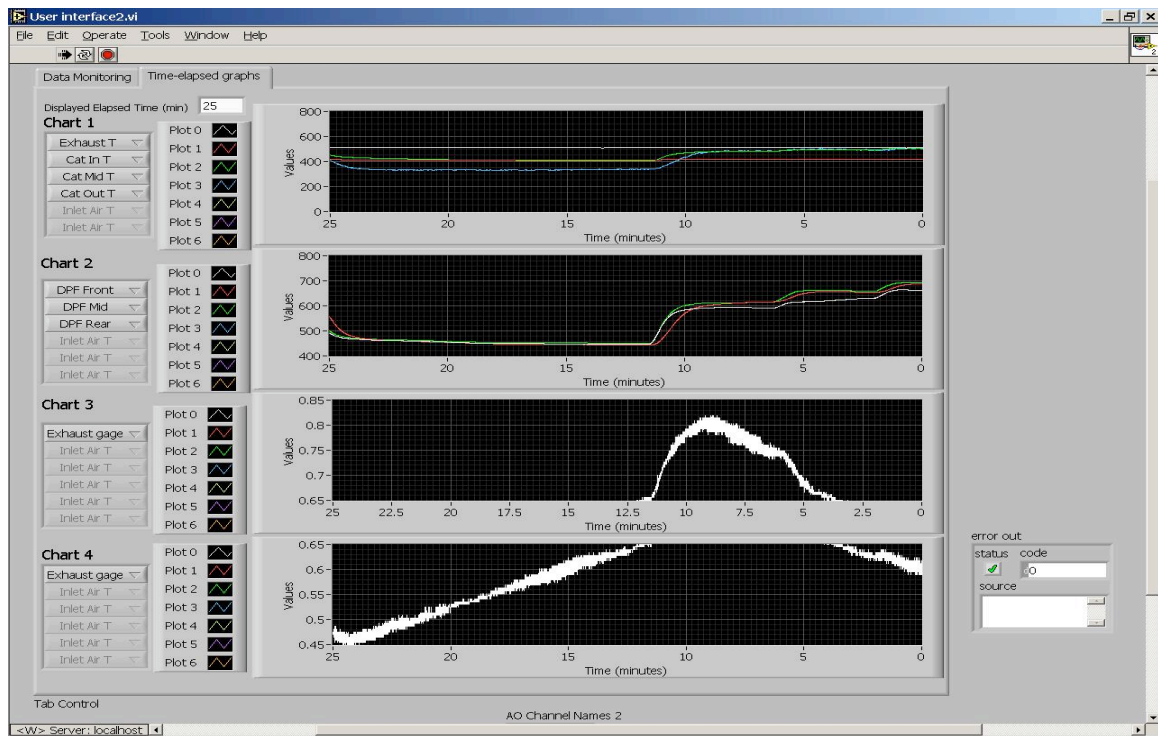


Figure 3.11: LabVIEW user interface “Time-Elapsd Graphs” tab

add mode comments. Figure 3.11 shows a screen capture of the “Time-Elapsed Graphs” tab, which allows the user to select and monitor system performance with four charts customizable with drop-down menus.

## **3.2 Engine Operating Procedures and Strategies**

### ***3.2.1 Engine Start-up Procedure***

The start-up procedure begins with a visual safety inspection of the engine bench and surrounding environment. All electrical and mechanical equipment is examined to ensure proper connections. Engine oil level is checked, the fuel tank is filled and fuel level is recorded. Thermocouple placements and connections are verified, both to make certain accurate data is taken, and to eliminate any leaks from loose thermocouple fittings. Once these inspections are complete, the overhead exhaust fans and ventilation supply air are turned on. In the control room, the data acquisition program “Hatz User Interface2” is opened on the PC and begins to monitor all measurement devices. A visual inspection of the program interface confirms that all instrumentation in the test cell is connected and displaying the correct sensor information.

Before starting the engine, the power relay switch on the power supply console is switched on, initializing power to the drive motor controller. The drive motor’s control computer required approximately 5 seconds to perform a self-diagnostic then indicates “READY” when it has completed and it is safe to turn on the drive motor. On the drive motor control console, shown in Figure 3.12, the controller switch is verified as being in the “VELOCITY” position, thereby designating a constant speed to be maintained by the drive motor. The velocity control knob below the control switch is set to 542, which

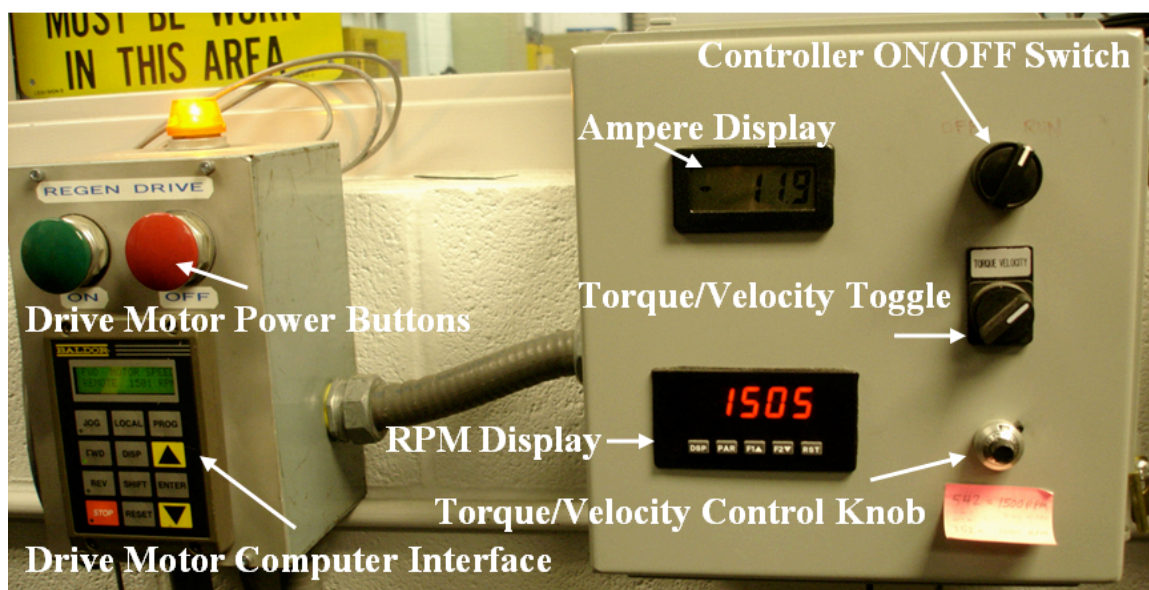


**Figure 3.12: Photograph of the drive motor power and control units**

corresponds to an engine speed of 1500 RPM. The drive motor is started by setting the control ON/OFF switch at the top of the console to “ON.” Once the engine achieves 1500 RPM, the load controller is set to provide an approximate exhaust temperature of 450°C. This load setting is maintained throughout the experiment.

### ***3.2.2 DPF PM Loading***

The goal of a soot loading cycle is to deposit approximately 2 grams of soot (~3 grams/liter) on the walls of the DPF. Two protocols for soot loading are investigated. In the first protocol, a backpressure threshold was chosen based on initial performance and used for several subsequent cycles. Once the post-regeneration backpressure fails to decrease below this baseline, a new threshold is defined by adding 0.25 psig to the previous value. However, it was discovered early on that this first protocol produced inconsistent soot loading amounts as residual ash builds up within the filter. A second protocol was then developed that required a baseline backpressure to be recorded for each

individual loading cycle, and a backpressure threshold is defined by adding a predetermined value to the baseline. In both cases, as the backpressure increases, the rate of soot production by the engine also increases. Thus, as residual ash continuously accumulates within the filter, loading cycle times become shorter and shorter. It is also known that using lube oil-doped fuel in the engine produces heavier soot, resulting in shorter loading times and subsequently faster backpressure increases throughout the experiment.

### ***3.2.3 DPF Forced Regeneration***

Once the DPF has been loaded with the desired amount of soot, this soot must be removed by actively regenerating the filter. This is achieved by increasing filter temperatures using supplemental fuel injected into the exhaust upstream of the DOC. The fuel flow rates are calibrated and adjusted to provide specific filter temperatures for specific periods of time. An entire regeneration cycle lasts a total of thirty minutes. For the first five minutes, the fuel flow rate is set such that the temperature of the substrate at the inlet of the DPF does not exceed 550°C, as to avoid initiating an uncontrolled regeneration during which soot oxidizes rapidly, often resulting in temperature excursions in excess of 1200°C. These extreme temperatures can damage most substrates as well as degrade catalyst performance, and should thus be avoided.

Filter temperatures are constantly monitored and fuel flow rates are adjusted every five minutes if needed. Temperature gradients are clearly visible along the length of the DPF, resulting from soot oxidation and fuel that passes through the DOC. Fuel injection rates are increased incrementally such that the temperature does not exceed

**Table 3.2: Supplemental fuel injection settings and flow rates**

<b>Pump Setting</b>	<b>Rate</b>	<b>Increment</b>	<b>Calc Max</b>
<b>%</b>	<b>mL/min</b>	<b>ml/min-%</b>	<b>mL/min</b>
<b>1</b>	0.353	0.353	35.294
<b>2</b>	0.714	0.361	35.714
<b>3</b>	1.053	0.338	35.088
<b>4</b>	1.412	0.359	35.294
<b>5</b>	1.765	0.353	35.294
<b>6</b>	2.143	0.378	35.714
<b>7</b>	2.449	0.306	34.985
<b>8</b>	2.857	0.408	35.714
<b>9</b>	3.158	0.301	35.088
<b>10</b>	3.529	0.372	35.294
<b>11</b>	3.871	0.342	35.191
<b>12</b>	4.286	0.415	35.714
<b>13</b>	4.615	0.330	35.503

725°C at any location. A list of pump settings and flow rates can be found in Table 3.2. This protocol has proven very effective in removing particulate matter from the filter, leaving only the residual ash. Backpressures following regeneration have been observed to return approximately to the initial baseline from the previous loading cycle. There is typically a small and consistent increase in baseline backpressure with each successive cycle resulting from the continuous accumulation of ash, which confirms both regeneration efficiency and repeatability.

### **3.3 Experimental Filters and Upstream Catalysts**

The DPFs and DOCs used in the present investigation are commercially available types and are found on a wide range of vehicle applications. The DPF is positioned at the end of the test section and it used to filter all material entrained within the exhaust gas.

**Table 3.3: Experimental DPF and DOC Specifications**

Test	DPF Specifications				DOC Specifications		
	Substrate Material	DPF CPSI	Manufacturer	PGM Loading	Substrate Material	DOC CPSI	Manufacturer
1	Cordierite	200	Delphi	10	Cordierite	300	Delphi
2	Mullite	100	DOW	0	Cordierite	300	DOW
3	Cordierite	200	Delphi	10	Cordierite	300	Delphi
4	SiC	300	NGK	0	Cordierite	300	NGK
5	Mullite	100	DOW	(high)	Cordierite	300	DOW
6	Cordierite	200	Delphi	120	Cordierite	300	Delphi
7	Cordierite	200	Delphi	120	Cordierite	300	Delphi

Substrates with different platinum group metal (PGM) catalyst loadings are evaluated to investigate the effect of ash on DPF catalyst activity. This material consists both of particulate matter and ash products resulting from the oil-doped fuel and normal engine oil consumption. The DOC is positioned immediately upstream of the DPF and is primarily used to convert NO to NO<sub>2</sub>, which has been shown to effectively oxidize PM at temperatures as low as 250°C. A description of the DPFs and DOC used in this experiment can be found in Table 3.3.

### 3.4 Characterization Techniques

Surface and analytical chemical characterization techniques are employed in this study in order to examine the morphology and composition of the ash accumulated within the filters. Results from these studies can be compared both to other engine bench studies, as well as field-aged filters. Each characterization technique used in this study is outlined in its theory of operation, equipment and instrumentation, and sample preparation. A brief discussion of qualitative and quantitative information that can be obtained from each is also provided. In Section 3.3.1, Electron Probe Microanalysis (EPMA) is discussed. Section 3.3.2 contains information on Scanning Electron

Microscopy (SEM). Scanning electron microscopy is detailed in Section 3.3.3. Finally, X-ray Diffraction (XRD) and Inductively Coupled Plasma - Atomic Emission Spectroscopy (ICP-AES) are described in Sections 3.3.4 and 3.3.5, respectively.

#### ***3.4.1 Electron Probe Microanalysis***

Electron Probe Microanalysis (EPMA) is used to characterize DPF and DOC materials, providing both elemental and spatial information. EPMA data is acquired by collecting and analyzing X-rays emitted from a sample when probed by a high-energy electron beam. The X-ray detectors and sophisticated accompanying software packages determine which elements are present based on the photoelectrons emitted and the location on the surface from which they originated.

A finely-focused beam of electrons from an electron gun impinges upon the surface of the sample in an Ultra-High Vacuum (UHV) chamber. The electron collisions impart energy to the electrons of the sample atoms, inducing an energized state. As a result, energy is released in the form of X-ray radiation—a high-energy photon—during the electron relaxation process when the electrons “jump” back to a lower energy state. The amount of X-ray energy released during this relaxation process is identical to the amount of energy consumed during the excitation process. Thus, since each element has a unique set of energy states, elements can be identified by comparing the X-rays produced.

A schematic of the X-Ray production process used in EPMA is shown in Figure 3.13 [71]. The schematic depicts the four mechanisms that are accessible for the production of X-rays. The first mechanism is described as the impingement of an incident X-ray from



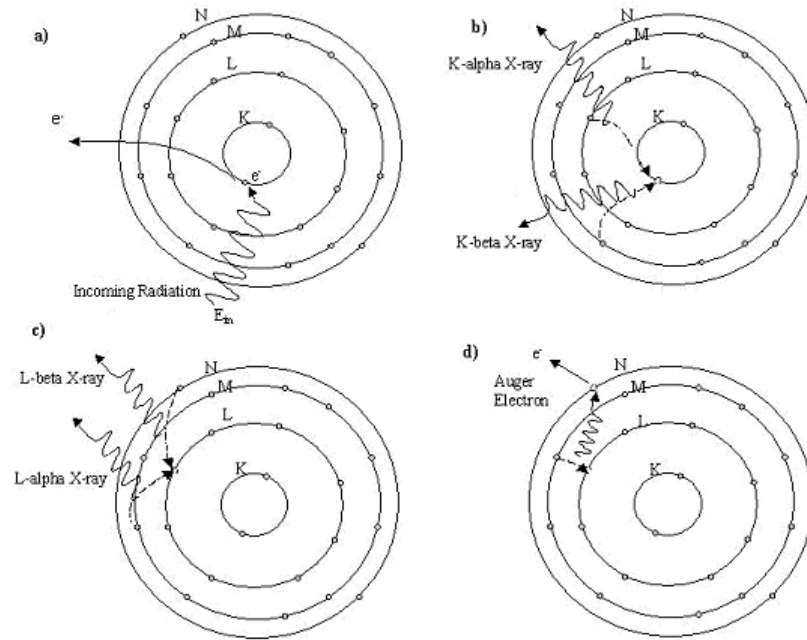


**Figure 3.13: Schematic of available electron emission pathways<sup>[71]</sup>**

a radioactive or electron gun, which collides with an electron. Energy from the X-ray is transferred to the electron providing sufficient energy to overcome the binding energy of the atom. The energy from the emitted electron is equal to that of the incident X-ray minus the potential energy barrier binding the electron. The second mechanism is the release of energy from K-orbital electrons. Once an electron is emitted, it leaves a vacancy in the orbital. Thermodynamics demands that an electron from either the L-orbital or M-orbital occupies these vacancies. During this transition, energy is released from the electrons in the form of X-rays, referred to as the K-line, and is unique for each element. The third mechanism is similar to the second with electrons emitting X-rays while moving to vacancies in the L-orbital. In this case, an electron jumps from the M-orbital to the N-orbital. The X-rays emitted by this mechanism are referred to the L-line, and are most commonly utilized for the analysis of high atomic number elements. The

fourth mechanism involves the release of “Auger” electrons. These electrons are emitted when K-line or L-line X-rays collide with the electrons in the outer most shell of the atom. Since the ionization energy is small for these electrons, they are readily expelled from the atom. The energy with which they leave the atom is equal to the potential energy of the parent-orbital binding energy minus the potential difference between the two orbitals of the shifted electrons [70-73].

A Cameca Model SX-52 EPMA device, shown in Figure 3.14, is used in the current investigation and is located at the University of Tennessee. The device is comprised of 5 vertical wavelength-dispersive spectrometers, a high-resolution energy dispersive solid-state detector and an electron optical column to produce a high electron



**Figure 3.14: Photograph of the Cameca Electron Probe Microanalysis hardware**

beam. The beam is produced by a self-biasing LaB<sub>6</sub> cathode with double aperture beam regulation and a 0.5 to 300 nA beam current capable of fully-automated alignment, focus and astigmatism correction. The X-ray spectrometers have a range of 0.22 to 0.83 sin-theta with a 40-degree X-ray take-off angle and a resolution of  $1.0 \times 10^{-5}$  sin-theta. An XFlash 2000 solid-state energy dispersive detector with a resolution of less than 159 eV at 1000 counts per second and less than 170 eV at 30,000 counts per second is used to analyze elements in the atomic range of Na to U (atomic number 11 to 92).

Line-scans and elemental maps are obtained for front, middle and rear sections of each DPF and DOC. Line-scans are traces of elemental concentrations of Si, Al, Mg, P, S, Ca, Zn, Ce and Pt which are measured from the emitted X-ray radiation collected over a cross-section of interest. In the DPF, line scans are used to observe penetration levels of various species into the filter wall, as well as to identify catalyst and washcoat thicknesses. Elemental maps are rastered areas of the DOC and DPF over which X-ray data is collected and discretized, producing an image showing the locations and relative intensities of each element, as well as an overall electron backscatter image.

Sample preparation for EPMA is a delicate process, particularly for ash-loaded DPF samples. Both DOC and DPF samples are prepared in the same manner to simplify the preparation process. The samples must first be embedded in epoxy in such a manner that the morphology of the ash layer is not disturbed. This is achieved by first submerging the inlet end of the DPF in a very low viscosity epoxy and applying a vacuum to the exit end. This forces the epoxy through the channels in a similar manner to the exhaust gases, resulting in minimal ash layer disturbance. The epoxy used is a low-viscosity resin that is specially blended to fill pore sizes smaller than 1  $\mu\text{m}$ . Within

two minutes the entire sample is completely submerged and left to harden in the vacuum environment. Once the epoxy has set, the sample is divided into cross-sections approximately 0.5 cm thick. These sections in turn are visually inspected and the sections containing a large number of the cells of interest are placed into molds and again embedded in epoxy. Once hardened, the molded sample is again cross-sectioned using a diamond saw, exposing the surface of interest and providing an even base surface, and is polished to a 1  $\mu\text{m}$  finish. The resulting available area for analysis is approximately 2.54 cm in diameter and contains cross-sections of approximately 20 to 75 channels, depending on cell density.

Elemental maps and electron backscatter images acquired using EPMA provide qualitative information regarding the ash layer that forms on the channel walls. Of particular interest is the relative ash layer thickness and density, as well as to investigate possible ash penetration into the filter walls. Quantitative measurements regarding porosity and permeability of the ash layer and substrate are left to a future investigation. In addition to elemental maps, elemental line scans can be used to provide qualitative information regarding ash layer composition and ash penetration into the wall as a function of distance along a user-defined scan path.

#### ***3.4.2 Scanning Electron Microscopy with Energy Dispersive X-Ray Spectroscopy***

Scanning Electron Microscopy (SEM) and Energy Dispersive X-ray Spectroscopy (EDS) are essentially identical in operation to Electron Probe Microanalysis. A high-energy beam is focused onto a sample that is positioned within a UHV chamber. The surface of the sample is discretized by computer software and rastered by the electron

beam. The incident beam induces the release of high-energy electrons and X-ray radiation. An electron and/or X-ray detector counts the number of incident particles on the detector for each scanned area of the sample. The computer then interprets the total number of electrons or X-rays counted and processes them using an image generating routine, which produces and displays an image based on the relative electron and/or X-ray intensities.

Two types of electron data are produced using this method: secondary electrons and backscattered electrons. Secondary electrons are emitted from the surface atoms of the sample being analyzed; these are the primary source of information, yielding surface topography and morphology data. Backscattered electrons are produced when the incident beam electrons are reflected back to the detectors. The intensity of these reflected electrons is directly proportional to the atomic number of the elements present in the sample. However, backscattered electrons are reflected relatively deep within a sample and therefore do not yield accurate surface topography.

EDS is used to determine the concentration of elements within the top few atomic layers of the sample area being scanned. X-rays emitted from the surface are characteristic to the parent element from which they originated. Detecting the energy of the X-rays produced by a sample provides an energy spectrum from which elements can be identified [70-72].

In the present investigation, DPF and DOC surface topographies are obtained using a Leo 1525 field emission SEM outfitted with a Link Oxford EDS detector. The system, located at the University of Tennessee, is shown in Figure 3.15. DPF samples are taken from various locations within the filter, and are approximately 25 mm<sup>2</sup> in

observable surface area. Images of primary interest are those showing a cross-section where the ash layer comes into contact with the substrate wall and/or any washcoat material. Sections of DPF and DOC are cut and mounted to conductive sample holders using carbon tape. The samples are then coated with a 3 nm layer of gold, allowing for increased image resolution while retaining all available elemental information for EDS analysis. Finally, the samples are placed in a UHV chamber and analyzed. It should be noted that extreme care is given with respect to minimizing disturbance of the ash layer.

### ***3.4.3 Powder X-ray Diffraction***

X-ray diffraction is based on Bragg's Law (Eq. 3.1) and used to identify chemical compounds present within a sample. When a crystalline structure is bombarded with monochromatic X-ray radiation of wavelength  $\lambda$ , Bragg reflections occur due to atomic lattice spacing that acts as a three-dimensional grating that diffracts the incident X-rays at specific angles. These reflections occur only when Bragg's law is satisfied:

$$n\lambda = 2d \sin(\theta) \quad (\text{Eq. 3.1})$$

where  $n$  is the order of reflection,  $\lambda$  is the wavelength of the incident X-rays,  $d$  is the atomic spacing and  $\theta$  is the angle between the surface and the X-ray beam. If Bragg's law is not satisfied, then no predictable X-ray reflections will be produced.

In typical XRD devices, including the one used in the present investigation, an incident X-ray beam made up of monochromatic X-rays of a specified wavelength is directed toward the sample. A spectrum is acquired by measuring the angle and intensity of X-rays reflected off the surface with the use of an X-ray detector mounted on a rotating arm. The spectrum data consists of a series of peaks located at angles at which



**Figure 3.15: Photograph of the scanning electron microscopy hardware with energy dispersive spectrometry detector**

X-rays are reflected and has an intensity corresponding to the total number of reflected X-rays of that specific wavelength. Since each compound has a crystalline structure with unique spacing between atomic layers, the diffraction angles and relative intensities can be used to determine the compounds present in the sample. It is also known that the total amount of X-ray energy reflected at a specific wavelength is dependant on the available concentration of the compound in the sample, and is observable in the XRD spectra by being proportional to the area under the peaks obtained [70, 71, 74, 75].

In this study, approximately 3 grams of ash material is extracted from the inlet channels of the DPF. The material is placed in a recessed section of a sample holder and spread to a thickness of approximately 1.5 mm. The sample material is held in place using a non-crystalline ethyl acetate and polyester resin, which itself possesses a relatively “flat” observable intensity profile through the range of angles over which data is collected. Scans are obtained using a Philips wide-angle XRD that utilizes a Cu  $K\alpha$  radiation source. The X-Ray Diffractometer is a Phillips Panalytical Model X’Pert Pro MPD, shown in Figure 3.16, and is located at the University of Tennessee. Intensity patterns are obtained over a  $2\theta$  range of  $5^\circ$  to  $70^\circ$  in a scan mode of  $0.2^\circ$  in 2 seconds. Sophisticated search-match software, as well as hand analysis, is used to determine the chemical composition of the residual ash found in the filter following accelerated ash loading engine bench experiments.

#### ***3.4.4 Inductively Coupled Plasma - Atomic Emission Spectrometry***

ICP-AES is a form of analytical atomic spectroscopy used to identify elements present within various media and quantify their concentration. Identification is achieved



in a manner similar to EPMA by analyzing the electromagnetic radiation emitted as the electrons relax from an excited state to their ground state. The procedure consists of three basic stages: atom formation, electron excitation and emission. Prior to excitation, the atoms must be separated from any matrix it is bound to, which provides an atomic emission spectra that is free of interferences. Once excited, the atom will emit light that is characteristic of that element. Ideally, the energy source would be variable to provide an appropriate amount excitation energy without appreciable ionization.

Plasma is an electrically neutral, highly ionized gas that consists of ions, electrons, and atoms. Analytical plasma is maintained by energy derived from an electric or magnetic field. The plasma must be formed in a chemically inert environment in order to prohibit the formation of undesirable molecular species that could affect the accuracy of the measurement. Most analytical plasmas operate with pure argon or helium, eliminating the possibility of combustion. Plasmas are characterized by their temperature, as well as their electron and ion densities. For analytical plasmas, temperatures typically range from 6000 to 8000 K. These high temperatures assure that most of samples are completely atomized, though some molecular species do exist and can be measured in the plasma.

The plasma used for ICP is a radio frequency-induced plasma that utilizes an induction coil to produce a magnetic field, operating between 1 and 5 kilowatts. The induction coil is wrapped around the ICP torch two or three time and is cooled by water that continually passes through it. All ICPs have a bank of capacitors that are continuously tuned to mach the inductance of the plasma. The coil is made of either silver or gold, providing minimal RF resistance and preventing oxidation upon contact



**Figure 3.16: Photograph of the scanning electron microscopy hardware with energy dispersive spectrometry detector**

with air. A typical ICP torch, as shown in 3.17, consists of a quartz tube that has three separate gas inlets. Gas enters the plasma through the outer channel with a tangential flow rate ranging from 8 to 20 L/min. An auxiliary gas with flow rate of 0.5 to 3 L/min travels up the center channel. The nebulizer gas has a laminar flow pattern with flow rates ranging from 0.1 to 1 L/min and injects the samples into the plasma. The analytical region is approximately 1 cm above the induction coils, providing the best optical viewing area and maximum sensitivity.

The plasma emits a continuum of background radiation ranging from the visible to ultraviolet region. It is known that the radiation originates from electrons, Ar and Ar<sup>+</sup>, as well as other atomic and molecular species in the matrix. Sample blanks can help offset these background photons, but there is an ever-present level of instability in the continuum background, which plays a role in limiting the sensitivity of the ICP-AES. The lower detection limit is 0.03 parts per billion for calcium and 0.90 parts per billion (ppb) for zinc, both of which are well below the required range for this experiment. The detection limits for phosphorus and sulfur are 18 and 20 ppb, respectively, again providing ample resolution. The error and repeatability associated with ICP-AES varies depending on the combination of elements present in the sample, the quality of sample preparation and even the machine being used, and are considered minimal in the scope of this investigation.

A Perkin Elmer Optima 4200 ICP with concentric nebulizer and cyclonic spray chamber was used for this investigation. Analysis was performed by the Geo-Analytical Laboratory of the Saskatchewan Research Council.

In this investigation, the DPF is divided into equal sections along the axial centerline and sent to a third-party laboratory for analysis. Sample preparation includes grinding up each sample and combining it with lithium borate, followed by fusion at high temperature ( $\sim 1000^{\circ}\text{C}$ ) for 30 to 45 minutes. The fused sample material is then dissolved in 1.6 M nitric acid before being analyzed. The number of steps involved in sample preparation, and the difficulty associated with dissolving automotive catalyst and substrate material are both inherent sources of error that limit accuracy and repeatability. However, this error is not considered significant and thus is not quantified in this investigation. Results from ICP-AES are used to quantify ash composition and location through the filter. A section of substrate loaded with ash is cut into five sections of equal size and analyzed independently. Samples of the lube oil and the fuel doped with lube oil are also analyzed, which allows for calculation of ash product formation and recovery.

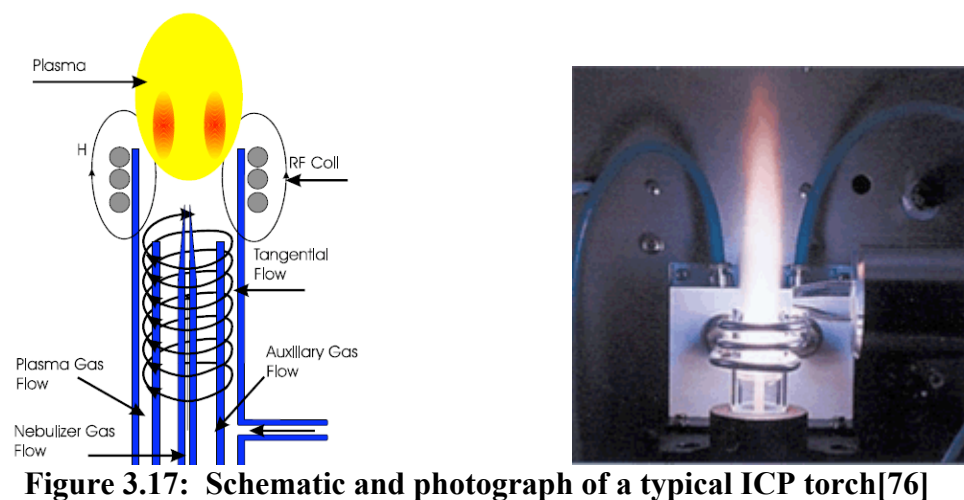




**Figure 3.18: Photograph of an Inductively Couple Plasma Atomic Emission Spectrometer**

## **CHAPTER 4**

### **RESULTS AND DISCUSSION**

The exhaust gas temperature of a single-cylinder diesel engine, running at constant speed for the entirety of this experiment, is used to determine the engine load setting. While typical exhaust gas temperatures for on-road diesel engine applications can range anywhere from 250 to 500°C, a target exhaust temperature of 400°C was selected to enhance continuous regeneration efficiency as well as to increase fuel consumption and engine soot output rate in order to shorten test length. It is also understood that the quantity of soot and ash produced by the engine is strongly a function of engine load. The goal of the experiment is to develop an accelerated protocol that produces and deposits ash in a manner similar to that observed in full-scale engine testing and on-road applications. Thus, special attention is given to selecting and maintaining engine bench settings such that exhaust temperature and backpressure remain in ranges considered representative of full-scale engine operating parameters. Since the rate of soot production is a strong function of engine backpressure, significant differences in soot loading times are observed between substrates.

Results are presented by substrate material. Sections 4.1 and 4.2 discuss results from experiments carried out on two cordierite filters with different PGM loadings. The majority of experiments observed in literature were conducted on cordierite substrates with varying amounts of PGM loading. Thus, results for experiments carried out on

cordierite substrates are considered a good starting point for evaluating DPF performance when the accelerated ash-loading protocol is applied. The porosity of cordierite is typically in the range of 40 to 50%, though exact measurements are not carried out as they were not required for the development of this protocol. The presence of a washcoat and catalyst material will inherently decrease the filter wall permeability with varying severity based on the wall surface morphology and washcoat layer thickness. The first experiment is carried out on a substrate coated with a low PGM loading, and the second on a substrate with a high PGM loading. The effect of the catalyst layer on exhaust backpressure is clearly visible in the data, and has significant implications with regard to implementing the protocol.

Sections 4.3 and 4.4 outline results from experiments carried out on two mullite substrates: the first with no catalyst material, and the second with a high PGM loading. Mullite has been introduced as a high porosity substrate material with mechanical properties similar to those of cordierite. The high porosity acicular material provides lower engine backpressures without sacrificing filtration efficiency. The DPF channel walls also provide more surface area over which catalyst material may be applied, enhancing continuous regeneration performance. The filter wall morphology also has significant implications with regard to ash layer morphology, as will be addressed in both the experimental and characterization results.

Section 4.5 presents discussion of results from an experiment carried out on a non-catalyzed SiC filter. Silicon carbide (SiC) is widely used in passenger vehicle applications because of its increased durability when subjected to high temperatures, especially temperature excursions experienced during active regeneration. The porosity

of SiC is typically the same as or slightly lower than that of cordierite (40 to 50%), but SiC has a major advantage in having a melting temperature of 2200°C, nearly 1000°C greater than that of cordierite. This provides some passive protection against damage that may occur should the DPF experience an uncontrolled regeneration during which temperatures can exceed 1600°C. In cases where active regeneration is employed to remove soot from the filter, this regeneration strategy can be carried out at higher temperatures, resulting in faster and more complete regenerations. In the present investigation, only one experiment was carried out on a non-catalyzed SiC DPF. Despite the higher melting temperature, the regeneration strategy is not varied in the interest of continuity between experiments.

Finally, comparisons between the results from each experiment are discussed in Section 4.6. In particular, the effects of ash on exhaust backpressure and soot lightoff are quantified. Additionally, the composition of the fuel, lube-oil and ash is examined, and the ash distribution and ash recovery within each substrate is quantified.

## **4.1 Cordierite Substrate with Low PGM Loading**

### ***4.1.1 Cordierite Substrate with Low PGM Loading - Experimental Results***

This experiment was the third experiment carried out overall. While the protocol is varied over the course of the experiment, it has already been recognized that exhaust backpressure is a strong function of the residual ash buildup within the filter, as well as the soot accumulated over the course of the loading cycle. Thus, when using a backpressure threshold to determine the point at which active regeneration is initiated, the threshold must be increased to account for ash buildup and subsequent increase in



baseline backpressure. For this experiment, the backpressure threshold is increased only as needed, which is to say, when the pseudo-steady-state backpressure does not drop below the backpressure threshold immediately following an active regeneration. This prevents too much soot from depositing within the filter, but results in an inconsistent amount of soot being loaded from cycle to cycle. The effects of this inconsistent soot loading are most visible in the DPF solid temperature profile shown in Figure 4.1, where the temperature excursion resulting from the exothermic oxidation of the carbonaceous particulate matter is observed to vary from cycle to cycle, indicating different amounts of soot present in the filter prior to regeneration.

The effects of inconsistent soot loading are visible to a lesser extent in the exhaust gas temperature profiles as seen in Figure 4.2, where the DPF exit gas temperature is the only gas temperature measured downstream of the filter. Variations in the remaining exhaust gas temperature profiles are the result of changes in engine load between loading and regeneration cycles. Finally, changes in the active regeneration protocol result in variations in DOC and DPF inlet gas temperatures.

The effect of ash accumulation within the DPF is immediately visible in the exhaust backpressure data shown in Figure 4.3, where the overall backpressure trend increases fairly linearly over time. The DPF mass data shown in Figure 4.4 exhibits fairly linear trends for both loaded DPF masses (soot and ash, prior to regeneration) and clean DPF masses (ash only, after regeneration) versus time, indicating that the relationship between backpressure and ash accumulation would be roughly linear within the repeatability limits of the current experiment.

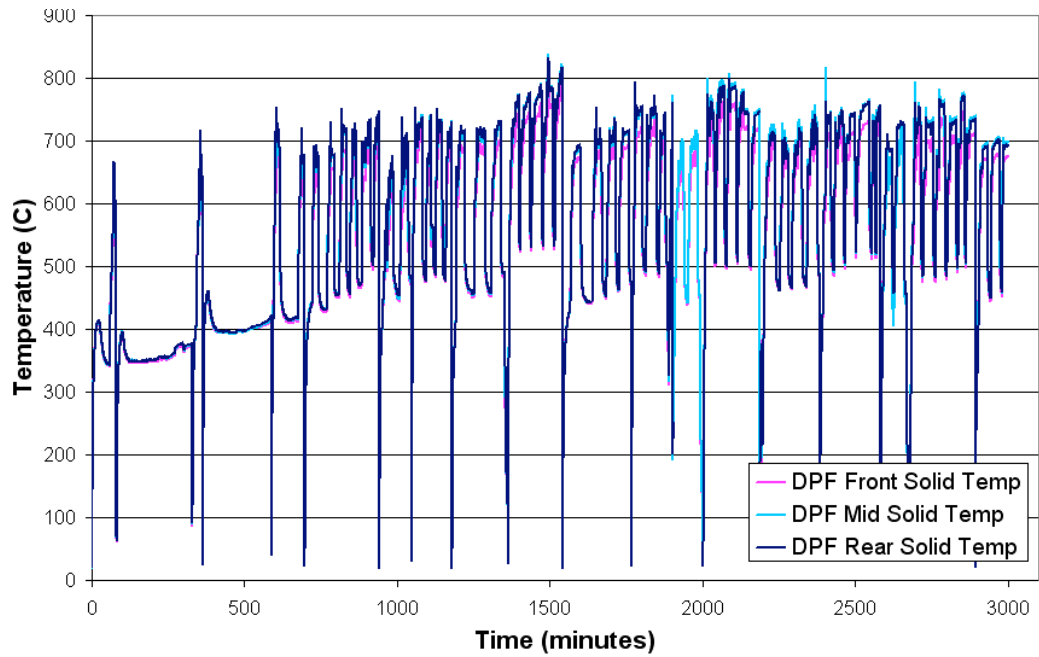


**Figure 4.1: DPF solid temperatures versus time for cordierite substrate with low PGM loading**

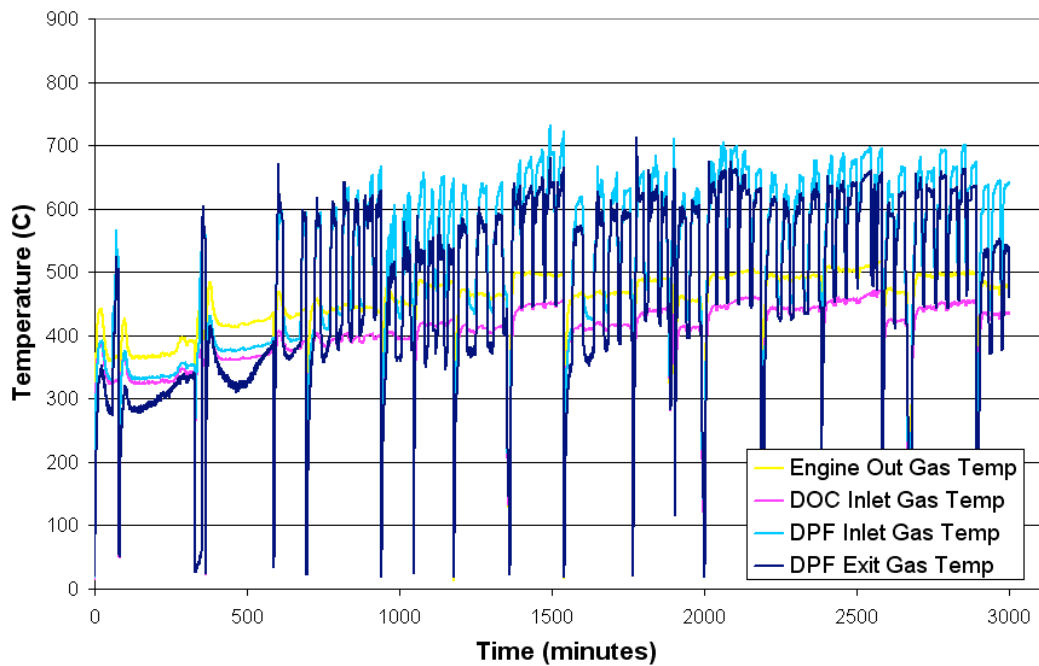


**Figure 4.2: Exhaust gas temperatures at various locations versus time for cordierite substrate with low PGM loading**

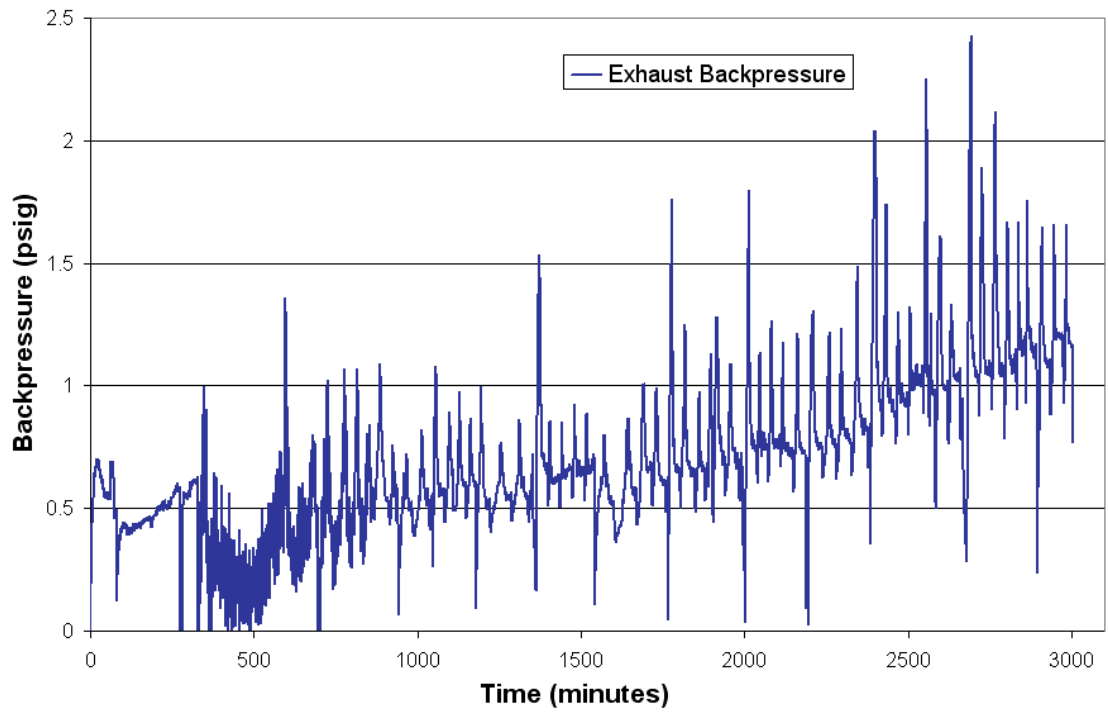


**Figure 4.3: Exhaust backpressure versus time for cordierite substrate with low PGM loading**

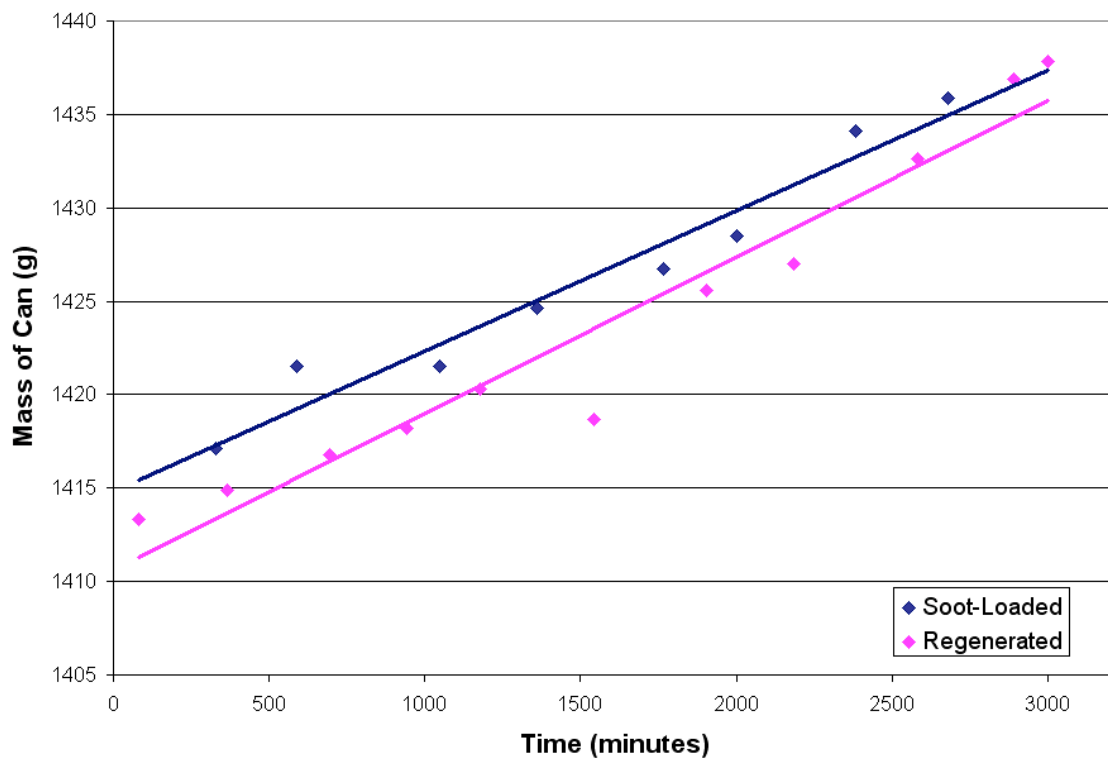


**Figure 4.4: DPF mass data versus time for cordierite substrate with low PGM loading**

In summary, the experimental results illustrate fair repeatability of the accelerated ash loading protocol. Though parameters such as engine load and backpressure thresholds are varied during this particular experiment, the temperature profiles remain within the desired operating window. Inconsistencies observed in the mass data plot are attributed to a combination of inconsistent soot loadings, and a regeneration strategy that evolved over the course of this particular experiment. Results from this experiment play an important role in further development and implementation of the protocol. The overall implications of experimental repeatability and material properties will be addressed in Section 4.6.

#### ***4.1.2 Cordierite Substrate with Low PGM Loading - Characterization Results***

Upon completion of the engine experiment, the sample is divided into quarter sections lengthwise. The first is completely embedded in epoxy to preserve the ash layer prior to cutting the sample into cross-sections. The second is cut into five sections and sent to the third-party laboratory for ICP analysis. The third is cut apart for visual examination and SEM analysis. The fourth piece is retained for additional characterization if necessary.

Photographs are taken of various areas of interest. Photographs taken of cross-sections from the front and rear sections are shown in Figures 4.5 and 4.6, respectively, and demonstrate the disparity in ash accumulation between the front and rear sections of the DPF. The ash layer on the channel walls was observed to remain intact, while the ash in the center channel of the channels was easily knocked loose during cutting. Thus, thicker cross-sections were required in the rear to maintain the ash layer intact.

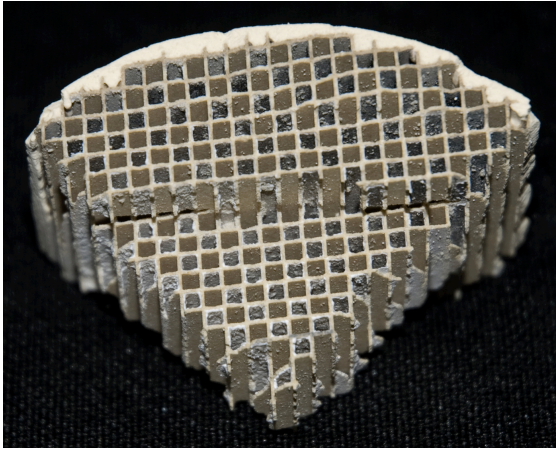


**Figure 4.5: Photograph of one-quarter sample from front section of cordierite substrate with low PGM loading**

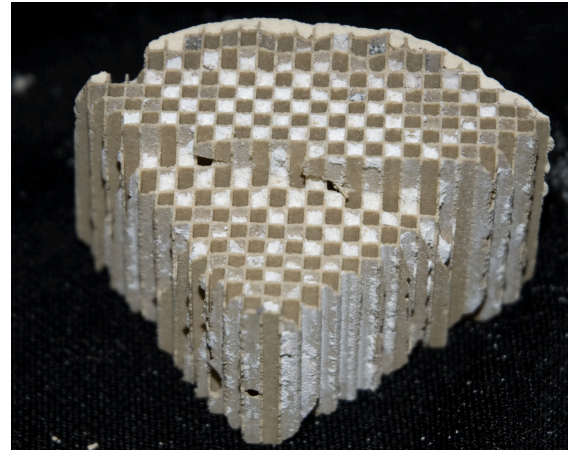


**Figure 4.6: Photograph of one quarter sample from rear section of cordierite substrate with low PGM loading**

A close-up photograph of the specific samples used for SEM analysis is shown in Figure 4.7 and provides an excellent representation of the ash distribution along the length of the channels. A single plugged channel is observed in the front-middle section, but this occurrence is considered an anomaly. The ash layer is characterized at locations 0.5", 3.0" and 5.0" from the inlet representing the front, middle and rear of the filter using EPMA and SEM.

EPMA is utilized to observe the cross-sectional morphology of the ash layer that forms. Specifically, elemental maps depicting the relative concentrations of calcium, zinc, phosphorus and sulfur are used to characterize the ash layer in a large number of cells from throughout the filter. The maps presented here are selected as representative of the overall trend observed. The ash layer is characterized at locations 0.5", 3.0" and 5.0" from the inlet representing the front, middle and rear of the filter. The first image taken from the inlet section is shown in Figure 4.8. It is observed that the relative concentration of phosphorus is approximately equal to that of calcium, and sulfur approximately equal

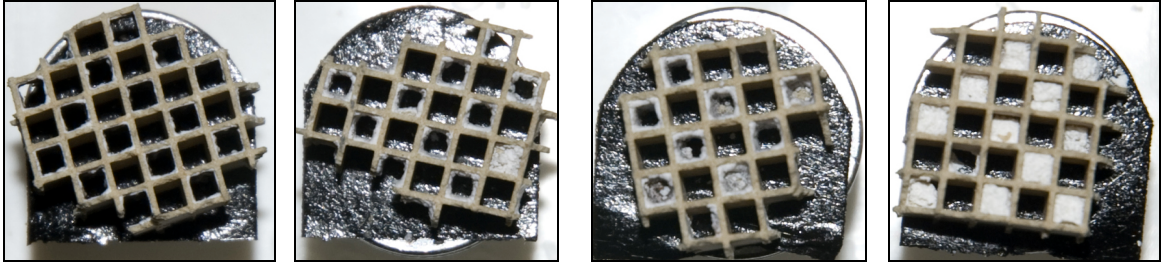


**Figure 4.7: Photographs of representative samples extracted from the front, front-middle, middle and rear sections of the cordierite substrate with low PGM loading**

to zinc. Thus for simplicity, only the maps for the electron backscatter, calcium and zinc are shown in the rest of this section. The rationale for the selection of these elements will be discussed further in Section 4.6.

The elemental maps for the front section of the DPF, shown in Figures 4.8 and 4.9, show a relatively thin ash layer formed on the walls of the channel. The ash layer is fairly dense and in most cases covers the entire inside perimeter of the cell. This has significant implications with regard to the backpressure increase as a function of ash loading, though this impact is not quantified in this investigation.

Figures 4.10 and 4.11 present elemental maps for the middle section of the DPF, and show an ash layer that is significantly thicker than that observed in the front section, resulting in a smaller void area through which exhaust gas can flow. In addition, the ash distribution over the channel walls is not nearly as symmetric as that seen closer to the inlet. The exhaust gas flow pattern will vary depending on axial location of each cell and the overall geometry of the system. It is also understood that some of the ash from the front and middle sections will break loose and deposit in the rear of the channel. It is believed that these two factors are primarily responsible for the asymmetrical ash distribution trend observed in the results.

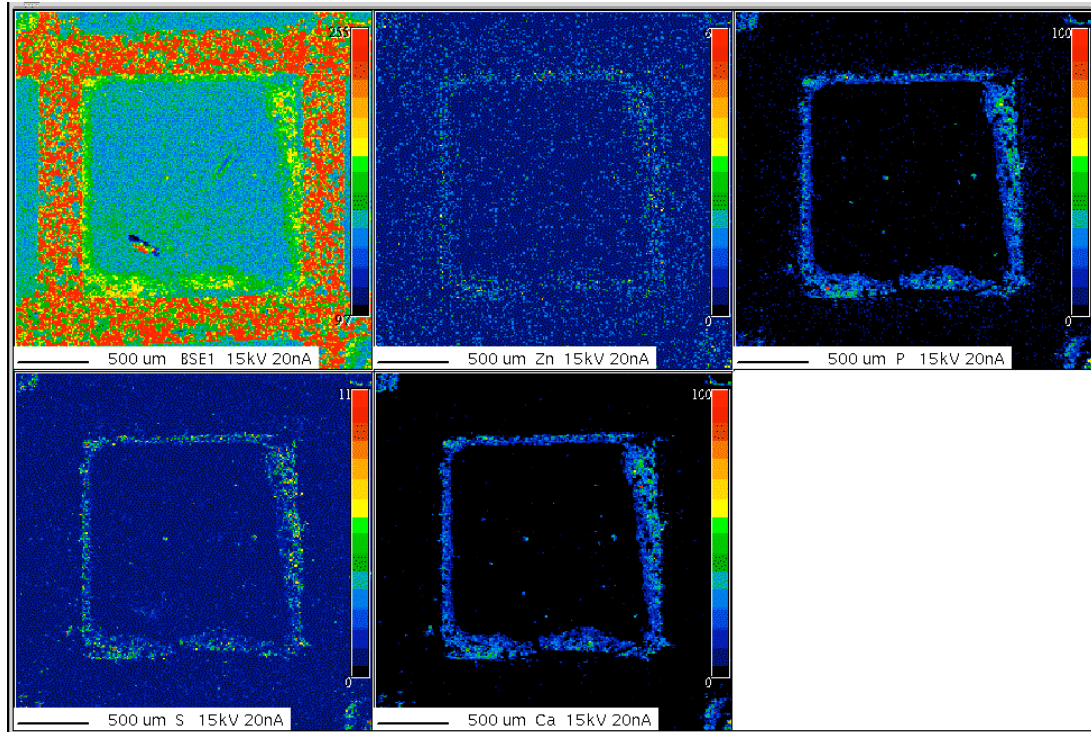


**Figure 4.8: EPMA Elemental maps of front section of cordierite substrate with low PGM loading**

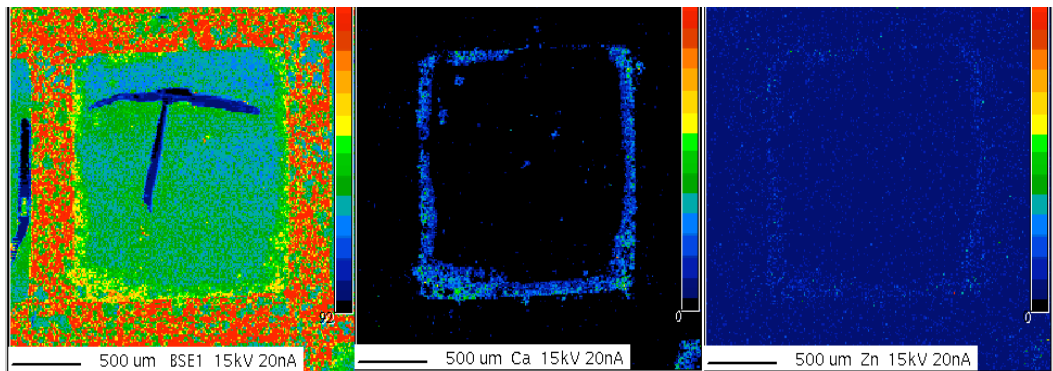


**Figure 4.9: EPMA Elemental maps of front section of cordierite substrate with low PGM loading**



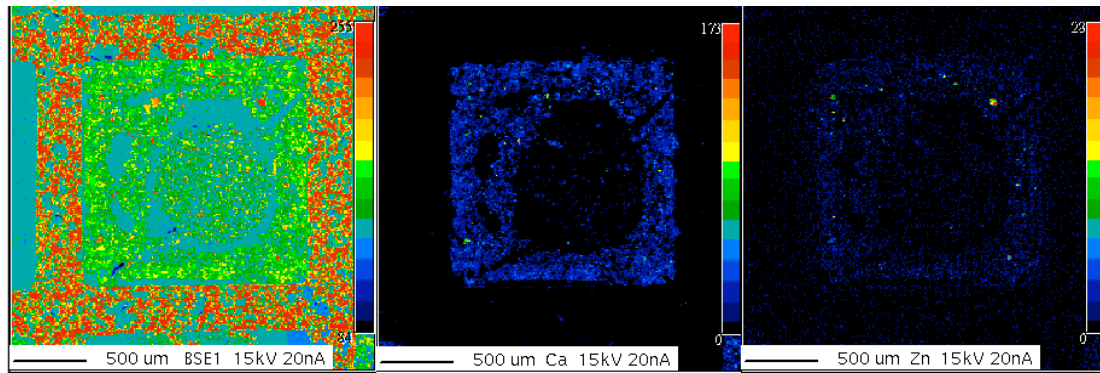


**Figure 4.10: EPMA Elemental maps of middle section of cordierite substrate with low PGM loading**

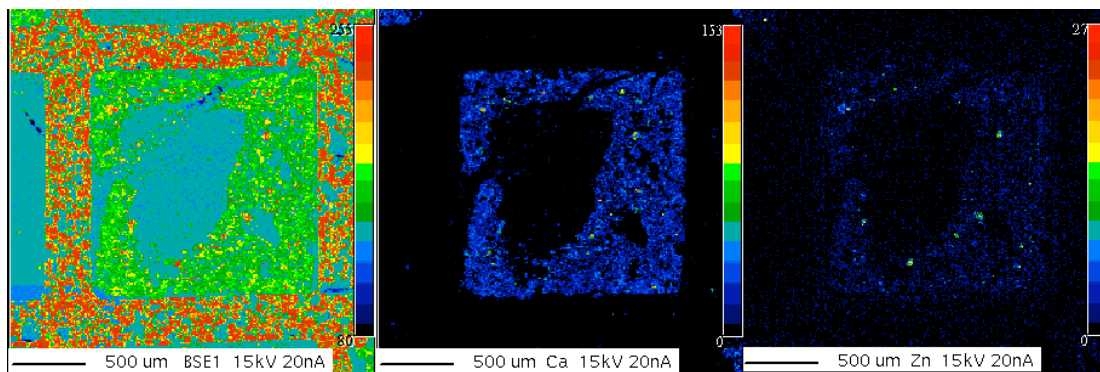


**Figure 4.11: EPMA Elemental maps of middle section of cordierite substrate with low PGM loading**

The elemental maps of the rear section of the DPF are shown in Figures 4.12 and 4.13, and show channels that are completely plugged with ash. The ash does not appear to be tightly packed, suggesting that some of the deposits formed upstream in the channel before separating from the wall and depositing in the rear. The relatively low exhaust gas flow rate through the rear of the filter will have little effect in compacting the ash layer. The majority of the rear cross-sections were very similar to the channel shown in Figure 4.10. However, enough channels possessed a distribution similar to that of the second elemental map shown in Figure 4.11 to merit mention. These distributions were observed primarily in cells furthest from the axial centerline of the DPF, and the ash



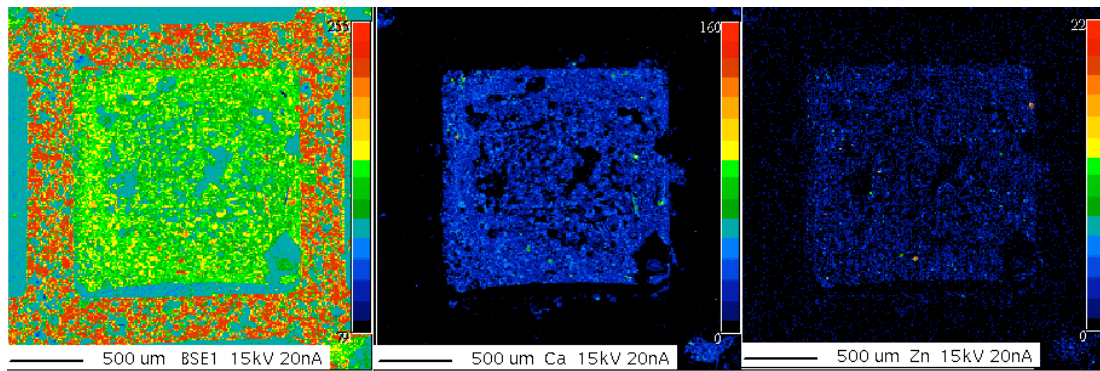


**Figure 4.12: EPMA Elemental maps of rear section of cordierite substrate with low PGM loading**

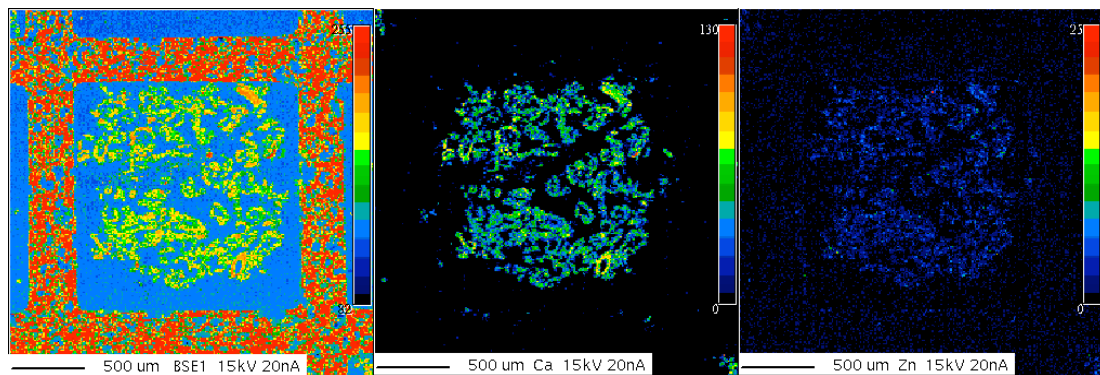


**Figure 4.13: EPMA elemental maps of rear section of cordierite substrate with low PGM loading**

appears to be loosely packed, perhaps the result of aforementioned ash deposits blowing down from upstream, as well as less ash material depositing in the outer channels.

To gain a more detailed understanding of the ash layer morphology and distribution along the length of the channel, SEM was employed to observe the ash and substrate under high magnification. Again, representative channels are selected for each section and shown in Figures 4.14 through 4.16. Similar to the results observed with EPMA, the ash layer is thinnest near the DPF inlet and gradually increases in thickness along the length of the channel. Perhaps the most interesting results with regard to channel-to-channel comparisons come in the rear section channels. While the ash

completely blocked the channels in most cases, the morphology of ash itself is observed to vary from smaller agglomerates such as that observed in Figure 4.16a, to larger agglomerates as seen in Figure 4.16b, with the larger agglomerates being found in channels along the outer radius of the DPF. Upon further observation of the rear section channels, it is noted that there is no observable ash layer, but instead what appears to be an accumulation of ash agglomerates. As mentioned earlier in this section, this is likely a combination of low flow rate through the rear section of the channel, and the accumulation of ash that breaks away from the upstream ash layer. This is all consistent with the widely acknowledged phenomenon that the filter fills with ash from the rear forward. These images also provide a more visual understanding of the effect of ash accumulation of engine backpressure.

For each channel, the ash layer is examined under greater magnification, particularly the region in which the ash comes into direct contact with the substrate. The morphology of the ash layer was found to be consistent between channels of the front and middle sections, and varied only slightly for the rear section. While special care is given to avoid the disturbance of the ash layer during sample preparation, the ash layer remained completely intact in only a few channels. Representative channels are again selected, this time from the front and rear sections. Images acquired under increasing magnification, displayed in Figures 4.17a through 4.17e, show minimal ash penetration into the DPF wall. The bright white line observed in each image is attributed to the presence of catalyst material and surface charging. It should also be noted that some (if not all) of the ash observed within the channel wall is the result of contamination during sample preparation. The ash layer, however, remains distinctly visible, and is observed

to consist of relatively fine grains accumulated in a moderately porous layer. The substrate is observed to possess a porous sponge-like morphology with an average pore size slightly larger than that of the ash particles. It can be seen that with the exception of areas damaged during sample preparation, the ash layer remains in solid contact with the filter wall. During sample preparation, it was observed that the ash layer was extremely brittle, suggesting that it may be susceptible to breakage when exposed to the inherent vibration associated engines and on-road driving, resulting in more ash depositing in the rear section. The ash layer in the rear of the filter, shown in Figures 4.18a through 4.18e, was more susceptible to damage during sample preparation, so focus is placed on the ash itself. The ash in the rear section is observed to be less densely packed, and consisted of a combination of small and large agglomerates, indicating much of the ash had formed upstream and broken loose.

Overall, the ash distribution and morphology that is observed during the characterization of the cordierite substrate with low PGM is consistent with results observed in literature. As expected, the ash layer is thinnest toward the inlet of the DPF and increases along the length of the filter until the channels become completely filled. Results show that calcium and phosphorus are present in the greatest concentrations among the elements investigated, and will be quantified later in this chapter. Finally, there was no distinct ash layer visible in the rear section channels, suggesting that the majority of the ash found in the rear of the filter originated from the brittle ash layers present on the upstream channel walls. It is believed that the protocol implemented for this experiment produced excellent results for both the experiment itself and the subsequent characterization of the DPF.

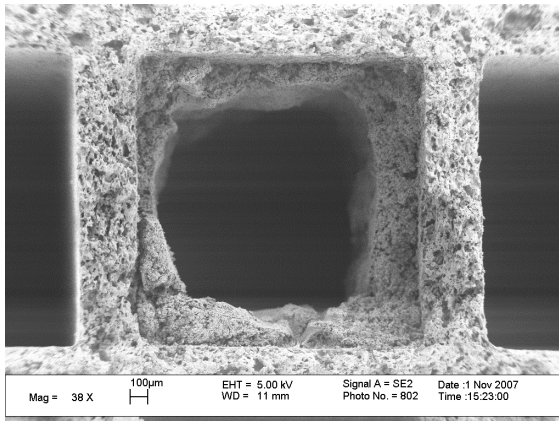


**Figure 4.14a: SEM image of front section channel (38X)**

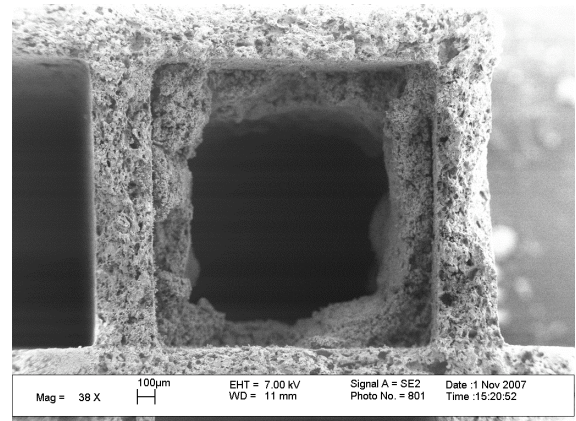


**Figure 4.14b: SEM image of front section channel (38X)**

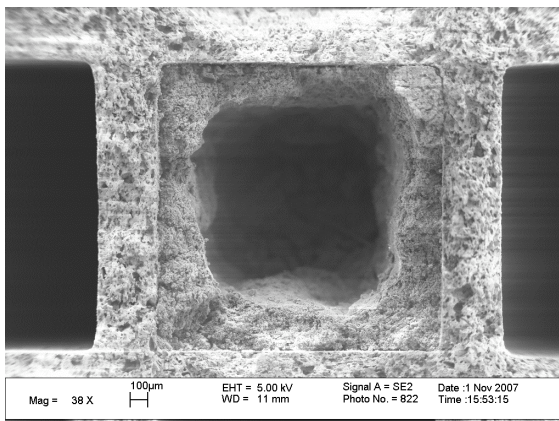


**Figure 4.15a: SEM image of middle section channel (38X)**

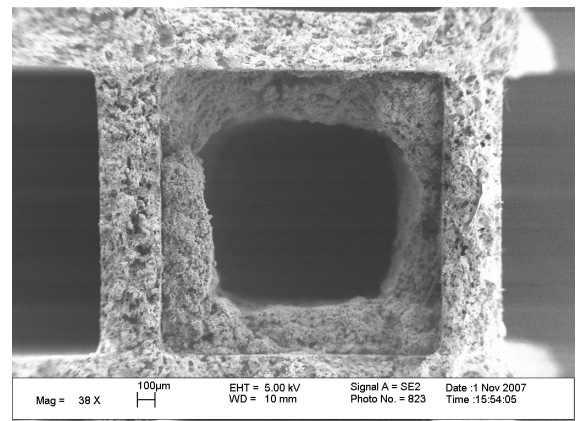


**Figure 4.15b: SEM image of middle section channel (38X)**

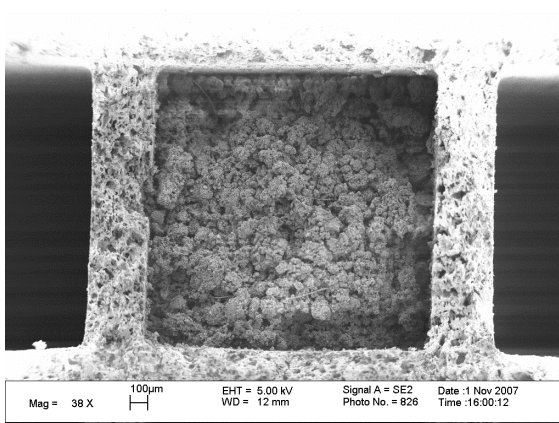


**Figure 4.16a: SEM image of rear section channel (38X)**

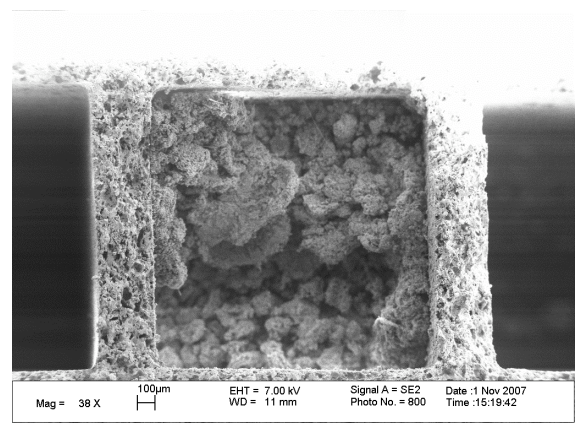


**Figure 4.16b: SEM image of rear section channel (38X)**



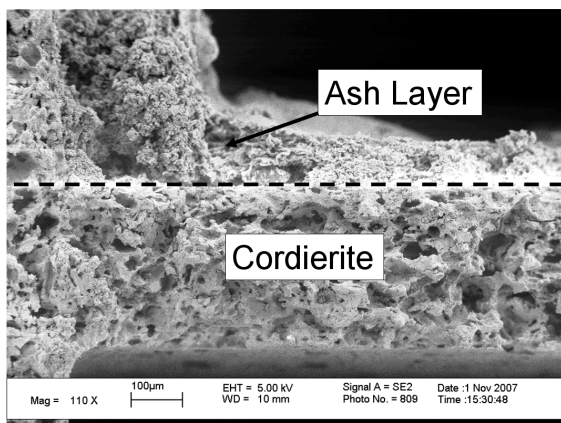


**Figure 4.17a: SEM image of front section channel (110X)**

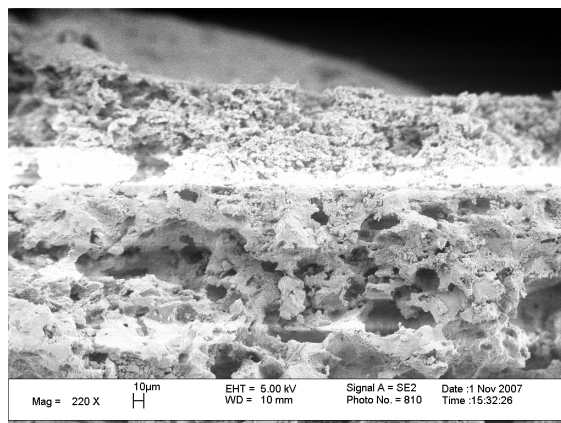


**Figure 4.17b: SEM image of front section channel (220X)**

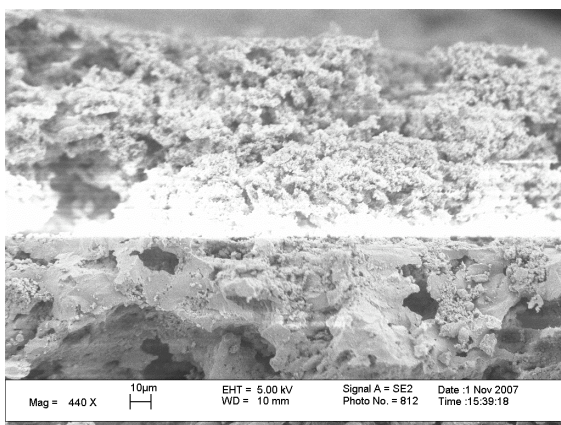


**Figure 4.17c: SEM image of front section channel (440X)**

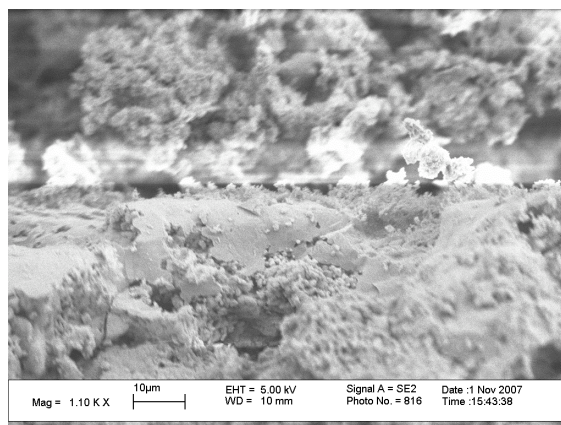


**Figure 4.17d: SEM image of front section channel (1100X)**

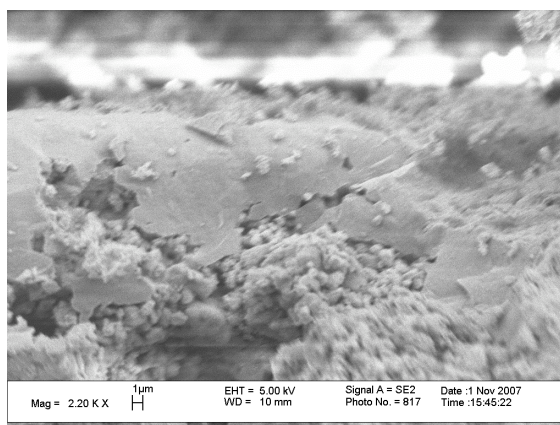


**Figure 4.17e: SEM image of front section channel (2200X)**

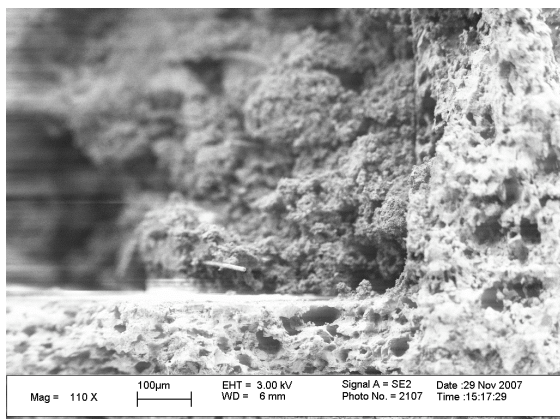


**Figure 4.18a: SEM image of rear section channel (110X)**

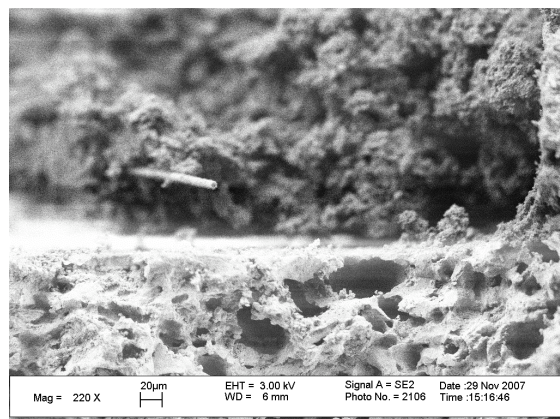


**Figure 4.18b: SEM image of rear section channel (220X)**

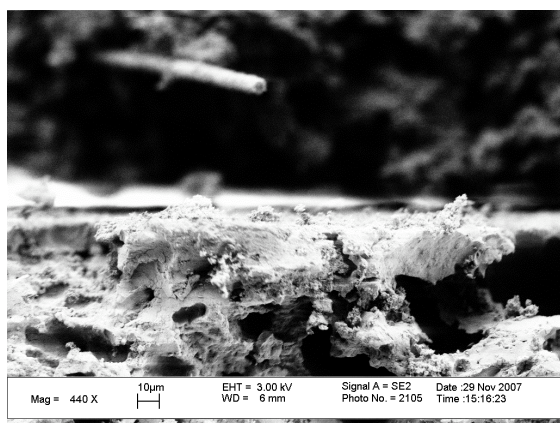


**Figure 4.18c: SEM image of rear section channel (440X)**

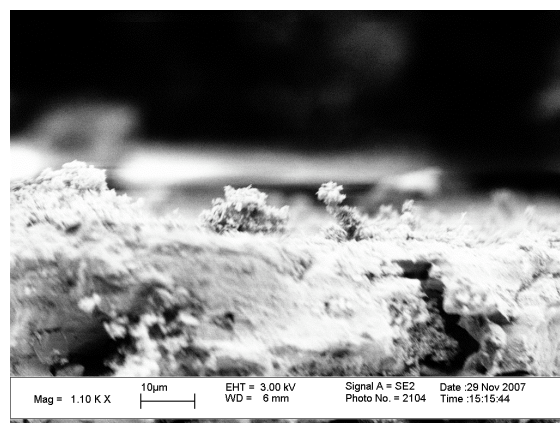


**Figure 4.18d: SEM image of rear section channel (1100X)**

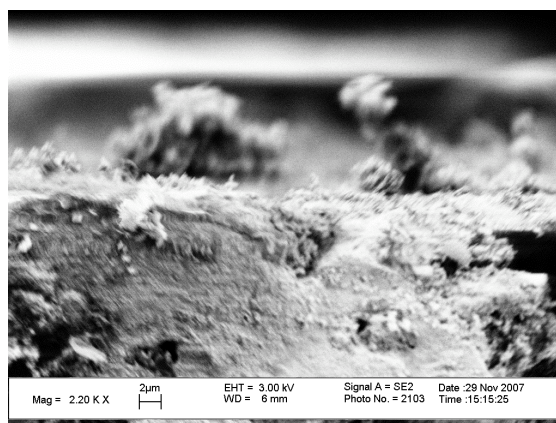


**Figure 4.18e: SEM image of rear section channel (2200X)**

## **4.2 Cordierite Substrate with high PGM Loading**

### ***4.2.1 Cordierite Substrate with High PGM Loading – Experimental Results***

This experiment is the seventh and final experiment carried out during this investigation. No changes were made to the protocol over the course of the experiment. Both loading and regeneration cycles were carried out at the same constant engine load, and the same 30-minute regeneration strategy was applied for every regeneration cycle, eliminating experimental variables. In observing the DPF solid temperatures shown in Figure 4.19, it is clear that the protocol provides a consistent and repeatable temperature profile. A few temperature excursions are observed, which correspond to additional soot loading during engine warm-up after obtaining a loaded DPF mass. As a result, loaded masses are recorded only five times to minimize the threat of damage to the filter.

The repeatability of the protocol is confirmed in observing the exhaust gas temperature profiles displayed in Figure 4.20. Variations in the temperature profile occurred early in the test as a result of problems with the supplemental fuel injection system and the engine load controller. These issues were corrected early on, providing a long period over which the protocol is applied without incident. An important point worth mention is that the exhaust temperature and DOC inlet gas temperature remain fairly constant throughout the experiment, resulting in consistent aging environments

The exhaust backpressure profile shown in Figure 4.21 again illustrates a steadily increasing trend over the entire experiment. The “spikes” in the backpressure data correspond to the aforementioned additional soot loading associated with the acquiring of loaded filter masses. The additional soot accumulation decreases the soot/ash layer permeability, thus increasing exhaust backpressure and engine soot production. The

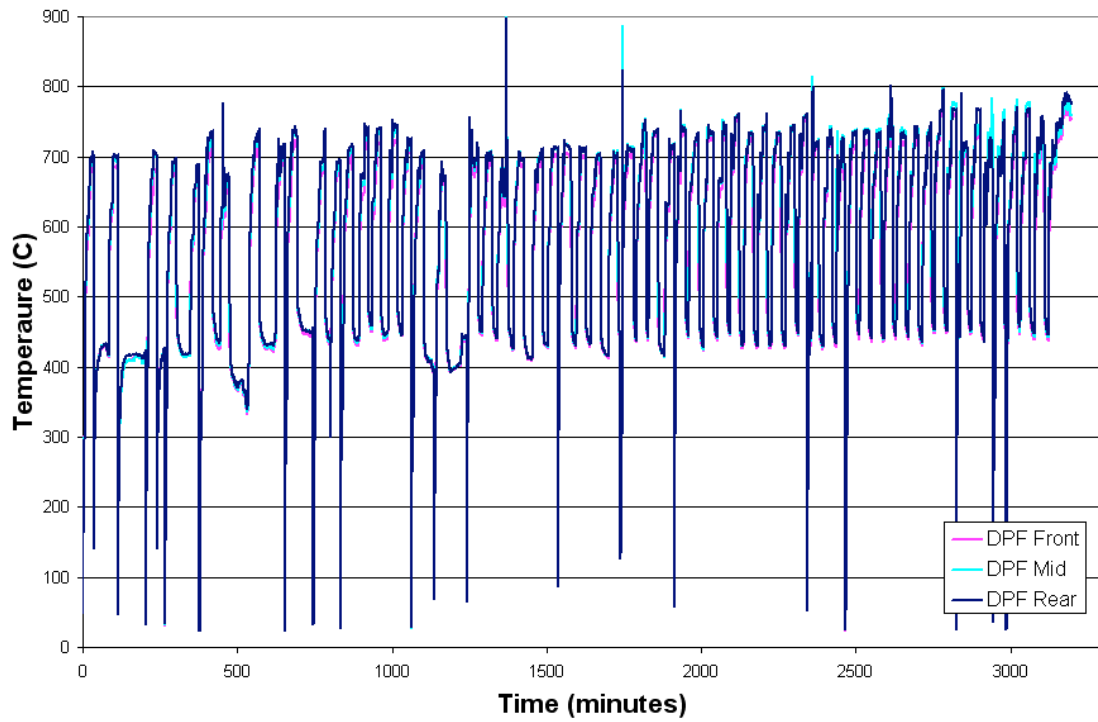


**Figure 4.19: DPF solid temperatures versus time for cordierite substrate with high PGM loading**

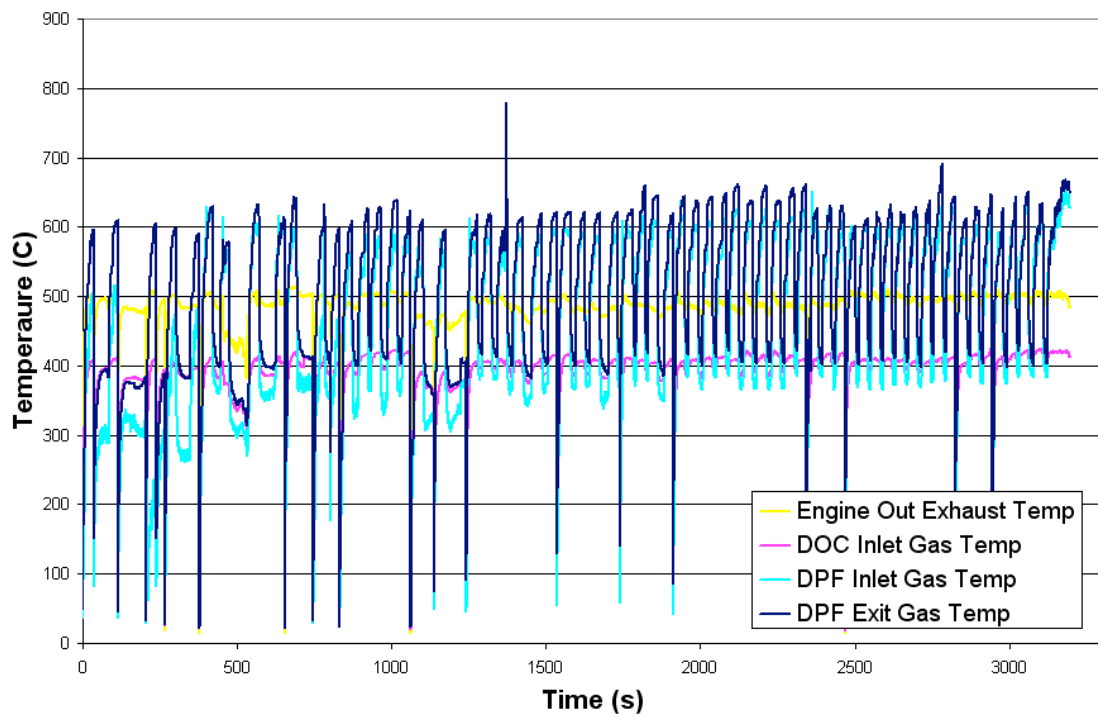


**Figure 4.20: Exhaust gas temperatures at various locations versus time for cordierite substrate with high PGM loading**



backpressure increase is compounded further by increased exhaust gas space velocity resulting from supplemental fuel injection and subsequent increases in gas temperature. It should also be noted that the initial exhaust backpressure observed for this DPF is the highest of all the experiments. This results in a higher engine soot production rate, which translates into shorter loading cycle times. Overall, the exhaust backpressure data shows a repeatable trend that steadily increases over the course of the experiment.

The effectiveness of the accelerated ash loading protocol is further demonstrated by the DPF mass data, shown in Figure 4.22. The first observation is that both lines are extremely linear, confirming good repeatability in the soot loading protocol, as well as indicating that the regeneration strategy is consistent and efficient in removing soot from the DPF. It is also observed that the trend lines are nearly parallel, and that the vertical gap between the two represents a consistent soot loading of two grams for the entire experiment. As mentioned earlier, the higher backpressures associated with this substrate and catalyst coating results in a high engine soot production rate. This presents the most difficult of conditions under which the protocol must provide consistent soot loading, and the mass data confirms that the protocol achieves the target soot loading.

In summary, the experimental results demonstrate the excellent repeatability of the protocol. Even with higher exhaust backpressures resulting in increased soot production, the protocol provides very consistent soot loading. Comparing these results to those of the first cordierite test, repeatability is greatly enhanced, primarily a result of using a constant engine load and employing a set active regeneration strategy. Overall, the results from this experiment further validate the protocol's effectiveness in achieving the desired DPF performance characteristics.

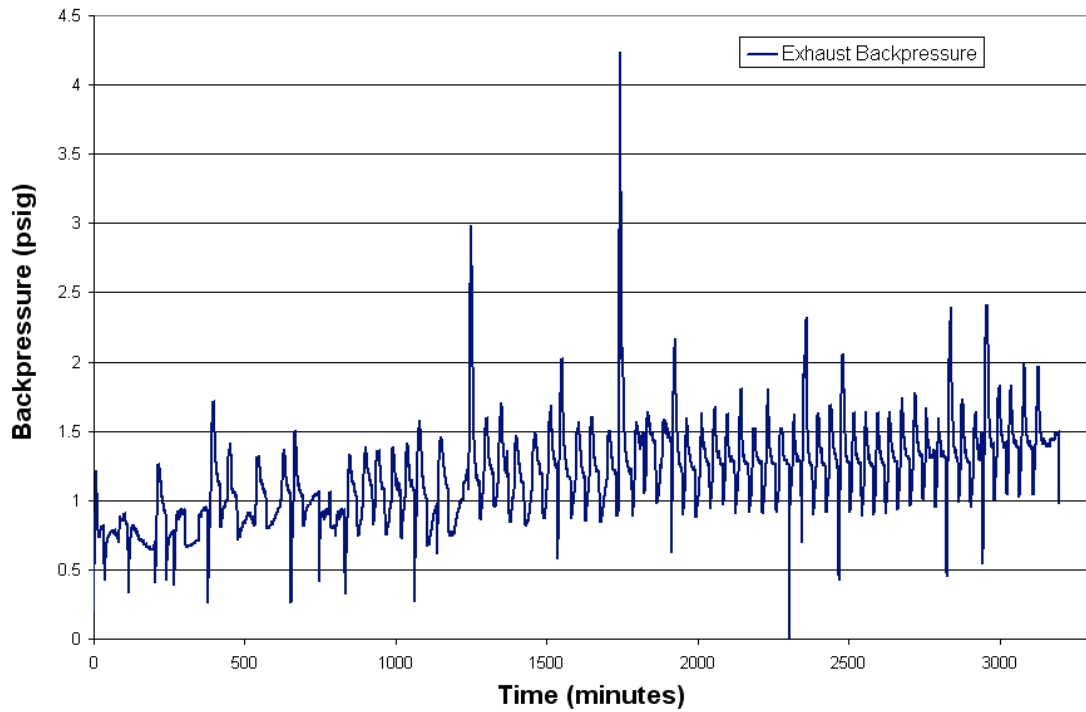


**Figure 4.21: Exhaust backpressure versus time for cordierite substrate with high PGM loading**

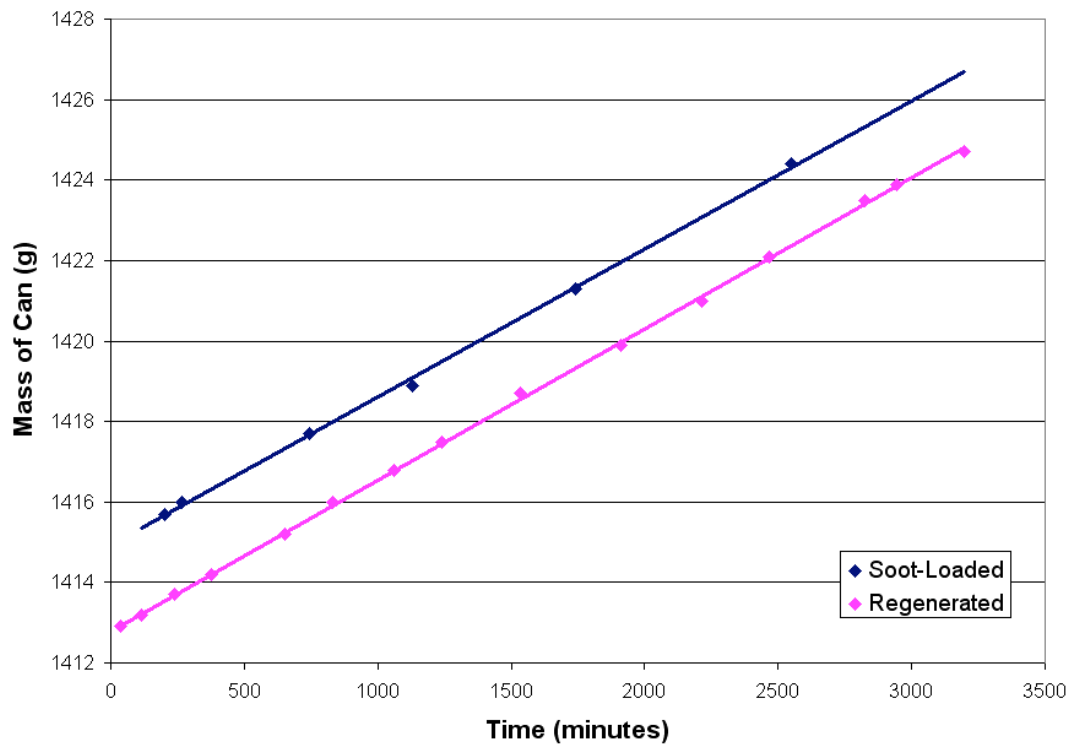


**Figure 4.22: DPF mass data versus time for cordierite substrate with high PGM loading**

#### ***4.2.2 Cordierite Substrate with High PGM Loading - Characterization Results***

Following the completion of the engine experiment, the sample is divided into quarter sections for EPMA, SEM analysis, and ICP analysis, with the fourth section retained for additional analysis if required.

Photographs are again taken of various areas of interest. Photographs taken of cross-sections from the front and rear sections are shown in Figures 4.23 and 4.24, respectively, and demonstrate the differences in ash accumulation between the front and middle of the DPF. It was observed that the ash layer near the inlet was very thin even prior to sample preparation, while the ash layer in the middle and rear sections consisted of loosely-packed ash. Thus, special care is taken to preserve the ash layer in the SEM samples.

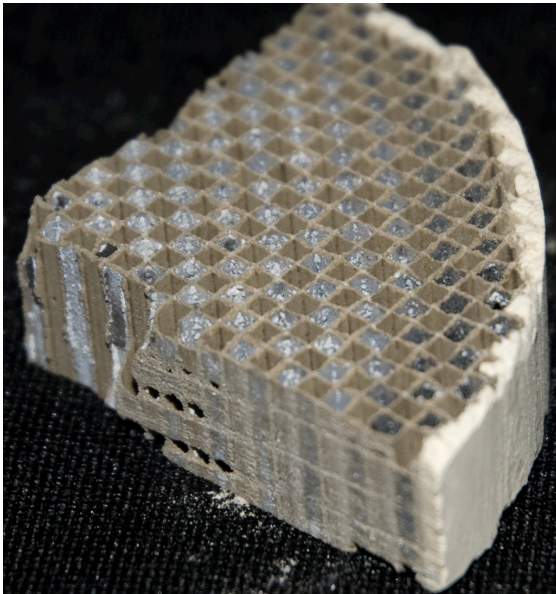


**Figure 4.23: Photograph of one-quarter sample from front section of cordierite substrate with high PGM loading**

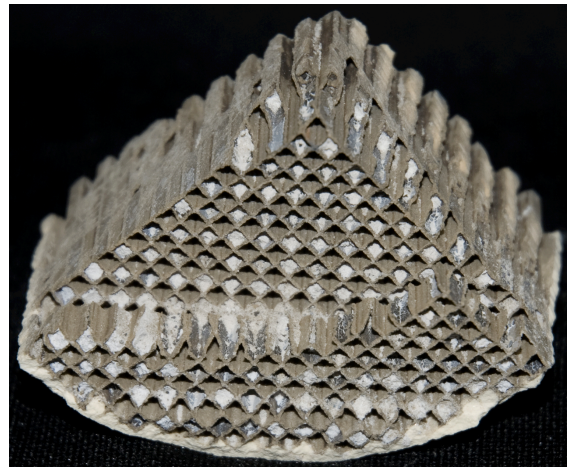


**Figure 4.24: Photograph of one-quarter sample from rear section of cordierite substrate with high PGM loading**

Photographs of the representative cross-sections analyzed using SEM, shown in Figure 4.25, depict an ash distribution along the length of the channel that differs from that observed in the first cordierite substrate. The ash layer is barely visible in the front section, but becomes more visible in the middle section, particularly in the corners. The ash is observed to plug the channels starting further upstream than the previous cordierite sample. The increase in PGM loading is likely a contributing factor to the inability of the ash layer to form and remain intact in the front and middle sections, resulting in more material breaking loose and depositing in the rear of the channels. The presence of the high PGM loading itself and the subsequent variation in ash distribution has important implications with regard to engine backpressure, though further experiments would be necessary in order to quantify impact of each of these contributors.

EPMA is again utilized to observe the cross-sectional morphology of the ash layer that forms in the DPF. Figures 4.26 and 4.27 depict an ash layer in the front section that is much thinner than that observed in the first cordierite substrate. This may be due, at least in part, to the increased presence of washcoat and catalyst material, perhaps providing a smoother textured surface that is more difficult for ash to accumulate and remain attached, instead breaking loose and depositing in the rear of the DPF.

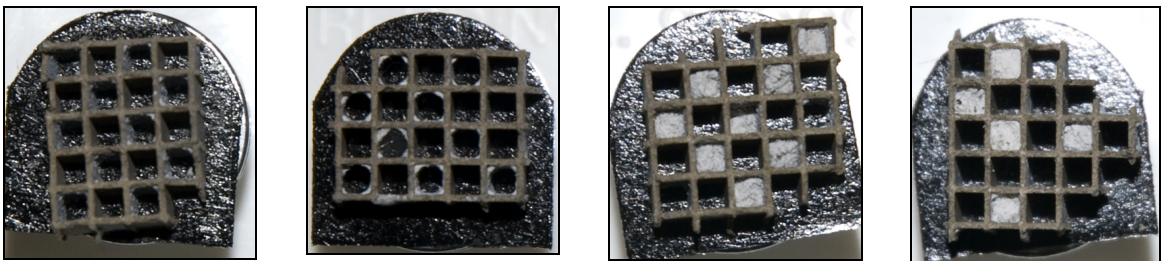


**Figure 4.25: Photographs of representative samples extracted from the front, middle, middle-rear and rear sections of cordierite substrate with high PGM loading**

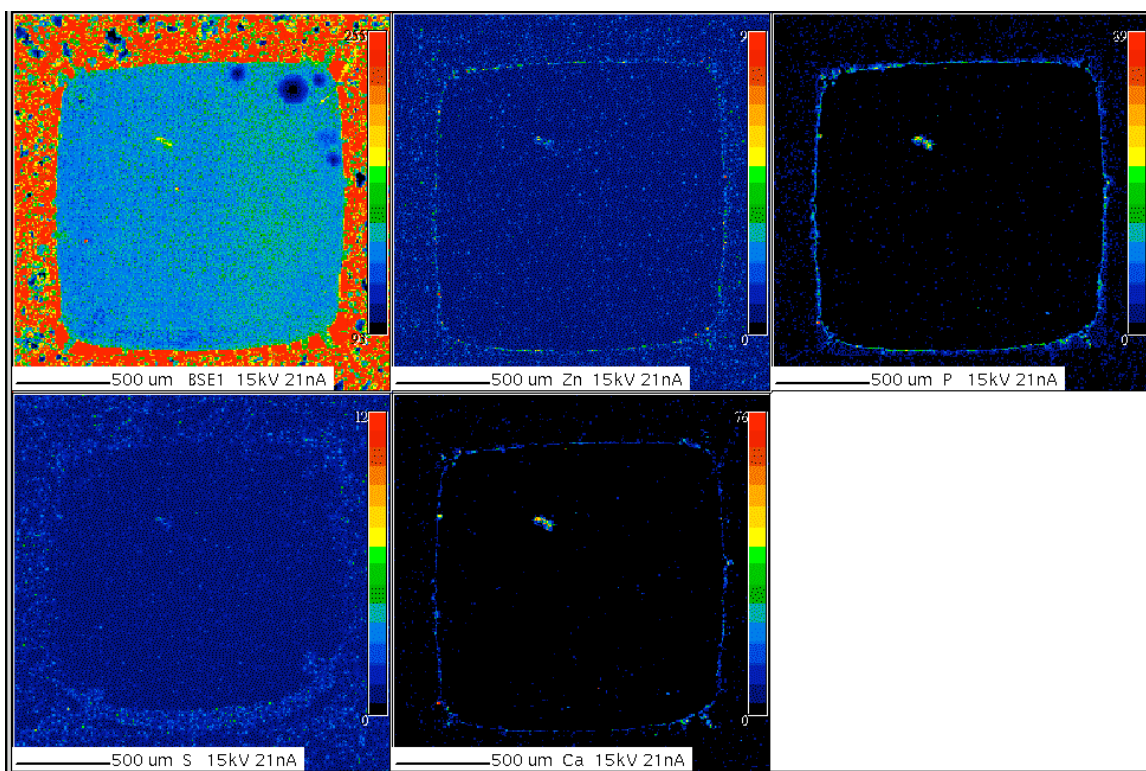


**Figure 4.26: Elemental maps of front section of cordierite substrate with high PGM loading**

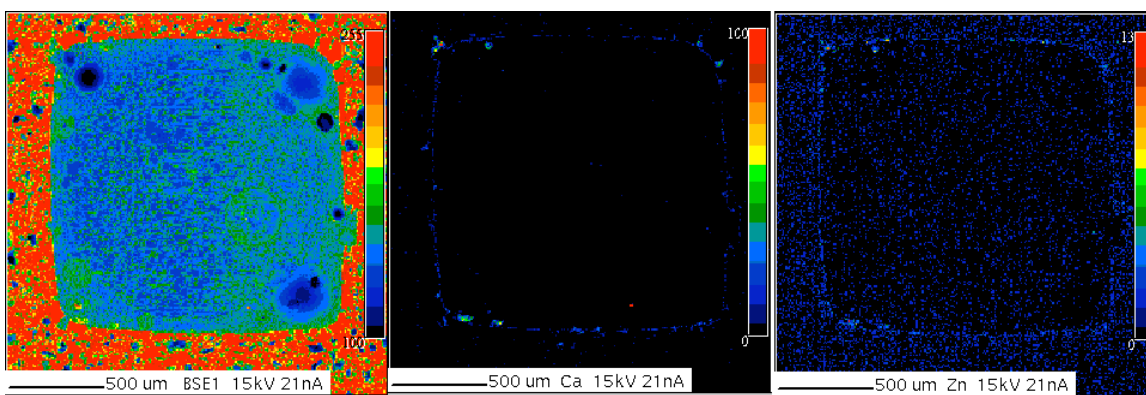


**Figure 4.27: Elemental maps of front section of cordierite substrate with high PGM loading**



The elemental maps representing the middle section of the DPF, shown in Figures 4.28 and 4.29, show an ash layer that is on average much thicker than that observed in the front section of the same substrate. However, the ash layer thickness around the perimeter of the wall is clearly less consistent than that observed in the first cordierite substrate. In addition, it is observed that portions of the ash layer have broken loose from the wall and drifted toward the center of the channel during sample preparation. The same sample preparation method was used for all five samples, and it is noted that this phenomenon was not observed in any other substrate. This further supports the

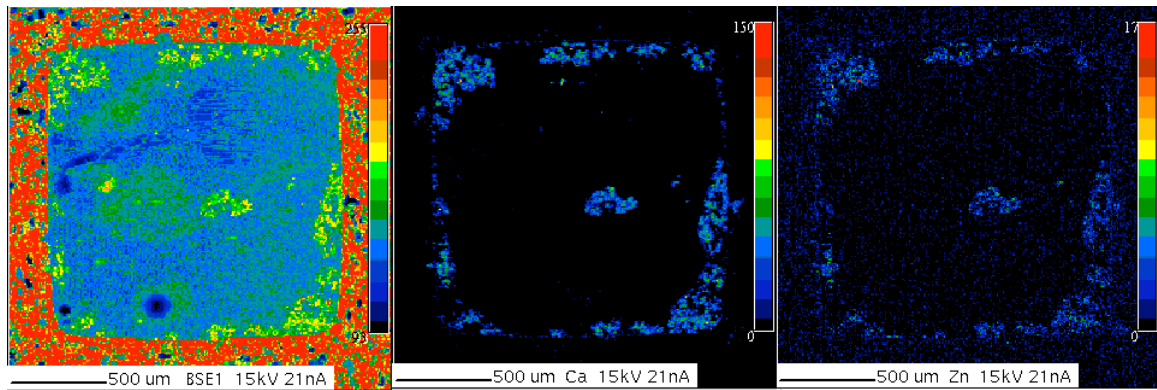


**Figure 4.28: Elemental maps of middle section of cordierite substrate with high PGM loading**

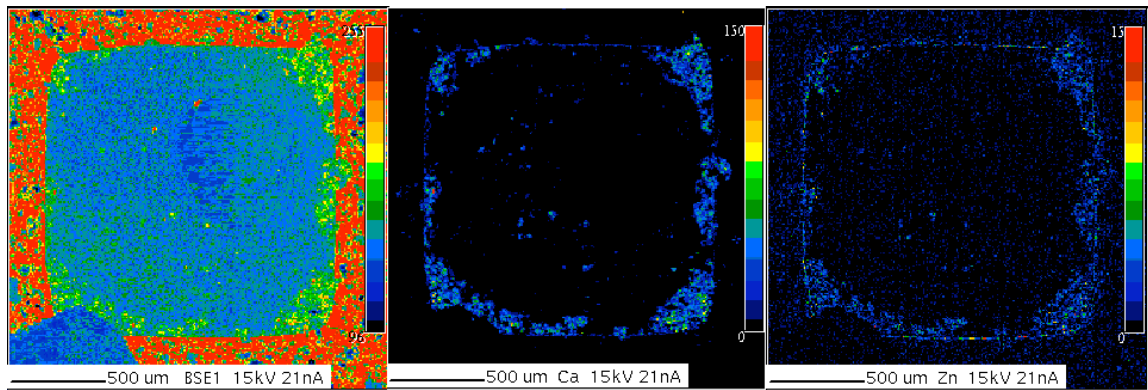


**Figure 4.29: Elemental maps of middle section of cordierite substrate with high PGM loading**

hypothesis that the presence of washcoat and catalyst material on the filter wall hinders the formation of an ash layer like that observed in the first cordierite as well in all of the other samples. The obvious benefit of this phenomenon with regard to DPF performance is increased exposure of the exhaust stream to the catalyst layer, resulting in more effective continuous regeneration performance. Different ash distributions within the filter will also have important implications with regard to backpressure performance, affecting total filtration volume, channel wall permeability and exposure of catalyst material to the exhaust stream.

The elemental map shown in Figure 4.30 represents the vast majority of the channels in the rear section observed during analysis, while the elemental map shown in Figure 4.31 represents a smaller portion of the channels that are located furthest from the axial centerline of the filter. Both maps show channels that are completely plugged with ash. In both cases the ash again appears to be loosely packed, and since there is no visible ash layer formed along the channel wall, it is assumed that the majority of this ash was formed upstream in the channel before detaching from the channel wall and depositing in the rear. Other characterization methods are used to further investigate this ash distribution and morphology.

Scanning electron microscopy is again used to further characterize the ash morphology and distribution along the length of several representative channels. Once again, the ash layer is observed to increase in thickness from front to rear, with the rear channels being completely plugged with ash. The ash layer in the inlet cells shown in Figures 4.32a and 4.32 b is barely discernable. The ash layer becomes readily visible in

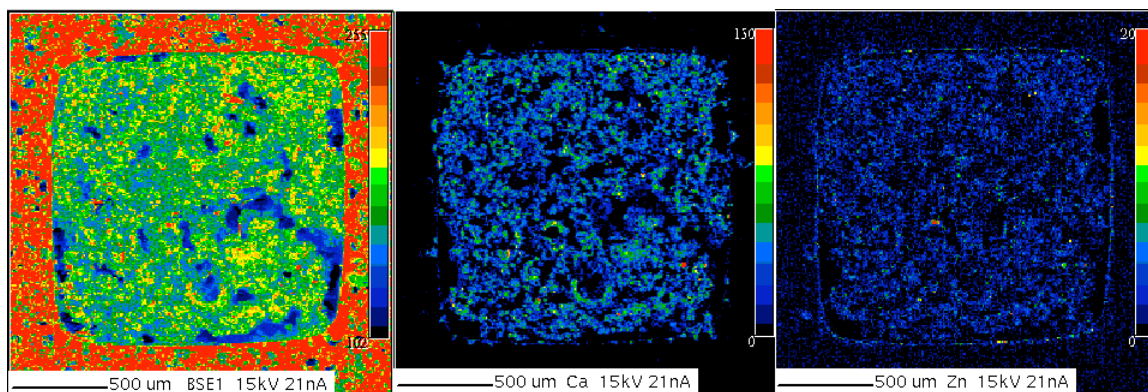


**Figure 4.30: Elemental maps of rear section of cordierite substrate with high PGM loading**

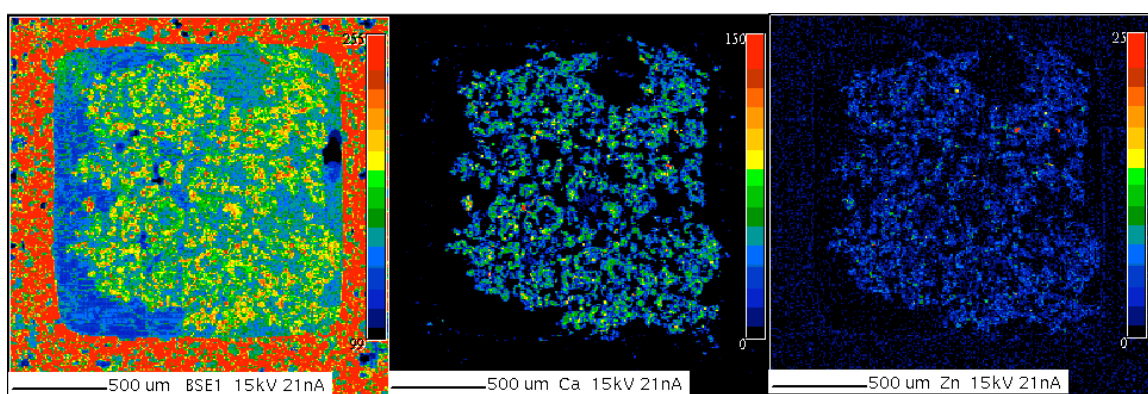


**Figure 4.31: Elemental maps of rear section of cordierite substrate with high PGM loading**

channel where the ash layer can form and remain intact. Finally, the rear channels presented in Figures 4.34a and 4.34b are completely filled with ash. As seen in the first substrate, there is no distinct visible ash layer along the perimeter of the channel. However, the ash consists of much finer particles and appears to be more tightly packed than that observed in the first cordierite substrate. The finer texture may be the direct result of the smoother channel surface and propensity of the ash layer to break away from the channel walls. The smoother channel surface is likely less porous and thus also responsible for the higher backpressures observed during the experiment.



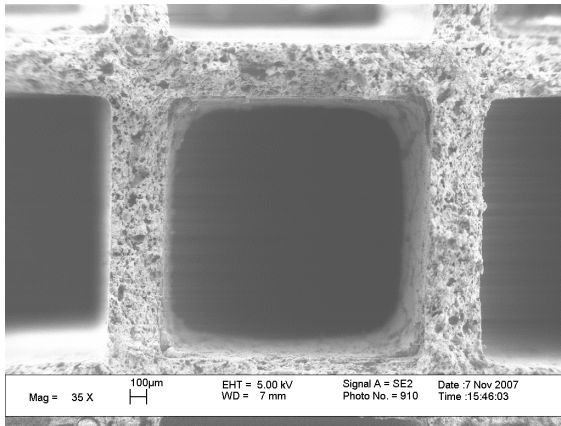


**Figure 4.32a: SEM image of front section channel (38X)**

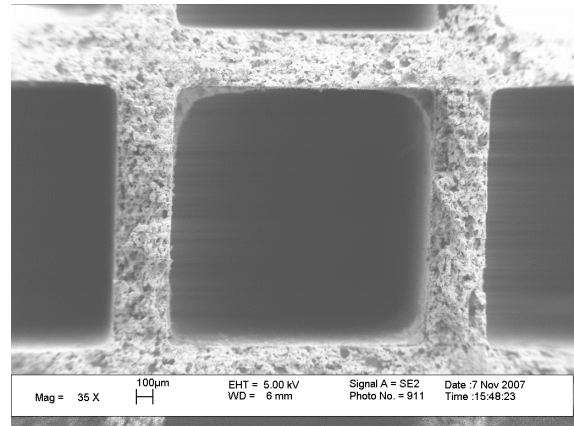


**Figure 4.32b: SEM image of front section channel (38X)**

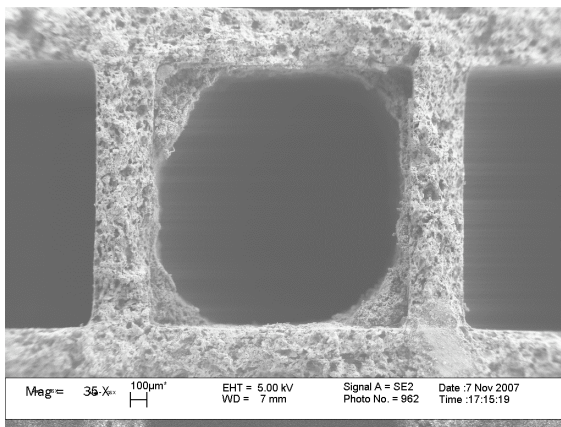


**Figure 4.33a: SEM image of middle section channel (38X)**

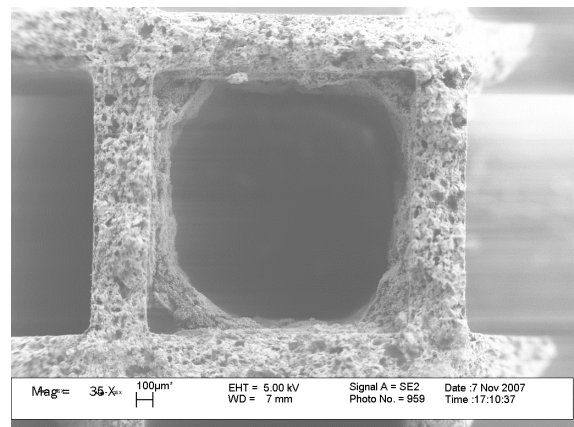


**Figure 4.33b: SEM image of middle section channel (38X)**

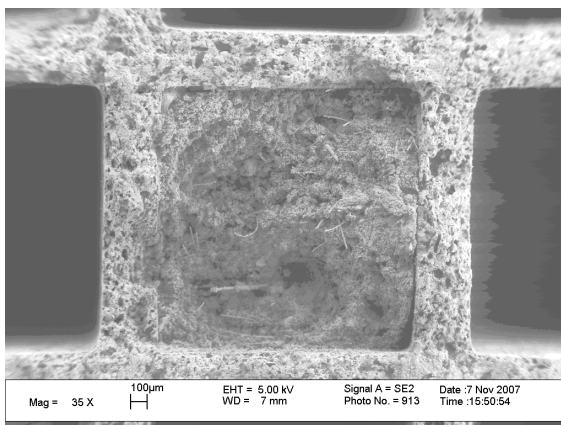


**Figure 4.34a: SEM image of rear section channel (38X)**

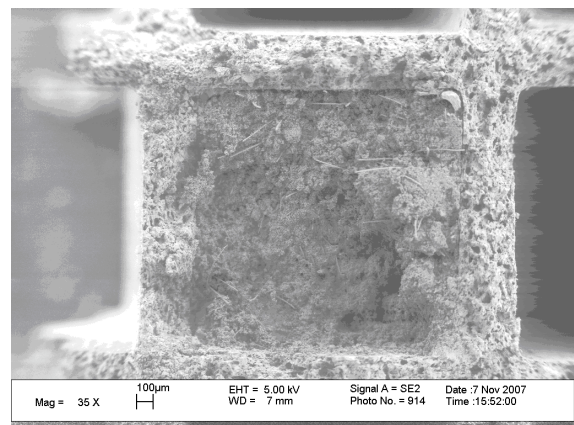


**Figure 4.34b: SEM image of rear section channel (38X)**

The ash layer is now examined under higher magnification. Images representing the front section are presented in Figures 4.2.35a through 4.2.35e show the thing ash layer more clearly. The washcoat and catalyst are also visible and appear to round out the corners of the channel. Ash can also be seen sparsely covering the channel walls. Images from the rear channels, shown in Figures 4.36a through 4.2.36e again show a finer ash that is more compacted. It is also noted that the catalyst washcoat is not nearly as visible, and the ash is not observed to penetrate the substrate wall. As mentioned before, special care it taken to minimize disturbance of the ash layer during sample preparation. It is understood the finer ash morphology coupled with a smoother wall texture further complicates the sample preparation process, and some disturbance is expected. Thus, several samples from the rear section are prepared both to gain a broader understanding of the trends present, and to increase the probability of acquiring images of an ash layer that is fully intact. While the amorphous nature of the ash deposits results in inconsistent focal lengths and complicates image acquisition, it is the region in which the ash comes into contact with the channel wall that is of primary interest, and thus attention is directed there. Examination of the ash-wall interface under higher magnification also shows what appears to be a thin ash layer that is present in the rear channels. The morphology of this ash is also observed to differ slightly from that seen in the front section, though results appear to be consistent within each respective region. Overall, the ash distribution is observed to differ drastically from that observed in the first cordierite substrate. The morphology of the ash within the channel was observed to differ as well, though the ash layer directly adjacent to the channel wall appears very similar to that observed in the first characterization results. It is believed that the

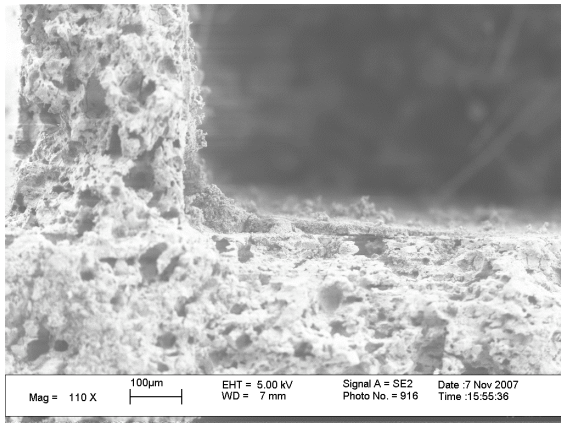


**Figure 4.35a: SEM image of front section channel (110X)**

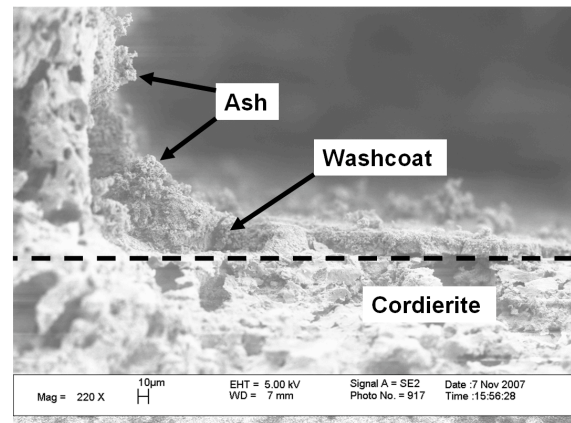


**Figure 4.35b: SEM image of front section channel (220X)**

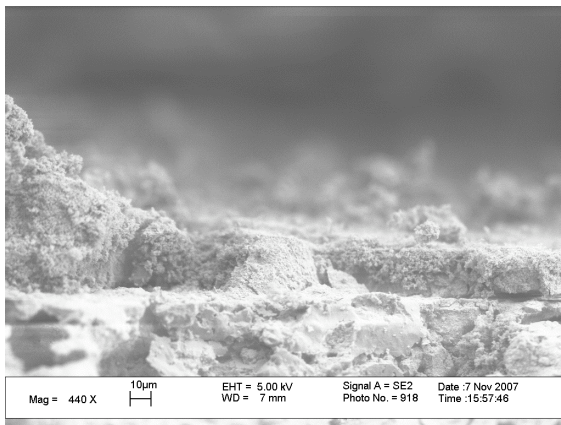


**Figure 4.35c: SEM image of front section channel (440X)**

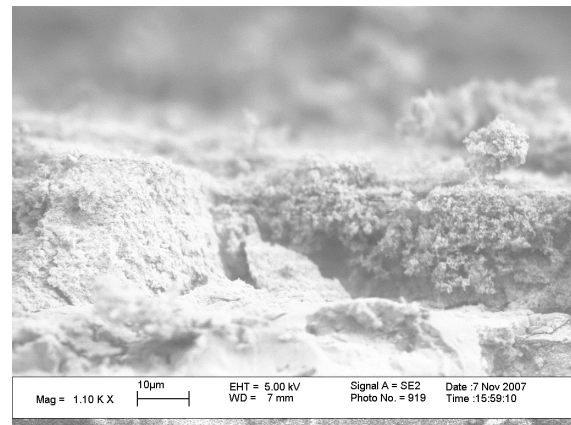


**Figure 4.35d: SEM image of front section channel (1100X)**

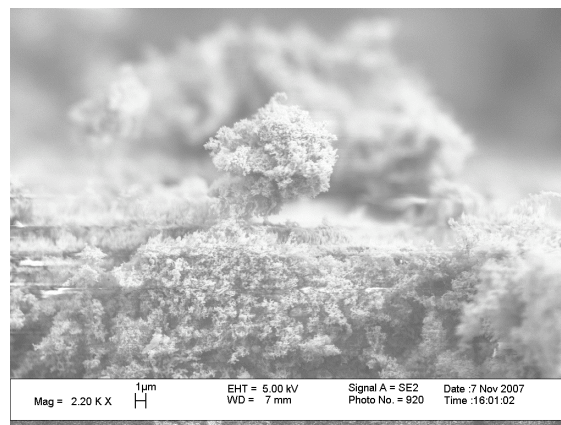


**Figure 4.35e: SEM image of front section channel (2200X)**



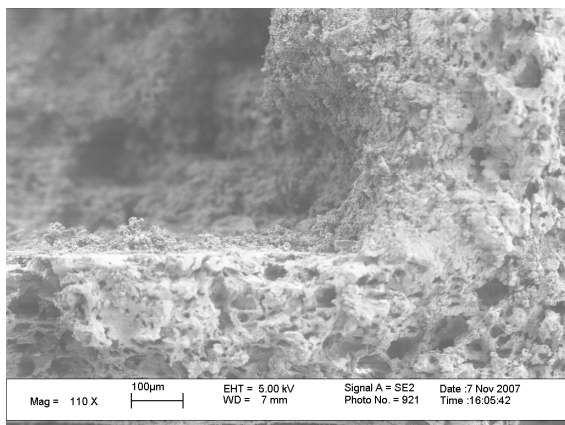


**Figure 4.36a: SEM image of rear section channel (110X)**

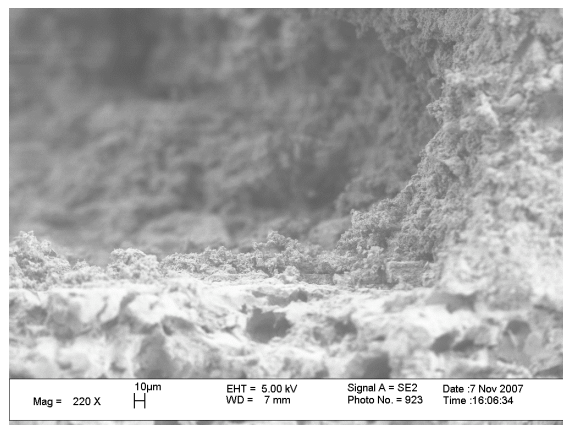


**Figure 4.36b: SEM image of rear section channel (220X)**

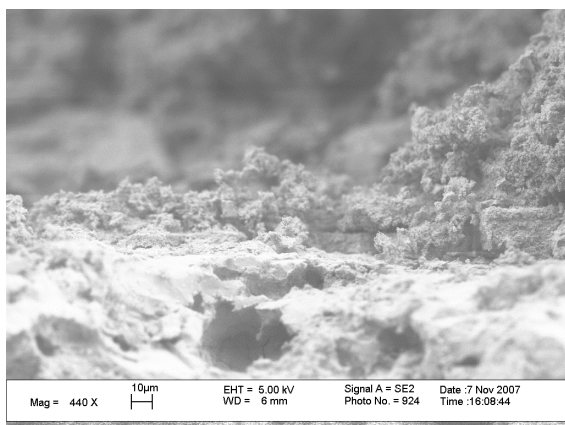


**Figure 4.36c: SEM image of rear section channel (440X)**

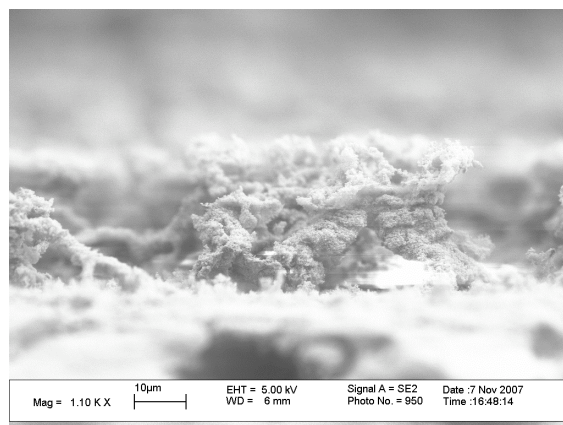


**Figure 4.36d: SEM image of rear section channel (1100X)**

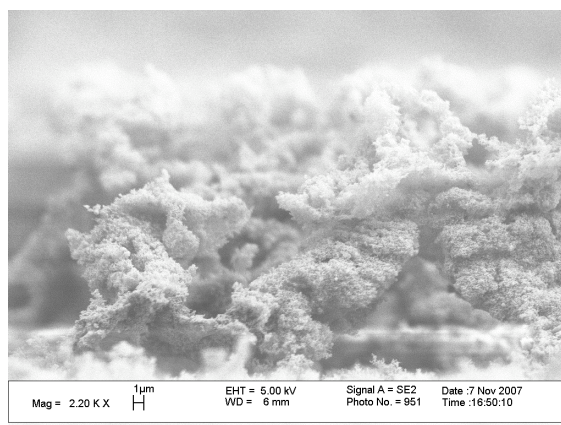


**Figure 4.36e: SEM image of rear section channel (2200X)**

increased presence of washcoat and catalyst material is responsible for the differences in ash distribution. However, in general, the ash layer is again observed to increase in thickness from front to rear, which is consistent with all experiments in this investigation. Calcium and phosphorous are again shown to be present in the highest concentrations of all the elements of interest. Quantification of these elements and their distribution within the DPF will be addressed in Section 4.6. Finally, it is believed that the protocol implemented for this experiment successfully produced results that are consistent with trends observed in other experiments and in literature.

### **4.3 Mullite Substrate with no PGM Loading**

#### ***4.3.1 Mullite Substrate with No PGM Loading – Experimental Results***

This experiment was the second carried out overall. The protocol is actively varied throughout the entire experiment to investigate the effects of engine load on soot loading rate, as well as to determine the best method for completely regenerating the filter. Engine load is increased during the regeneration cycle to provide higher exhaust temperatures that will better facilitate the oxidation of soot accumulated within the filter. Engine load is an important factor during the loading cycle for two reasons: higher engine loads result in both higher exhaust temperatures and increased fuel consumption rates, providing more favorable conditions for continuous regeneration and shortening testing time, respectively.

As outlined in the previous section, exhaust backpressure is a strong function of both the soot accumulated over the course of the loading cycle and the residual ash buildup within the filter. Over the course of this experiment, several backpressure

thresholds are investigated to determine the corresponding soot loading that results. To accomplish this, the DPF can is initially removed following every loading and regeneration cycle so that the mass of soot loaded can be calculated for each individual cycle. While this process provided results that proved useful in determining an outline for the loading and regenerating protocol, the absence of an effective and repeatable regeneration strategy is apparent in analyzing the mass and backpressure data over the entirety of the experiment. During the latter half of the experiment, the backpressure threshold scheme is employed and refined. The focus is shifted to the development of an effective regeneration strategy that can be employed for the remainder of the overall investigation.

The effects of varying the engine load and backpressure threshold, as well as the frequent engine shutdown for mass measurement are visible in the DPF solid temperature profile shown in Figure 4.37. To avoid loading too much soot and the possibility of an uncontrolled regeneration, the backpressure threshold is initially defined as only 0.10 psi above the baseline backpressure, and increased in small increments. The lower backpressure thresholds, coupled with an ad-lib regeneration scheme, resulted in more frequent regenerations. As the backpressure threshold is increased, loading times increased slightly. Twice near the midway point of the experiment, the backpressure threshold was increased too much, and the additional soot loading resulted in an uncontrolled regeneration in the filter during which DPF solid temperatures reached 1200°C. The filter was removed and inspected for damage with no cracks or soot leakage being observed. The temperature excursions can also be observed in the exhaust gas temperature profile as seen in Figure 4.38, though not nearly as severe. The backpressure

threshold necessary to achieve an approximate soot loading of 2 grams (~3 grams/liter) was then determined to be approximately 0.2 psig above the baseline. This value is used to determine the length of the loading cycles for the duration of the experiment. Upon implementing the protocol using this established backpressure threshold, the temperature profile becomes much more repeatable. Repeatability is further enhanced as the active regeneration strategy is refined, as seen in the latter portions of both temperature profiles.

The most interesting data in this experiment is the backpressure profile shown in Figure 4.39. While several trends corresponding to variations in backpressure threshold and regeneration strategy are apparent, the overall trend appears fairly level when compared to the trends observed for the cordierite substrates. The uncontrolled regenerations are visible in the two backpressure spikes near the midway point of the experiment, the result of rapid soot accumulation and increased space velocity during active regeneration. Once the protocol with established backpressure threshold was applied around the 2000-minute mark, the backpressure profile becomes more repeatable. The variations in backpressure peaks between cycles are attributed to ash accumulation within the filter and subsequent decrease in soot accumulation during each cycle. As seen in Figure 4.40, the mass data is scattered for the first half of the experiment, again the result of changing protocol parameters. Most notable are points where the clean masses decrease over time, indicating incomplete regenerations and highlighting the need for an effective and repeatable regeneration strategy. This strategy is developed and applied in conjunction with the established backpressure threshold, resulting in very linear mass data starting at the 2000-minute mark.

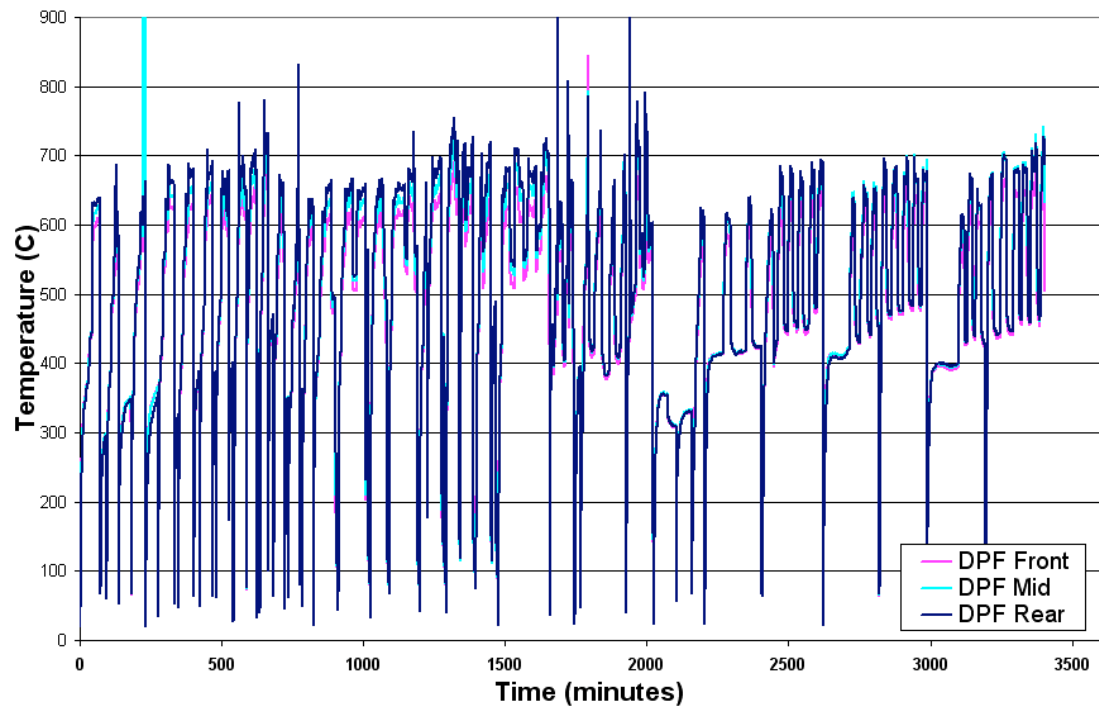


**Figure 4.37: DPF solid temperatures versus time for non-catalyzed mullite substrate**

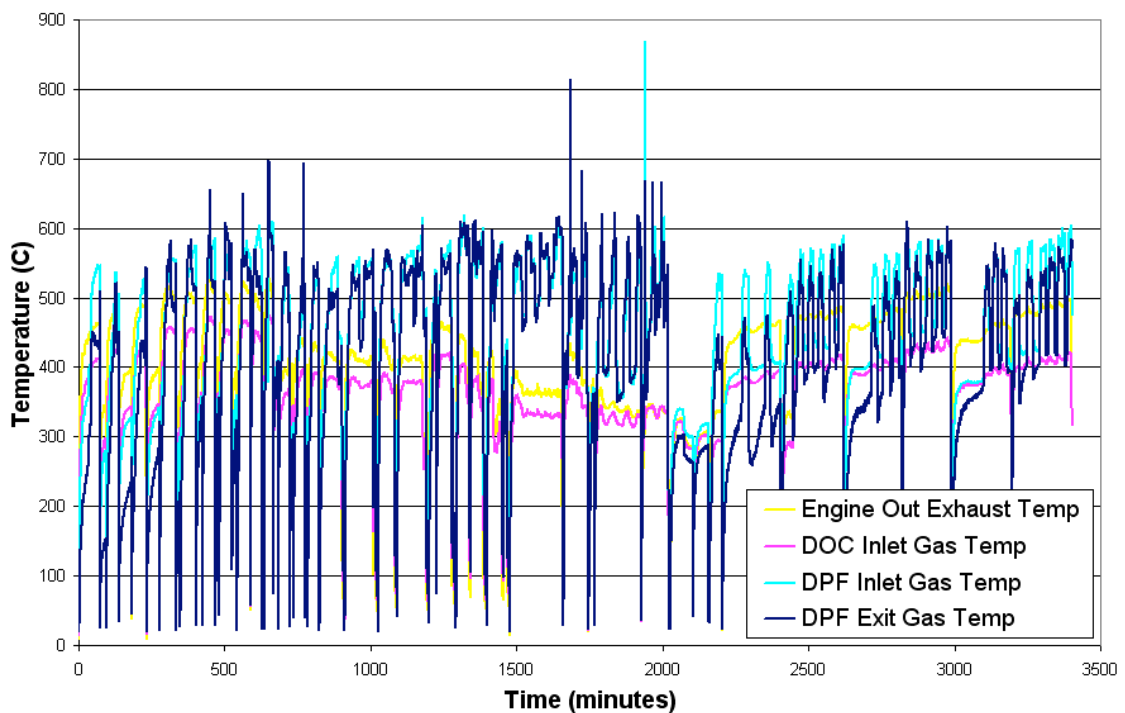


**Figure 4.38: Exhaust gas temperatures at various locations versus time for non-catalyzed mullite substrate**



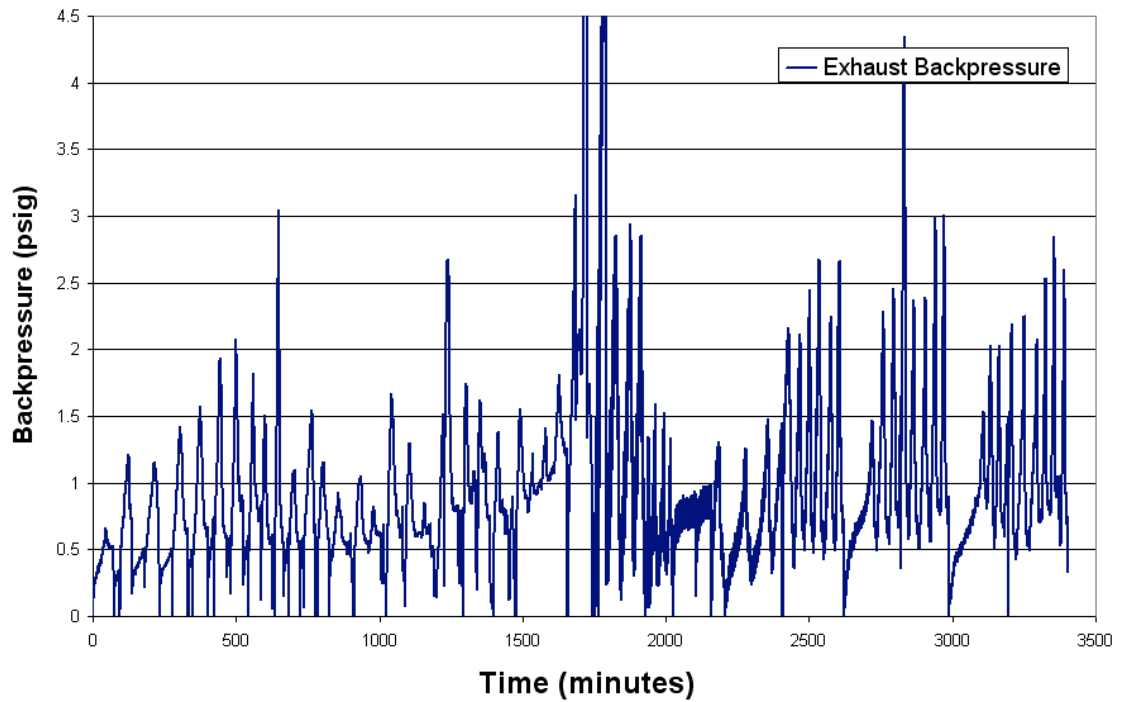


**Figure 4.39: Exhaust backpressure versus time for non-catalyzed mullite substrate**

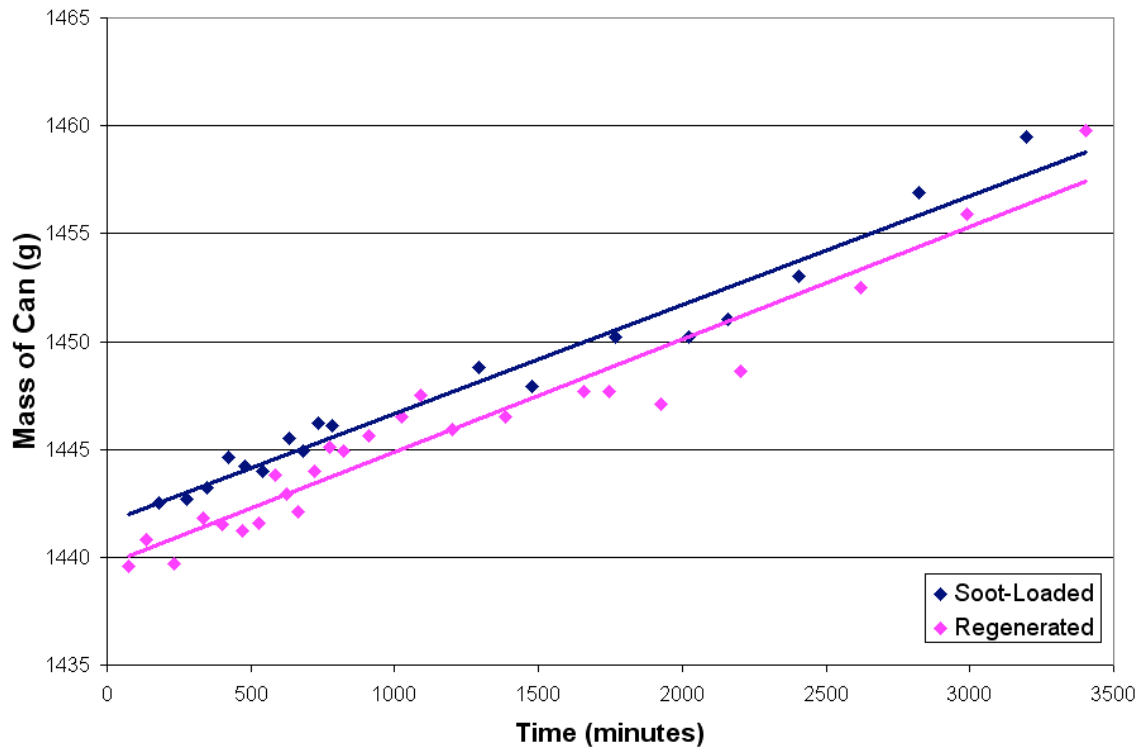


**Figure 4.40: DPF mass data versus time for non-catalyzed mullite substrate**

#### ***4.3.2 Mullite Substrate with no PGM - Characterization Results***

Following the completion of this engine experiment, the sample is divided into quarter sections. All four sections were consumed in the development of a sample preparation method that minimized disturbance of the ash distribution and morphology, and thus there was no sample remaining for ICP analysis.

Photographs are taken of various areas of interest are used to visually characterize trends in ash formation. Figures 4.41 and 4.42 are photographs taken of cross-sections from the front and rear sections, respectively. The inlet channels appear to be nearly devoid of ash, while rear channels are completely plugged with ash. The darker color of the inlet channels of the front section is likely the result of residual soot from the exhaust pipe breaking loose and depositing in the DPF during the final cool down cycle.

Photographs of the samples analyzed using SEM, displayed in Figure 4.43 show an ash layer that increases in thickness along the length of the channel. The rear channels are completely plugged with loosely packed ash, making sample preparation difficult.

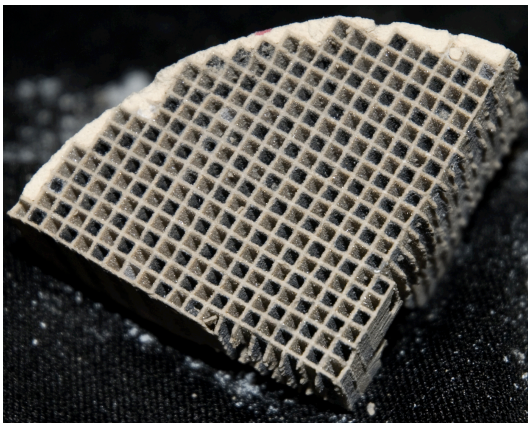


**Figure 4.41: Photograph of one-quarter sample from front section of non-catalyzed mullite substrate**

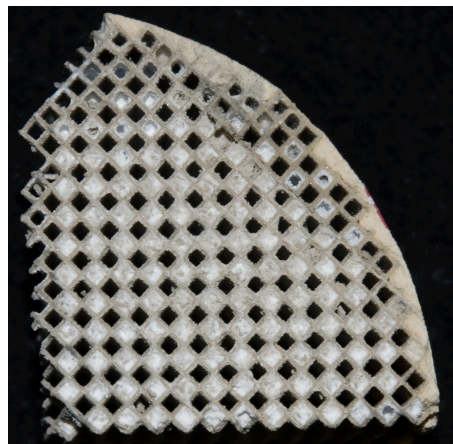


**Figure 4.42: Photograph of one-quarter sample from rear section of non-catalyzed mullite substrate**

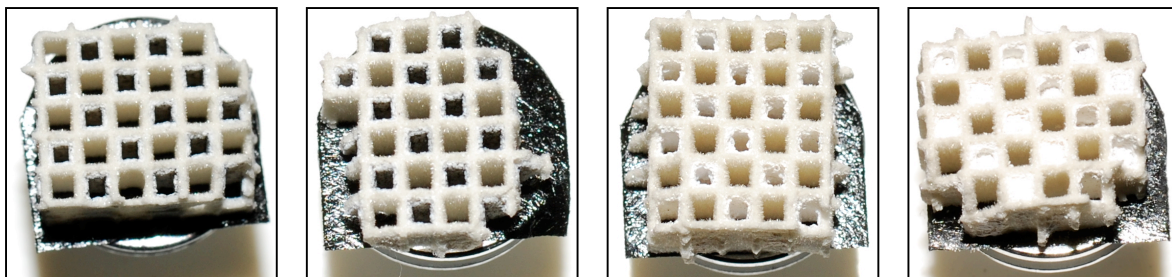


**Figure 4.43: Photographs of representative samples extracted from the front, front-middle, middle and rear sections of non-catalyzed mullite substrate**

EPMA elemental maps of the non-catalyzed mullite substrate provide a great visual understanding of the underlying reason for which mullite substrates outperform other substrates with regard to backpressure. Calcium and phosphorus are again observed to be the most prevalent of the elements of interest and thus are again selected to represent the ash layer. Once again, the maps shown are considered representative of the overall trends observed in the front, middle and rear sections at locations 0.5", 3.0" and 5.0" from the inlet of the DPF, respectively.

Elemental maps for the front section are presented in Figures 4.44 and 4.45. The maps show an ash layer that is visibly thicker than that observed in the cordierite filter, but is clearly more porous. This increases the effective filtration area, distributing the ash over a larger area of the cross section. The textured channel wall also facilitates the formation of an ash layer that is more likely to remain intact and not break away, further enhancing ash distribution. The result is a more porous ash layer that performs more efficiently than other substrate materials with respect to backpressure.

The elemental maps for the middle section of the DPF, shown in Figures 4.46 and 4.47, depict an ash layer that is slightly thicker than that observed in the front section. While the thickness is nearly the same, it appears that the density of the ash layer is

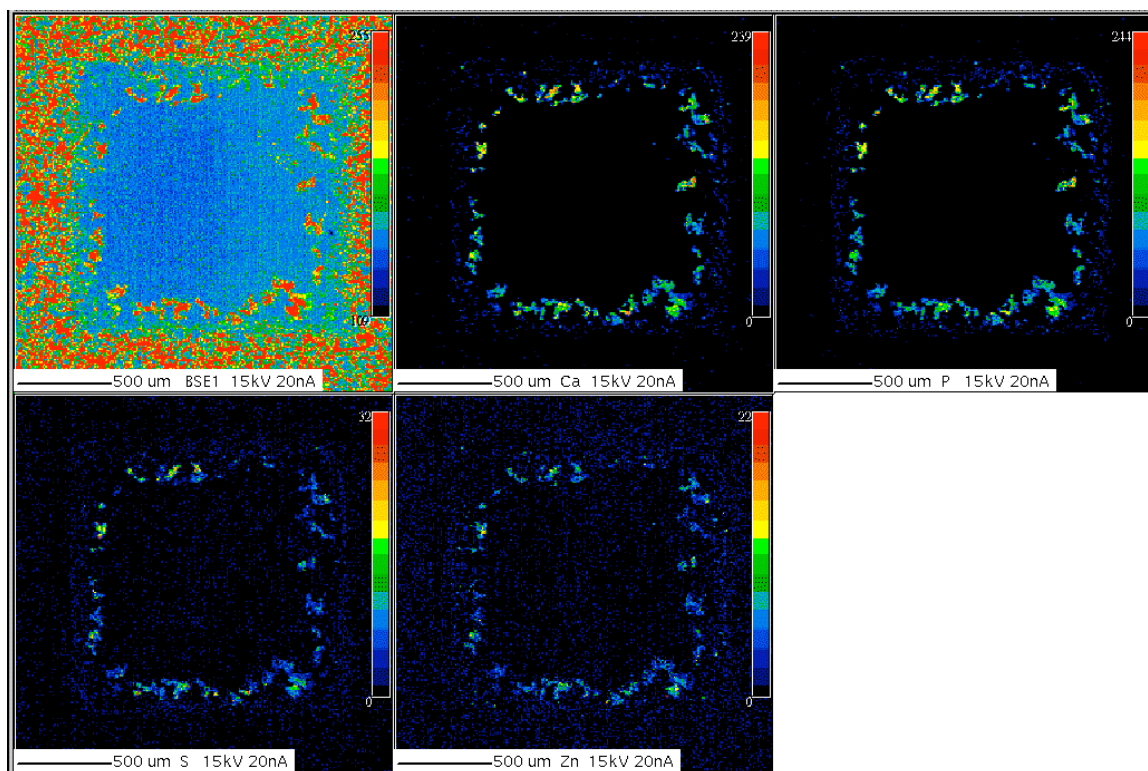


**Figure 4.44: Elemental maps of front section of non-catalyzed mullite substrate**

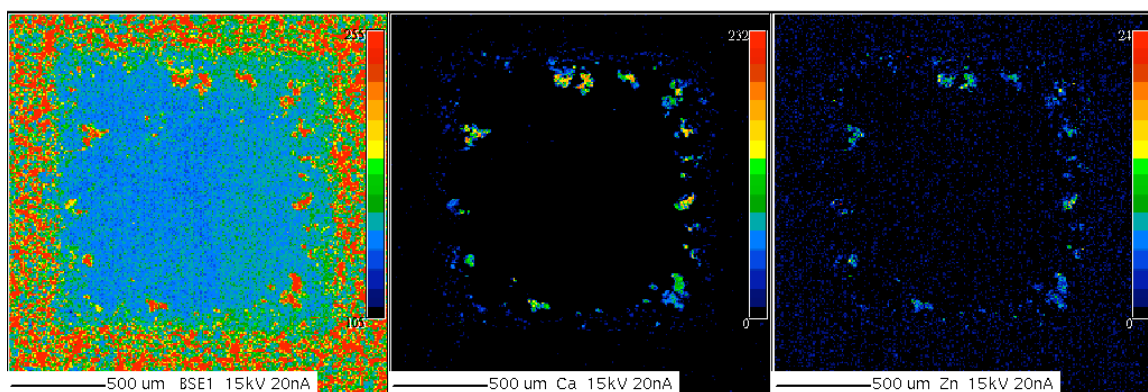


**Figure 4.45: Elemental maps of front section of non-catalyzed mullite substrate**



higher, though it remains very porous. It is likely that some ash from the front and middle sections still breaks away and deposits in the rear despite the coarser texture of the wall. However, these images further confirm that the ash does remain more distributed along the length of the channel than observed in results with other substrate materials. The development and preservation of a porous ash layer is again a clear advantage with respect to exhaust backpressure.

The elemental maps of the rear section of the DPF are presented in Figures 4.48 and 4.49, and again show channels that are completely plugged with ash. However, the manner in which the ash plugged the channels varied with respect to radial location

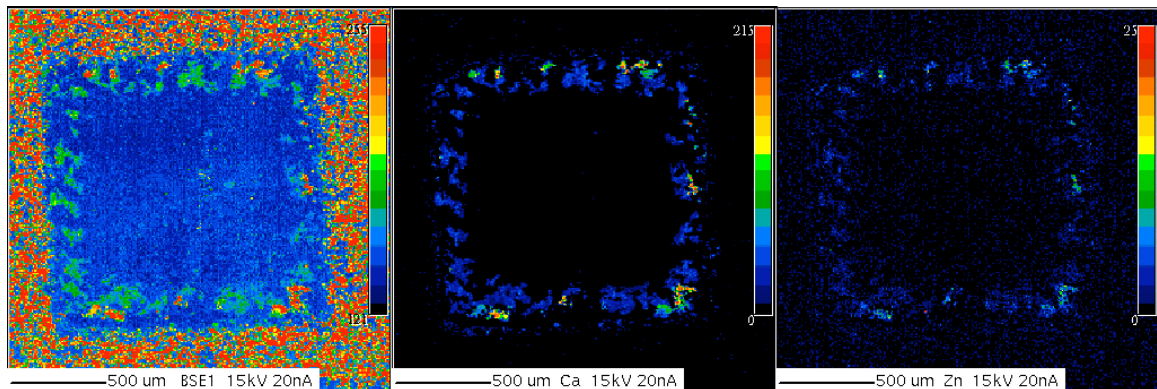


**Figure 4.46: Elemental maps of middle section of non-catalyzed mullite substrate**

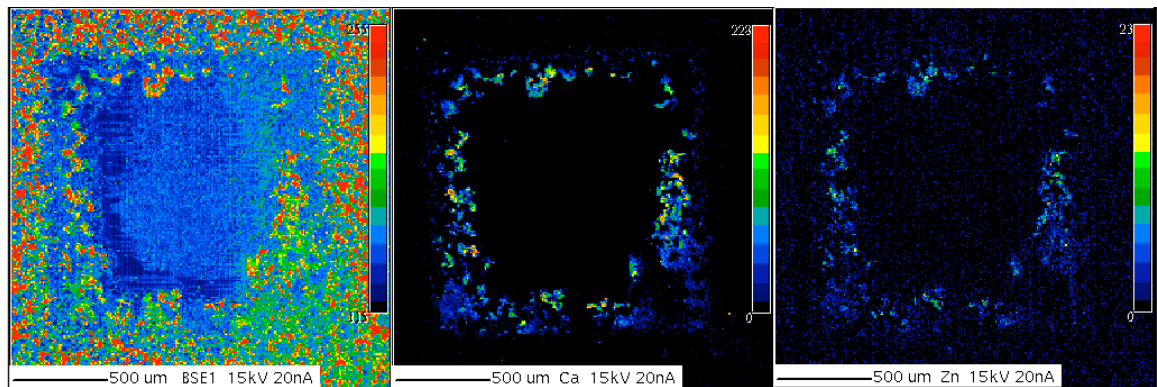


**Figure 4.47: Elemental maps of middle section of non-catalyzed mullite substrate**

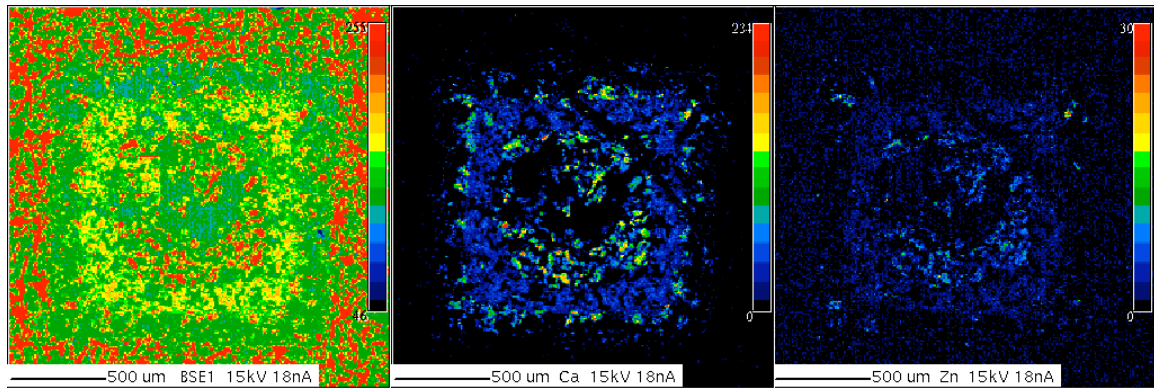


**Figure 4.48: Elemental maps of rear section of non-catalyzed mullite substrate**

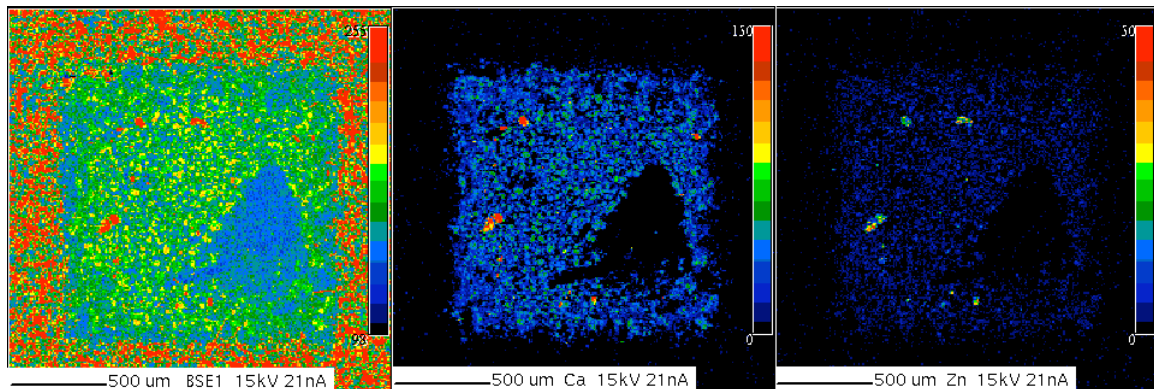


**Figure 4.49: Elemental maps of rear section of non-catalyzed mullite substrate**

within the filter, and can be characterized as two distinct regions. Figure 4.48 accurately represents the majority of channels, which are located within approximately one inch of the axial centerline. Unlike the trends in ash layer morphology and distribution observed in the cordierite substrate, there is a distinct ash layer visible along the perimeter of the channel. It can also be seen that the center of the channel is filled with ash material that likely formed upstream, broke loose, and deposited in the rear of the DPF. Figure 4.49 was selected as a representation of a smaller portion of the channels located around the outer perimeter of the DPF. Unlike the center channels, there is no visible ash layer along the channel wall. Instead, the channels appear to be plugged with a uniform

distribution of loosely-packed ash particles. It is also noted that these channels often have voids present in the ash, likely the result of lesser flow through these channels. Overall, the ash deposit remains very porous, further contributing to the backpressure advantage experienced with the mullite filters.

To further investigate the morphology and distribution of ash within the DPF, Scanning Electron Microscopy is utilized to examine the areas of interest under high magnification. Once again, representative channels are selected for the front, middle and rear sections, represented by Figures 4.50 through 4.52. The ash layer is once again observed to increase in thickness from front to rear, though the increase in thickness is not as extreme as that observed with cordierite. The ash layer in the inlet sections, presented in Figures 4.50a and 4.50b, is barely discernable under lower magnifications. However, EPMA results show that the ash layer is only slightly thinner than that of the middle section, shown in Figures 4.51a and 4.51b. It is observed that the acicular morphology of the substrate itself protrudes relatively far into the channel void, allowing the ash layer to form in and among these protrusions. The ash layer becomes more visible in the middle section as the substrate protrusions become covered and less visible. For the first time in this investigation, a distinct ash layer is visible in the rear section, as seen in Figures 4.52a and 4.52b. It is noted that the ash was loosely packed within the rear channels, and the ash in the center region of these channels that was observed in EPMA was knocked loose and lost during sample preparation. This analysis provides a visual example of the manner with which ash deposits over a larger volume within the DPF, and shows the underlying reasons for the lower backpressures observed during the engine experiment.



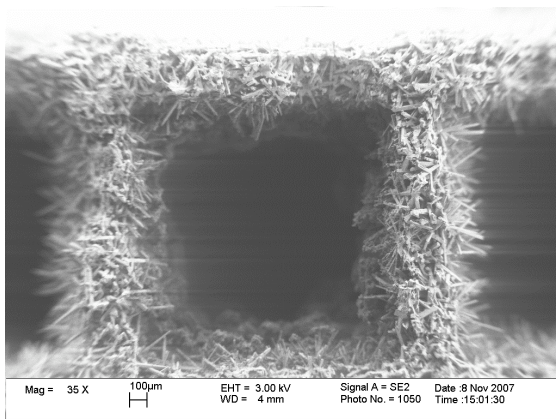


**Figure 4.50a: SEM image of front section channel (38X)**

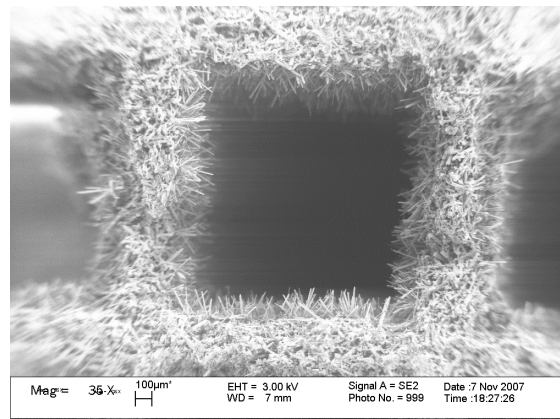


**Figure 4.50b: SEM image of front section channel (38X)**

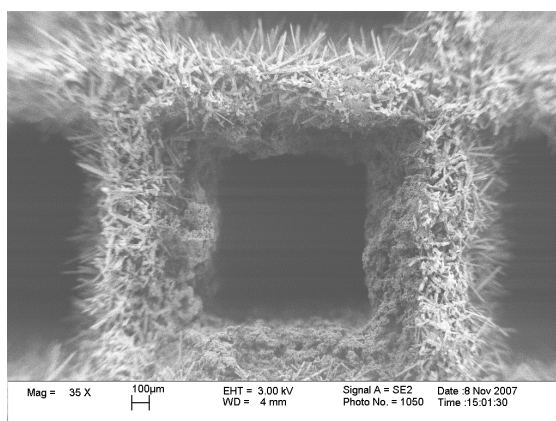


**Figure 4.51a: SEM image of middle section channel (38X)**

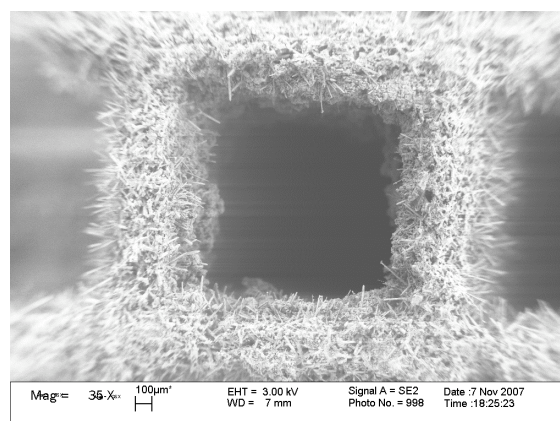


**Figure 4.51b: SEM image of middle section channel (38X)**

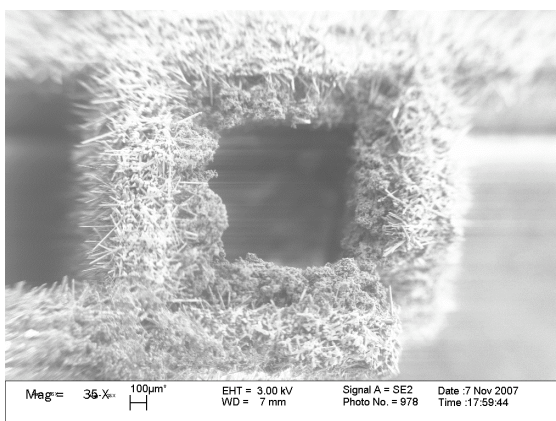


**Figure 4.52a: SEM image of rear section channel (38X)**

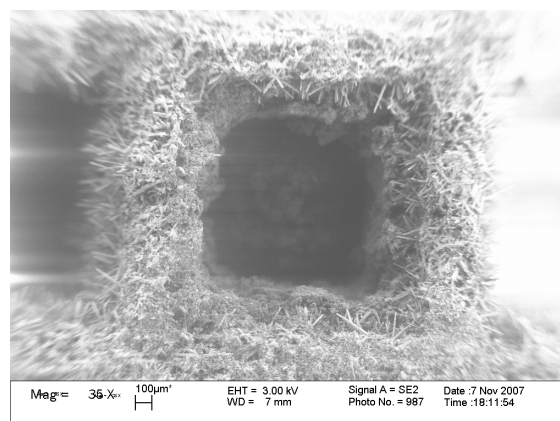


**Figure 4.52b: SEM image of rear section channel (38X)**



Representative channels are again selected from the front and rear sections for examination under greater magnification. In particular, the region in which the ash comes into direct contact with the substrate is analyzed to better understand the morphology of the substrate and ash layer. Images of the front section acquired under increasing magnification are presented in Figures 4.53a through 4.53f. These images clearly show the presence of the ash layer that has formed within the protrusions of the acicular substrate. Larger ash agglomerates are trapped in the less dense region of the channel wall, while smaller particles deposit deeper within the surface of the channel wall. This distribution lessens the impact of ash accumulation on backpressure. Images of a rear section channel acquired under increasing magnification are presented in Figures 4.54a through 4.54e. These images exhibit an ash layer that has formed and extended beyond the protrusions of the substrate wall. The ash layer becomes visibly denser toward the center of the channel where it appears similar to the layers observed in the cordierite substrates. Thus, in addition to the plugging of the rear channels, backpressure will also increase as a result of ash layers that grow and extend beyond the substrate protrusions, forming a more compact layer. This phenomenon cannot be readily observed in the experimental data due to the protocol being refined during this experiment. However, this theory will be further addressed in the next section. One more noteworthy observation with regard to the ash-substrate interface is that despite the ash layer appearing less dense overall, it is more structurally solid and thus more likely to remain intact. This integrity is the result of the ash layer forming within the channel wall protrusions, providing a natural frame that reinforces the ash layer and prevents breakage and separation from the channel wall.

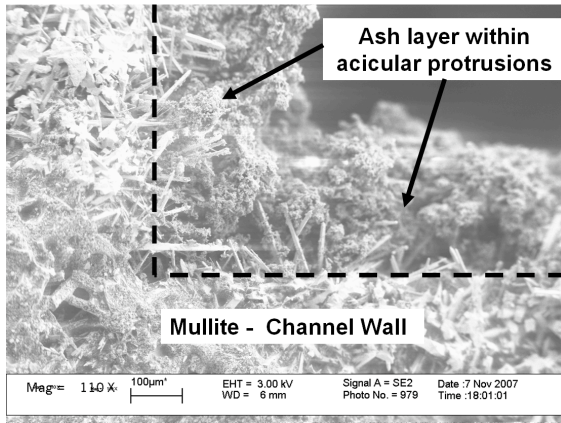


**Figure 4.53a: SEM image of front section channel (110X)**

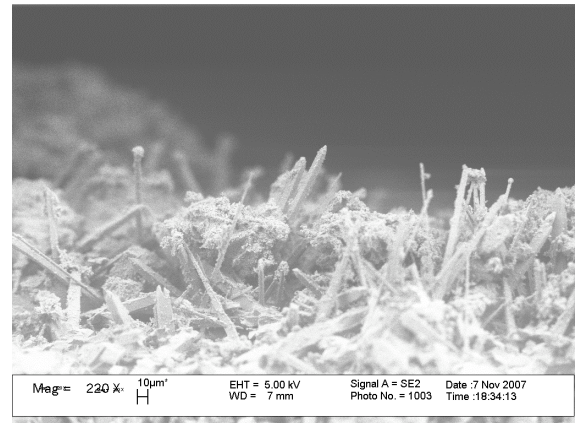


**Figure 4.53b: SEM image of front section channel (220X)**

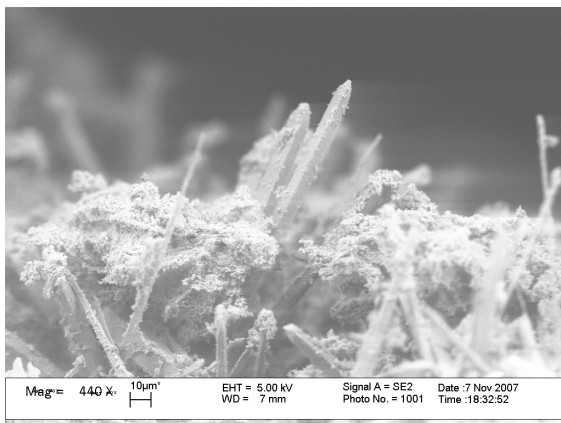


**Figure 4.53c: SEM image of front section channel (440X)**

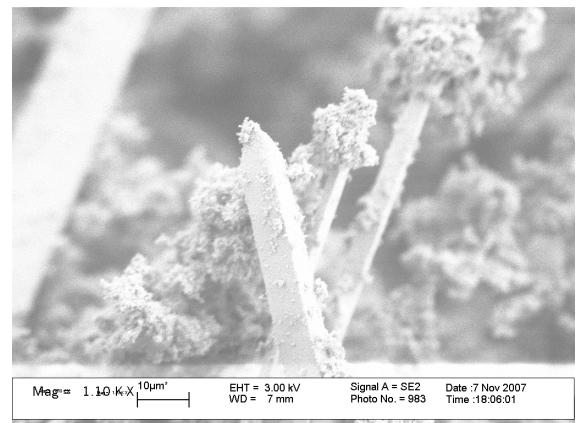


**Figure 4.53d: SEM image of front section channel (1100X)**

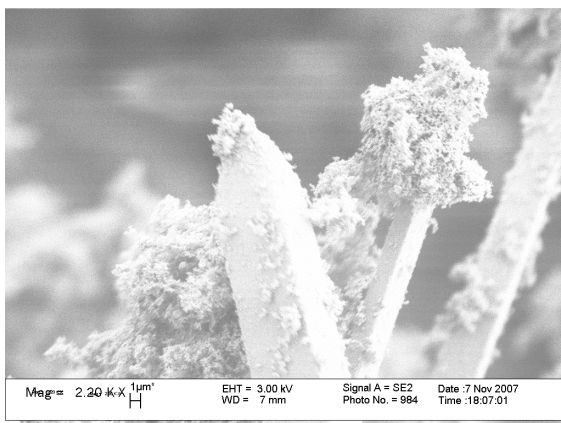


**Figure 4.53e: SEM image of front section channel (2200X)**

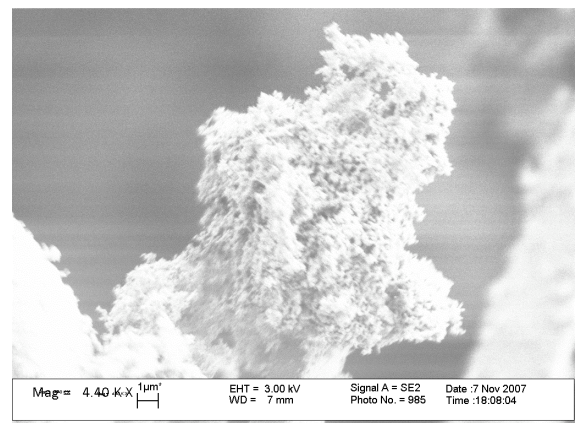


**Figure 4.53f: SEM image of front section channel (4400X)**

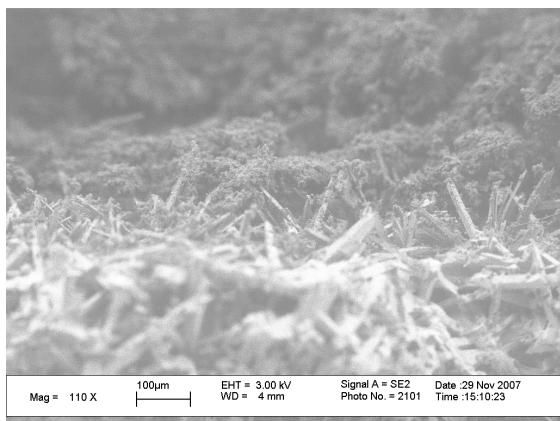


**Figure 4.54a: SEM image of rear section channel (110X)**

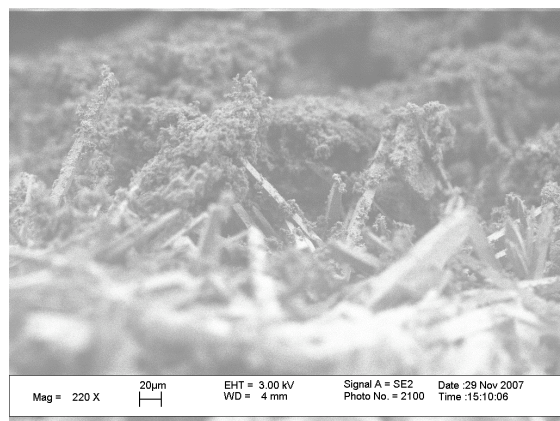


**Figure 4.54b: SEM image of rear section channel (220X)**

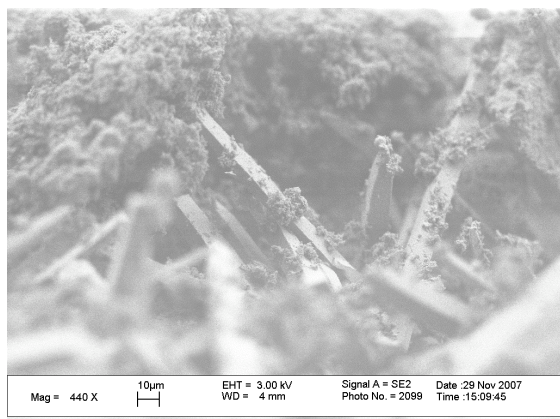


**Figure 4.54c: SEM image of rear section channel (440X)**

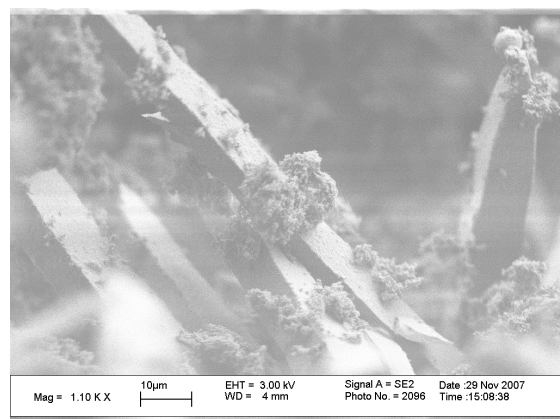


**Figure 4.54d: SEM image of rear section channel (1100X)**

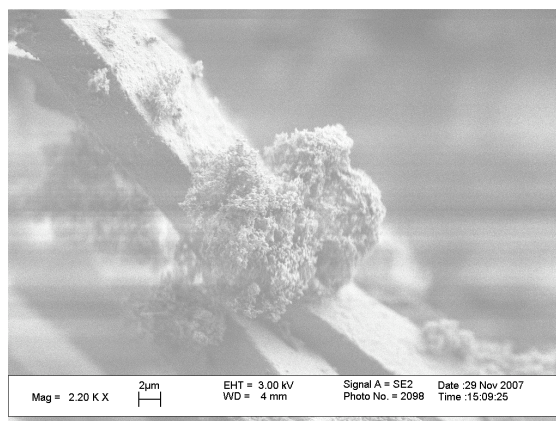


**Figure 4.54e: SEM image of rear section channel (2200X)**

Overall, the morphology of both the substrate and ash layer differs drastically from that observed in other substrates such as cordierite and silicon carbide. Namely, the acicular morphology of the substrate wall allows the ash to penetrate and deposit at varying depths within the channel wall, providing a more porous ash layer. The ash layer that forms becomes integrated with the wall, increasing the likelihood that it will remain intact rather than breaking away and depositing in the rear of the filter. Since ash is more evenly distributed throughout the filter, ash accumulation has a far lesser effect on backpressure. There is a threshold at which this advantage is lost, which occurs when the ash layer extends beyond the acicular protrusions of the channel wall.

Similar to the results obtained with the cordierite substrates, calcium and phosphorus are present in the greatest concentrations among the elements investigated, and will be quantified later in this chapter. The ash layer was again observed to increase in thickness from front to rear, though this increase was of a far smaller magnitude. Finally, there was distinct ash layer visible in the rear section channels, which is the first observed in this investigation. This is the result of the depth filtration principle. Since exhaust gasses flow along the path of least resistance, ash is naturally distributed fairly evenly throughout the length of the filter. Since the ash initially penetrates the channel wall, very little ash breaks loose and deposits in the rear. As the ash layer continues to grow and extend beyond the channel wall protrusions, more ash begins to break loose and deposit in the rear, creating the two distinct regions observed with EPMA analysis. The resulting overall ash layer is very porous and likely to remain intact, maintaining a more even ash distribution than that observed in other substrates.

## **4.4 Mullite Substrate with High PGM Loading**

### ***4.4.1 Mullite Substrate with High PGM Loading – Experimental Results***

This experiment was the fifth carried out overall. By this point, the protocol had been developed and is ready to be applied without variation for an entire experiment to verify repeatability and to identify trends in DPF behavior. Engine load setting is chosen such that the exhaust temperature is approximately 450°C, and is held constant for both loading and regeneration cycles for the entire experiment. The backpressure threshold is defined for each loading cycle by adding 0.20 psi to the baseline backpressure established following engine warm-up or post-regeneration cool-down.

The DPF solid temperature profile shown in Figure 4.55 demonstrates the excellent repeatability of the entire experiment. Approximately 200 minutes of data are missed due to the DAQ system crashing, though nothing of consequence was observed during that time. It is immediately visible that the loading times are significantly longer than those observed in any other experiment. This is due both to the high porosity of mullite and the continuous regeneration efficiency resulting from the high PGM loading. As ash accumulates within the filter, the loading times eventually shorten and begin to resemble those observed in previous experiment. The repeatability of the protocol is further validated by the exhaust gas temperature profile presented in Figure 4.56.

It is theorized that the morphology of the channel wall creates different stages of ash layer formation. Initially, the ash deposits in voids on the surface. This results in a very porous ash layer. As ash continues to deposit, all the voids are filled, and a layer begins to form over the top, similar to the type of layer that forms in the cordierite filters. A graphic representation of this theory conjecture can be found in Figure 4.57. It is also

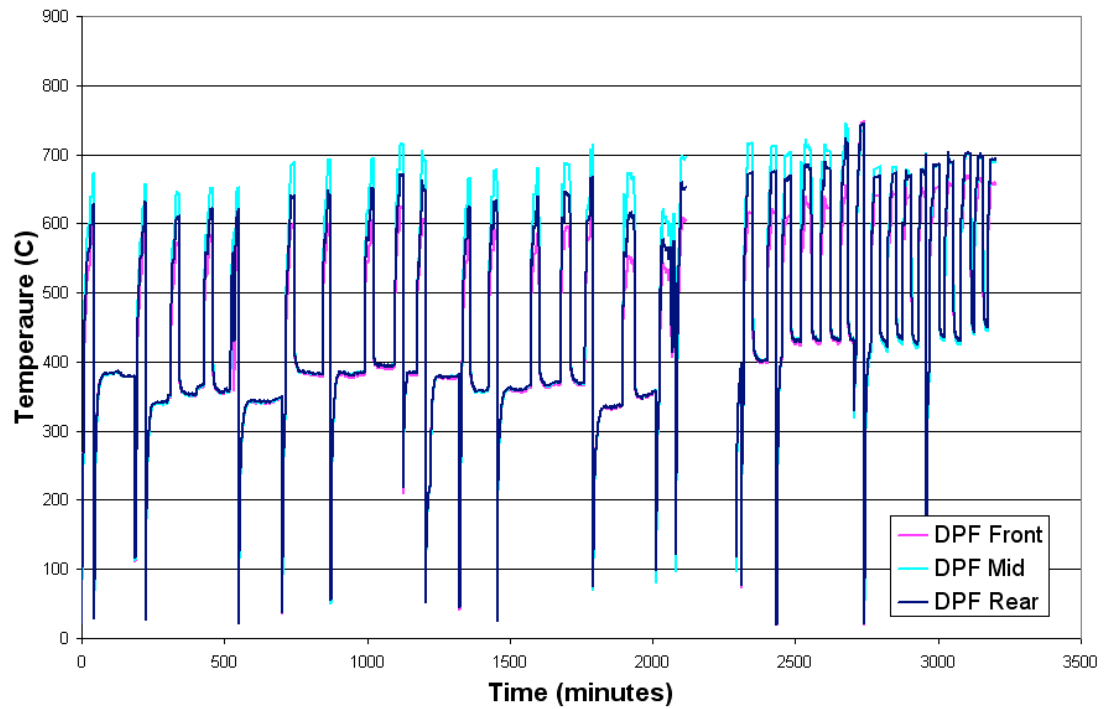


**Figure 4.55: DPF solid temperatures versus time for mullite substrate with high PGM loading**

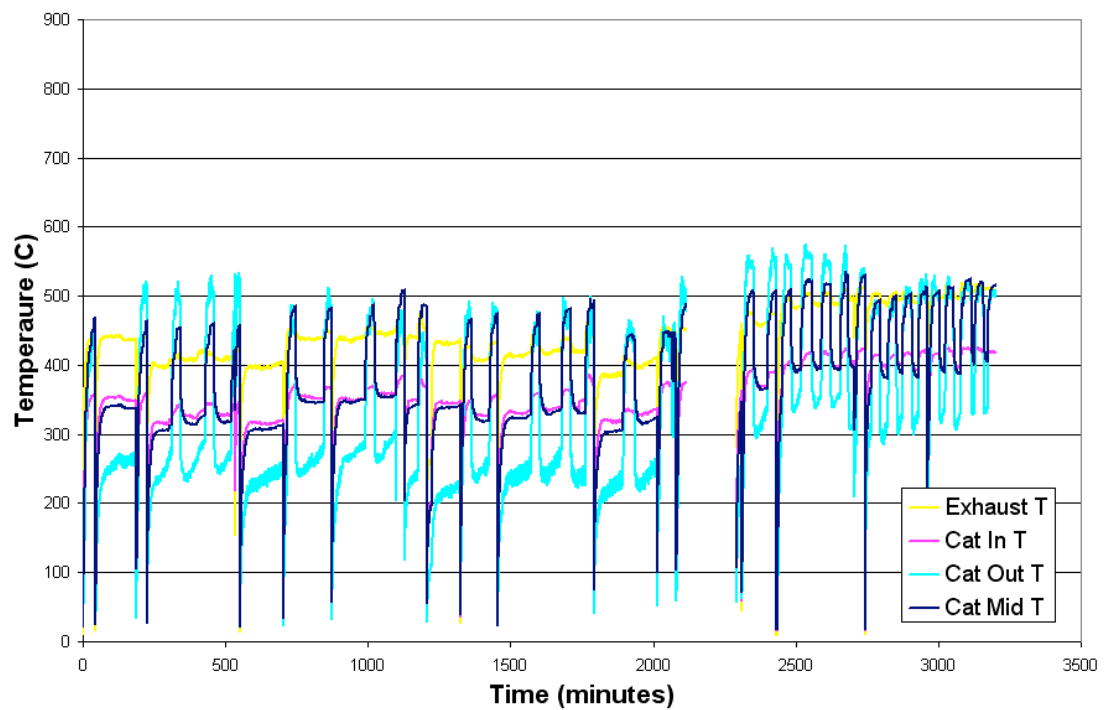


**Figure 4.56: Exhaust gas temperatures at various locations versus time for mullite substrate with high PGM loading**



observed in both temperature profiles that temperatures begin to increase around the 2000-minute mark. This phenomenon is also visible in the exhaust backpressure profile shown Figure 4.58. While it appears more material is being loaded in the filter, the mass data indicates a very linear trend over the entire experiment, as seen in Figure 4.59, confirming no increase in the rate of ash accumulation.

Overall, the test results indicate that the protocol satisfies all of the requirements set forth. The temperature profiles demonstrate excellent repeatability, and allow trends in DPF performance to be identified. The backpressure data also exhibits great repeatability with an easily identifiable trend. Finally, the mass data confirms that the protocol consistently loads the desired amount of soot and effectively regenerates the DPF every cycle. The DPF must be characterized to evaluate the ash layer and determine if the results compare favorably with results published in literature.

#### ***4.4.2 Mullite Substrate with High PGM Loading - Characterization Results***

Following the completion of this engine experiment, the sample is divided into quarter sections. Three samples are again used for EPMA, SEM and ICP analysis, with a fourth again retained for future analysis. Photographs taken of various areas of interest are catalogued and utilized to visually characterize trends in ash formation.

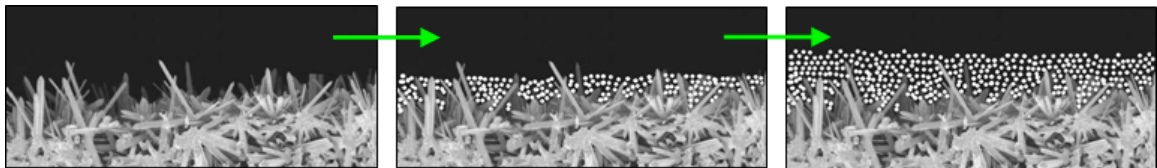


**Figure 4.57: Graphic representation of ash layer formation stages for mullite DPF**

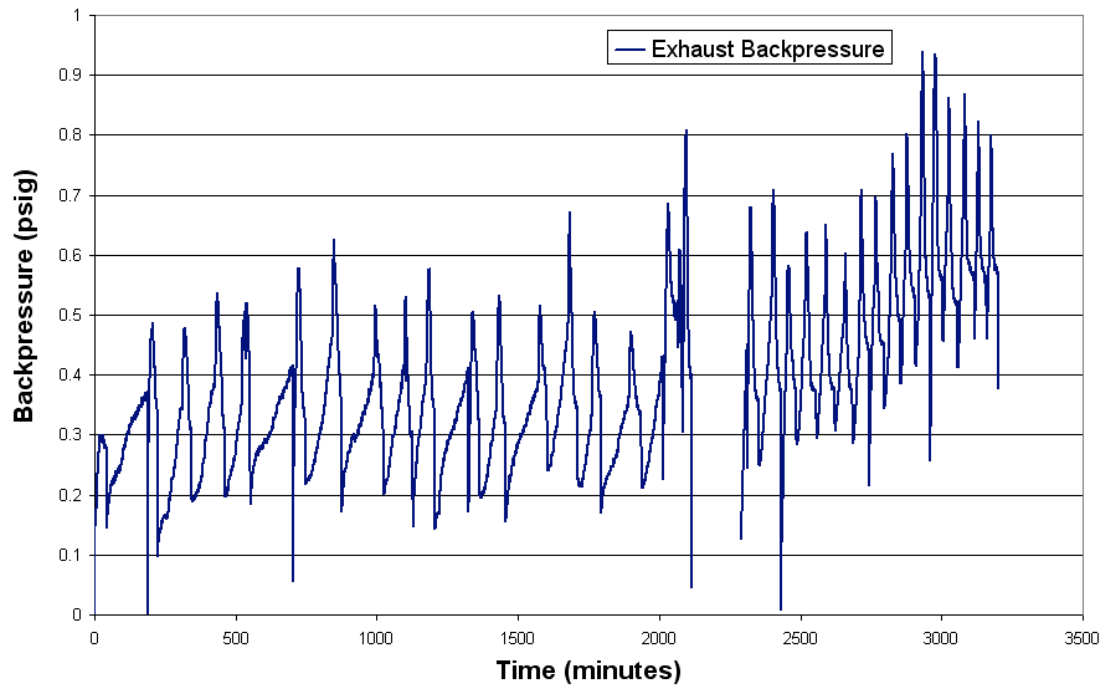


**Figure 4.58: Exhaust backpressure versus time for mullite substrate with high PGM loading**

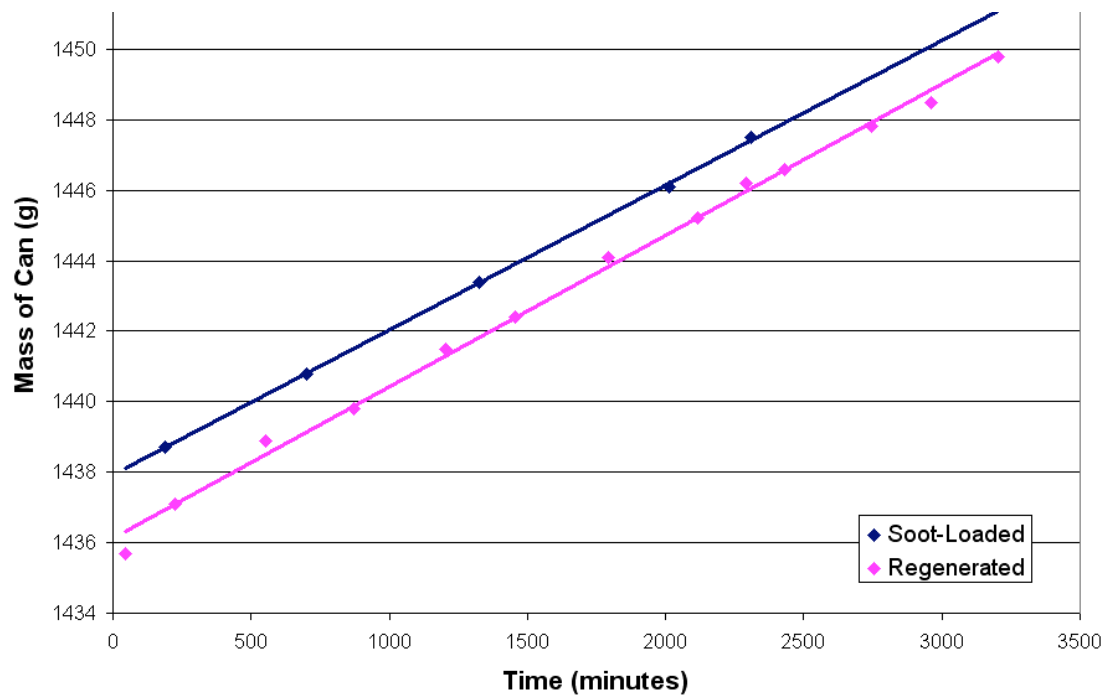


**Figure 4.59: DPF mass data versus time for mullite substrate with high PGM loading**



Photographs taken of cross-sections from the front and middle sections, presented in Figures 4.61 and 4.62, again show a drastic difference in the amount of ash present.

Photographs of the samples analyzed using SEM, as seen in Figure 4.63, depict an ash layer that consistently increases in thickness along the length of the channel, with the rear-most channel completely plugged. The front section appears to be devoid of any ash material, but further analysis reveals the presence of an ash layer that is again morphologically unique to mullite.

EPMA is again employed to investigate the cross-sections of channels located throughout the filter. Elemental maps displaying relative concentrations of the common lube-oil constituents such as calcium, zinc, phosphorus and sulfur, are used to identify the ash layer and observe how it forms along the substrate wall. The maps presented were selected as representative channels from the front, middle and rear channels, the same

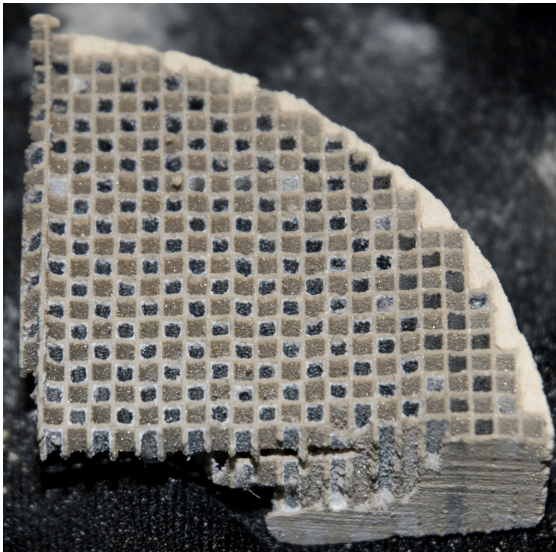


**Figure 4.61: Photograph of one-quarter sample from middle section of mullite substrate with high PGM loading**

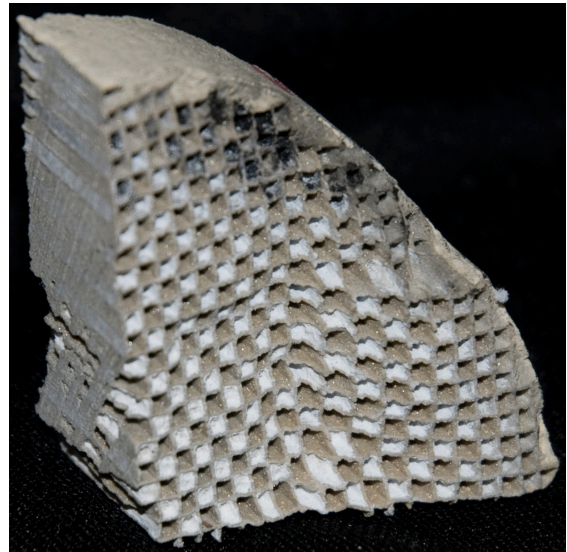


**Figure 4.62: Photograph of one-quarter sample from middle section of mullite substrate with high PGM loading**

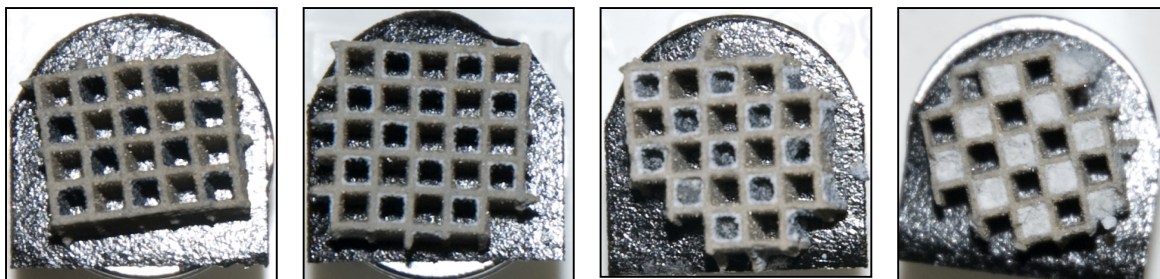


**Figure 4.63: Photographs of representative samples extracted from the front, front-middle, middle and rear sections of mullite substrate with high PGM loading**

regions observed in the other substrates. It is observed in Figure 4.63 that calcium and zinc once again provide the clearest representation of the ash. Thus, the remaining maps are again simplified to show only these metals and the backscatter image.

The elemental maps representing the front section of the DPF, presented in Figures 4.64 and 4.65, show an ash layer of moderate thickness and but is highly porous. This is consistent with the ash layer observed with the first mullite DPF shown in the previous section. When compared to the results from the cordierite substrate, the porosity of the ash layer is significantly higher. This is the primary reason for the minimal impact of ash accumulation on engine backpressure. The discontinuities in the ash layer are a combined result of the amorphous nature of the channel wall and the coarseness of the blade used during sample preparation. It is not possible to achieve a perfectly flat cross section with the tools available, but special care is taken to prepare samples as flat as possible without disturbing the ash layer. It is also likely that some of this ash layer broke away and deposited in the rear during the experiment.

The elemental maps for the middle section of the DPF, shown in Figures 4.66 and 4.67, exhibit an ash layer that is clearly thicker and denser than that observed in the front

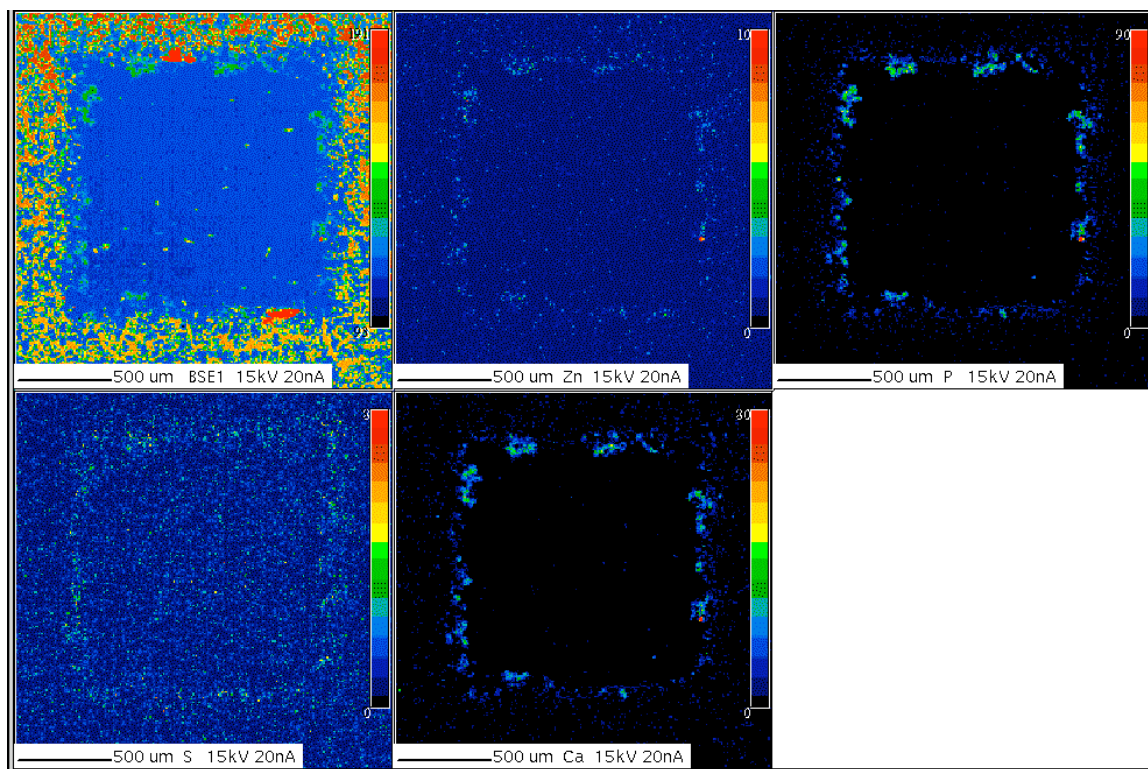


**Figure 4.64: Elemental maps of front section of mullite substrate with high PGM loading**

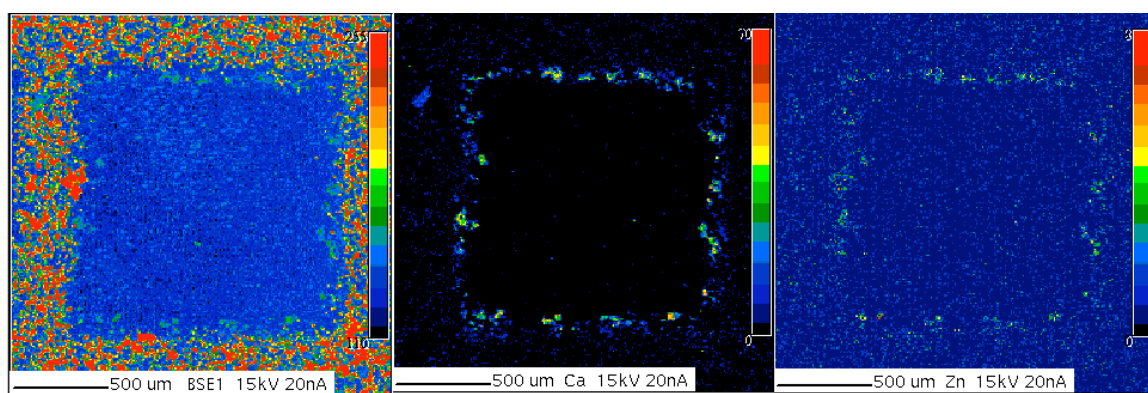


**Figure 4.65: Elemental maps of front section of mullite substrate with high PGM loading**



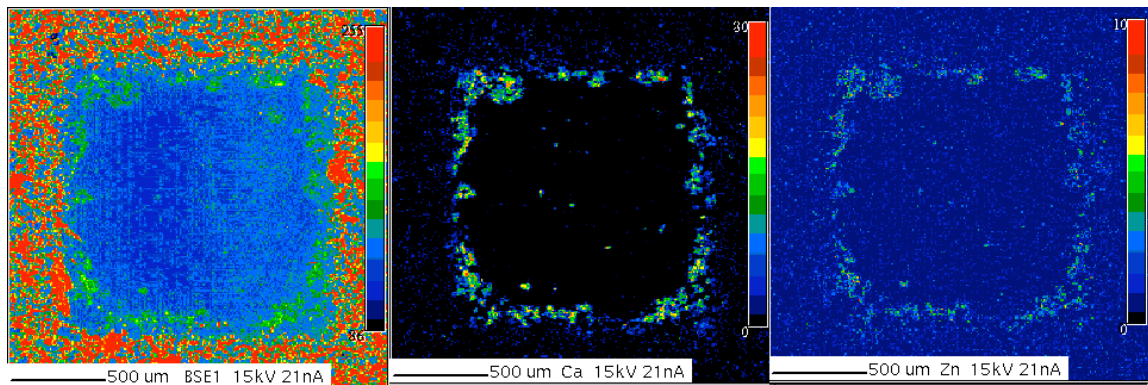


**Figure 4.66: Elemental maps of middle section of mullite substrate with high PGM loading**

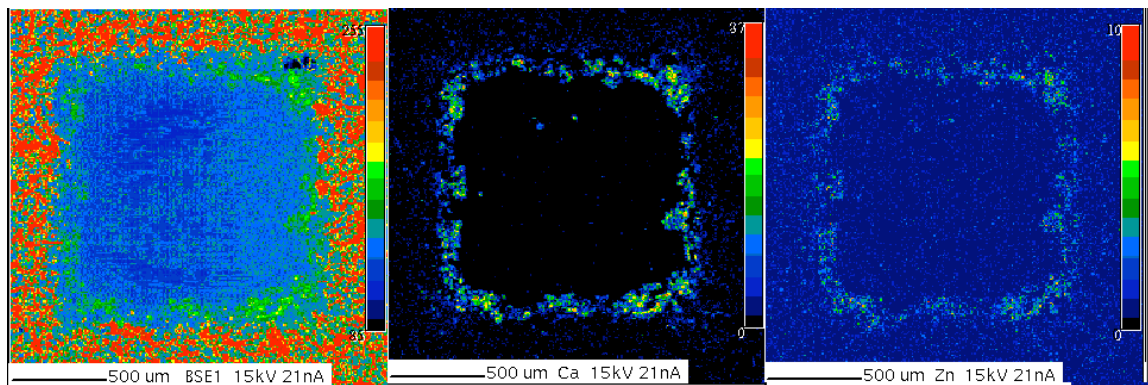


**Figure 4.67: Elemental maps of middle section of mullite substrate with high PGM loading**

section. This observation illustrates that sample preparation has minimal effect on the ash layer itself, and thus the discontinuities mentioned in the front section are likely natural occurrences that result from the amorphous channel wall and the ash layer breaking off during the experiment. EPMA elemental maps of the middle section show several small pieces of ash that have broken loose and shifted to the void section of the channel.

The elemental maps of the rear section of the DPF are presented in Figures 4.68 and 4.69 and show channels that are nearly plugged with ash. Unlike the rear channels of

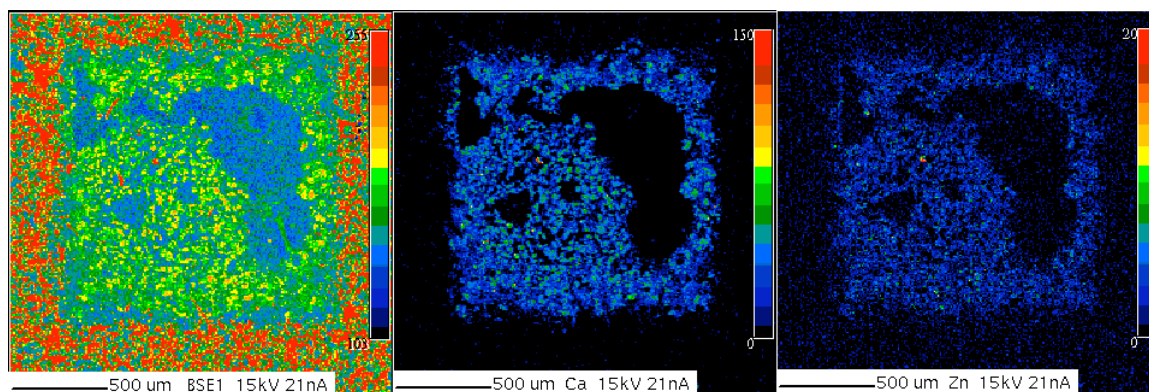


**Figure 4.68: Elemental maps of rear section of mullite substrate with high PGM loading**

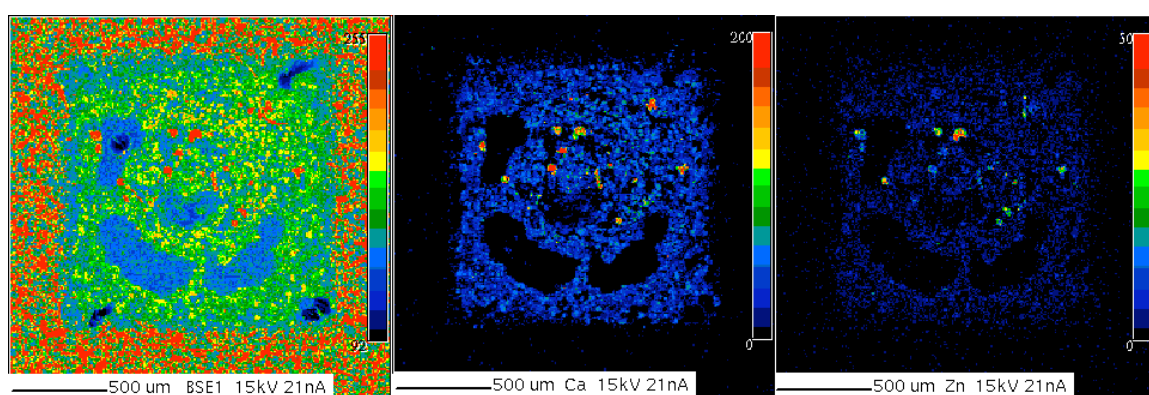


**Figure 4.69: Elemental maps of rear section of mullite substrate with high PGM loading**

the first mullite substrate analyzed, the ash layer in the rear channels is not as discernable around the perimeter of the channel wall. One possible explanation is the high PGM loading in the substrate that was observed to greatly increase the efficiency of continuous regeneration, minimizing soot deposition and subsequent flow restriction. Thus, the majority of the exhaust gas passes through the front and middle section of the DPF, and no ash layer is formed in the rearmost sections.

To further examine the ash distribution within the DPF and the ash-substrate interface under high magnification, scanning electron microscopy is again employed. Representative channels are selected for each section and displayed in Figures 4.70

through 4.72, with ash layer thicknesses observed to be very similar between channels within each respective section. Consistent with previous results, the ash layer is thinnest near the DPF inlet, as seen in Figures 4.70a and 4.70b. The ash layer increases in thickness along the length of the channel, though this increase is extreme, as shown in images from the middle section shown in Figures 4.71a and 4.71b. The absence of a visible ash layer in the rear channels matches the observations made following review of EPMA results. It can be seen in Figures 4.72a and 4.72b that the ash within the rear channels consists of a large variety of different size agglomerates. The larger agglomerates are portions of the ash layer that has formed upstream and broken loose. The size of these agglomerates on average is consistent with gaps observed in the ash layer of the front and middle sections, supporting the theory. This further supports the theory of upstream ash formation and subsequent break off and accumulation in the rear section.

Upon examination of a representative front section channel under increasing magnification, the ash layer is again observed to have formed around the acicular protrusions of the channel wall, as observed in Figures 4.73a through 4.73e. The morphology of the ash layer and ash itself is nearly identical to that observed in the front section of the first mullite substrate, demonstrating good agreement between the results of the two experiments. Upon examining a single acicular protrusion under extremely high magnification as in Figure 4.73e, a thin cracked coating is visible on the surface. Energy Dispersive X-ray Spectroscopy was used to identify this layer as the washcoat and catalyst layer containing platinum that was applied to the filter prior to the experiment being carried out. The manner in which the catalyst coating is applied to the



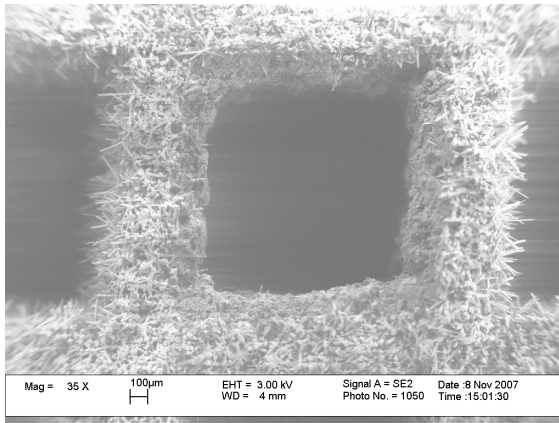


**Figure 4.70a: SEM image of front section channel (38X)**

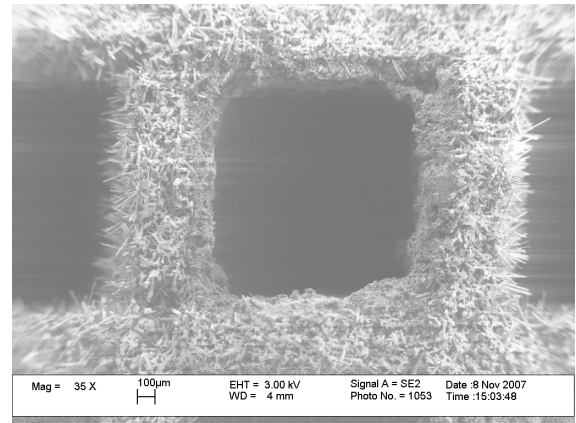


**Figure 4.70b: SEM image of front section channel (38X)**

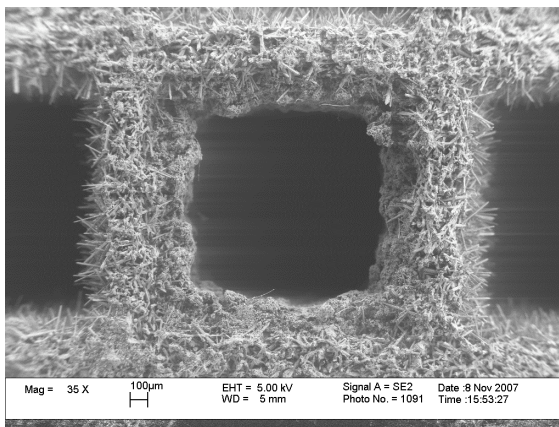


**Figure 4.71a: SEM image of middle section channel (38X)**

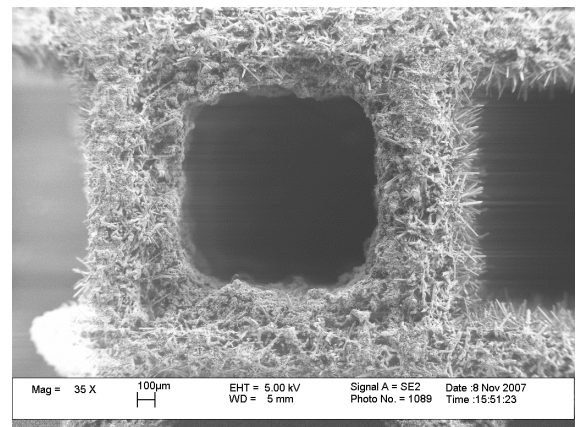


**Figure 4.71b: SEM image of middle section channel (38X)**

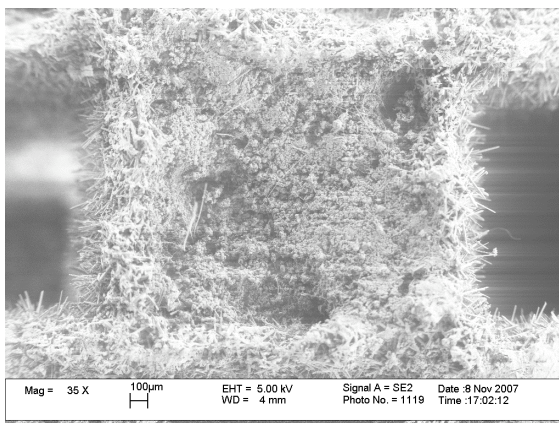


**Figure 4.72a: SEM image of rear section channel (38X)**

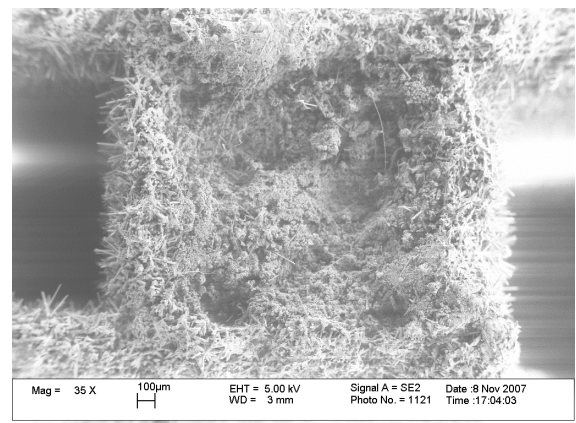


**Figure 4.72b: SEM image of rear section channel (38X)**

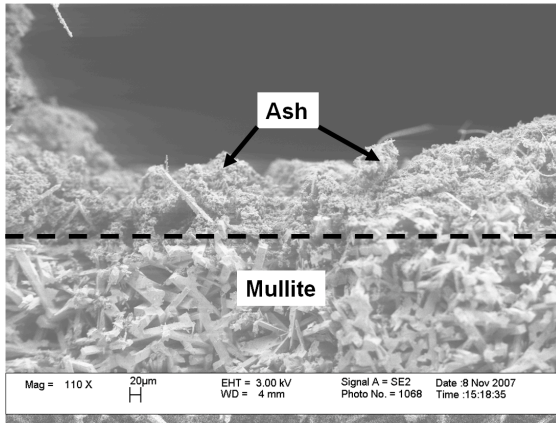


**Figure 4.73a: SEM image of front section channel (110X)**

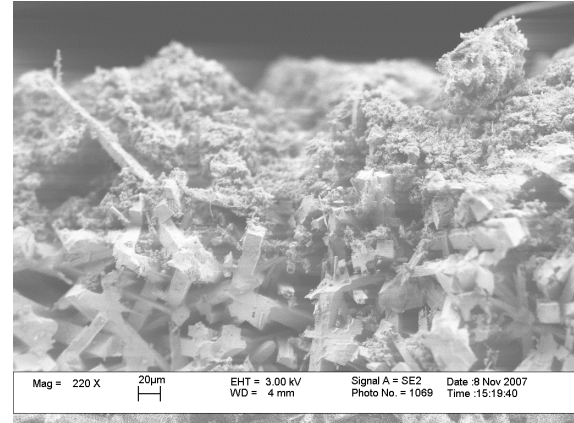


**Figure 4.73b: SEM image of front section channel (220X)**

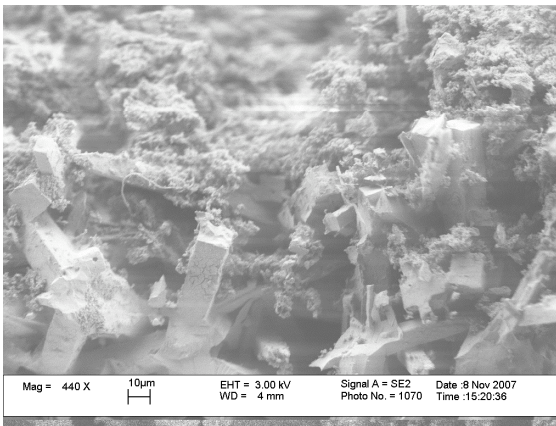


**Figure 4.73c: SEM image of front section channel (440X)**

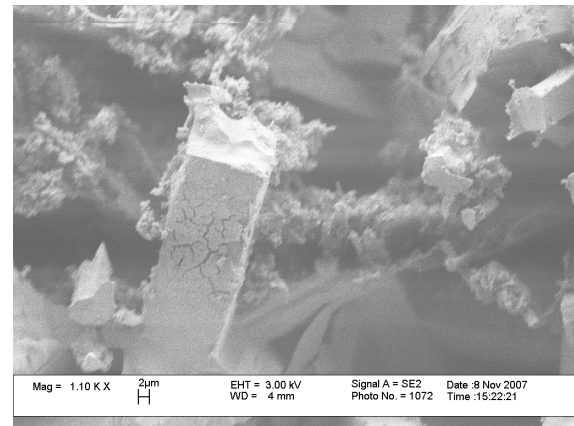


**Figure 4.73d: SEM image of front section channel (1100X)**

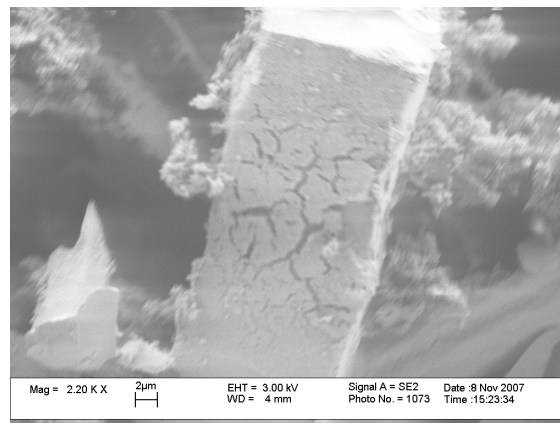


**Figure 4.73e: SEM image of front section channel (2200X)**



substrate has significant implications with regard to both backpressure increase and exposure to the exhaust gas stream. Since the layer of washcoat with catalyst is relatively thin with respect to the acicular segments themselves, there is an inherently minimal increase in baseline backpressure. Assuming the catalyzed washcoat covers a large percentage of the segments within the filter, this provides a far greater area over which the exhaust gas can flow, greatly increasing the efficiency of continuous soot oxidation. This increases loading times and has other implications with regard to the manner in which ash accumulates and distributes within the DPF. This advantage was clearly visible in the experimental data as the loading times were on average far longer than those observed in the non-catalyzed mullite DPF, and the total number of regenerations required was less than half.

Images of the ash layer in the rear section of the DPF are presented in Figures 4.74a through 4.74e. The ash layer along the channel wall reveals a less dense ash deposit, consistent with the absence of a macroscopic ash layer along the channel wall. The ash fragments themselves appear very porous under high magnification, and ash penetration into the channel wall was again observed to be minimal. Examination of a single acicular protrusion in the rear section did not clearly identify a large presence of catalyst material as was identified in the front section, raising questions about the distribution of the catalyst material within the filter. ICP analysis of a quarter section of the DPF indicates a fairly even distribution of the catalyst material over the length of the channels, thus increasing the efficiency of continuous regeneration throughout the filter. Results with regard to ICP oil and ash analysis will be addressed in Section 4.6.

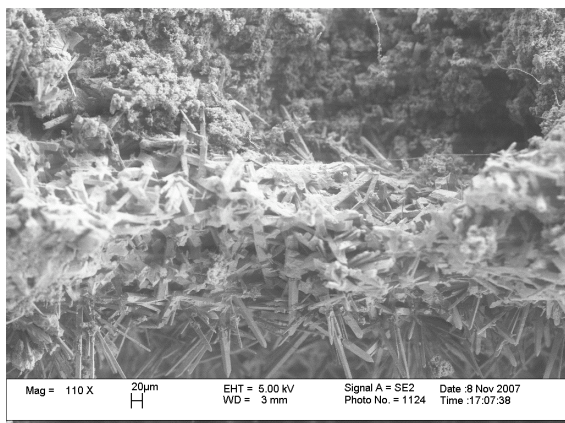


**Figure 4.74a: SEM image of rear section channel (110X)**

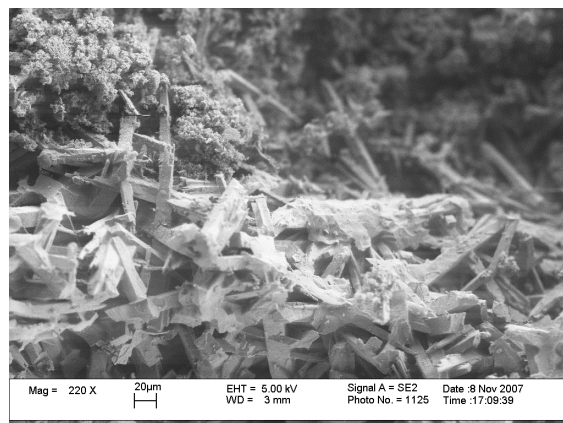


**Figure 4.74b: SEM image of rear section channel (220X)**

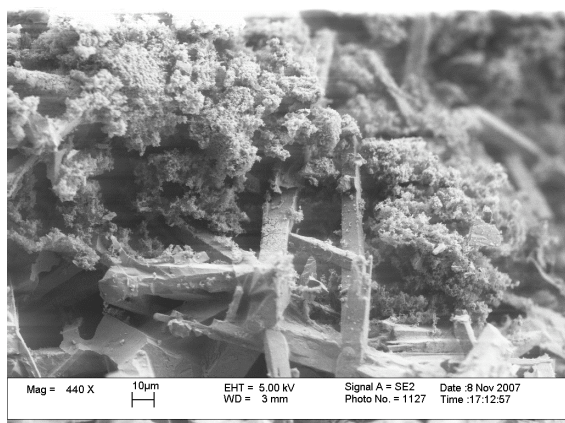


**Figure 4.74c: SEM image of rear section channel (440X)**

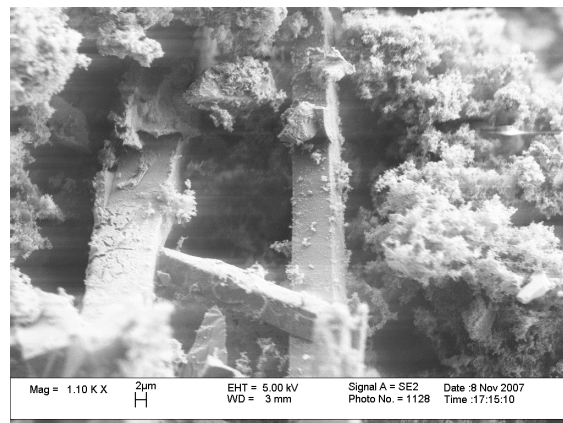


**Figure 4.74d: SEM image of rear section channel (1100X)**

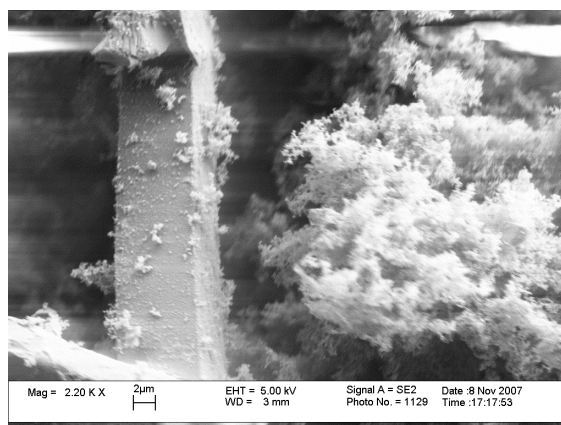


**Figure 4.74e: SEM image of rear section channel (2200X)**

Overall, the characterization results from the catalyzed mullite DPF provide valuable insight that is not readily available in literature. First, the ash is well distributed throughout the DPF, though the ash layer thickness still increases from front to rear. Investigation also provides further visual understanding of the manner with which the ash layer forms within the protrusions of the acicular channel wall, resulting in better distribution, increased porosity and greater structural integrity. The density of the ash particles themselves was observed to vary based on location along the channel and even within the cross section itself. The composition and distribution of the ash will be quantified in Section 4.6. The mullite has shown to possess a drastically different morphology from the other materials analyzed during this investigation. Though filtration efficiency was not quantified in this investigation, the manufacturer reports efficiencies as high as 99.9%. Thus, the acicular structure provides a highly porous substrate, excellent structural integrity, increased surface area for catalyst material in addition to highly efficient filtration performance. More investigations are required to verify the performance of mullite in a variety of applications and environments. For this experiment, mullite exhibits excellent performance attributes, and characterization yielded interesting results regarding the principles by which mullite achieves these superior advantages.

## **4.5 Silicon Carbide Substrate With No PGM Loading**

### ***4.5.1 SiC Substrate With No PGM Loading – Experimental Results***

This experiment is the fourth carried out overall. By this stage in the investigation, the protocol has been developed and is applied without variation.

However, it was discovered halfway through the experiment that the upstream DOC had melted and warped, possibly the result of post injection problems. The damage to the upstream DOC resulted in higher backpressures and decreased production of NO<sub>2</sub> for continuous regeneration. The higher backpressure increases the rate of soot production, which in turn raises DPF temperatures during both loading and regeneration cycles. Upon discovery of the problem, the DOC was replaced and the experiment was continued. The effects of the damaged DOC and subsequent replacement are clearly visible in all of the experimental data. The most pronounced changes are observed in the DPF solid temperature plots, shown in Figure 4.75. The temperature profiles indicate good repeatability, with the small variations attributed to inconsistent soot loading as a result of damage to the DOC. Following the replacement of the DOC, the temperature data is observed to shift down approximately 100°C over the course of two cycles. It is also observed that loading times increase, indicating a decrease in backpressure and subsequent soot production, as well as an increase in continuous regeneration efficiency. Heretoforth, the data is said to have two regions of showing good repeatability and providing useful information.

The existence of two distinct experimental regions is also observed in the exhaust gas temperature data displayed in Figure 4.76. Again, good repeatability is observed within the respecting regions, with variations in the earlier region attributed to higher backpressure and inconsistent soot loading. It is interesting to observe the effect of backpressure and continuous regeneration efficiency on the overall system temperature profile. Lower backpressures result in slightly lower engine out exhaust temperature, less soot being produced and a more effective continuous regeneration of that soot. In the

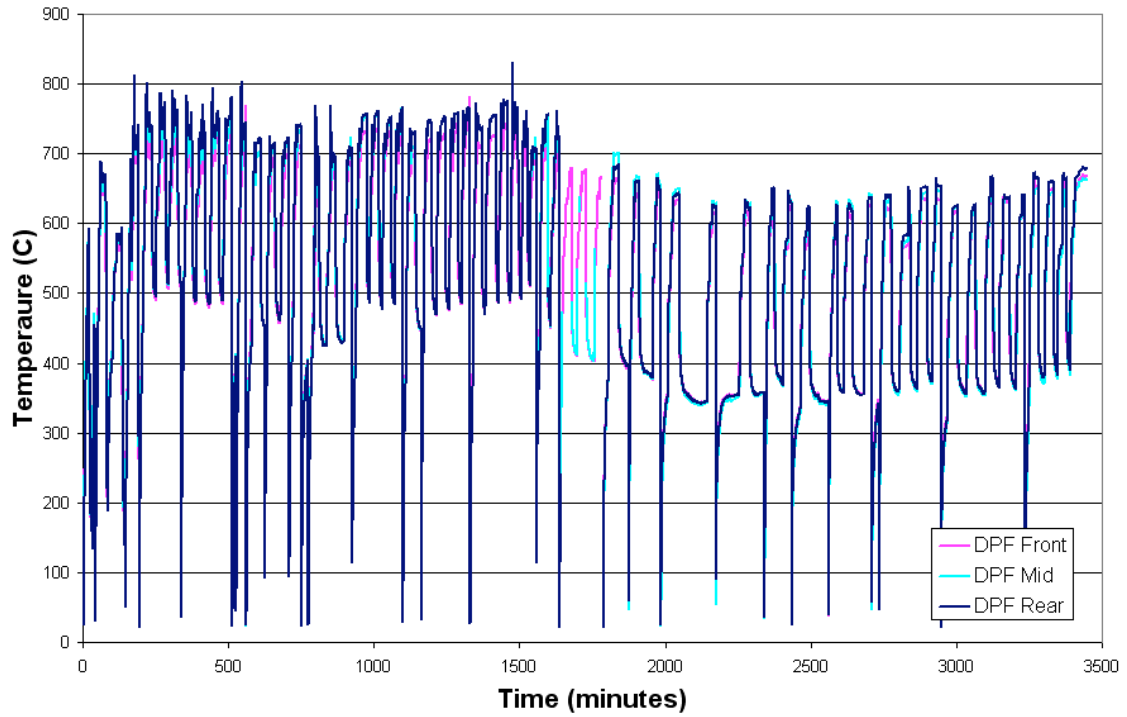


**Figure 4.75: DPF solid temperatures versus time for non-catalyzed SiC substrate**

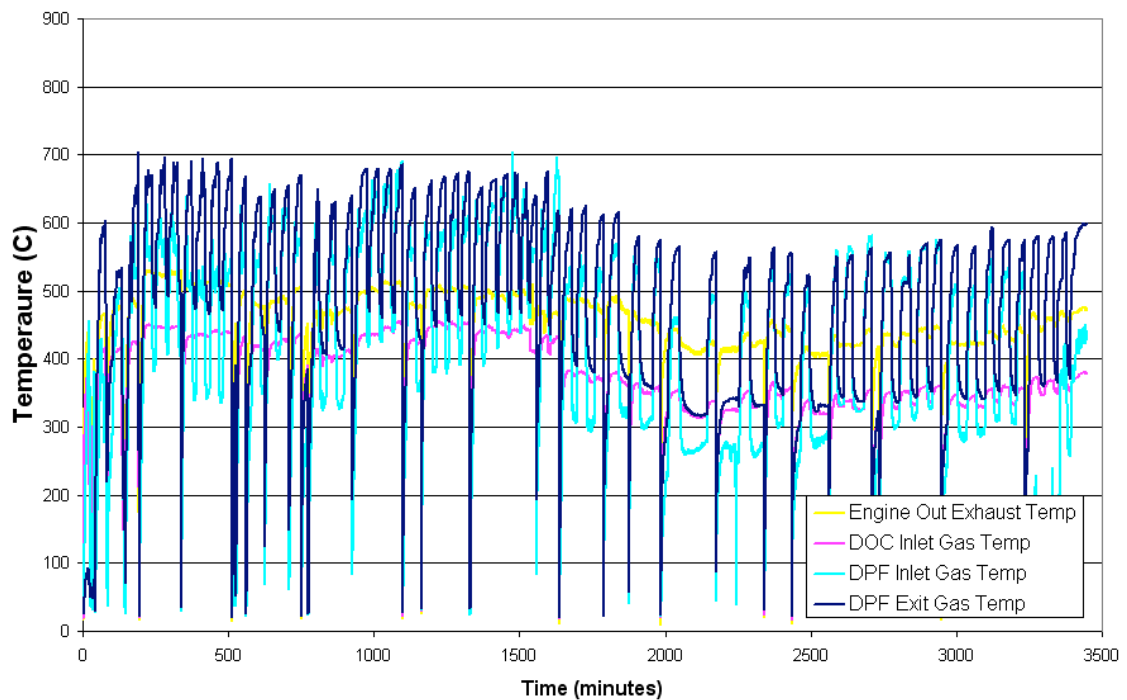


**Figure 4.76: Exhaust gas temperatures at various locations versus time for non-catalyzed SiC substrate**

latter region, the temperature trend is observed to increase slightly over the remainder of the experiment, further confirming the effect of backpressure on system temperatures.

The exhaust backpressure profile, shown in Figure 4.77, provides a visual understanding of the impact that problems with the DOC had on system performance. It is believed that the DOC was either faulty or damaged early on in the experiment, possibly the result of problems with the supplemental fuel injection system. It is possible that the damage worsened until finally the DOC experienced a catastrophic failure, at which point the problem was identified and rectified. Since the DOC used in the latter stage of the experiment was cut from the same monolith as the first, it can be inferred from the pressure drop between regions that the problem with the DOC developed early in the experiment. Since the data showed good repeatability, there was no indication of a problem until the catastrophic failure and subsequent spike in backpressure. Despite the problems with the DOC, the backpressure is observed to slightly increase over time in both regions with approximately equal slopes. This will be discussed in more detail in Section 4.6.

For ease of viewing and understanding, the DPF mass data is divided into the two regions and plotted independently in Figures 4.78 and 4.79. The former shows a trend in which the loaded and clean masses appear to converge, the result DOC warping and subsequent associated increases in backpressure that decrease the apparent loading cycle length. The latter plot shows a trend in which the masses diverge slightly, though the trend is based on only a few data points.. In both cases, the clean DPF masses show great linearity, confirming the efficiency of the regeneration strategy and further indicating the problem with engine backpressure and consistent soot loading. Nominally, the loaded

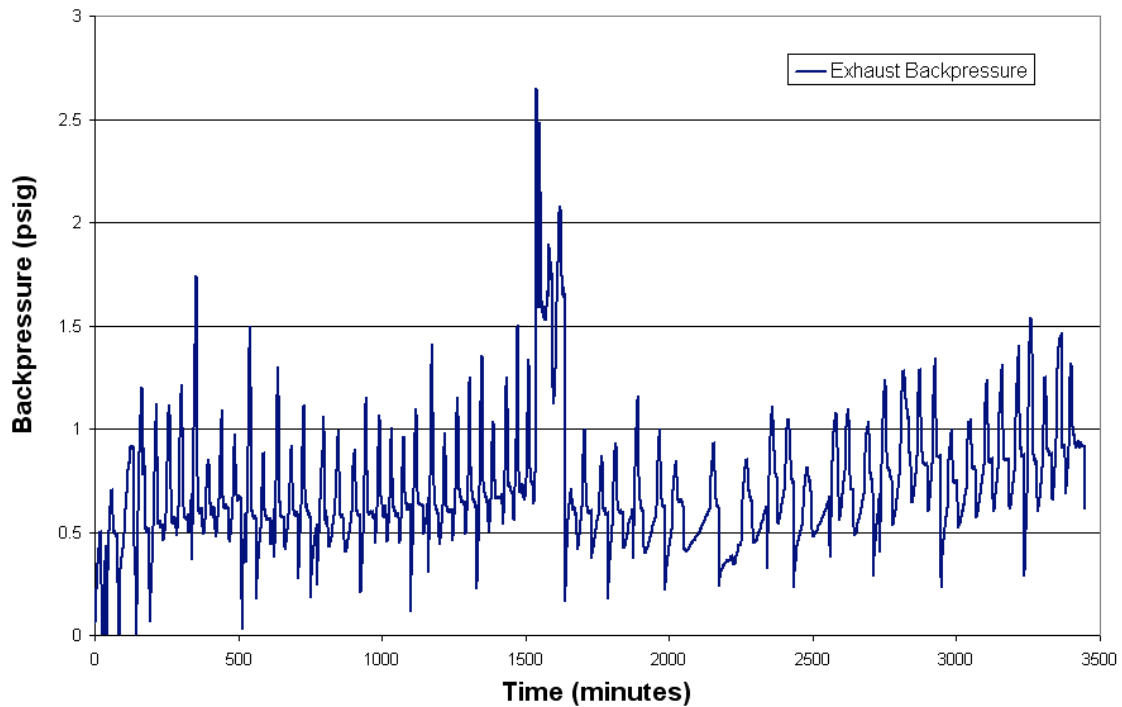


**Figure 4.77: Exhaust backpressure versus time for non-catalyzed SiC substrate**

and clean trends would be parallel, as seen in both Sections 4.2 (cordierite high PGM) and 4.4 (mullite high PGM).

In summary, despite problems experienced with the upstream DOC, the protocol provided very repeatable results in both regions of operation. While the circumstances under which this experiment was completed were not ideal, the results demonstrate the flexibility of the protocol with regard to different operating conditions, even during the same experiment. While neither the loading protocol or regeneration strategy were varied to capitalize on the advantages of SiC, the data clearly shows that the protocol provides a consistent rate of ash formation within the filter while maintaining filter backpressures and temperatures within the designated operating windows.

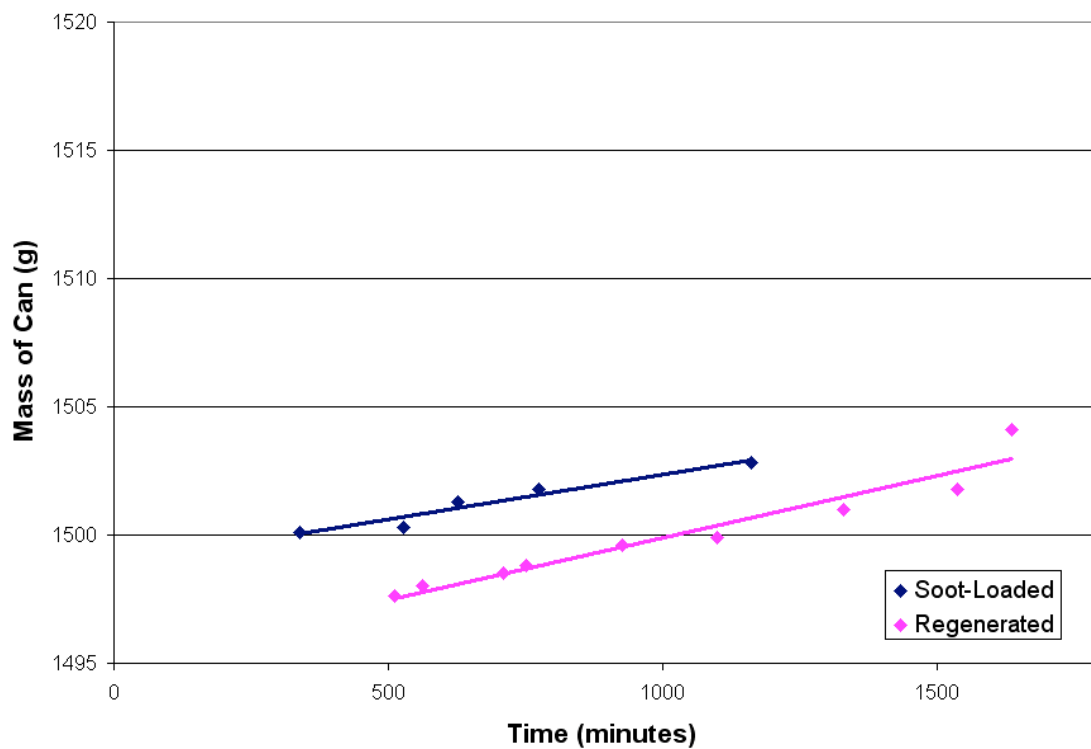


**Figure 4.78: DPF mass data versus time for non-catalyzed SiC substrate**

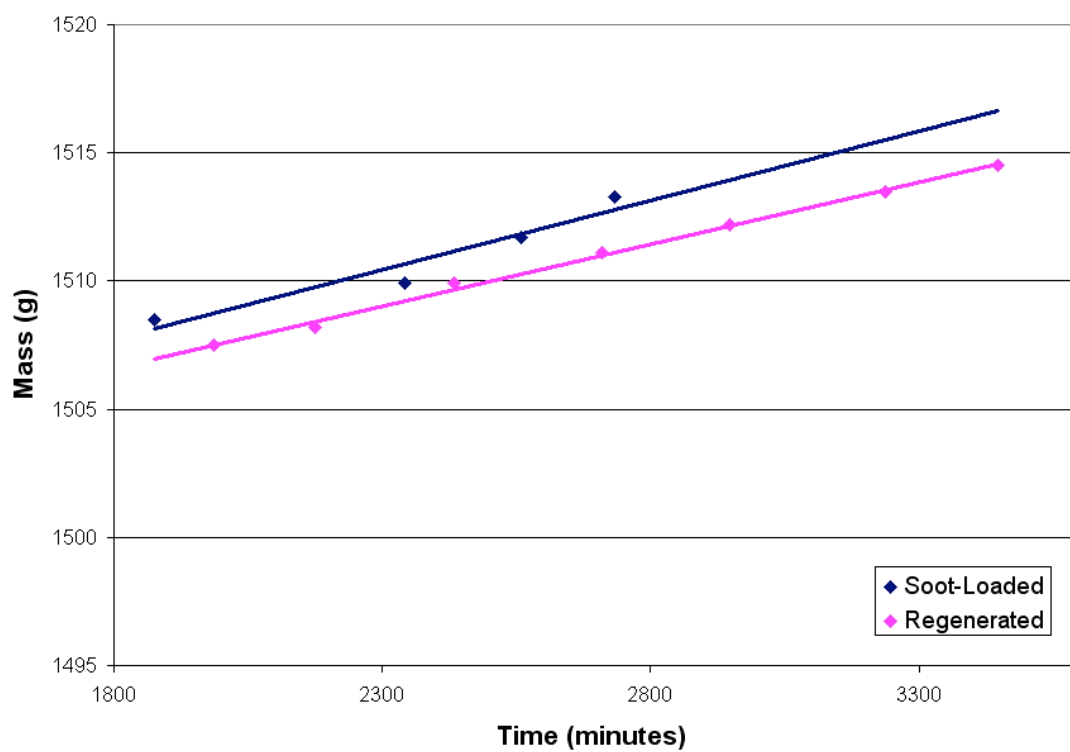


**Figure 4.79: DPF mass data versus time for non-catalyzed SiC substrate**



#### ***4.5.2 SiC Substrate With No PGM Loading) - Characterization Results***

Upon completion of the engine experiment, the DPF is divided into quarter sections for characterization using EPMA, SEM and ICP analysis. Photographs taken of cross-sections from the front and middle sections are presented in Figure 4.80 and Figure 4.81, respectively. A radial variation in ash distribution is clearly visible and more pronounced than the variations observed in the other substrates evaluated in this investigation. This trend was observed to some extent in all experiments, and it is believed that exhaust system geometry is responsible at least in part for this ash distribution. The ash in the channels that are completely plugged was observed to be very loosely packed, presenting difficulty in SEM sample preparation.

Photographs of the samples analyzed using SEM, shown in Figure 4.82, again depicts an ash layer that drastically increases in thickness. Approximately one half of the channels in the middle section are observed to be completely plugged up with ash, whereas nearly all channels in the rear section are completely plugged.

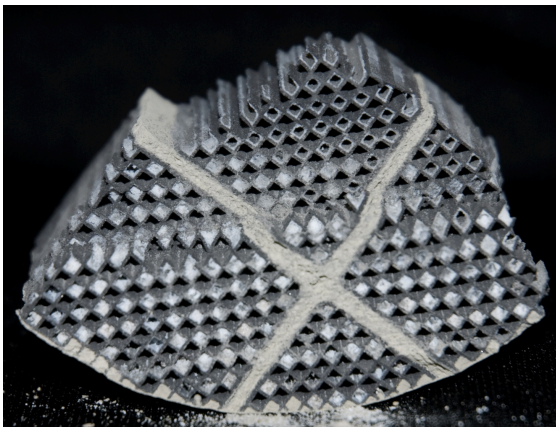


**Figure 4.80: Photograph of one-quarter sample from front section of non-catalyzed SiC substrate**

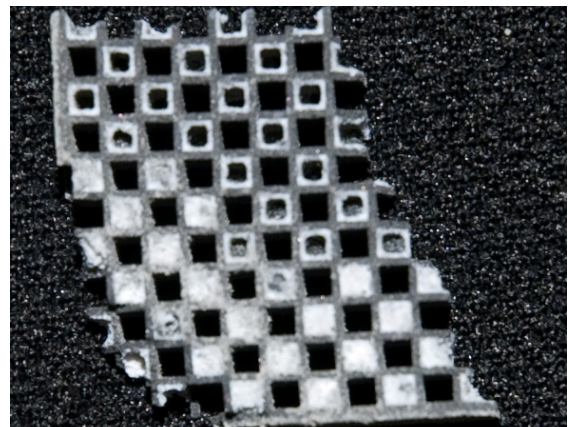


**Figure 4.81: Photograph of small cross-section from middle section of non-catalyzed SiC substrate**

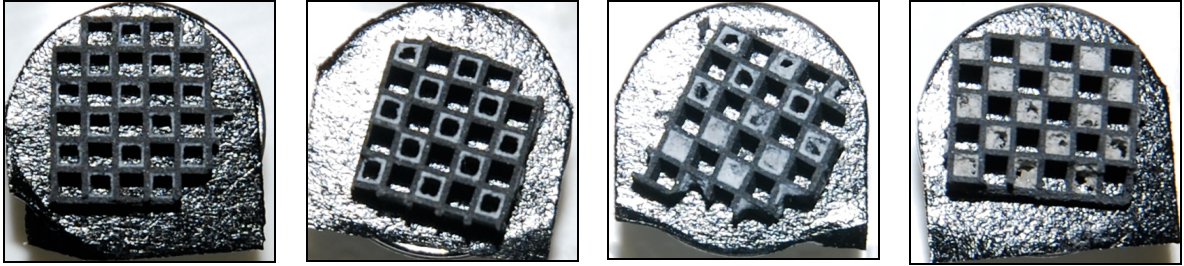


**Figure 4.82: Photographs of representative samples extracted from the front, front-middle, middle and rear sections of non-catalyzed SiC substrate**

EPMA is used to characterize the ash layer distribution by observing the relative concentrations of calcium, zinc, phosphorus and sulfur in a large number of cells from throughout the filter. The maps presented here represent the front, middle and rear sections of the DPF in a manner similar to that presented in previous section. Upon examining the first elemental map for the front section, shown in Figure 4.83, it is again observed that the relative concentration of phosphorus is approximately equal to that of calcium, and sulfur approximately equal to zinc. Once again, for the sake of simplicity, the remaining elemental maps show only the backscatter image, calcium and zinc.

The elemental maps for the front section of the DPF are presented in Figures 4.83 and 4.84, and show a relatively thin and porous ash layer formed on the walls of the channel. The ash layer is fairly dense and in most cases covers the entire inside perimeter of the cell. This has significant implications with regard to the backpressure increase as a function of ash loading, though this impact is not quantified in this investigation. The morphology of the SiC channel wall has a fairly rough texture, though not like that of mullite, and thus the ash layer does not integrate with the wall but rather forms a porous layer on top, with ash observed to break away and deposit in the rear of the DPF.

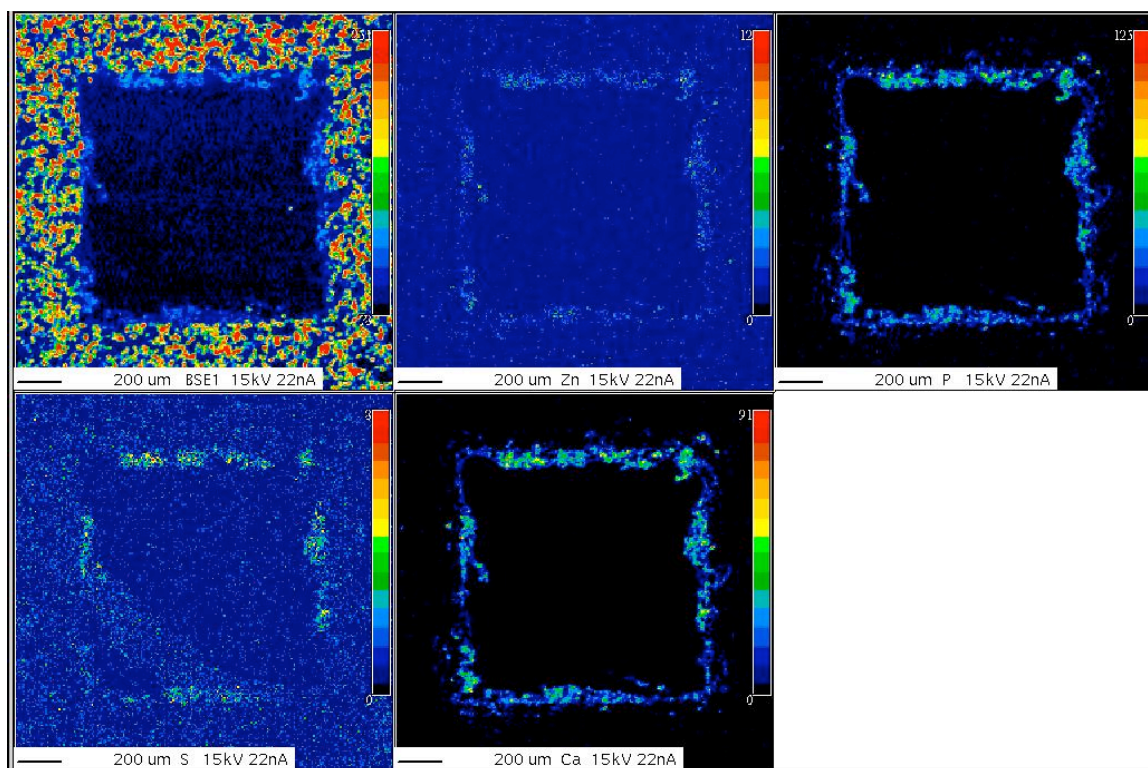


**Figure 4.83: Elemental maps of front section of non-catalyzed SiC substrate**

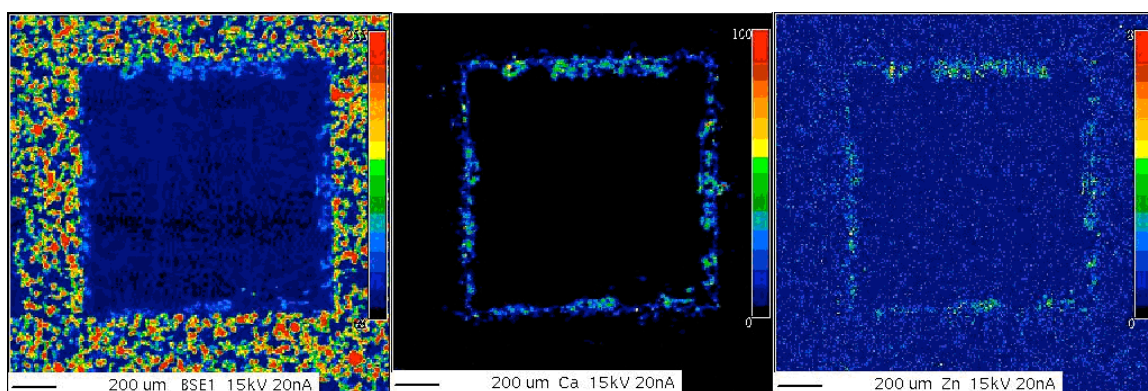


**Figure 4.84: Elemental maps of front section of non-catalyzed SiC substrate**



The elemental maps for the middle section of the DPF, shown in Figures 4.85 and 4.86, depict an ash layer that is clearly thicker than that observed in the front section.

The shape of the ash layer in the middle section was varied from channel to channel, with the only consistency being in the average thickness of the layer. These variations in ash distribution over the cross section are likely again the result of exhaust system geometry, and the layer itself being loosely packed and susceptible to breakage due to vibration.

The elemental maps of the rear section of the DPF, displayed in Figures 4.87 and 4.88, show channels that plugged with large ash agglomerates that are very loosely packed. This ash morphology presents problems during sample preparation since the ash will inherently drift once the sample is embedded in epoxy. Despite this disturbance, the

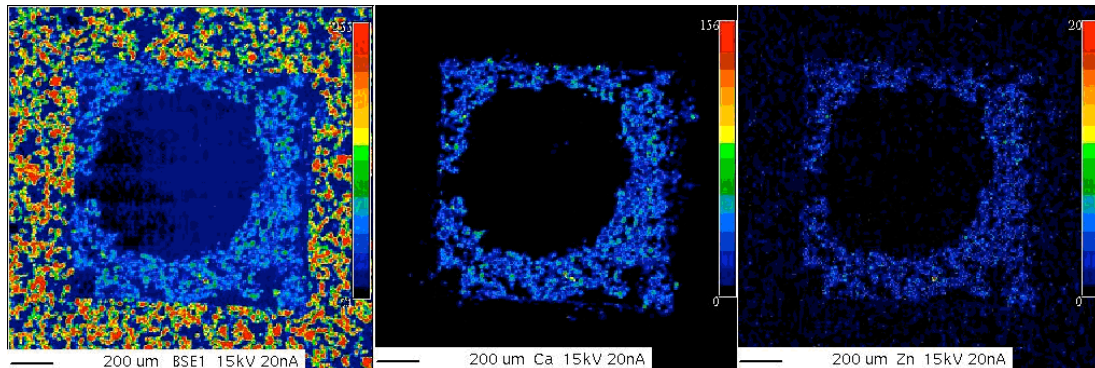


**Figure 4.85: Elemental maps of middle section of non-catalyzed SiC substrate**

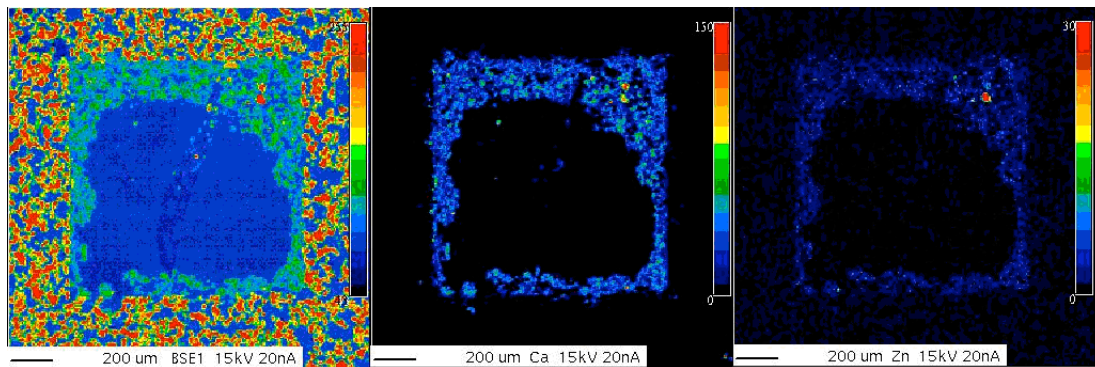


**Figure 4.86: Elemental maps of middle section of non-catalyzed SiC substrate**

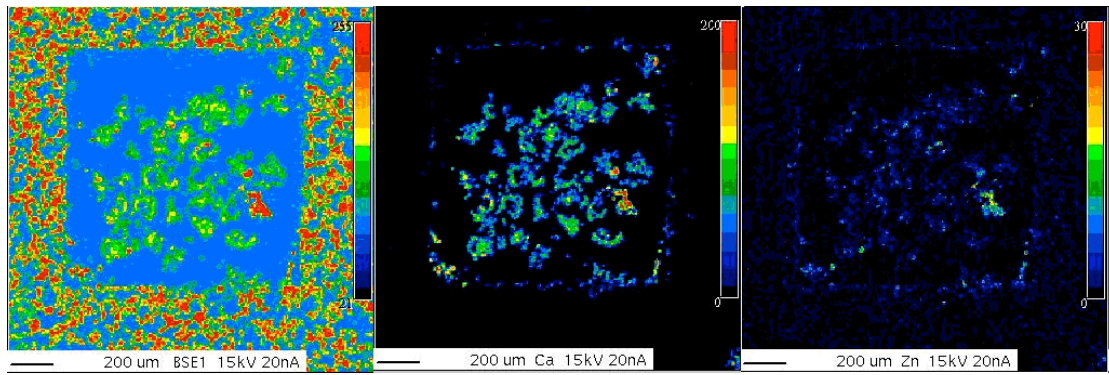


**Figure 4.87: Elemental maps of rear section of non-catalyzed SiC substrate**

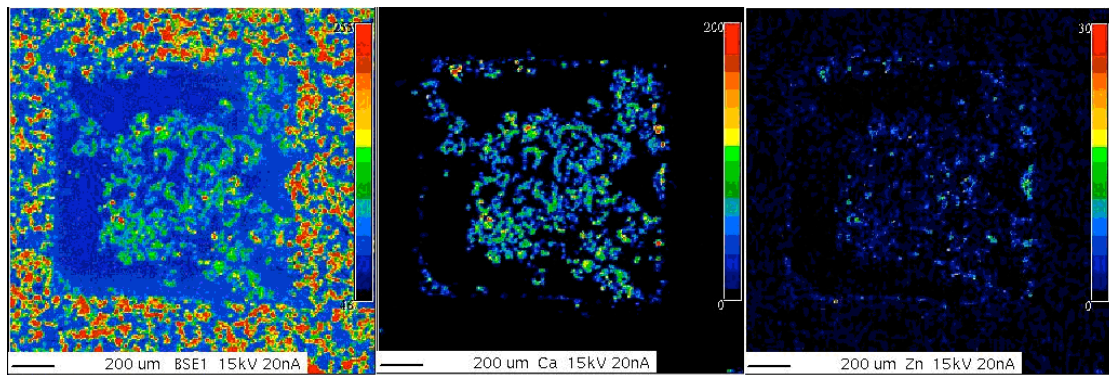


**Figure 4.88: Elemental maps of rear section of non-catalyzed SiC substrate**

general morphology of the ash layer can still be observed. In addition, the presence of a thin ash layer along the channel wall is visibly present. This layer likely formed in the early part of the engine experiment before ash started to break loose from the upstream sections and deposit in the rear.

The relatively high porosity of the ash in the rear section has significant implications with regard to ash distribution within the filter, specifically, along the length of the channels. This distribution and its effect on engine backpressure will be quantified in Section 4.6.

SEM is used to gain a more detailed understanding of the ash layer morphology and distribution along the length of the channel. Representative channels are selected for

the front, middle and rear sections and displayed in Figures 4.89 through 4.91.

Consistent with EPMA results the ash layer is thinnest in the front section and increases in thickness along the length of the channels. As noted earlier in this section, approximately one half of the middle channels were plugged with ash. This ash material did not remain intact during sample preparation, and thus only the ash layer that formed along the channel wall is visible. Another observation worth noting is that while there was a thin ash layer visible in the elemental maps of the rear section, there is no distinct ash layer visible in the SEM images of rear channels. Once again, it is believed that the addition of the epoxy used for EPMA sample preparation caused the ash in the rear sections to shift within the channel. The distribution of ash along the length of the channel will be quantified using ICP analysis, with results presented in Section 4.6. It is not believed that sample preparation ICP will have a significant adverse effect on ash distribution.

The ash layer present in the front and rear sections is now examined under greater magnification, with focus placed on the region in which ash comes into contact with the substrate. Representative channels are again selected from the front and rear sections for observation under increasing magnification. Further analysis of the ash layer in the front section reveals minimal ash penetration into the channel wall, as seen in Figures 4.92a through 4.92e. Observation of the substrate itself reveals the third distinct substrate morphology seen in this investigation. The size of the pores on the surface of the channel wall is observed to be nearly the same as the average size of the ash particles present, and greater magnification is necessary to clearly define the interface between the ash layer and the channel wall. The morphology of the ash itself is similar to that observed in the



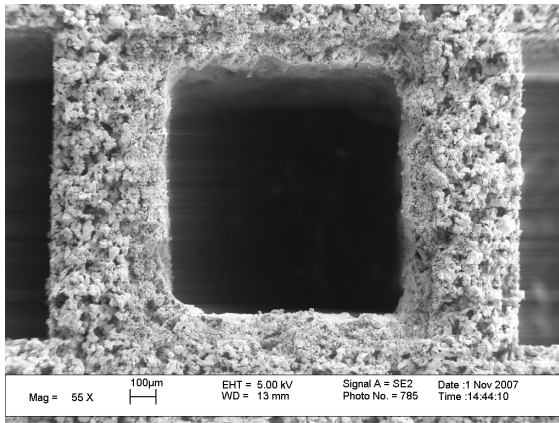


**Figure 4.89a: SEM image of front section channel (38X)**

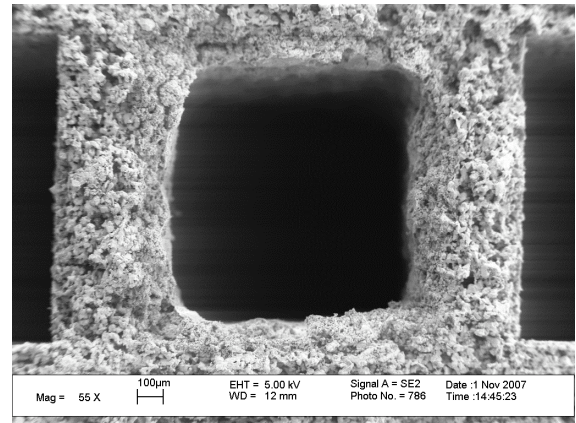


**Figure 4.89b: SEM image of front section channel (38X)**

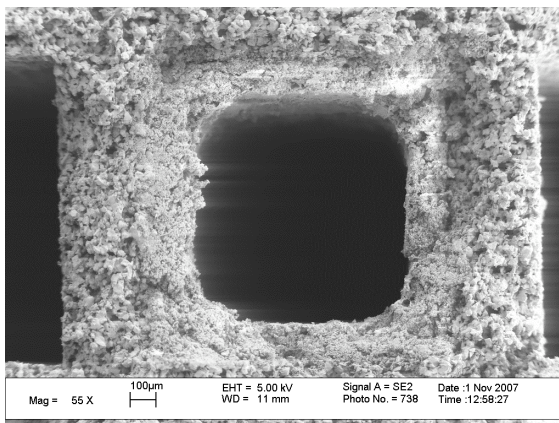


**Figure 4.90a: SEM image of middle section channel (38X)**

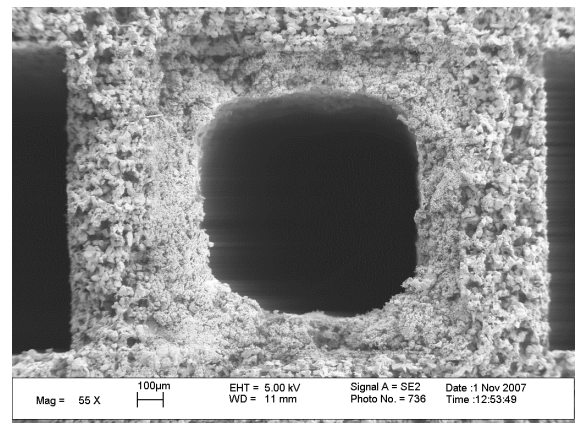


**Figure 4.90b: SEM image of middle section channel (38X)**

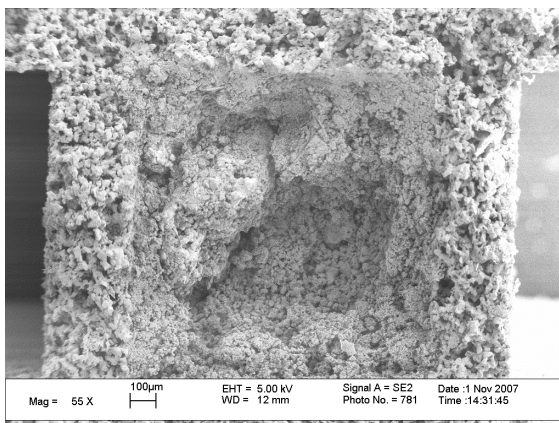


**Figure 4.91a: SEM image of rear section channel (38X)**

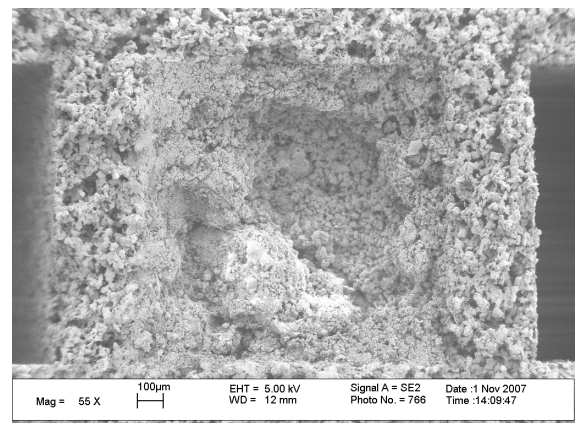


**Figure 4.91b: SEM image of rear section channel (38X)**

previous substrates, affirming that the protocol provides consistent operating conditions.

Images of the ash present in the rear section of the DPF, shown in Figures 4.93a through 4.93e, provide a more informative visual understanding of the physical interaction between the channel wall and the ash layer. The ash particles observed in the rear section are slightly smaller than the pores seen on the surface of the channel wall, which allows some shallow penetration of ash into the wall. This has implications with regard to both filtration efficiency and backpressure increase. While filtration efficiency is not quantified in this investigation, trends in backpressure increase as a function of ash accumulation will be addressed in Section 4.6.

While the morphology and distribution of ash within the DPF is not identical to that observed in either the mullite or cordierite substrates, the trends observed are consistent with expectations in general. Namely, the ash layer is observed to again increase in thickness between the front and rear sections, with the rear channels completely filled with ash. Results again show that calcium and phosphorus are the most prevalent of the elements selected for analysis using EPMA elemental maps, which has been consistent through all of the experiments. There is a thin ash layer observed in the rear section of the DPF, though this layer is not discernable in the SEM images. The morphology of the ash in the rear section supports the theory that the majority of the ash had formed upstream in the channel before breaking loose and depositing in the rear. Overall, results indicate that the protocol that was developed and implemented for this experiment produces excellent results in both the experiment itself and the subsequent characterization of the DPF.



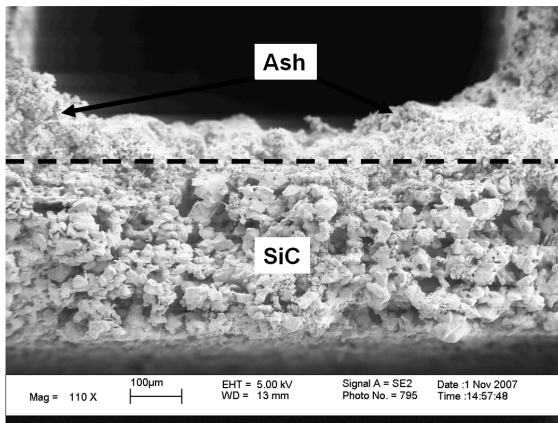


**Figure 4.92a: SEM image of front section channel (110X)**

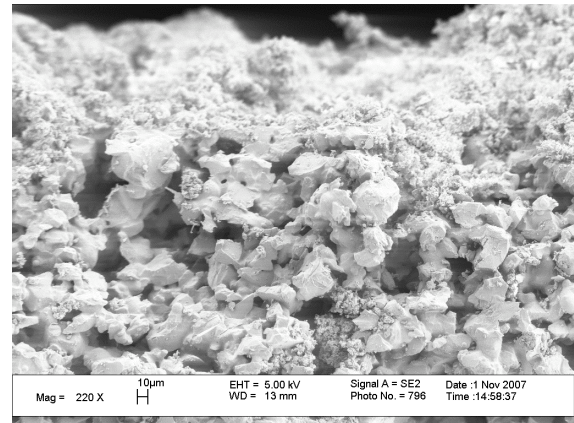


**Figure 4.92b: SEM image of front section channel (220X)**

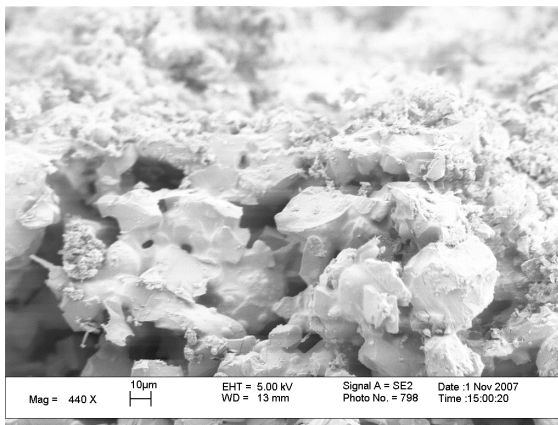


**Figure 4.92c: SEM image of front section channel (440X)**

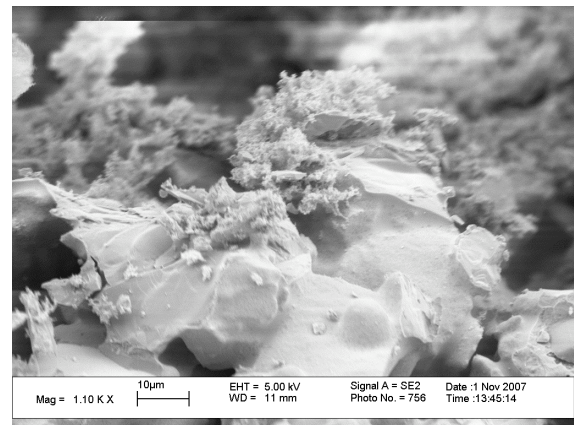


**Figure 4.92d: SEM image of front section channel (1100X)**

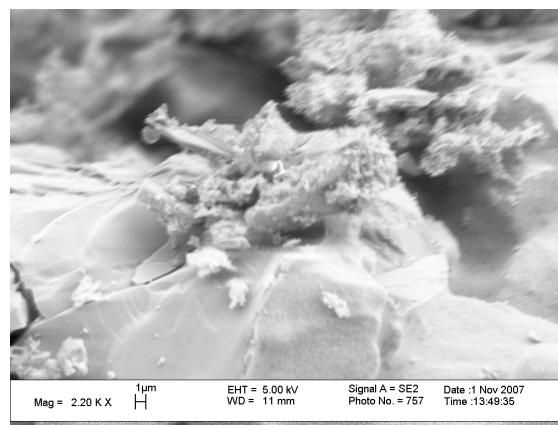


**Figure 4.92e: SEM image of front section channel (2200X)**

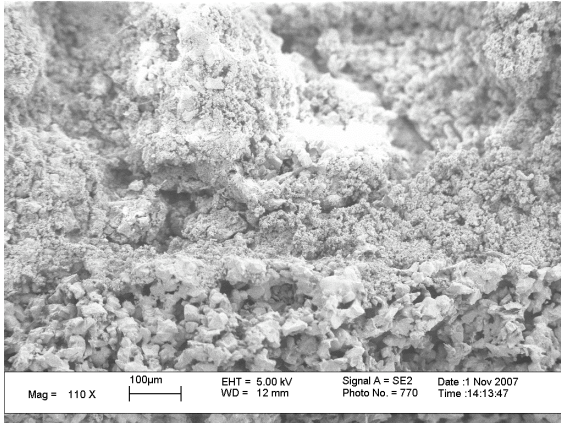


**Figure 4.93a: SEM image of rear section channel (110X)**

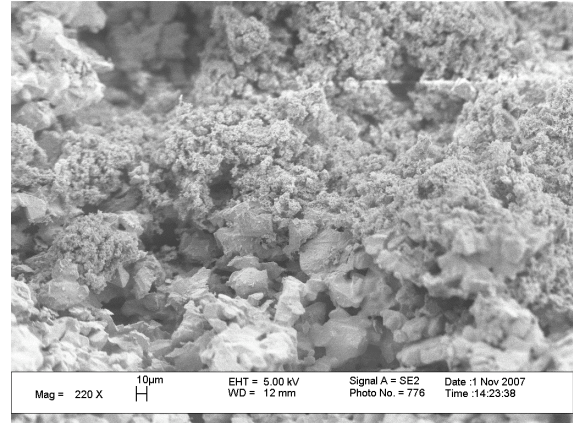


**Figure 4.93b: SEM image of rear section channel (220X)**

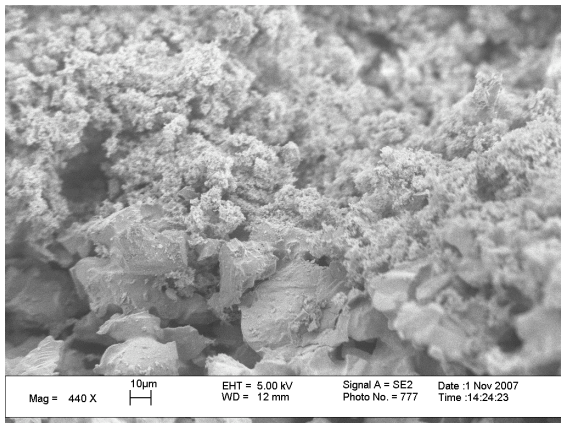


**Figure 4.93c: SEM image of rear section channel (440X)**

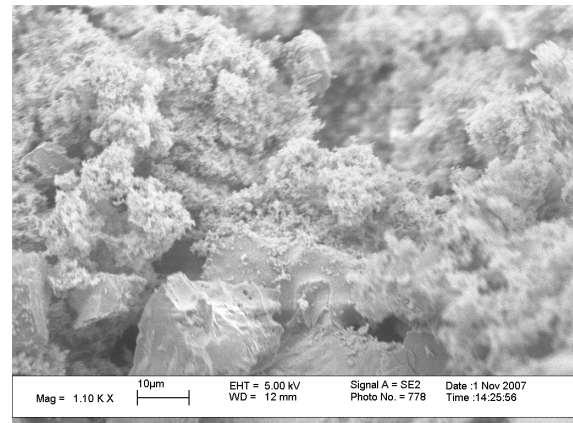


**Figure 4.93d: SEM image of rear section channel (1100X)**

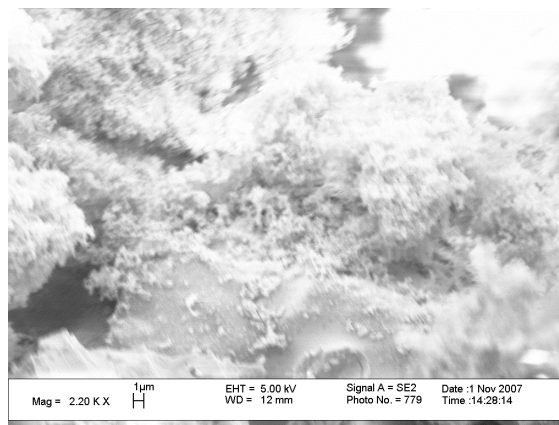


**Figure 4.93e: SEM image of rear section channel (2200X)**

## **4.6 Overall Performance Evaluation and Comparisons**

### ***4.6.1 Effects of ash accumulation on system performance***

The purpose of this investigation was not specifically to compare the performance characteristics of different substrates and catalyst loadings. However, there is an inherent requirement to possess a broad understanding of the types of conditions that may be experienced by the system so that the protocol developed can be successfully applied and produce repeatable results over a broad range of operating conditions.

Engine backpressure was recognized as the parameter of primary interest in the development of a protocol that is predicated on the accumulation and regeneration of a consistent amount of soot. While a real-time method of monitoring the mass of soot accumulated within the DPF is not feasible for the relatively small masses desired, it has been shown in the previous sections that soot-loading amounts can be estimated by evaluated changes in exhaust backpressure. The effect of ash accumulation on backpressure is clearly visible in the backpressure plots for each substrate, while the magnitude of each effect varies between substrates. Figure 4.94 shows the effect of ash accumulation on the baseline backpressure for each of the substrates discussed in Sections 4.1 through 4.5.

The most obvious point of interest is the trend line for Test 2 that has a negative slope, indicating a decrease in backpressure as ash accumulates in the DPF. Prior to this particular test, an effective regeneration strategy had not been developed, so it is likely that many of the regenerations performed in the first half of the test were not complete. Thus, both ash and the remaining soot produce the increase in backpressure observed in the data. It is also noted that the aforementioned catastrophic failure of the DOC during

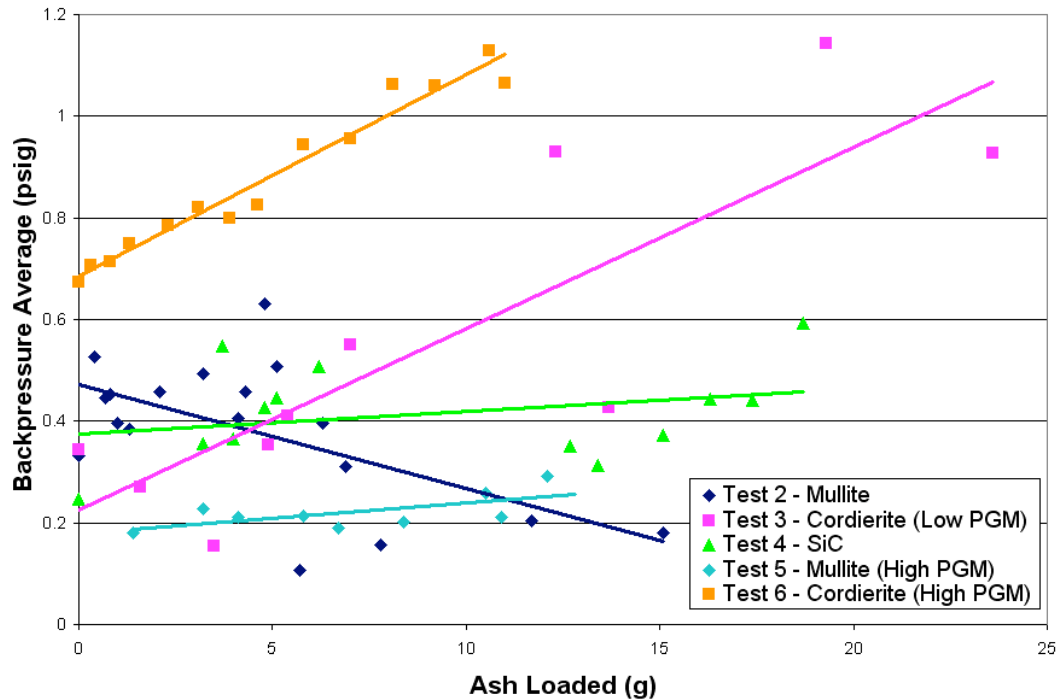


**Figure 4.94: Baseline backpressure averages versus ash accumulation**

Test 4 was discovered by observing a drastic increase in system backpressure. In order to extract useful information regarding backpressure trends, skewed data must be eliminated and the remaining data plotted in two groups representing periods both before and after the DOC replacement. Figure 4.95 is presented as a modification of Figure 4.93, with data from Test 2 removed and the data from Test 4 plotted in two groups. This modification enhances the interpretability of the data, demonstrating the variations in system performance for which the protocol must be able to compensate.

First, it is noted that the initial backpressure for the highly-catalyzed cordierite substrate DPF is dramatically higher than that of the lightly-catalyzed cordierite substrate. It is understood that both the amount of catalyst/washcoat material and the manner in which it is applied will determine the overall effect on backpressure. It is also noted that



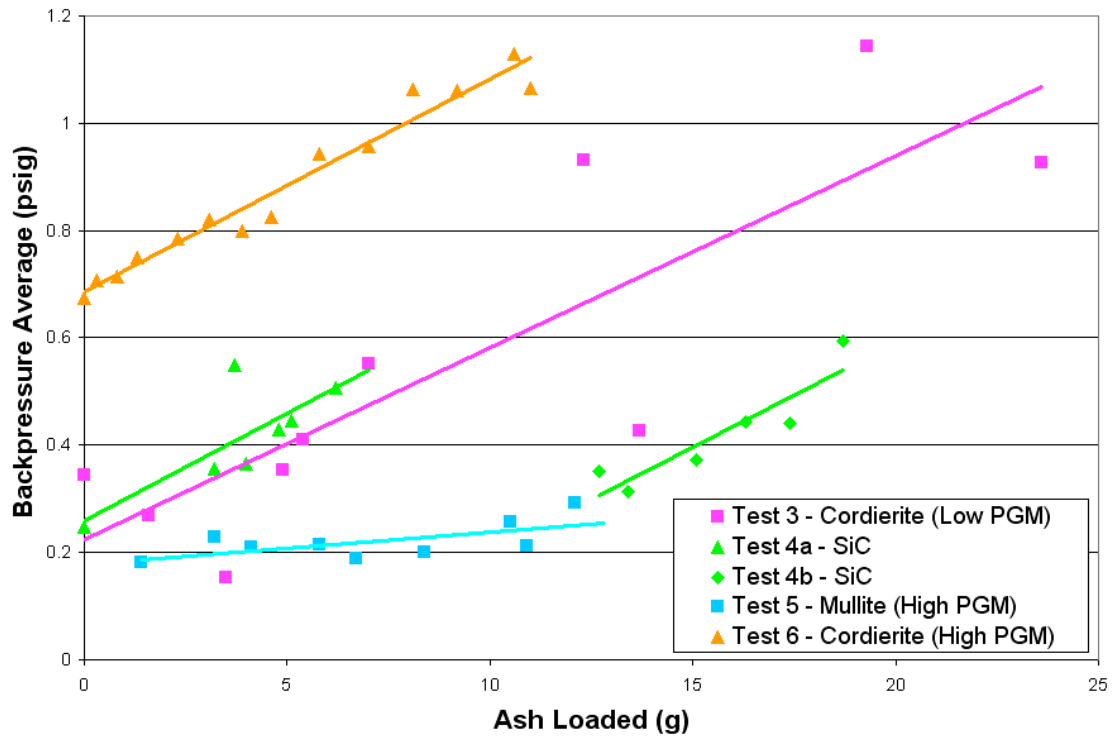


**Figure 4.95: Baseline backpressure averages versus ash accumulation (modified view)**

the slopes of the trend lines associated with the both cordierite substrates are nearly parallel, indicating that the accumulation of ash has the same effect on both catalyzed and non-catalyzed cordierite substrates. This trend cannot be confirmed for other substrates since backpressure data from the first mullite test is not considered usable, and no test was performed on a catalyzed SiC substrate.

For both SiC data sets, it is observed that the associated trend lines are nearly parallel to the trend lines for cordierite, with the initial backpressure only slightly higher than that of the non-catalyzed cordierite substrate. However, it is believed that the trend line associated with the first SiC data set is steeper because of the progressive DOC warping and eventual failure. It is also observed that, following the replacement of the

DOC, the baseline backpressure nearly returns to its initial value. This confirms that, while there are some consistent trends observed in the SiC data, another test would need to be performed to confirm the legitimacy of these trends.

For mullite, both the initial backpressure and the rate of increase with respect to ash accumulation are lower than those observed for cordierite and mullite. This result suggests mullite possesses several advantages as a DPF substrate material with regard to engine performance. While the scope of this investigation did not include evaluation of cost and other factors important to DPF system performance such as filtration efficiency and thermal fatigue resistance, the temperature and backpressure results presented here do demonstrate mullite's lower backpressure characteristics. It is believed that the protocol developed can be used to further evaluate the performance of mullite and other potential substrate materials in an accelerated manner to identify new advantages or complications associated with each.

Another performance characteristic of interest is the light-off temperatures, defined as the temperature at which the exhaust backpressure values are first observed to decrease during regeneration. This temperature is strong function of both the type of soot and catalyst materials present. Over the course of each experiment, continuous regeneration efficiency decreases, due to higher soot production rates resulting from increased backpressure, and DOC deactivation resulting in less NO<sub>2</sub> being produced. Figure 4.96 presents these lightoff temperatures as a function of soot accumulation.

It is first noted that the vast majority of the data points from all 5 tests fall in the range between 580°C and 620°C. The first set of SiC data points are clearly higher than the rest, again due to the failure of the DOC and subsequent problems associated with

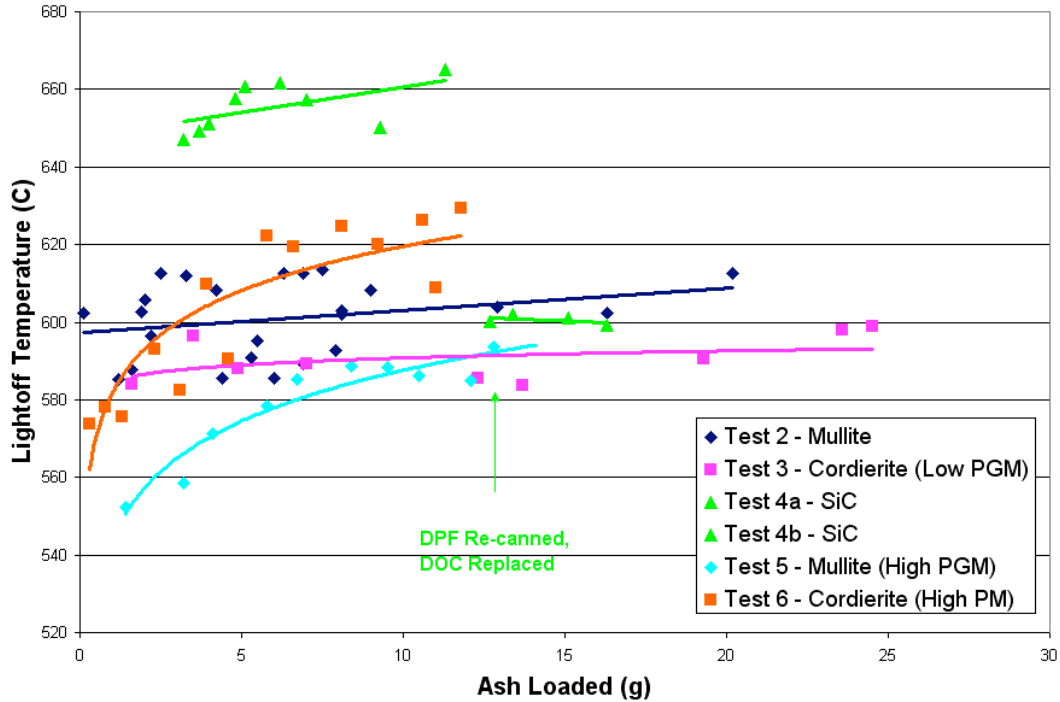


**Figure 4.96: Soot lightoff temperature versus ash accumulation**

backpressure. Once the DOC is replaced, the values fall into the aforementioned range and remain consistent for the remainder of the test.

It is also noted the light-off temperatures for the two highly-catalyzed substrates are initially lower but increase into the aforementioned common range after approximately 5 grams of ash accumulation. This phenomenon is due to the enhanced continuous regeneration associated with the increased catalyst loadings. As ash accumulates, the catalyst material becomes covered and thus is no longer exposed to the soot layer, decreasing the influence of the catalyst on regeneration.

Overall, the accumulation of ash has minimal effect on non-catalyzed and lightly-catalyzed substrates, while the impact on highly-catalyzed substrates is clearly visible, particularly during the first 5 grams of ash accumulation. Highly-efficient continuous



regeneration is desired to minimize repetitive backpressure increases associated with soot accumulation and active regeneration. However, for systems requiring periodic active regeneration, results indicate that ash accumulation has minimal impact on soot light-off temperature.

#### **4.6.2 Chemical Analysis of Fuel, Lube-oil and Ash-loaded Substrates**

The ash-loaded substrates from Tests 3, 4 and 5 were analyzed using ICP to quantify the amount of ash present as well as the distribution of the ash along the length of the DPF. In addition, ICP analysis of the lube-oil and the doped fuel provides valuable information regarding the presence of ash constituents, and allows for an approximation of the amount of ash produced over the course of the experiment. Table 4.1 shows the DPF test matrix, which provides pertinent information such as PGM loading, DOC length, and ash loading. Combining this data with the analysis of the ash-loaded substrates allows for a calculation of ash recovered by the DPF.

Table 4.2 lists the concentrations of zinc, sulfur, calcium and phosphorus in the substrates, lube-oil and doped fuel. In addition, the masses associated with these concentrations as well as the calculated recovery percentage for each element are calculated and presented. It is observed that the concentrations of phosphorus are

**Table 4.1: DPF test matrix with ash accumulation and performance summary**

Test #	Substrate Material	PGM Loading (g/ft <sup>3</sup> )	DOC Length (in)	Number of Regens	Total Ash (g)	Lightoff Temp		BP Slope	
						Avg °C	+/- °C	psig/gash	Intercept
2	Mullite	0	6"	64	20.2	600.93	9.83	-0.021	0.473
3	Cordierite	10	6"	65	24.5	590.48	5.91	0.036	0.225
4	SiC	0	6"	61	19.7	638.61	26.94	0.004	0.376
5	Mullite	(high)	3"	33	14.1	578.7595	13.78	0.006	0.178
7	Cordierite	120	6"	63	11.8	580.565	7.65	0.040	0.685

**Table 4.2: Quantification of ash constituents in oil, fuel and ash-loaded substrates**

		Test 3 - Cordierite (Low PGM)				Test 4 - SiC (No PGM)				Test 5 - Mullite (High PGM)			
		Zn	S	Ca	P	Zn	S	Ca	P	Zn	S	Ca	P
Average Concentration	wt %	0.55	0.51	1.42	0.00	0.28	0.18	0.60	0.12	0.45	0.27	0.71	0.12
Mass in DPF	g	2.29	2.11	5.95	0.00	1.35	0.89	2.91	0.56	1.89	1.14	3.00	0.53
Concentration in Oil	wt%	0.13	0.75	0.35	0.12	0.12	0.38	0.23	0.11	0.12	0.38	0.23	0.11
Mass in Oil	g	3.42	19.90	9.33	3.17	3.30	10.10	6.14	2.93	3.30	10.10	6.14	2.93
Recovery	%	66.9%	10.6%	63.7%	0.0%	40.9%	8.8%	47.3%	19.0%	57.5%	11.3%	48.9%	18.0%
Concentration in Fuel + Oil	wt%	0.00	0.03	0.01	0.00	0.01	0.03	0.01	0.01	0.01	0.03	0.01	0.01
Mass in fuel	g	2.50	14.92	6.72	2.25	3.07	16.46	5.57	2.96	3.07	16.46	5.57	2.96
Recovery	%	91.4%	14.2%	88.5%	0.0%	44.0%	5.4%	52.2%	18.8%	61.8%	6.9%	53.9%	17.8%

relatively small compared to the concentrations of the other elements of interest. In addition, the recovery masses are greatest for calcium in all three substrates, further identifying calcium as the primary ash constituent. Calculated masses of calcium and zinc, in particular, indicate an ash recovery of around 90% for the cordierite substrate, while the recovery percentages for the SiC and mullite substrates are on the order of 50% to 60%. It is noted that a change in lube-oil formulation occurred between Test 3 and Test 4 and is responsible, at least in part, for this disparity in recovery.

To observe the distribution of ash within the cordierite DPF, a quarter-section is cut into five segments of equal length for analysis. Figure 4.97 shows the measured weight percentage of four ash constituents as a function of position along the direction of flow within the DPF. Consistent with observations made during EPMA and SEM analysis, ash levels are relatively small near the inlet and increase along the length of the DPF. Furthermore, the ash concentrations in the rear-most sections of the DPF are lower. This is the result of both the presence of channel plugs at the end of the inlet channels and ash clogging upstream that prevents ash material from reaching the rear-most section. Overall, the distribution is consistent with analysis presented in the preceding sections.

The ash distribution for non-catalyzed SiC substrate is quantified by dividing a quarter-section of substrate into three equal segments. The reduction in the number of sections is both to reduce analysis time and minimize loss of ash material during sample preparation. Figure 4.98 presents this data for the same four ash constituents. Calcium is again observed to be present in the greatest amounts, with the most dramatic increase occurring between the front and middle sections. Concentrations of the remaining elements are relatively low and exhibit minimal variation along the length of the DPF. It is noted, however, that phosphorus levels in the SiC substrate are significantly higher than those observed in the cordierite substrate, again the result of a change in lube-oil formulation. Nonetheless, the overall ash distribution is observed to increase between the inlet and exit, consistent with EPMA and SEM results.

The ash distribution in the highly-catalyzed mullite substrate is illustrated in Figure 4.99. Unlike the previous two distributions, concentrations of all four ash constituents are observed to increase along the length of the DPF. These results differ from predictions made during EPMA and SEM analysis in which the ash appeared to be more evenly distributed throughout the DPF. It is possible that variations in ash density, and perhaps even the presence of elements not quantified, are responsible for the disparity between visual and quantitative results.

Overall, the ash recovery and distributions observed are in agreement with results presented in previous sections and referenced literature. While these results provide some insight with regard to trends that differ between substrates, a more comprehensive study, including multiple tests carried out on each substrate, is necessary to draw any firm conclusions. The elements selected as representative constituents account for

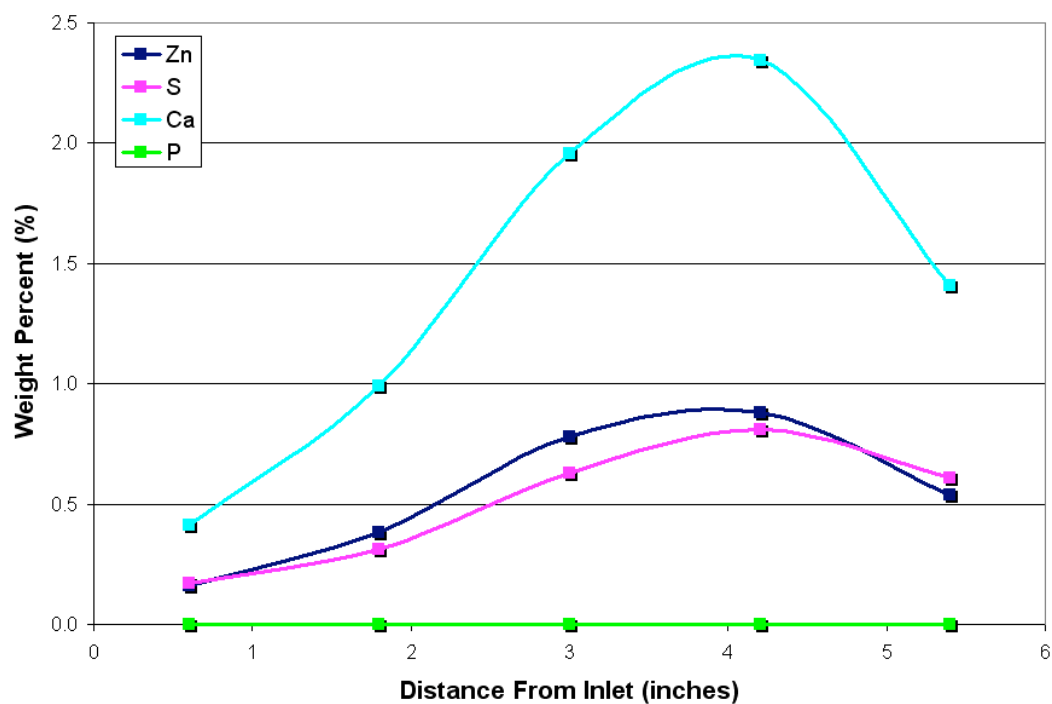


**Figure 4.97: Quantification of ash constituents by location in lightly-catalyzed cordierite substrate (Test 3)**

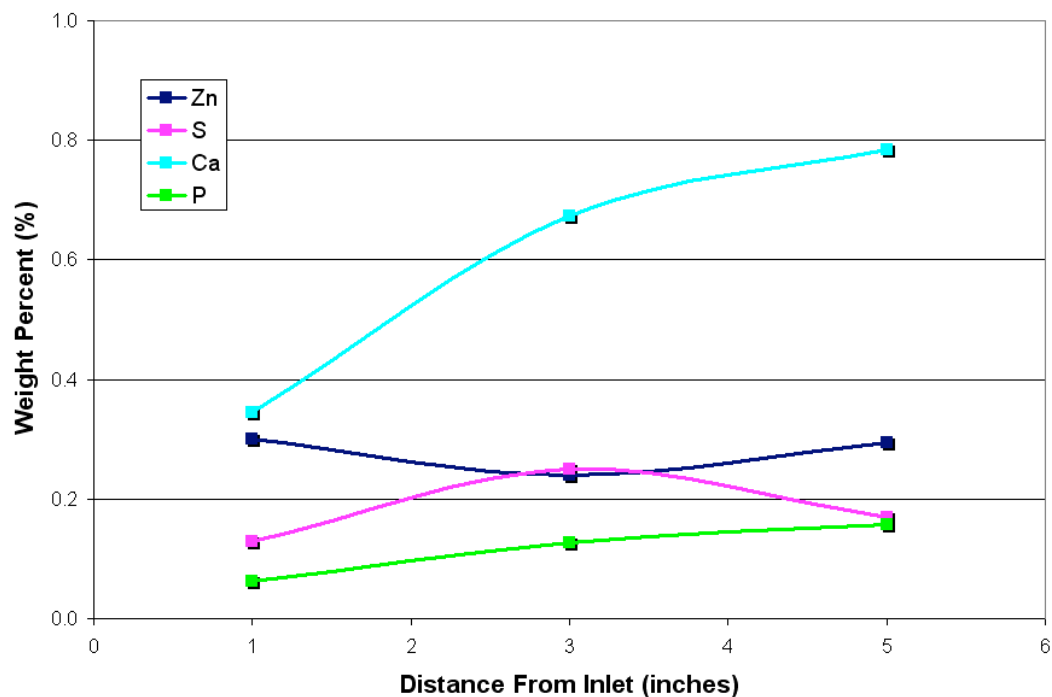


**Figure 4.98: Quantification of ash constituents by location in non-catalyzed SiC substrate (Test 4)**

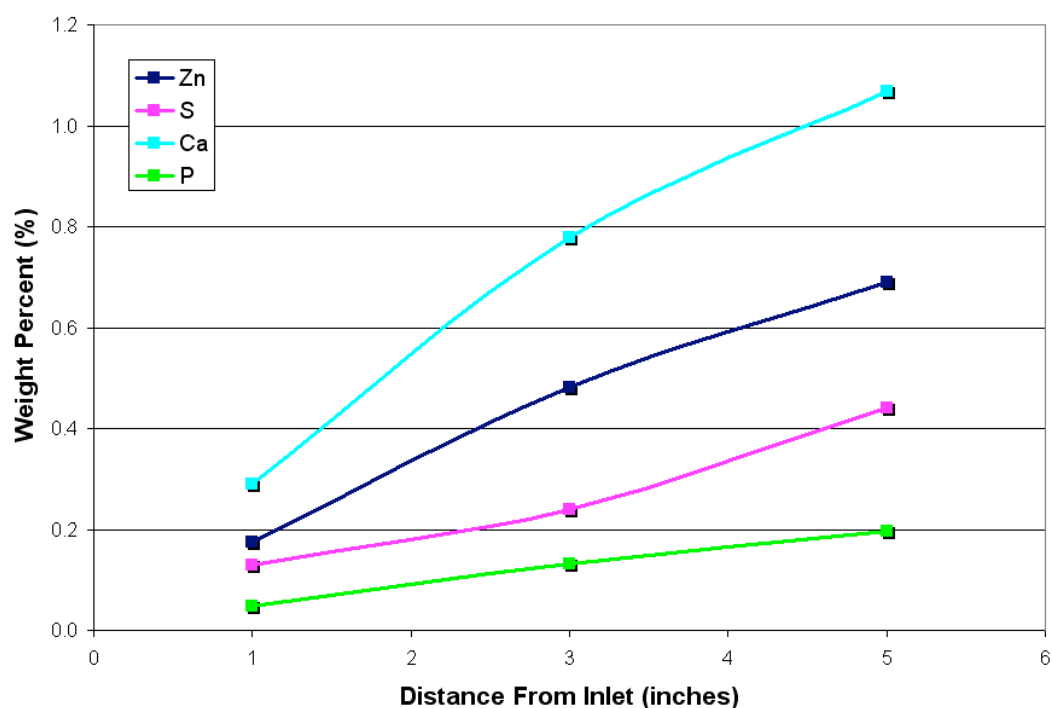


**Figure 4.99: Quantification of ash constituents by location in highly-catalyzed mullite substrate (Test 5)**

approximately 40% of the total ash present within the DPF. Expanded analysis of the ICP data revealed relatively high concentrations of iron present in all three substrates, accounting for approximately 2%, 5% and 8% of the total ash present in the SiC, cordierite and mullite substrates, respectively. The remainder of the mass increase that is not associated with these five elements is likely accounted for by the presence of more common elements such as oxygen and carbon that combine with the primary ash elements to form compounds.

To identify compounds present, the ash from three substrates was analyzed using XRD. While this method cannot be used to quantify the presence of these compounds, identification is an important step in understanding the ash composition and accounting

for disparities between calculated and measured ash masses. Figure 4.100 presents the XRD data for ash extracted from the SiC substrate. Figure 4.101 shows the XRD data for the ash collected from the highly-catalyzed mullite DPF. Finally, Figure 4.102 displays the XRD data for ash taken from the highly-catalyzed cordierite substrate.

For all three substrates, results clearly indicate the presence of calcium sulfate ( $\text{CaSO}_4$ ), calcium phosphate ( $\text{Ca}_3(\text{PO}_4)_2$ ), and zinc phosphate ( $\text{Zn}(\text{PO}_3)_2$ ). It is also possible that calcium sulfite ( $\text{CaSO}_3$ ) is present, though several of the relative peak intensities and associated scan angles are difficult to distinguish from those associated with other compounds. Additionally, it is likely that simple oxides of calcium and zinc are present in the ash, though these compounds are not easily identifiable with the instrument and software used.

Chemical analysis of several ash-loaded substrates provides valuable information regarding the composition of the lube-oil, doped fuel and ash. Calculations indicate the DPF successfully traps the vast majority of ash, though not all of the measured mass increase can be accounted for using the methods available for this investigation. Combined results from ICP and XRD indicate that calcium sulfate is the most prevalent of the identified compounds. Calcium phosphate and zinc phosphate are both present, though in lesser quantities as indicated by the smaller concentrations of phosphorus observed. Overall, the results and conclusions reached here are consistent with those in previous studies. It is believed that the protocol successfully produces the desired ash layers in a repeatable fashion, thus facilitating the accelerated evaluation of both old and new technologies.

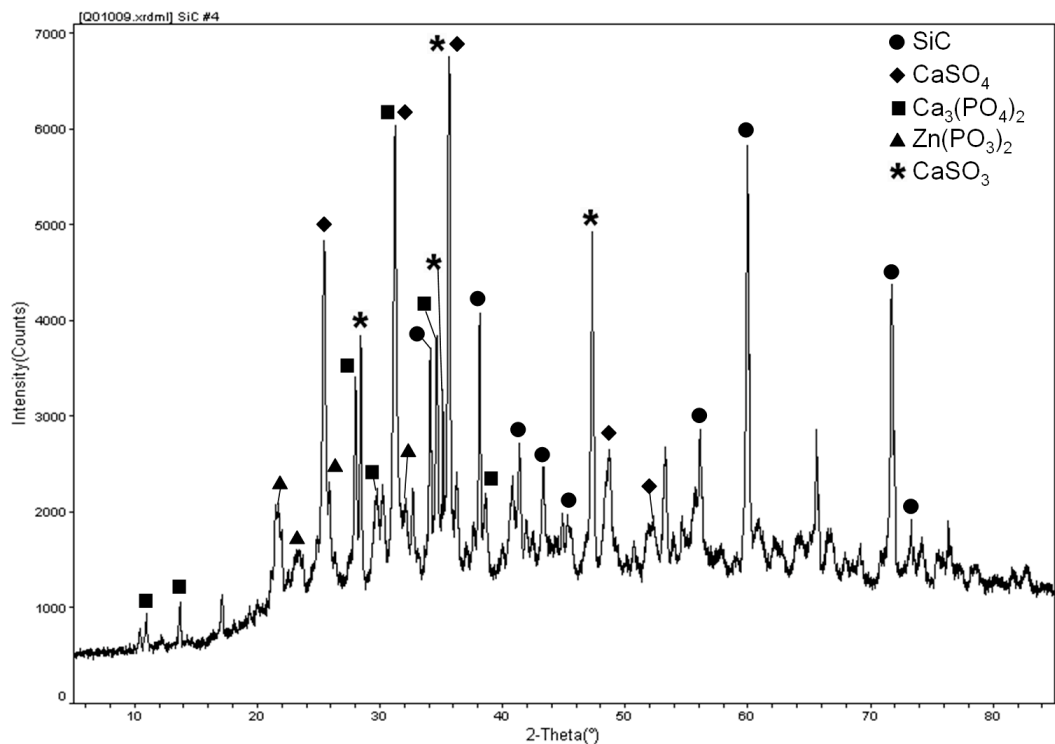


**Figure 4.100: XRD patterns of accumulated ash in non-catalyzed SiC DPF**

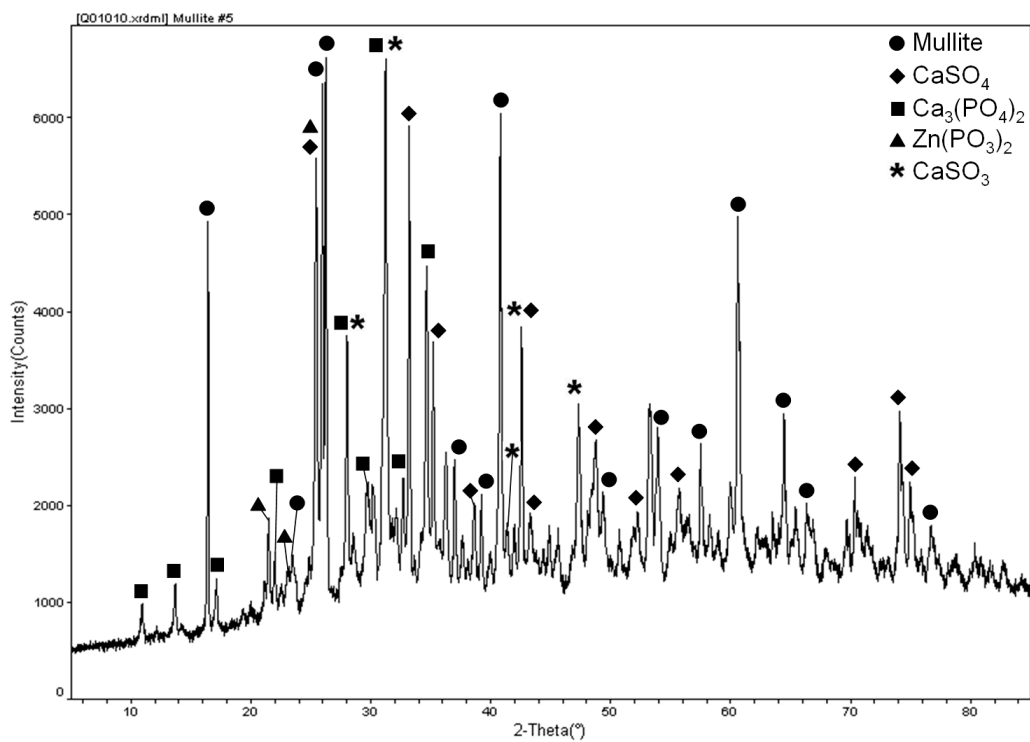


**Figure 4.101: XRD patterns of accumulated ash in highly-catalyzed mullite DPF**



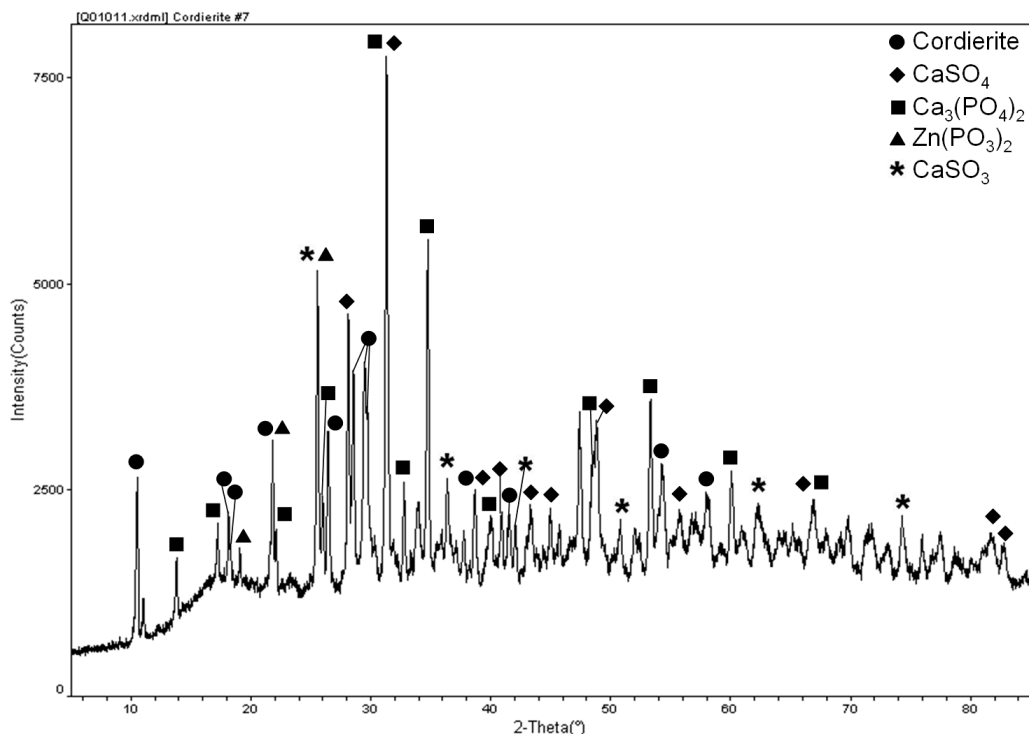


**Figure 4.102: XRD patterns of accumulated ash in highly-catalyzed cordierite DPF**

#### 4.7 Comparisons of Characterization Results to Literature

To support the validity of this accelerated ash loading protocol using a small engine and diesel fuel doped with lube oil, several published results from other investigations are presented with results from the present investigation, allowing side-by-side comparisons of ash morphology and distribution.

Instead of removing ash from the DPF for ICP-AES analysis, the sample preparation method for the present investigation involves the complete digestion of the substrate and ash material by acid. ICP analysis performed in other investigations involved the removal of ash from the substrate using various methods, and results consistently indicated contamination of the ash sample by substrate material. While the

sample preparation method for ICP-AES in the present investigation allows for the quantification of ash recovery and distribution, these results cannot be directly compared to results published in other investigations. This section will focus on the comparison of optical images, EPMA elemental maps and SEM images.

The simplest method of comparing the distribution of ash is to visually observe the relative thickness of the ash layer at various locations within the DPF. Figure 4.103 provides a comparison of the ash layers formed in two cordierite substrates. The first set of photographs (left) show the ash layer in a non-catalyzed cordierite substrate aged on an engine bench for 600 hours at high load with only natural lube oil consumption. The second set of photographs (right) shows the ash layer observed in the lightly-catalyzed cordierite substrate evaluated in Test 3 of the present investigation. The ash layers in both substrates are observed to increase in thickness along the length of the channel, with the rear-most section being completely plugged with ash. While the overall dimensions of the two DPF substrates were different, the ash layers at each relative location were very similar, indicating that the substrate selected for the small-scale rapid ash loading evaluation was appropriately sized for the engine.

To evaluate the chemical distribution and overall morphology of the ash layer within an individual channel for these two substrates, EPMA elemental maps are used to identify the relative concentrations of calcium, zinc, phosphorus and sulfur. A comparison of these elemental maps is presented in Figure 4.104. The channels shown represent the middle section in the center of the DPF. The first two sets of maps (top) represent ash layers formed using two low-ash oil formulations. The third set (bottom) represents the ash layer formed in the highly-catalyzed cordierite substrate evaluated in

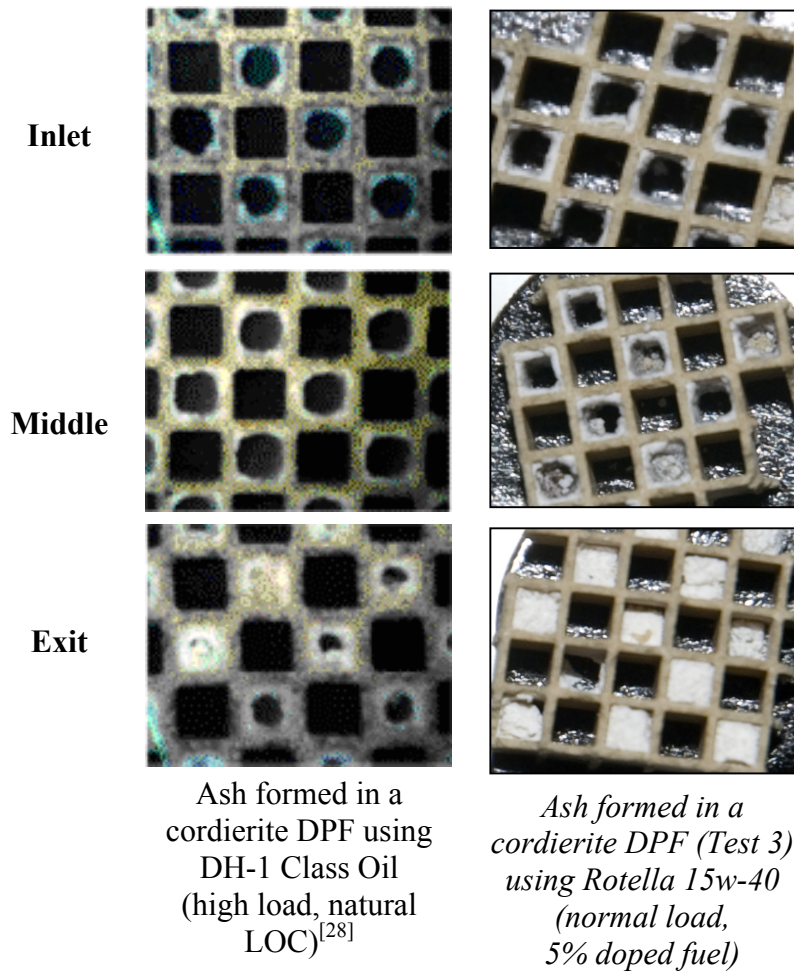
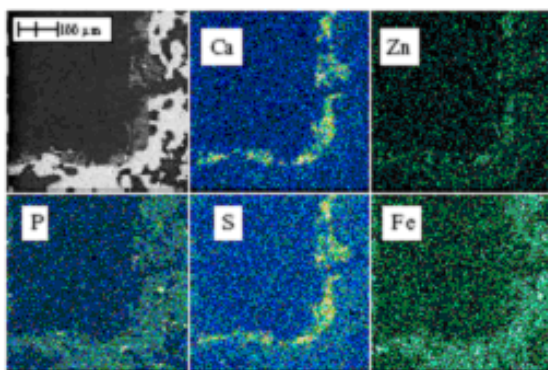
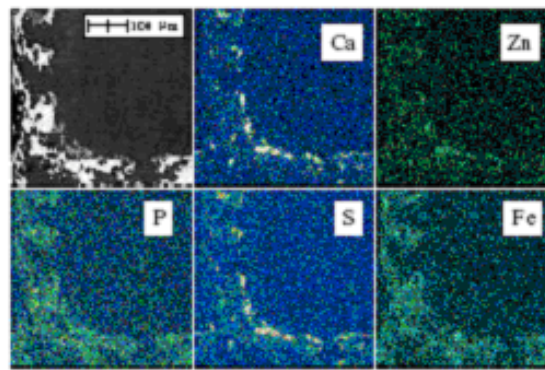


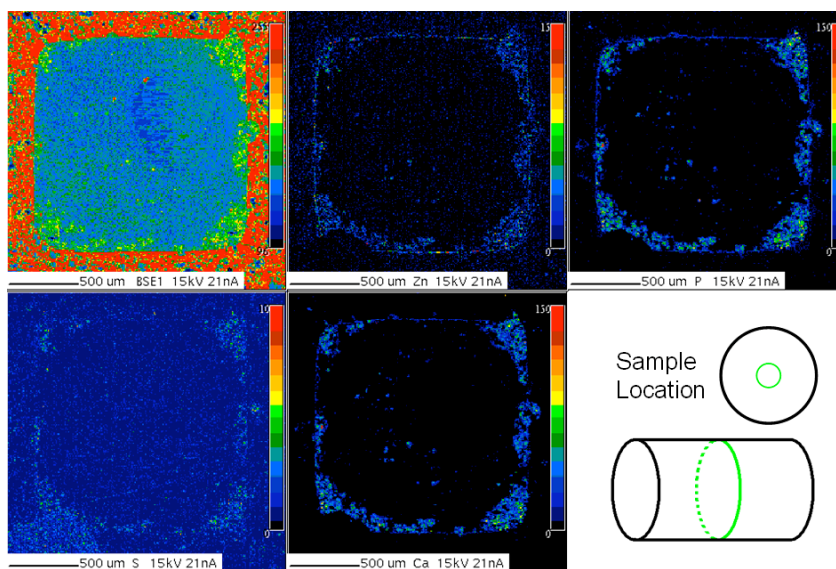
**Figure 4.103: Visual comparison of ash layers formed in two cordierite substrates**



Ash layer formed in a cordierite DPF using  
“Low Ash A” 10w-30  
(varying load, natural LOC)<sup>[28]</sup>



Ash layer formed in a cordierite DPF using  
“Low Ash B” 10w-30  
(varying load, natural LOC)<sup>[28]</sup>

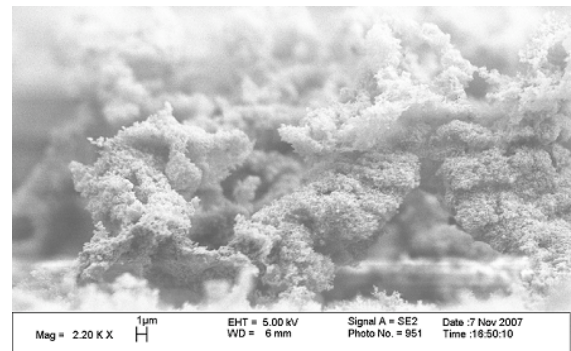
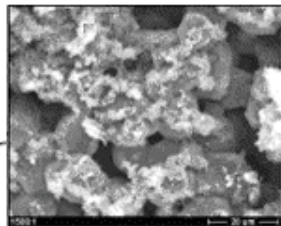
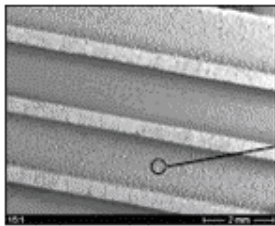


*Ash layer formed in a cordierite DPF (Test 7) using Rotella 15w-40  
(normal load, 5% doped fuel)*

**Figure 4.104: EPMA elemental map comparison of ash layers formed in two cordierite substrates**

Test 7 of the present investigation. Both ash layers appear macroscopically porous, potentially the result of ash agglomerates breaking away from the channel wall and depositing in the rear of the DPF. The relative concentrations of zinc and phosphorus in particular compare very favorably between the two investigations, further confirming the validity of the accelerated ash loading protocol.

Further evaluation of the ash layer was carried out using images acquired under high magnification using SEM. Figure 4.105 shows the ash layer formed in two cordierite substrates. The first ash layer (left) was formed using an engine bench to aged the DPF for 25 hours with varying load and natural lube oil consumption. The second ash layer (right) was acquired during analysis of the highly-catalyzed cordierite DPF evaluated in Test 7 of the current investigation. The morphology of the ash layer and individual ash agglomerates compares very favorably between the two investigations. The image selected from the current investigation is considered representative of the



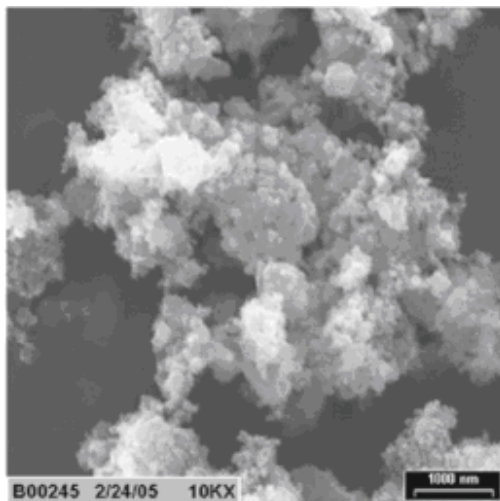
Ash produced in a non-catalyzed cordierite substrate using SAE 0w-40 (varying load, natural LOC)<sup>[27]</sup>

*Ash produced in highly-catalyzed cordierite substrate (Test 7) using Rotella 15w-40 (normal load, 5% doped fuel)*

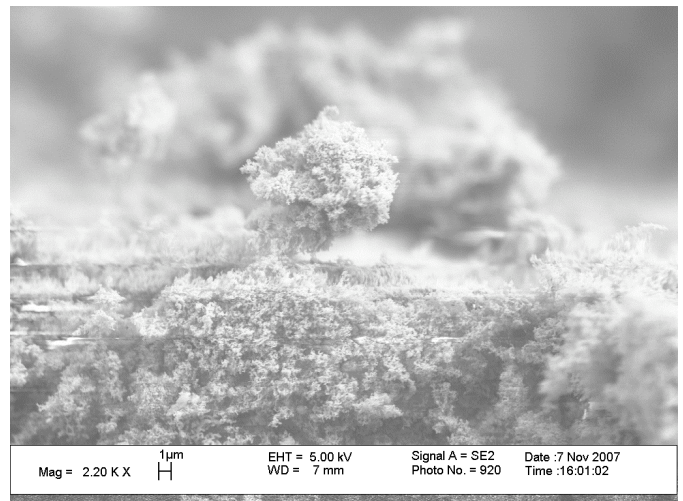
**Figure 4.105: SEM image comparison of ash agglomerates formed in two cordierite substrates**

majority of ash observed over the course of the investigation. Thus, these results once again support the validity of the accelerated testing protocol.

Finally, SEM analysis is again employed to compare individual ash particles within the DPF. Figure 4.106 presents SEM images of ash formed in two cordierite substrates acquired under extremely high magnification. The first image (left) represents ash formed in a DPF that was aged during an on-road experiment carried out with 23 tractor trailers retrofitted with SCR-DPF systems. The second image (right) shows an ash particle formed in the highly-catalyzed cordierite substrate evaluated in Test 7 of the present investigation. While differences in the resolution and contrast of the SEM instruments used in the two investigations provide different visual representations of the ash, the overall size and morphology of the ash is still apparent and both compare favorably between the two experiments.



Ash produced in a non-catalyzed cordierite substrate using SAE 15w-40 (on-road, normal LOC)<sup>[48]</sup>



*Ash produced in highly-catalyzed cordierite substrate (Test 7) using Rotella 15w-40 (normal load, 5% doped fuel)*

**Figure 4.106: SEM image comparison of ash particles formed in two cordierite substrates**

Overall, characterization of the ash layers formed in the substrates aged using the accelerated ash loading protocol developed during the present investigations compares favorably with previous published works. It is again noted that there is a very limited number of relevant characterization results available in published literature, especially with regard to SiC and mullite, making it difficult to draw any conclusions with appreciable certainty. However, based on the results available, it is believed that the accelerated ash loading protocol described in this study can be used as an adequate tool for the rapid performance evaluation of diesel particulate filters.



## **CHAPTER 5**

### **CONCLUSION**

Increased lube-oil consumption by means of fuel doping using a laboratory-scale diesel engine is shown to result in a dramatic increase in the rate of ash accumulation. The rate of accelerated lube-oil consumption was estimated to be ~50 times that of natural lube oil consumption, with the 60 hour experiments simulating approximately 90,000 miles of operation. While any method of artificially increasing lube-oil consumption brings with it inherent differences in ash formation and system performance, this investigation has shown that doping diesel fuel with a specific amount of lube oil provides a favorable method of simulating high-mileage ash accumulation in a relatively short amount of time.

Due to differences in backpressure resulting from different substrate porosities and the accumulation of ash during the experiments, the amount of soot accumulated is approximated by observing the increase in backpressure during the loading cycle. While the soot production rate has been shown to be a strong function of backpressure, results indicate that this technique provides a reasonably accurate and repeatable method of achieving the desired soot loading level. The importance of achieving this target soot loading level is two-fold. First, if too little soot is loaded, the number of active regenerations will increase, resulting in a larger associated fuel penalty that is an important concern for real-world applications. If too much soot is accumulated, there is

increased potential for an uncontrolled regeneration that could produce severe temperature excursions and damage the DPF. The protocol developed during this investigation found that a backpressure increase of 0.20 psi resulted in the desired soot loading of 3 grams per liter. The protocol is shown to consistently meet these soot loading requirements.

For this backpressure-based soot loading protocol to remain effective, the carbonaceous portion of the engine-out soot must be oxidized both by continuous regeneration and active regeneration to minimize the impact of soot accumulation on engine backpressure. Efficient continuous regeneration by  $\text{NO}_2$  occurs only at lower temperatures ( $\sim 300^\circ\text{C}$ ), which are typically experienced by most aftertreatment systems during normal engine operation. While  $\text{NO}_2$  is observed to extend the length of the loading cycle by continuously oxidizing a portion of the engine-out soot particles, the DPF must be actively regenerated periodically to remove soot particles that accumulate within the channels. This is achieved by injecting supplemental fuel into the exhaust stream upstream of the DOC, thus increasing exhaust temperatures ( $\sim 700^\circ\text{C}$ ) through the DPF and facilitating oxidation of PM by  $\text{O}_2$ . While these higher temperatures decrease the soot oxidation efficiency of  $\text{NO}_2$ , regeneration activity via  $\text{O}_2$  increases significantly.

To consistently remove all particulate matter from the DPF, an effective and repeatable active regeneration strategy was developed and employed. Exhaust gas temperatures were increased by injecting atomized diesel fuel into the exhaust stream upstream of the DOC. The fuel is injected using a calibrated metering pump, allowing for precise control of the flow rates. The exhaust gas and DPF solid temperatures associated with each injection rate must be calculated for different substrates and

configurations. To begin the active regeneration process, the fuel injection rate is set to produce DPF inlet gas temperatures of approximately 550°C. This temperature is in the lower part of the temperature range in which oxidation by O<sub>2</sub> is possible, and is selected to slowly heat the system up and minimize the potential of initiating uncontrolled regenerations. The fuel rate is incrementally increased every five minutes until DPF temperatures reach approximately 725°C. This injection rate is maintained until the total regeneration time reaches the predefined length (thirty minutes), at which time the supplemental fuel injection is shut off and the next loading cycle begins. Results indicate that this strategy produces very repeatable temperature profiles and is very efficient in removing all PM from the DPF, although it is a lengthy cycle.

Characterizations of the substrates aged using this accelerated ash loading protocol reveal several distinct trends in ash composition, morphology and distribution within the DPF. Consistent with referenced literature, the ash layer thickness and total quantity of ash present in the inlet channels increases along the length of the DPF. The thickness of the ash layer is a strong function of the channel wall morphology, affecting the ability of ash to remain intact with the channel wall. In all substrates, varying amount of ash material was observed to break loose from the channel walls upstream and deposit in the rear of the filter, completely plugging the channels as far as one half the length of the DPF. The density of the ash layers and material deposits, as well as the overall distribution of ash, was observed to have significant impact on engine backpressure. Visual observation of the ash layers in the cordierite and SiC substrates revealed that these layers are fairly dense and relatively thin, resulting in dramatic increases in engine backpressure. The ash layer in the mullite substrates was observed to be much thicker,

less dense and better distributed along the length of the DPF, resulting in a less significant backpressure increase over the course of the experiment. While a more detailed analysis to quantify the density and permeability of each ash layer is left to future investigation, the density of the ash layer, distribution throughout the DPF, and total mass accumulation have all been shown to be equally important design considerations in the development of an effective and durable DPF system.

The lube-oil and diesel fuel used for this investigation are considered common based on composition and commercial availability. Consistent with referenced literature, calcium sulfate and zinc phosphate are identified with great likelihood as the primary constituent of the ash that is formed using the developed protocol. XRD results indicated the presence of other calcium and zinc compounds but cannot be quantified at this time. In addition, the presence of iron in the ash identifies another potential source of ash that could become relatively significant once the usage of newer low-ash lube-oil formulations becomes more prevalent.

The protocol developed to accelerate the formation and accumulation of ash within a DPF has been shown to satisfy all efficiency and repeatability requirements outlined prior to the investigation. It is recommended as a rapid screening tool for the development of new DPF substrates, system configurations and oil formulations with the knowledge that ash accumulation is the single most critical aspect affecting the durability of DPF aftertreatment systems.

To summarize, the main features of the accelerates ash loading protocol are a backpressure-based method for accurately determining the soot present in the DPF as ash accumulates, and an active regeneration strategy that effectively removes all soot from

the DPF by raising exhaust temperatures to facilitate oxidation of carbonaceous material by O<sub>2</sub>. All temperatures and backpressures experienced by the system are comparable to those that are commonly observed in a variety of real-world applications, maximizing the relevance and legitimacy of this testing protocol and subsequent results. In addition, a comprehensive characterization study has been performed for comparison to more field-aged samples once they become available.

## **LIST OF REFERENCES**

- [1] Mori, K. (1997). Worldwide Trends in Heavy-Duty Diesel Engine Exhaust Emission Legislation and Compliance Technologies. (SAE Technical Paper Series 970753). Warrendale, PA: SAE International.
- [2] Pihl, J. Byproduct Formation During Regeneration of Lean NO<sub>x</sub> Traps. Thesis: University of Wisconsin-Madison, 2005.
- [3] Farrauto, R.J. and Voss, K.E. "Monolithic Diesel Oxidation Catalysts," Appl. Catal. B: Environmental 10 (1996) 29-51.
- [4] Energy Information Administration. (2007, October 3). *Crude Oil and Total Petroleum Imports Top 15 Countries*. Retrieved October 22, 2007, from [http://www.eia.doe.gov/pub/oil\\_gas/petroleum/data\\_publications/company\\_level\\_imports/current/import.html](http://www.eia.doe.gov/pub/oil_gas/petroleum/data_publications/company_level_imports/current/import.html)
- [5] Energy Information Administration. Emissions of Greenhouse Gases in the United States: April 2 <http://www.eia.doe.gov/oiaf/1605/87-92rpt/cover.html>
- [6] Environmental Protection Agency. (2007, August 14). *Clean Air Markets*. Retrieved October 22, 2007, from <http://www.epa.gov/airmarkets/emissions/>
- [7] Wikipedia Foundation, Inc. (2007, September 15). *Global Warming*. Retrieved October 24, 2007, from [http://en.wikipedia.org/wiki/Global\\_warming](http://en.wikipedia.org/wiki/Global_warming)
- [8] U.S. Environmental Protection Agency. (2007, August 1). *Vehicle standards and regulations*. Retrieved January 21, 2008, from <http://epa.gov/otaq/standards.htm>
- [9] Moulijn, J.A., van Diepen, A.E. & Kapteijn, F. "Catalyst Deactivation: Is it Predictable? What to do?" Appl. Catal. A: General 212 (2001) 3-16.
- [10] Blanchard, G., Seguelong, T., Michelin, J., Schuerholz, S., & Terres, F. (2003). Ciera-based fuel-borne catalysts for series diesel particulate filter regeneration. (SAE Technical Paper Series 2003-01-0378). Warrendale, PA: SAE International.
- [11] Montanaro, L. & Negro, A. (1998). On the Effects Induced by the Accumulation of Sodium, Iron and Cerium, on Diesel Soot Filters.



(SAE Technical Paper Series 980540). Warrendale, PA: SAE International.

- [12] Vincent, M. W., Richards, P.J., & Catterson, D. J. (2003). A Novel Fuel Borne Catalyst Dosing System for Use with a Diesel Particulate Filter. (SAE Technical Paper Series 2003-01-0382). Warrendale, PA: SAE International.
- [13] Campenon, T., Wouters, P., Blanchard, G., Macaudiere P. & Seguelong, T. (2004). Improvement and Simplification of DPF System Using a Ceria-based Fuel-borne Catalyst for Diesel Particulate Filter Regeneration in Serial Applications. (SAE Technical Paper Series 2004-01-0071). Warrendale, PA: SAE International.
- [14] Blanchard, G., Colignon, C., Griard, C., Rigauddau, C., Salvat, O. & Seguelong, T. (2002). Passenger Car Series Application of a New Diesel Particulate Filter Sstem Using a New Ceria-Based Fuel-Borne Catalyst: From the Engine Test Bench to European Vehicle Ceritification. (SAE Technical Paper Series 2004-01-2781). Warrendale, PA: SAE International.
- [15] Bouchez, M., Dementhon, J. B., Messaoudi, I., Guyon, M. & Noirot, R. (2001). Influence of Both Catalyst Geometry and Fuel Sulfur Conent on Nox Adsorber Poisoning. (SAE Technical Paper Series 2001-01-1934). Warrendale, PA: SAE International.
- [16] Ogyu, K., Ohno, K., Hong, S. & Komori, T. (2004). Ash Storage Capacity Enhancement of Diesel Particulate Filter. (SAE Technical Paper Series 2004-01-0949). Warrendale, PA: SAE International.
- [17] Mohammed, H. Lakkireddy, V. R., Johnson, J. H. & Bagley, S. T. (2006). Experimental and Modeling Study of a Diesel Oxidation Catalyst and a Catalyzed Diesel Particulate filter Using 1-D 2-Layer Model. (SAE Technical Paper Series 2006-01-0466). Warrendale, PA: SAE International.
- [18] McCullough, G., Douglas, R. & McDowell, N. (2004) Deactivation of Oxidation Catalysts by Oil-Derived Sulphur. (SAE Technical Paper Series 2004-01-1738). Warrendale, PA: SAE International.

- [19] Eaton, S. J., Nguyen, K. & Bunting, B. G. (2006). Deactivation of Diesel Oxidation Catalysts by Oil-Derived Phosphorus. (SAE Technical Paper Series 2006-01-3422). Warrendale, PA: SAE International.
- [20] Dou, D. & Bailey, O. H. (1998). Investigation of NO<sub>x</sub> Adsorber Catalyst Deactivation. (SAE Technical Paper Series 982594). Warrendale, PA: SAE International.
- [21] McCullough, G., Douglas, R., McDowell, A. P. N. & Kenny, R. G. (1998). An Experimental Evaluation of the Oil Fouling Effects of Two-Stroke Oxidation Catalysts. (SAE Technical Paper Series 982014). Warrendale, PA: SAE International.
- [22] Caprotti, R., Field, I., Michelin, J., Schuerholz, S. & Terres, F. (2003). Development of a Novel DPF Additive. (SAE Technical Paper Series 2003-01-3165). Warrendale, PA: SAE International.
- [23] Takeuchi, Y., Hirano, S., Kanauchi, M., Ohkubo, H., Nakazato, M., Sutherland, M., et al. (2003). The Impact of Diesel engine Lubricants on Deposit Formation in Diesel Particulate Filters. (SAE Technical Paper Series 2003-01-1870). Warrendale, PA: SAE International.
- [24] Okada, S., Kweon, C., Stetter, J. C., Foster, E., Shafer, M. M., Christensen, C. G., et al. (2003). Measurement of Trace Metal composition in Diesel Engine Particulate and its Potential For Determining Oil Consumption. (SAE Technical Paper Series 2003-01-0076). Warrendale, PA: SAE International.
- [25] Manni, M., Carriero, M. & Rosellin, A. (2002). A Study of Oil consumption on a Diesel Engine with Independently Lubricated Turbocharger. (SAE Technical Paper Series 2002-01-2730). Warrendale, PA: SAE International.
- [26] Bardasz, E., Cowling, S., Panesar, A., Durham, J., & Tadrous, T. (2005). Effects of lubricant derived chemistries on performance of the catalyzed diesel particulate filters. (SAE Technical Paper Series 2005-01-2168). Warrendale, PA: SAE International.
- [27] Givens, W., Buck, W., Jackson, A., Kaldor, A., Hertzberg, A., Moehrmann, W., et al. (2003). Lube formulation effects on transfer of elements to exhaust

- after-treatment system components. (SAE Technical Paper Series 2003-01-3109). Warrendale, PA: SAE International.
- [28] Nemoto, S., Togawa, S., Kishi, Y., Ishikawa, T., Matsuura, K., Hashimoto, T., et al. (2004). Impact of oil-derived ash on continuous regeneration-type diesel particulate filter – JCAPII oil WG report. (SAE Technical Paper Series 2004-01-1887). Warrendale, PA: SAE International.
- [29] Nord, K., Haupt, D., Ahivik, P. & Egeback, K. E. (2004). Particulate Emissions From an Ethanol Fueled Heavy-Duty Diesel Engine Equipped with EGR, Catalyst and DPF. (SAE Technical Paper Series 2004-01-1987). Warrendale, PA: SAE International.
- [30] Stetter, J., Forster, N., Ghandhi, J., & Foster, D. (2003, August). The impact of oil consumption mechanisms on diesel exhaust particle size distributions and detailed exhaust chemical composition. Paper presented at DEER Conference, Newport, RI.
- [31] Allansson, R., Blakeman, P., Cooper, B., Hess, H., Silcock, P., & Walker, A. (2002). Optimising the low temperature performance and regeneration efficiency of the continuously regenerating diesel particulate filter (CR-DPF) system. (SAE Technical Paper Series 2002-01-0428). Warrendale, PA: SAE International.
- [32] Jacquot, F. & Brillhac, J. F. (2004). Soot Oxidation by O<sub>2</sub> and/or NO<sub>2</sub> in the Presence of Catalysts Under Lean-Burn and Rich Atmospheres. (SAE Technical Paper Series 2004-01-1943). Warrendale, PA: SAE International.
- [33] Allansson, R., Goersmann, C., Lavenius, M., Phillips, P. R., Uusimaki, A. J. & Walker, A. P. (2004). The Development and In-Field Performance of Highly Durable Particulate Control Systems. (SAE Technical Paper Series 2004-01-0072). Warrendale, PA: SAE International.
- [34] Guo, G., Xu, N., laing, P. M., Hammerle, R. H. & Maricq, M. M. (2003). Performance of a Catalyzed Diesel Particulate Filter System During Soot Accumulation and Regeneration. (SAE Technical Paper Series 2003-01-0047). Warrendale, PA: SAE International.

- [35] Kandylas, I. P., Haralampous, O.A., & Koltsakis, G. C. (2002). Diesel Soot Oxidation with NO<sub>2</sub>: Engine Experiments and Simulations. *Industrial & Engineering Chemistry Research*, 41, 5372-5384.
- [36] Kim, D., Lee, H. S., Chun, K. M., Hwang, J. H., Lee, K. S. & Chun, B. H. (2002). Comparison of Soot Oxidation by NO<sub>2</sub> Only and Plasma-Treated Gas Containing NO<sub>2</sub>, O<sub>2</sub>, and Hydrocarbons. (SAE Technical Paper Series 2002-01-2704). Warrendale, PA: SAE International.
- [37] Hawker, P., Huthwohl, G., Henn, J., Kock, J., Luders, H., Luers, B. et al. (1998). Effect of a Continuously Regenerating Diesel Particulate Filter on Non-Regulated Emissions and Particulate Size Distribution. (SAE Technical Paper Series 980189). Warrendale, PA: SAE International.
- [38] England, S. B., Rutland, C. J. & Foster, D. E. (2006). Investigation of the Effect of DPF Loading and Passive Regeneration on Engine Performance and Emissions Using an Integrated System Simulation. (SAE Technical Paper Series 2006-01-0263). Warrendale, PA: SAE International.
- [39] Ranalli, M., Hossfeld, C., Kaiser, R., Schmidt, S. & Elfinger, G. (2002). Soot Loading Distribution as a Key Factor for a Reliable DPF System: An Innovative Development Methodology. (SAE Technical Paper Series 2002-01-2158). Warrendale, PA: SAE International.
- [40] Andersson, S., Akerlunt, C. and Blomquist, M. (2002). Low Pressure EGR Calibration Strategies for Reliable Diesel Particulate Filter Regeneration on HDD Engines. (SAE Technical Paper Series 2002-01-2780). Warrendale, PA: SAE International.
- [41] Lee, J., Kwon, C., Kim, S., & Yeo, G. (2005). Control of diesel catalyzed particulate filter system I (The CPF system influence assessment according to a regeneration condition). (SAE Technical Paper Series 2005-01-0661). Warrendale, PA: SAE International
- [42] Rumminger, M. D., Zhou, X., Balakrishnan, K., Edgar, B. L. & Ezekoye, O. A. (2001). Regeneration Behavior and Transient Thermal Response of Diesel

- Particulate Filters. (SAE Technical Paper Series 2001-01-1342). Warrendale, PA: SAE International.
- [43] Florchinger, P., Zink, U., Cutler, W. & Tomazic, D. (2004). DPF Regeneration-Concept to Avoid Uncontrolled Regeneration During Idle. (SAE Technical Paper Series 2004-01-2657). Warrendale, PA: SAE International.
- [44] Kong, Y., Kozakiewicz, T., Johnson, R., Huffmeyer, C., Huckaby, J., Baurley, J., et al. (2005). Active DPF Regeneration for 2007 Diesel Engines. (SAE Technical Paper Series 2005-01-3509). Warrendale, PA: SAE International.
- [45] Kodama, K., Hiranuma, S., Doumeki, R., Takeda, Y. & Ikeda, T. (2005). Development of DPF System of Commercial Vehicles (Second Report) - Active Regeneration Function in Various Driving Condition -. (SAE Technical Paper Series 2005-01-3694). Warrendale, PA: SAE International.
- [46] Hanamura, K., Suzuki, T., Tanaka, T., & Miyairi, Y. (2003). Visualization of combustion phenomena in regeneration of diesel particulate filter. (SAE Technical Paper Series 2003-01-0836). Warrendale, PA: SAE International.
- [47] Kimura, K., Lynskey, M., Corrigan, E. R., Hickman, D. L., Wang, J., Fang, H. L., et al. (2006). Real World Study of Diesel Particulate Filter Ash Accumulation in Heavy-Duty Diesel Trucks. (SAE Technical Paper Series 2006-01-3257). Warrendale, PA: SAE International.
- [48] McGeehan, J. A., Yeh, S., Couch, M., Hinz, A., Otterholm, B., Walker, A., et al. (2005). On The Road to 2010 Emissions: Field Test Results and Analysis with DPF-SCR System and Ultra Low Sulfur Diesel Fuel. (SAE Technical Paper Series 2005-01-3716). Warrendale, PA: SAE International.
- [49] INCO. (2006, March). *Evaluation of Diesel Particulate Filter Systems at Stobie Mine*. Retrieved July 19, 2007, from page 124 at <http://www.deep.org/reports/stobiedpf.pdf>
- [50] Richards, P., Terry, B., Chadderton, J. & Vincent, M. W. (2004). Retrofitting Urban Busses to Reduce PM and NO<sub>2</sub>. (SAE Technical Paper Series 2004-01-1939). Warrendale, PA: SAE International.

- [51] Fayard, J. C. & Seguelong, T. (2004). A New DPF System for Duty Cycle Vehicles. (SAE Technical Paper Series 2004-01-1937). Warrendale, PA: SAE International.
- [52] Jeuland, N., Dementhon, J. B., Gagnepain, L., Plassat, G., Coroller, P., Momique, J. C., et al. (2004). Performances an Durability of DPF (Diesel Particulate Filter) Tested on a Fleet of Peugeot 607 Taxis: Final Results. (SAE Technical Paper Series 2004-01-0073). Warrendale, PA: SAE International.
- [53] Schaefer-Sindlinger, A., Lappas, I., Vogt, C.D., Ito, T., Kurachi, H., Makino, M., et al. (2007). Efficient material design for diesel particulate filters. *Topics in Catalysis*, 42-43, 307-317.
- [54] Zhan, R., Huang, Y., & Khair, M. (2006). Methodologies to control DPF uncontrolled regenerations. (SAE Technical Paper Series 2006-01-1090). Warrendale, PA: SAE International.
- [55] Hiranuma, S., Takeda, Y., Kawatani, T., Doumeki, R., Nagasaki, K., & Ikeda, T. (2003). Development of DPF system for commercial vehicle – Basic characteristic and active regenerating performance. (SAE Technical Paper Series 2003-01-3182). Warrendale, PA: SAE International.
- [56] Joshi, A., Chatterjee, S., Sawant, A., Akerlund, C., Andersson, S., Blomquist, M., et al. (2006). Development of an Actively Regenerating DPF System for Retrofit Applications. (SAE Technical Paper Series 2006-01-3553). Warrendale, PA: SAE International.
- [57] Edgar, B. L., Balakrishnan, K., Zhou, X. & Rumminger, M. D. (2000). Experiments and Analysis of Diesel Particulate Filter Loading and Regeneration. (SAE Technical Paper Series 2000-01-3087). Warrendale, PA: SAE International.
- [58] Ohno, K., Shimato, K., Taoka, N., Santae, H., Ninomiya, T., Komori, T., et al. (2000). Characterization of SiC-DPF for Passenger Car. (SAE Technical Paper Series 2000-01-0185). Warrendale, PA: SAE International.

- [59] Song, J., Alam, M., Zello, V., Boehman, A. L., Bishop, B. & Walkton, F. (2002). Fuel Sulfur Effect on Membrane Coated Diesel Particulate Filter. (SAE Technical Paper Series 2002-01-2788). Warrendale, PA: SAE International.
- [60] Pfeifer, M., Votsmeier, M., Kogel, M., Spurk, P. C., Lox, E. S. & Knoth, J. F. (2005). The Second Generation of Catalyzed Diesel Particulate Filter Systems for Passenger Cars - Particulate Filters with Integrated Oxidation Catalyst Function -. (SAE Technical Paper Series 2005-01-1756). Warrendale, PA: SAE International.
- [61] Mao, F. & Li, C. G. (2005). Performance Validation of an Advanced Diesel Particulate Filter With High Catalyst Loading Capacity. (SAE Technical Paper Series 2005-01-3696). Warrendale, PA: SAE International.
- [62] Nakamura, K., Kimura, K., Nishino, A, Tokuda, K., Aoki, M., Ogawa, M., et al. (1994). Thermal and Mechanical Properties of Mullite-Crystallized Glass Ceramics DPF with Pulse-Wave Corrugated Honeycomb Structure. (SAE Technical Paper Series 940520). Warrendale, PA: SAE International.
- [63] Pyzik, A., Han, C., Li, C., Malanga, M., Mao, F., Merrick, D., et al. (2005, August). *Development of Acicular Mullite Materials for Diesel Particulate Filters Application*. Paper presented at DEER Conference, Chicago, IL.
- [64] Ecopoint Inc. (2005). *Wall-Flow Monoliths*. Retrieved November 3, 2007, from [www.DieselNet.com](http://www.DieselNet.com)
- [65] Pyzik, A. J., & Li, C. G. (2005). New Design of a Ceramic Filter for Diesel Emission Control Applications. *International Journal of Applied Ceramic Technology*, 2(6), 440-451.
- [66] Manni, M., Pedicillo, A., & Bazzano, F. (2006). A study of lubricating oil impact on diesel particulate filters by means of accelerated engine tests. (SAE Technical Paper Series 2006-01-3416). Warrendale, PA: SAE International.
- [67] Sutton, M., Britton, N., Otterholm, B., Tengström, P., Frennfelt, C., Walker, A., et al. (2004). Investigations into lubricant blocking of diesel particulate

- filters. (SAE Technical Paper Series 2004-01-3013). Warrendale, PA: SAE International.
- [68] Bardasz, E., Mackney, D., Britton, N., Kleinschek, G., Olofsson, K., Murray, I., et al. (2003). Investigation of the interactions between lubricant-derived species and aftertreatment systems on a state-of-the-art heavy duty diesel engine. (SAE Technical Paper Series 2003-01-1963). Warrendale, PA: SAE International.
- [69] Bunting, B.G., More, K., Lewis, S., Toops, T. (2005) Phosphorus Poisoning and Phosphorus Exhaust Chemistry with Diesel Oxidation Catalysts. (SAE Technical Paper Series 2005-01-1758). Warrendale, PA: SAE International.
- [70] Riviere, J.C. *Surface Analytical Techniques*. (1990). NY: Oxford UP.
- [71] Macdonald, R.J., Taglauer, E.C., Wandelt, K.R. (Eds.). (1996). *Surface Science Principles and Current Applications*. Berlin: Springer-Verlag.
- [72] Niemantsverdriet, J.W. (2000). *Spectroscopy in Catalysis: An Introduction (2nd ed.)*. Weinheim: Wiley-VCH Verlag GmbH.
- [73] Liu, D.R., Park, J.S. (1993). "Electron Microprobe Characterization of Phosphorus Containing Deposits on used Automotive Catalyst Surfaces," Appl. Catal. B: Environmental 2 49-70.
- [74] Ozawa, M., Loong, C.K. (2002) In Situ X-ray & Neutron Powder of Redox Behavior in CeO<sub>2</sub>-Containing Oxide Catalysts Catalysis Today 50 (329-342)
- [75] Parola, V.L., Deganello, G., Tewell, C.R., & Venezia, A.M. (2002). "Structural Characterization of Silica Supported CoMo Catalysts by UV Raman Spectroscopy, XPS and X-ray Diffraction Techniques," Appl. Catal. A: General 235 171-180.
- [76] Cutler, W. A. & Merkel, G. A. (2000). A New High Temperature Ceramic Material for Diesel Particulate Filter Applications. (SAE Technical Paper Series 2000-01-2844). Warrendale, PA: SAE International.
- [77] Merkel, G. A., Cutler, W. A. & Warren, C. J. (2001). Thermal Durability of Wall-Flow Ceramic Diesel Particulate Filters. (SAE Technical Paper Series 2001-01-0190). Warrendale, PA: SAE International.



- [78] Noriyuki, T., Ohno, K., Hong, S., Sato, H., Yoshida, Y. & Komori, T. (2001). Effect of SiC-DPF with High Cell Density for Pressure Loss and Regeneration. (SAE Technical Paper Series 2001-01-0191). Warrendale, PA: SAE International.
- [79] Hashimoto, S., Miyairi, Y., Hamanaka, T., Matsubara, R., Harada, T. & Miwa, S. (2002). SiC and Cordierite Diesel Particulate Filters Designed for Low Pressure Drop and Catalyzed, Uncatalyzed Systems. (SAE Technical Paper Series 2002-01-0322). Warrendale, PA: SAE International.
- [80] Ohno, K., Taoka, N., Furuta, T., Kudo, A. & Komori, T. (2002). Characterization of high Porosity SiC-DPF. (SAE Technical Paper Series 2002-01-0325). Warrendale, PA: SAE International.
- [81] Ogyu, K., Kudo, A., Oshimi, Y., Sata, H., Ohno, K. (2003). Characterization of Thin Wall SiC-DPF. (SAE Technical Paper Series 2003-01-0377). Warrendale, PA: SAE International.
- [82] Pyzik, A. J., Todd, C. S., & Han, C. (2008). Formation mechanism and microstructure development in acicular mullite ceramics fabricated by controlled decomposition of fluorotopaz. *Journal of the European Ceramic Society*, 28, 383–391.
- [83] Ichikawa, S., Uchida, Y., Otsuka, A., Harada, T., Hamanaka, T., Nagashima, K., et al. (2003). Material Development of High Porous SiC for Catalyzed Diesel Particulate Filters. (SAE Technical Paper Series 2003-01-0380). Warrendale, PA: SAE International.
- [84] Yuuki, K., Ito, T., Sakamoto, H., Matsubara, R., Hashimoto, S. & Hamanaka, T. (2003). The Effect of SiC Properties on the Performance of Catalyzed Diesel Particulate Filter (DPF). (SAE Technical Paper Series 2003-01-383). Warrendale, PA: SAE International.
- [85] Tao, T., Cutler, W. A., Voss, K., & Wei, Q. (2003). New Catalyzed Cordierite Diesel Particulate Filters for Heavy Duty Engine Applications. (SAE Technical Paper Series 2003-01-3166). Warrendale, PA: SAE International.

- [86] Bardon, S., Bouteiller, B., Bonnail, N., Girot, P., Glize, V., Oxarango, L., et al. (2004). Asymmetrical Channels to Increase DPF Lifetime. (SAE Technical Paper Series 2004-01-0950). Warrendale, PA: SAE International.
- [87] Ichikawa, S., Uchida, Y., Kaneda, A., Hamanaka, T. (2004). Durability Study on Si-SiC Material for DPF(2). (SAE Technical Paper Series 2004-01-0951). Warrendale, PA: SAE International.
- [88] Kuki, T., Miyari, Y., Kasai, Y., Miyazaki, M., & Miwa, S. (2004). Study on Reliability of Wall-Flow Type Diesel Particulate Filter. (SAE Technical Paper Series 2004-01-0959). Warrendale, PA: SAE International.
- [89] Konstandopoulos, A. G. & Kladopoulou, E. (2004). The Optimum Cell Density for Wall-Flow Monolith Filters: Effects of Filter Permeability, Soot Cake Structure and Ash Loading. (SAE Technical Paper Series 2004-01-1133). Warrendale, PA: SAE International.
- [90] Min, J., Lee, C., Kim, S., Jung, H. & Kim, Y. (2005). Development and Performance of Catalytic Diesel Particulate Filter Systems for Heavy-Duty Diesel Systems. (SAE Technical Paper Series 2005-01-0664). Warrendale, PA: SAE International.
- [91] Yamaguchi, S., Fujii, S., Kai, R., Miyazaki, M., Miyairi, Y. & Miwa, S. (2005). Design Optimization of Wall Flow Type Catalyzed Cordierite Particulate Filter for Heavy Duty Diesel. (SAE Technical Paper Series 2005-01-0666). Warrendale, PA: SAE International.
- [92] Nuskowski, J., Thompson, G. J., Moles, N., Chiaramonte, M., & Hu, J. (2006). Pressure Drop and Cleaning of In-Use Ash Loaded Diesel Particulate Filters. (SAE Technical Paper Series 2006-01-3256). Warrendale, PA: SAE International.
- [93] Stunnenberg, F., Kleijwegt, P. & de Vries Feyens, A. W. L. (2001). Future Heavy Duty Diesel Lubricants For Low Emission Engines. (SAE Technical Paper Series 2001-01-3768). Warrendale, PA: SAE International.

- [94] Kyto, M., Aakko, P., Nylund, N. & Niemi, A. (2002). Effect of Lubricant on Particulate Emissions of Heavy Duty Diesel Engines. (SAE Technical Paper Series 2002-01-2770). Warrendale, PA: SAE International.
- [95] Arrowsmith, S. (2003). Challenges for Future Heavy Duty Diesel Lubricant Development: PC-10/DX-2/Euro IV. (SAE Technical Paper Series 2003-01-1964). Warrendale, PA: SAE International.
- [96] Jung, H., Kittelson, D. B. & Zachariah, M. R. (2003). The Influence of Engine Lubricating Oil on Diesel Nanoparticle Emissions and Kinetics of Oxidation. (SAE Technical Paper Series 2003-01-3179). Warrendale, PA: SAE International.
- [97] Kurihara, I., Takeshima, S. & Yashima, H. (2004). Development of Low-Ash Type Heavy Duty Diesel Engine Oil for After-treatment Devices. (SAE Technical Paper Series 2004-01-1955). Warrendale, PA: SAE International.
- [98] Czerwinski, J., Petermann, J.-L., Ulrich, A., Mueller, G. & Wichser, A. (2005). Particle Emissions of a TDI-Engine with Different Lubrication Oils. (SAE Technical Paper Series 2005-01-1100). Warrendale, PA: SAE International.
- [99] Hoshino, T., Kubo, K., Nakamura, K., Yamashita, M., Hashimoto, T., Tomizawa, K., et al. (2005). New Four-stroke Diesel Engine Oil Standards for Japanese Market : JASO DH-2 and DL-1. (SAE Technical Paper Series 2005-01-3718). Warrendale, PA: SAE International.
- [100] Takamura, S., Kumakura, A., & Yoshida, H. (1998). Development of New Generation Low Ash Type Diesel Engine Oils for Heavy Duty Vehicles. (SAE Technical Paper Series 982719). Warrendale, PA: SAE International.
- [101] Baik, D. S., Oh, S. G., Han, Y. C. & Lee, J.-S. (2004). The Effect and Behavior of Continuous Regeneration DPF for HD Diesel Engine. (SAE Technical Paper Series 2004-01-3041). Warrendale, PA: SAE International.
- [102] Ahlstrom, A. F. & Odenbrand, C. U. I. (1989). Combustion characteristics of soot deposits from diesel engines. *Carbon*, 27(3), 475-483.

- [103] Rothe, D., Zuther, F. I., Jacob, E., Messerer, A., Poschl, U., Niessner, R., et al. (2004). New Strategies for Soot Emission Reduction of HD Vehicles. (SAE Technical Paper Series 2004-01-3046). Warrendale, PA: SAE International.
- [104] Jacquot, F., Logie, V., Brillhac, J. F., & Gilot, P. (2002). Kinetics of the oxidation of carbon black by NO<sub>2</sub>: Influence of the presence of water and oxygen. *Carbon*, 40, 335-343.
- [105] Soeger, N., Mussmann, L., Sesselmann, R., Leippe, G., Gietzelt, C., Bailey, O., et al. (2005). Impact of Aging and NOX/Soot Ratio on the Performance of a Catalyzed Particulate Filter for Heavy Duty Diesel Applications. (SAE Technical Paper Series 2005-01-0663). Warrendale, PA: SAE International.
- [106] Neely, G. D., Sasaki, S., Huang, Y., Leet, J. A. & Stewart, D. W. (2005). New Diesel Emission Control Strategy to Meet US Tier 2 Emissions Regulations. (SAE Technical Paper Series 2005-01-1091). Warrendale, PA: SAE International.
- [107] Sua, D. S., Jentoft, R. E., Müller, J.-O., Rothe, D., Jacob, E., Simpson, C. D., et al. (2004). Microstructure and oxidation behaviour of Euro IV diesel engine soot: a comparative study with synthetic model soot substances. *Catalysis Today*, 90, 127–132.
- [108] Fayard, J. -C., Joubert, E. & Seguelong, T. (2005). A New Active DPF System for "Stop & Go" duty Cycle Vehicles: Durability and Improvements. (SAE Technical Paper Series 2005-01-1754). Warrendale, PA: SAE International.
- [109] Hurta, R. H. & Haynes, B. S. (2005). On the origin of power-law kinetics in carbon oxidation. *Proceedings of the Combustion Institute*, 30, 2161–2168.
- [110] Nakane, T., Ikeda, M., Hori, M., Bailey, O. & Mussmann, L. (2005). Investigation of the Aging Behavior of Oxidation Catalysts Developed for Active DPF Regeneration Systems. (SAE Technical Paper Series 2005-01-1759). Warrendale, PA: SAE International.
- [111] Vander Wal, R. L., Yezerets, A., Currier, N. W., Kim, D. H., & Wang, C. M. (2007). HRTEM Study of diesel soot collected from diesel particulate filters. *Carbon*, 45, 70–77.

- [112] Balle, P., Bockhorn, H., Geiger, B., Jan, N., Kureti, S., Reichert, D., et al. (2006). A novel laboratory bench for practical evaluation of catalysts useful for simultaneous conversion of NO<sub>x</sub> and soot in diesel exhaust. *Chemical Engineering and Processing* 45, 1065–1073.
- [113] Midwest Refineries. (2005). *Refining and Assaying*. Retrieved December 12, 2007, from <http://www.midwestrefineries.com/refiningandassaying.htm>
- [114] Liberatore, P. (1993, July). *Determination of majors in geological samples by ICP-AES*. Retrieved November 19, 2008 at <https://www.varianinc.com/media/sci/apps/icpes012.pdf>

## **VITA**

Adam Youngquist was born in Las Vegas, NV on 23 October 1981. He graduated from Colerain High School in June 2000. While there, he was a three sport athlete, garnering several varsity scholar athlete awards in addition to academic achievement awards in all four years. In addition, he was inducted into the National Honor Society and the Spanish Honor Society in 2000. Later, he graduated Magna Cum Laude from the University of Tennessee – Knoxville in May 2005 with a Bachelor of Science in Aerospace Engineering. While in attendance, Adam became a member of Tau Beta Pi and Sigma Gamma Tau. Beginning fall 2005, he attended the University of Tennessee – Knoxville where he earned his Master of Science degree in Mechanical Engineering in May of 2008.

Adam is a member of the Society of Automotive Engineers and The American Society of Mechanical Engineers.